



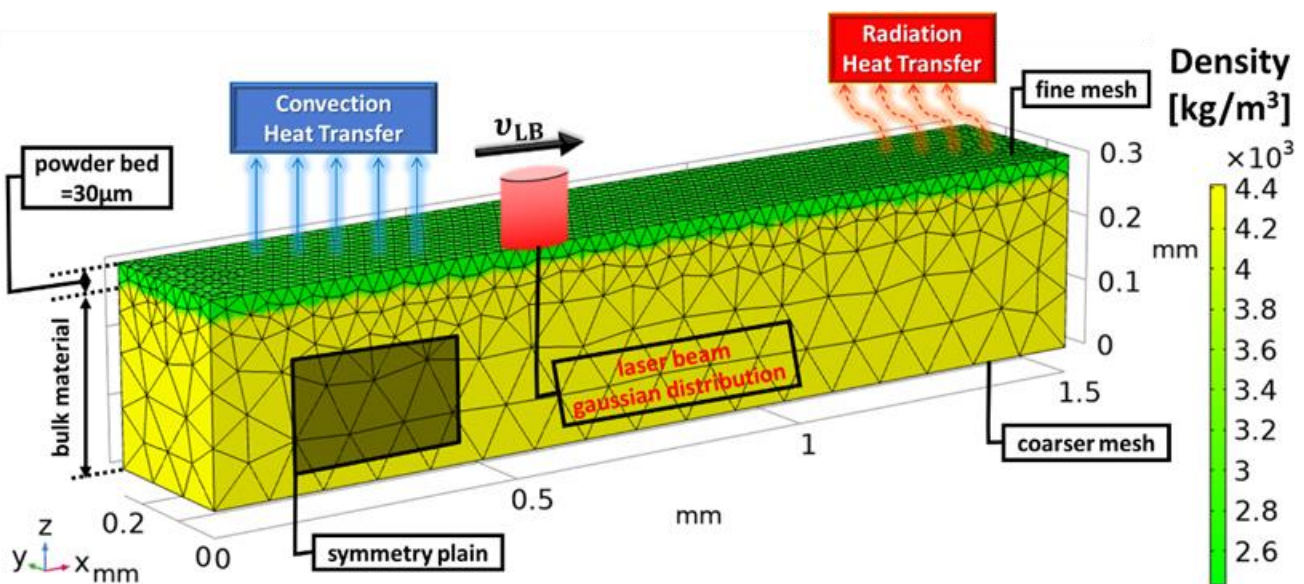
NATIONAL TECHNICAL UNIVERSITY OF ATHENS
SCHOOL OF MECHANICAL ENGINEERING

Diploma thesis

Study and modeling of the transition from conduction to keyhole mode during SLM process

Vasiliki E. Alexopoulou (02116097)

2020-2021



Section: Manufacturing Technology

Supervisor: A. Markopoulos, Assoc. Professor, NTUA

Acknowledgments

Both before as well as during the process of writing this diploma thesis several people directly or indirectly inspired or assisted me. The least I can do to express my gratitude to them is to acknowledge in the following lines their valuable contribution.

Sincere gratitude goes to Assoc. Prof. A. Markopoulos (NTUA) who was my diploma thesis supervisor at NTUA and commented and provided me with guidance with regard to the modeling and simulation of Selective Laser Melting (SLM).

Particularly helpful for the fine-tuning of this thesis was E. L. Papazoglou (PhD candidate, NTUA) who was kind enough to listen to my thoughts, provide me with feedback and shape many of the ideas included herein through various e-mails and Skype calls we exchanged.

Above all I wish to wholeheartedly thank my parents, Evaggelos and Margarita, who provided all kinds of support for the authoring of this thesis and have ensured by personal sacrifices that I receive the best possible education and my brother, Konstantinos who provided me his computer, when my own laptop crushed down...



Vasiliki E. Alexopoulou

Athens

July 2021

Table of Contents

Acknowledgments	2
Abstract	8
Abstract in Greek	9
Nomenclature	11
1. Introduction to Additive Manufacturing (AM)	14
1.1 Evolution of AM Technologies	14
1.2 Fundamental AM steps	15
1.3 AM Application Levels	17
1.3.1 Direct processes	17
1.3.1.1 Rapid prototyping	17
1.3.1.2 Rapid Manufacturing	18
1.3.1.3 Rapid Tooling	19
1.3.2 Indirect processes	20
1.3.2.1 Indirect prototyping	20
1.4 AM basic principles and processes	21
1.4.1 Polymerization	22
1.4.2 Stereolithography	22
1.4.3 Polymer Printing and –Jetting	24
1.4.4 Digital Light Processing	25
1.4.5 Micro Stereolithography	26
1.4.6 Sintering and Melting	27
1.4.6.1 Laser Sintering – Selective Laser Sintering (LS – SLS)	27
1.4.6.2 Laser Melting – Selective Laser Melting (SLM)	29
1.4.6.3 Electron Beam Melting	30
1.4.7 Extrusion – Fused Layer Modeling	31
1.4.7.1 Fused Deposition Modeling (FDM)	31
1.4.8 Powder-Binder Bonding – Three-Dimensional Printing (Drop on Powder Processes)	32
1.4.8.1 Three-Dimensional Printing – Z-Corporation	32
1.4.8.2 Three-Dimensional Printing – Prometal	34
1.4.9 Layer Laminate Manufacturing (LLM)	35
1.4.9.1 Layer Laminate Manufacturing, Laminated Object Manufacturing (LOM)	35

1.4.9.2 Layer Laminate Manufacturing, Paper Lamination, MCOR Matrix	36
1.4.9.3 Layer Laminate Manufacturing, Plastic Laminate Printers	37
1.4.9.4 LLM Machines for Metal Parts	38
1.4.10 Other Processes: Aerosolprinting and Bioplotter	39
1.4.10.1 Aerosolprinting	39
1.4.10.2 Bioplotter	39
1.4.11 Summary of AM Processes	40
1.5 Advantages of AM Processes	40
1.6 Challenges of AM Processes	41
1.7 Pros and Cons of AM with Respect to Conventional Manufacturing Techniques (CMTs)	42
1.8 AM Materials	44
1.9 Defects in AM Parts	45
1.9.1 Balling Phenomena	45
1.9.2 Porosity Defects	45
1.9.3 Cracks	46
1.9.4 Distortion	46
1.9.5 Stair-stepping effect	47
1.10 Post-processing of laser additive manufacturing (LAM) parts	48
1.11 AM Applications	50
1.11.1 Artistic	50
1.11.2 Personalized	51
1.11.3 Medical	53
1.11.4 Aerospace	54
1.11.5 Automotive	57
1.11.6 Industrial Applications Molds and Tooling	59
1.11.7 Remanufacture and Repair	59
1.11.8 Scanning and Reverse Engineering	60
1.11.9 Construction	61
1.11.10 Defense	62
1.12 AM Forecast	62
2. Selective Laser Melting (SLM)	64
2.1 Definition	64

2.2 SLM Basic Mechanism	64
2.3 SLM Advantages and Disadvantages	64
2.4 SLM Machine and Equipment	65
2.4.1 Basic Units and Process Layout	65
2.4.2 Preheating Stage	66
2.5 SLM Physical Phenomena	67
2.5.1 Laser beam	67
2.5.2 The Melting Pool	69
2.6 Processing Aspects	74
2.6.1 Starting Powder	74
2.6.2 Input Parameters (Laser Power, Scanning Speed, Layer Thickness, Scan Line Spacing)	74
2.6.3 Scanning Strategies	75
2.6.4 Laser Remelting and Laser Erosion	76
2.6.5 Single Track Scans	77
2.7 SLM Potential Defects	77
2.8 Microstructural features	81
2.8.1 Texture	81
2.8.2 Non-equilibrium microstructure	83
3. SLM State-Of-The-Art	84
4. Model and Simulation	99
4.1 Model Description	99
4.1.1 Size and Shape	99
4.1.2 Position	100
4.2 Material Properties	100
4.2.1 N ₂ Properties	100
4.2.2 Bulk Ti6Al4V properties	105
4.2.3 Porous Ti6Al4V	108
4.2.4 Model's material properties	113
4.2.5 Phase Change	114
4.3 Physical Model Governing Equations	115
4.3.1 Heat Transfer in Solids	115
4.3.2 Initial Condition	115

4.3.3 Boundary Condition	115
4.3.4 Deposited Beam Power	116
4.3.4.1 Surface perpendicular vector n	116
4.3.4.2 Deposited Beam Power P_o	116
4.3.4.3 Beam orientation vector e	119
4.3.4.4 Beam origin point O	119
4.3.4.5 Beam distribution type function $f(O, e)$	119
4.3.4.6 Standard deviation σ	120
4.3.5 Convective heat flux	120
4.3.6 Surface-to-Ambient Radiation	120
4.4 Deformed Geometry	121
4.4.1 Deformed Geometry vs Moving Mesh	121
4.4.2 Deforming Domain	121
4.4.3 Smoothing	121
4.4.4 Symmetry	123
4.4.5 Prescribed Normal Mesh Velocity	123
4.5 Numerical Computation:	127
4.5.1 Mesh	127
4.5.1.1 Cartesian meshing	127
4.5.1.2 Tetrahedral meshing	127
4.5.2 Mesh Refinement	129
4.5.3 Study	130
4.5.4 Visual Representation	130
4.5.5 Results Validation	130
5. Results and Discussion	131
5.1 Basic physical fundamental mechanisms used for the analysis of the results	131
5.1.1 Conduction mode vs transition mode vs keyhole mode	131
5.1.2 Definition of melting pool steady-state	131
5.1.3 The β_R determination	132
5.2 Simulation results and discussion	133
5.3 Comparison between simulation and experimental results	134
5.4 50W-1200mm/s analysis	138
5.5 195W-750mm/s analysis	139

5.6 195W-500mm/s analysis	141
5.7 Percentage reduction of maximum power intensity	143
5.8 Material removal rate.....	144
6. Conclusions	145
References.....	146

Abstract

Additive manufacturing (AM), also known as 3D printing, is a transformative approach to industrial production that enables the creation of lighter, stronger parts and systems. It is yet, another technological advancement made possible by the transition from analog to digital processes. In recent decades, communications, imaging, architecture and engineering have all undergone their own digital revolutions. Now, AM can bring digital flexibility and efficiency to manufacturing operations. Additive manufacturing uses data computer-aided-design (CAD) software or 3D object scanners to direct hardware to deposit material, layer upon layer, in precise geometric shapes. As its name implies, additive manufacturing adds material to create an object. By contrast, when an object is created by traditional means, it is often necessary to remove material through milling, machining or other means. While additive manufacturing seems new to many, it has actually been around for several decades. In the right applications, additive manufacturing delivers a perfect trifecta of improved performance, complex geometries and simplified fabrication. As a result, opportunities abound for those who actively embrace additive manufacturing.

The 1st chapter of this study is an introduction to AM processes. Evolution, fundamental steps, the categories and technologies, the advantages and challenges of AM are all presented. Moreover, the AM defects and post-processing are discussed. Finally, the most interesting applications and a forecast for the evolution of AM are given.

The 2nd chapter focuses on a specific AM technology, known as Selective Laser Melting (SLM). The basic mechanism and equipment used are described in this study. Furthermore, the physical phenomena and their effect on final part properties are discussed. In the end, the melting pool geometry, the input parameters (laser power, scanning speed, layer thickness, scan line spacing) and the different melting pool modes (conduction, keyhole, transition) are presented.

In the 3rd chapter, the SLM state-of-the-art is given. Both experimental and theoretical papers, that try to estimate or predict the melting pool geometry, are presented.

In the 4th chapter, a SLM simulation, that predicts the Ti6Al4V melting pool geometry, is developed. In this study, a heat transfer model coupled with deformed geometry physics, which utilize only one semi-empirical coefficient, is used. Temperature dependency of material thermophysical properties, material ablation, latent heat, convection, radiation and gaussian heat source physics are all taken into consideration.

In the 5th chapter, the simulation results are compared with experimental data, taken by bibliography. Detailed discussion about how process parameters and the semi-empirical coefficient affect the melting pool geometry and modes is also given.

Abstract in Greek

Οι Προσθετικές Κατεργασίες (ΠΚ), επίσης γνωστές και με τον όρο Τρισδιάστατη Εκτύπωση, αποτελούν μία νέα προσέγγιση της βιομηχανικής παραγωγής που επιτρέπουν τη δημιουργία ελαφρύτερων και στιβαρότερων τεμαχίων και συστημάτων. Ωστόσο, αυτή η τεχνολογική πρόοδος κατέστη δυνατή με τη μετάβαση από αναλογικές σε ψηφιακές διαδικασίες. Τις τελευταίες δεκαετίες, οι επικοινωνίες, η απεικόνιση, η αρχιτεκτονική και η μηχανική έχουν υποστεί όλες τις δικές τους ψηφιακές επαναστάσεις. Τώρα, οι ΠΚ μπορούν να προσφέρουν ψηφιακή ευελιξία και αποδοτικότητα στις κατασκευές. Η κατασκευή τεμαχίων με ΠΚ χρησιμοποιεί λογισμικό σχεδιασμού με τη βοήθεια υπολογιστή (CAD) και σαρωτές τρισδιάστατων αντικειμένων για να κατευθύνει το υλικό, να το αποθέσει, στρώση-στρώση, σε ακριβή γεωμετρικά σχήματα. Όπως υποδηλώνει το όνομα αυτών των κατεργασιών, η κατασκευή με ΠΚ προσθέτει υλικό για τη δημιουργία ενός αντικειμένου. Αντίθετα, όταν ένα αντικείμενο δημιουργείται με παραδοσιακά μέσα, είναι συχνά απαραίτητο να αφαιρεθεί το υλικό μέσω φρεζαρίσματος, τόννευσης ή άλλων μέσων. Ενώ οι ΠΚ φαίνονται νέες κατεργασίες για πολλούς, στην πραγματικότητα υπάρχουν εδώ και αρκετές δεκαετίες. Με κατάλληλες εφαρμογές, οι ΠΚ παρέχουν ένα τέλειο συνδυασμό βελτιωμένης απόδοσης, σύνθετων γεωμετριών και απλής κατασκευής.

Το 1ο κεφάλαιο αυτής της μελέτης είναι μια εισαγωγή στις ΠΚ. Παρουσιάζονται όλες οι εξελίξεις, τα θεμελιώδη βήματα, οι κατηγορίες και οι τεχνολογίες, τα πλεονεκτήματα και οι προκλήσεις των ΠΚ. Επιπλέον, συζητούνται τα ελαττώματα των ΠΚ και οι διεργασίες φινιρίσματος. Τέλος, δίνονται οι πιο ενδιαφέρουσες εφαρμογές των ΠΚ και μια πρόβλεψη για την εξέλιξη τους.

Το 2ο κεφάλαιο επικεντρώνεται σε μια συγκεκριμένη τεχνολογία ΠΚ, γνωστή ως Selective Laser Melting (SLM). Ο βασικός μηχανισμός και ο εξοπλισμός που χρησιμοποιούνται περιγράφονται σε αυτήν τη μελέτη. Επιπλέον, συζητούνται τα φυσικά φαινόμενα και η επίδρασή τους στις ιδιότητες του τελικού τεμαχίου. Στο τέλος, παρουσιάζονται η γεωμετρία του τήγματος, οι παράμετροι εισόδου (ισχύς λέιζερ, ταχύτητα σάρωσης, πάχος στρώσης, απόσταση γραμμής σάρωσης) και οι διάφοροι τύποι τήγματος (conduction, keyhole, transition mode).

Στο 3ο κεφάλαιο, δίνεται οι σύγχρονες επιστημονικές μελέτες που αφορούν το SLM. Παρουσιάζονται τόσο πειραματικές όσο και θεωρητικές δημοσιεύσεις, οι οποίες προσπαθούν να εκτιμήσουν ή να προβλέψουν τη γεωμετρία του τήγματος.

Στο 4ο κεφάλαιο, αναπτύσσεται μια προσομοίωση SLM, η οποία προβλέπει τη γεωμετρία του τήγματος σε υλικό Ti6Al4V. Σε αυτή τη μελέτη, χρησιμοποιείται ένα μοντέλο μεταφοράς θερμότητας σε συνδυασμό με τη φυσική της παραμορφωμένης γεωμετρίας και χρησιμοποιεί μόνο έναν ημι-εμπειρικό συντελεστή. Η εξάρτηση των υλικών θερμοφυσικών ιδιοτήτων του υλικού από την θερμοκρασία, η μεταφορά μάζας λόγω εξάτμισης, η λανθάνουσα θερμότητα, η συναγωγή θερμότητας, η ακτινοβολία και η φυσική που διέπει την γκαουσιανή κατανομή, που προσομοιώνει την πηγή θερμότητας, λαμβάνονται υπόψη.

Στο 5ο κεφάλαιο, τα αποτελέσματα της προσομοίωσης συγκρίνονται με πειραματικά δεδομένα, που λαμβάνονται από τη βιβλιογραφία. Παρέχεται επίσης λεπτομερής συζήτηση σχετικά με τον τρόπο με τον οποίο οι παράμετροι της διαδικασίας και ο ημιεμπειρικός συντελεστής επηρεάζουν τη γεωμετρία και τους τύπους του τήγματος.

Nomenclature

Symbols	SI unit	Definition
A_H	m^2	Area fraction of the surface occupied by the radiation-emitting holes
$A_{Ti}, A_{Al}, A_V,$ $A_{Ti6Al4V}$	1	Atomic mass number of Ti, Al, V, Ti6Al4V
B	1	Deformation parameter of the particle
C_1, C_2, C_3	1	Artificial material properties
C_p	J/kgK	Model heat capacity with latent heat included
$C_{p_{model}}$	J/kgK	Model heat capacity
$C_{p_{N2}}$	J/kgK	Nitrogen heat capacity
$C_{p_{powder}}$	J/kgK	Powder heat capacity
$C_{p_{Ti6Al4V}}$	J/kgK	Bulk Ti6Al4V heat capacity
D	m	Control volume depth
D_b	m	Laser beam diameter
d	m	Width of melt
d_g	m	Distance of x from e
E_p	J/mm ³ or J/mm ²	Energy Density
e	1	Beam orientatin vector
f	1	Beam distribution type function
Gr	1	Grashof number
g	m/s ²	Acceleration of gravity
H	m	Control volume height
h_{N2}	W/m ² K	Nitrogen convective heat transfer coefficient
J, I_1	1	Invariants
k	W/mK	Model thermal conductivity with latent heat included
k_B	J/K	Boltzmann constant
$k_{contact}$	W/mK	Thermal conductivity due to powder particle contact
k_{model}	W/mK	Model thermal conductivity
k_{N2}	W/mK	Nitrogen thermal conductivity
k_{powder}	W/mK	Powder thermal conductivity
k_R	W/mK	Powder bed thermal conductivity owing to radiation
$k_{Ti6Al4V}$	W/mK	Bulk Ti6Al4V thermal conductivity
L	m	Characteristic length of specimens
$L_{j \rightarrow j+1}$	J/kg	Latent heat due to transition from phase j to phase $j+1$

L_v	J/kg	Latent heat of vaporization
l	m	Length of melt
m	kg	Mass per atom of metal
N_A	atoms/mol	Avogadro number
Nu	1	Nusselt number
\mathbf{n}	1	Perpendicular vector to a surface
\mathbf{O}	m	Beam origin point
P	W	Laser power
P_o	W	Deposited beam power
Pr	1	Prandtl number
p_o	Pa	Ambient pressure
p_{sat}	Pa	Saturated vapor pressure
Q	W/m^2	Heat rate per unit surface
\mathbf{q}	W/m	Heat flux vector
\mathbf{q}_{conv}	W/m	Heat flux due to convection
\mathbf{q}_{LB}	W/m	Heat flux due to the laser
\mathbf{q}_{rad}	W/m	Heat flux due to radiation
Ra	1	Rayleigh number
s	m	Scan line spacing
T_∞	K	Ambient temperature
T_{max}	K	Maximum element of each element
$T_{pc,j \rightarrow j+1}$	K	From j to $j+1$ phase change temperature
T_v	K	Boiling point
t	m	Layer thickness
V_{evap}	m/s	Mass flux due to evaporation
v	m/s	Scanning speed
v_n	m/s	Normal mesh velocity
W	m	Control volume width
W_{mesh}	J	Mesh deformation energy
X, Y, Z	m	Material frame coordinates
\mathbf{x}	m	The position where the laser intensity is calculated via the gaussian distribution
x, y, z	m	Spatial frame coordinates
x_R	m	Powder median particle diameter

Greek symbols	SI unit	Definition
α	1	Material absorptivity
β_{N_2}	1/K	Nitrogen thermal expansion coefficient
β_R	1	Ratio of atoms that recombine to the surface to the atoms that evaporate from the melt surface
γ_{LV}	Pa	Melting pool surface tension
ϵ_H	1	Emissivity of the hole
ϵ_{powder}	1	Powder emissivity
$\epsilon_{Ti6Al4V}$	1	Bulk Ti6Al4V emissivity
θ	rad	Contact angle
θ_j	1	Fraction of contribution of phase j to the latent heat
κ	1	Artificial bulk moduli
λ	m	Laser wavelength
μ	Pa s	Nitrogen viscosity
ν	1	Artificial shear moduli
ρ	kg/m ³	Model density with latent heat included
ρ_f	1	Material reflectivity
ρ_{model}	kg/m ³	Model density
ρ_{N_2}	kg/m ³	Nitrogen density
ρ_{powder}	kg/m ³	Powder density
$\rho_{Ti6Al4V}$	kg/m ³	Bulk Ti6Al4V density
σ	m	Standard deviation of gaussian distribution
σ_B	W/m ² K ⁴	Stefan-Boltzmann constant
σ_r	Pa	Residual stress
τ	1	Material transmissivity
Φ	1	Flattened surface fraction of particle in contact with another particle
ϕ	1	Powder porosity

1. Introduction to Additive Manufacturing (AM)

1.1 Evolution of AM Technologies

Development of AM technologies was gradual over the first decade of its advent. However, recently owing to advancements in manufacturing, associated technologies, customer expectations and global markets, the development rates have witnessed a huge upsurge. The first AM patent was filed by Dr. Kodama (Japan, 1980). Dr. Charles Hull (SLA, 1987) is considered to be the forerunner of the effective commencement of AM/3DP. Almost around the same time, a patent by Carl Deckard (SLS, 1987) was filed and granted, and later acquired by 3D Systems. Dr. Scott Crump (FDM, 1989) filed the next patent which was granted, and later acquired by Stratasys (1992). This was a landmark development in the sense that a vast variety of RepRap (Replicating Rapid prototyper) modelers are based upon FDM technology. EOS GmbH (Hans Langer, 1989) was founded which focused largely on laser sintering, stereos and direct metal laser sintering systems. Several other systems emerged around the same time; these included laminated object manufacturing (LOM) by Helisys (Michael Feygin, 1990s), ballistic particle manufacture (BPM) (William Masters, 1990s), solid ground curing (SGC) by Cubital (Ifz Chak Pomerant et al., 1990s), 3DP by 3D systems (Emanuel Sachs, 1990s). Sanders Prototype (1996), Z Corp (1996) and Objet (1998) also came into being. LOM, SLA, BPM and SGC have not survived over the years due to various technical limitations. One remarkable event during the middle of the twentieth century needs special mention. This included development of two discrete categories of AM processes: first, high-end expensive AM systems for fabricating complex, intricate and high-value parts to be used in aerospace, automobile, medicine, jewelry, etc. applications; second, a moderately priced category of concept modelers to be used in concept modelling, functional prototyping, assembly validation, etc. applications. The second category of modelers emerged due to the highly competitive markets.

The twenty-first century saw a shift in the AM applications paradigm from R&D and prototyping to industrial and functional part fabrication. The term RP has gradually been replaced by AM, which includes both direct and indirect AM and involves a variety of aspects of prototyping, tooling and manufacturing. Emergence of technologies like selective laser melting (SLM) (2000), Envision Tec (2002), EBW/Exone (2005) was witnessed over time. Gradually, due to a variety of favorable features like improved prices, speeds, materials and accuracy, 3D Systems developed their first AM system priced below \$10,000. Next in line came the concept of a \$5000 desktop factory system that had to be shelved and did not come into being. Self-replicating machines based upon RepRap technology (Dr. Bowyer, 2009) led to a revolution in the AM market and led to this open-source technology transforming itself into an industrial practice through which every interested person could access the idea of AM printers. Since then, a large variety of AM printers based upon this technology have become widely available. Alternative AM processes emerged via B9 creators (2012). Form 1 Modeler (2012) also materialized around the same time. Over the last decade, progress in the field of AM has been so widespread that it is difficult to single out every noteworthy advancement [1].

1.2 Fundamental AM steps

Each AM process follows a series of steps in the process of conversion of 3D CAD data to a physical part. There is a variation in the extent and technique of AM utilization with change in part type. While simple parts can be directly printed, complicated parts need iterative designs and a multitude of considerations. Also, concept models and prototypes can be roughly prepared but components to be used as end products require careful planning as well as post-processing.

Basically, there are eight steps in all types of AM techniques which can be divided into pre-processing, machine processing and post-processing. Pre-processing includes design of part in CAD as well as converting it into STL file format which has to be exported to AM machine for further processing. During the second stage (machine processing), the CAD models are sliced into required thickness of layers and then the physical 3D model is generated with layer-by-layer deposition of material. In the third stage, the finished part is removed from machine and is processed with various methods in order to enhance its mechanical and other properties [2].

The eight fundamental AM steps that are more or less common to each technique can be understood as follows:

Step 1: Obtaining 3D CAD data of the desired part

3D CAD data which fully describes the part to be fabricated is obtained either directly from professional 3D software or from 2D data with additional information, or from reverse engineering or any other means. An important point to be kept in mind is that this data should fully represent the solid/surface for the part.

Step 2: Conversion of data from step 1 into .stl format

Most of the AM modelers take input in the form of .stl format which can be obtained directly as input from the CAD software utilized in step 1. External closed surfaces are described in this format and slices are calculated based upon this format.

Step 3: Transferring .stl file to modeler

This .stl file is transferred to the AM modeler along with necessary inputs regarding the tool path generation, machine parameters, orientation, as well as size and position.

Step 4: Setting up machine parameters

The machine should be properly set up, pre-warmed if necessary, proper power requirements should be provided, model material and raw material spools should be thoroughly checked, proper operation of valves, compressor, machine build center panel, build platform, etc. should be ensured before firing the build command.

Step 5: Part building

The superiority of AM processes emanates from the fact that the part building process is completely automated. However, intermittent checking can be undertaken to ensure power consistency, spool malfunction, software related issues, etc.

Step 6: Part removal from the modeler

This has to be undertaken in a judicious manner once the part is finished. This may require consideration of temperature of build volume, some inherent interlocking features of the machine, support layers at base, etc.

Step 7: Post-processing

There is a need to clean up the part before it can be put to final use. Some support features may be required to be taken care of with due consideration of the strength of the parts. Wherever required, this demands skill and expertise.

Step 8: Applications

Before final application, treatments like painting, improving texture, priming, improving surface finish and so on may be required. Sometimes, assembling individual components is also required if the parts are sub-components of a larger part.

However, for the ease of understanding, some of these eight steps can be combined and reclassified as the five AM steps named below [1] and presented in Fig. 1.1:

- CAD-based modelling
- Preparation of .stl file
- Slicing of layers
- Actual part building
- Finishing of end part

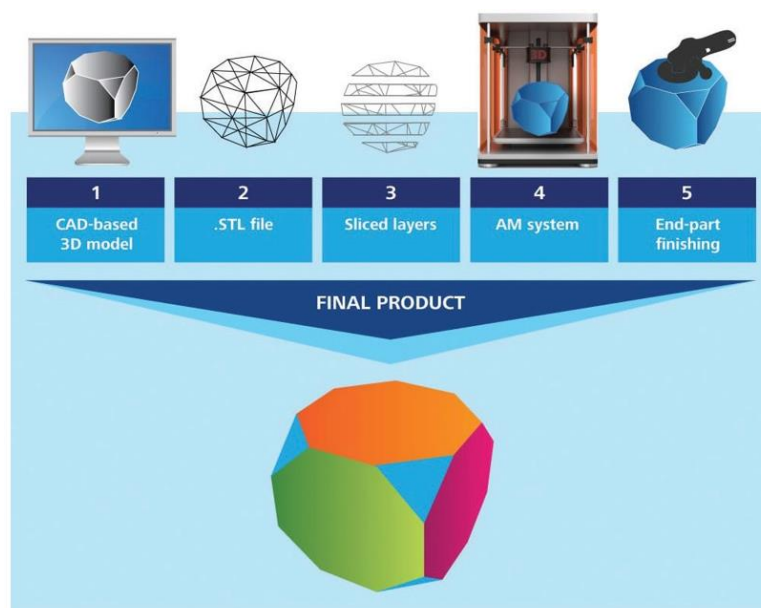


Fig. 1.1 AM Process Flow Chain.

1.3 AM Application Levels

AM technologies are characterized by the main application levels of rapid prototyping and rapid manufacturing.

Rapid prototyping includes all applications that result in prototypes, models, or mock-ups. Rapid manufacturing is applied when final products or simply products are to be generated.

1.3.1 Direct processes

All additive manufacturing processes are named *direct processes* to express that, out of the digital data model by means of an additive machine, a physical object – called a part – is directly generated. In contrast, some processes are named *indirect processes*. These processes do not apply the principle of layer manufacturing, and are consequently not considered as AM processes. Indeed, indirect processes are copy work, which normally is executed as vacuum casting using silicone molds.

1.3.1.1 Rapid prototyping

With regard to the application level rapid prototyping, two sublevels can be identified: *solid imaging* (generating a three-dimensional mock-up or a sculpture) on the one hand and *concept modeling* (generating a concept model) on the other.

By solid imaging or concept modeling a parts family is generated, which serves to verify a basic concept. The parts resemble a three-dimensional image or a sculpture. In most cases, they cannot be loaded physically. They merely show a special representation to judge the general appearance and the proportions. Therefore, these parts are also called *show-and-tell models*. Scaled concept models are often used to illustrate complex CAD drawings. In this context, they are also designated as *data control models*. The examination of the dimensions serves to check the CAD data.

Colored models manufactured by means of 3D printing are estimation tools for concept development. Coloring helps in the recognition of difficult zones of a product and to shorten discussions. Fig. 1.2 shows a solid image of a cut-away model of a combustion engine. Different colors of the model can be, for example, linked to the main topics of the items for discussion. In reality, the part is of course not colored.



Fig. 1.2 Solid image or concept model. Cut-away demonstration part of a combustion engine with 3D printing.

Functional prototyping is applied to examine and verify one or multiple separate functions of the later product or to take the decision for the production, even if the model cannot be used as a final part.

As shown in Fig. 1.3, the model of an adjustable air-outlet grille for the air conditioning of a passenger car can be used to check the air distribution at a very early stage of the product development.



Fig. 1.3 Functional prototyping: adjustable air-outlet grille for a passenger car; laser stereolithography.

However, this kind of manufacturing is not suitable for serial manufacture, with respect to the mechanical and especially the thermal properties of the material, as well as to the color and the final price.

1.3.1.2 Rapid Manufacturing

The application level rapid manufacturing includes all processes that produce final products or deliver parts that have to be assembled afterwards to produce a product. A part generated by additive manufacturing (AM) will be designated as (final) product if it shows all properties and functions which have been determined during the development process of the product. If the generated part is a positive, the process is called direct manufacturing. In the case of a negative, e.g., a die, mold, or gauge, it is called direct tooling. Direct manufacturing leads to products which are generated directly by means of an AM process. A large variety of materials of all main material types (plastics, metals, and ceramics) is available.

It is essential for the function of the part that material and manufacturing process are generating exactly those mechanical-physical properties which have been defined during the design process (generally the engineering). If this is achieved, they mimic their behavior.

Fig. 1.4 shows a dental bridge, made of three elements from a CoCr alloy, which was manufactured by means of selective laser melting, SLM. The data file was generated by a digitized dental imprint of the patient.

The dental bridge was designed applying professional dental software (3 shape), and directly manufactured by means of SLM. After finishing and adjustment, the bridge was ready for fitting to the patient. Compared with traditional technology, the production of a directly manufactured bridge was faster with customized fit and comparable costs.



Fig. 1.4 Direct manufacturing: dental bridge (three elements directly after manufacturing; without removing of support structure (left), after finishing (right); selective laser melting (SLM), CoCr alloy.

1.3.1.3 Rapid Tooling

Rapid tooling encompasses all additive manufacturing processes, resulting in cores, cavities, or inserts for tools, dies, and molds. In addition, two sublevels can be distinguished: direct tooling and prototype tooling.

From the technical point of view, direct tooling is equivalent to direct manufacturing, but is confined to tool inserts, dies, and molds, which are produced for quantity serial manufacture.

Direct tooling does not mean that a complete tool is manufactured. In fact, mainly cavities (tool inserts) or sliders are generated. The complete tool is made by assembling the inserts and standard components, as it is done during conventional tool manufacturing.

The layer-based technology of all additive manufacturing processes enables the generation of tool-internal hollow structures. This allows the production of mold inserts with internal conformal cooling channels (Fig. 1.5) which follow the outlines of the tool insert below its surface.



Fig. 1.5 Direct tooling: mold insert with conformal cooling channels (dark) and pneumatic ejectors (white); laser sintering/ laser melting; tool steel.

Prototype tooling: For the production of small series, manufacture of a mold in series quality is often too time- and cost-consuming. If only a few parts are required, or frequently details have to be modified, usually a pilot mold made from a substitute material meets the requirements. Molds of this type show the quality of functional prototypes; however, they belong – at least partly – to the functional application level direct tooling. The corresponding application- level ranges between rapid prototyping and rapid manufacturing. This sublevel is called prototype tooling (manufacturing of prototype tools).

1.3.2 Indirect processes

Additive manufacturing produces a geometrically exact and scaled physical image of the virtual data set. However, this process also shows disadvantages, at least with respect to the majority of actual additive processes.

Additive Manufacturing Processes:

- Work with process- and consequently machine-dependent materials, and are restricted with regard to coloring, translucence, transparency, and elasticity.
- Do not result in significant cost reductions with increasing production volumes.
- Consequently, are relatively expensive when manufacturing numerous parts, particularly in series production.

To overcome these disadvantages, additive manufactured parts can serve as master models for subsequent copying or reproduction processes. This procedure often is named the separation of properties: the geometrically exact master is quickly generated by means of an AM process, while the required volume and the part's properties (like coloring, etc.) are obtained by subsequent copying processes.

The copying or follow-up process is not a layer-based process and therefore cannot directly be assigned to additive manufacturing. Consequently, it is called an indirect process.

To sum up, indirect processes combine AM techniques with traditional methods [3].

1.3.2.1 Indirect prototyping

Indirect prototyping is applied to improve the properties of an AM part in order to fulfill the requirements of the user, if an additively manufactured part does not represent this directly. If, for example, an elastic part is required and cannot be generated directly by means of an additive manufacturing process due to material restrictions, a geometrically exact rigid AM part is manufactured and used as master model for a subsequent casting process.

Possible shrinkage will be compensated for by scaling of the master model used for production.

Many different secondary processes are applied. The best- known process is vacuum casting or room temperature vulcanization, RTV, which is also called silicone rubber molding. Most of the secondary processes as vacuum casting are totally or partly manual processes with long

cycle times and therefore only applicable for prototyping, small series, or one-of-a-kind production.

For the “system plug” (Fig. 1.6), plug housings with different colors as well as partly transparent ones are required. Based on an additively manufactured master in two parts for the housing, a silicone mold was generated. With this mold, approximately 15 different copies were made by means of vacuum casting.

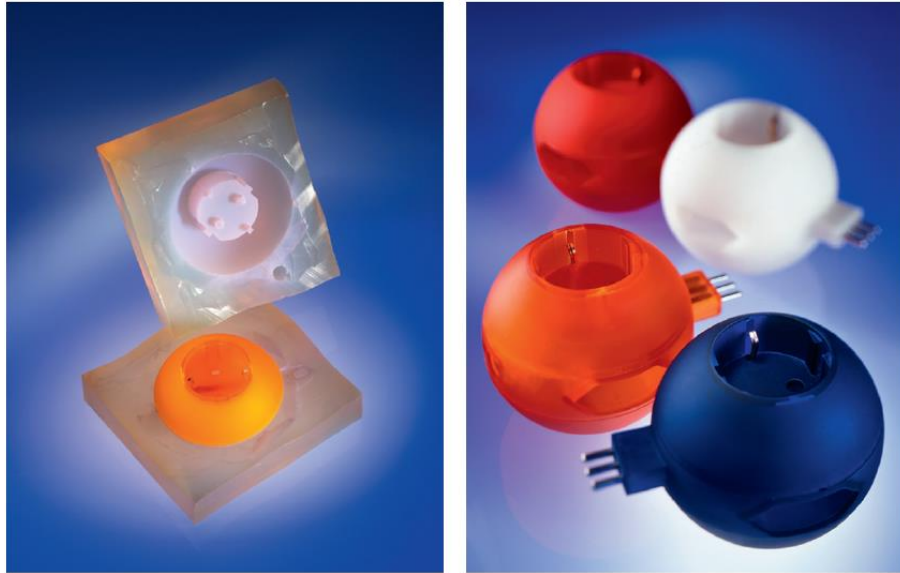


Fig. 1.6 Indirect prototyping: vacuum casting; system plug, master model made by means of stereolithography; mold with upper part of the plug housing (left), assembled plugs (right).

The cast parts served to be presented to an optional series producer in order to illustrate the new product and its qualities. The parts are prototypes, made from prototype material and thus not series products, even if they are functioning well [4].

1.4 AM basic principles and processes

The (physical) manufacturing process (the AM process) is focused on the revolving production of a single layer and its bonding to the preceding one. The process consists of only two steps that are repeated until the part is finished:

1. Generation of a single layer with a shape according to the contour and with a given layer thickness both based on the slice data.
2. Joining each new layer on top of the preceding one.

Today, there are considerably more than 100 different machines commercially available. All of them show the two basic manufacturing steps mentioned earlier. They only differ in the way, each layer is made, how successive layers are merged, and what material is processed.

The generation of the physical layer can be done using various materials, such as plastics, metals, or ceramics, supplied as powders, fluids, solids, foils, or sheets. Different physical

effects are used, such as photo-polymerization, selective fusing, melting, or sintering, cutting, particle bonding, or extrusion.

The contouring of each layer requires an energy source that generates the chosen physical effect and a handling device that controls the x-y coordinates. Commonly used are:

- lasers with galvo-type scanning devices, optical switches, or gantry-type handling systems
- electron beams,
- single- or multi-nozzle print heads,
- knives, extruders, or infrared heaters with plotters or DLP projectors.

All imaginable processes can be assigned to the following five basic families of AM processes [4]:

1.4.1 Polymerization

The selective solidification of liquid monomeric resin (of the epoxy-, acrylate, or vinyl ether type) by ultraviolet radiation is called (photo)-polymerization. There are various processes that differ only in the way the UV-radiation is generated and by the way the contouring is done. Some polymerization processes provide just a partially solidification. Consequently, a "green part" is made that requires additional curing to become a completely cured part. The additional curing is done after the build process using a special device called post-curing oven. It is equipped with UV emitting lamps to provide a complete and even solidification of the entire part.

During the build, polymerization processes need so-called supports. They are necessary to stabilize the entire part including overhangs, to match temporarily unconnected elements, to fix it on the platform, and to thwart distortion and warping. The supports are added to the 3D CAD model using automated software and have to be removed manually after the build. Some can be washed out automatically, using a special cleaning device.

1.4.2 Stereolithography

Stereolithography is not only the oldest but also still the most detailed AM process. It was invented and first commercialized by 3D Systems, Rock Hill, SC, USA. Laser stereolithography delivers parts with very good surfaces and fine details. The parts are created by local polymerization of the initially liquid monomers. Initiated by a UV-laser beam, the polymerization turns the liquid into a solid, leaving a scaled solid layer. The laser beam is directed by a galvo-type scanning device that is controlled according to the contour of each layer. A typical machine can be seen in Fig. 1.7.



Fig. 1.7 Laser Stereolithography (3D Systems).

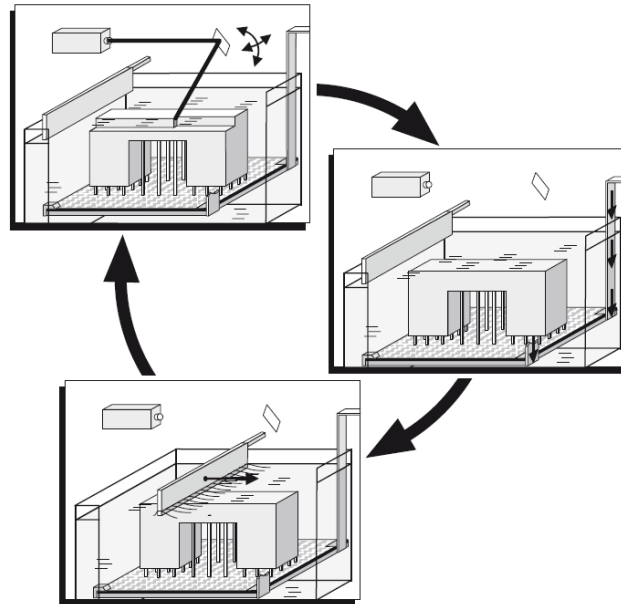


Fig. 1.8 Polymerization, laser stereolithography; scheme; solidification of a single layer, lowering of the platform, recoating (clockwise starting from top left).

A laser stereolithography machine consists of a build chamber filled with the liquid build material and a laser scanner unit mounted on top of it which generates the x-y contour. The build chamber is equipped with a build platform fixed on an elevator-like device that can be moved in the build (z-) direction (Fig. 1.8). On this platform the part is built. The laser beam simultaneously does the contouring and the solidification of each layer as well as the bonding to the preceding layer. The motion of the beam is controlled by the slice data of each layer and directed by the scanner.

As the beam penetrates the surface of the resin, an instantaneous solidification takes place. Depending on the reactivity and transparency of the resin, the layer thickness can be adjusted by the laser power and by its traveling speed.

After solidification of one layer, the build platform, including the partially finished part, is lowered by the amount of one layer thickness. A new layer of resin is applied. This is called recoating. Because of the low resin viscosity, the recoating procedure needs to be supported by wipers and vacuum depositing devices. The new layer is then solidified according to its contour. The process continues from the bottom to the top until the part is finished.

The process requires supports (Fig. 1.9, right), which limits the possible orientation of the part in the build chamber, because after removal the supports leave tiny spots on the surface. For this reason, the orientation should be chosen carefully. Because of the supports the parts cannot be nested to increase the packing density and the productivity accordingly.

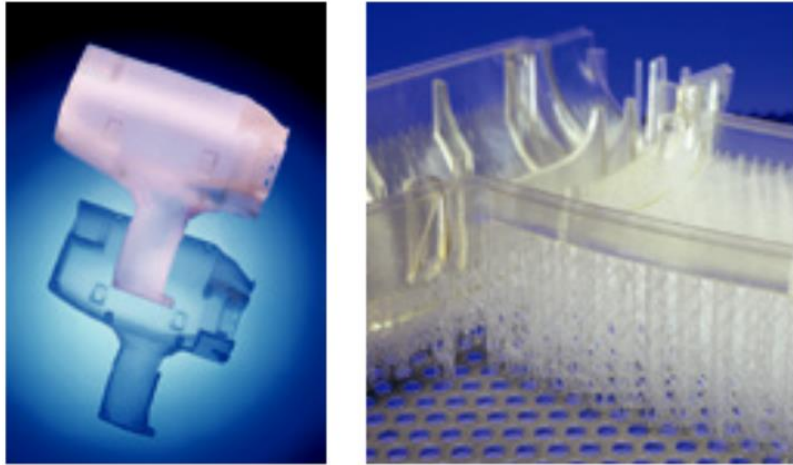


Fig. 1.9 Laser Stereolithography: thin-walled shell type parts (left), part with supports on the build platform (right).

After the build, the part is cleaned and finally fully post-cured in a UV chamber (post-curing oven). This process step is an integral part of the AM process and called “post processing”.

The parts can be sanded, polished, and varnished if necessary. These process steps are called “finishing”. Finishing is a process-independent step and not a part of the AM process. It depends only on the user requirements for the parts and possible restrictions regarding its application.

The available materials are unfilled and filled epoxy and acrylic resins. Unfilled materials show a comparably poor stability and heat deflection temperature. This can be improved by adding micro spheres or rice-grain shaped geometric objects made from glass, carbon, or aluminum. Today, these filled materials contain nano-particles made from carbon or ceramics.

Typical parts are concept models or thin-walled shell-type geometries such as drill housings or hair dryers (Fig. 1.9, left).

1.4.3 Polymer Printing and –Jetting

If the curable build material is applied by print heads, the process is called polymer printing or polymer jetting. The process is commercialized by Objet, Rehovot, Israel. It can be regarded as a 3D printing process; however, due to the part building by UV curing of liquid monomers it is a polymerization or stereolithography process.

The machine design very much resembles a 2D office printer (Fig. 1.10). The build material is directly applied to the build platform through a multi-nozzle piezo-electric print head. The solidification is done simultaneously by a twin light curtain. It is created by two synchronously traveling high performance UV lamps. The layer thickness is only 0.016 mm, which creates very smooth surfaces. Adjacent layers are processed by moving the platform in the z-direction. The process continues layer by layer until the part is finished.

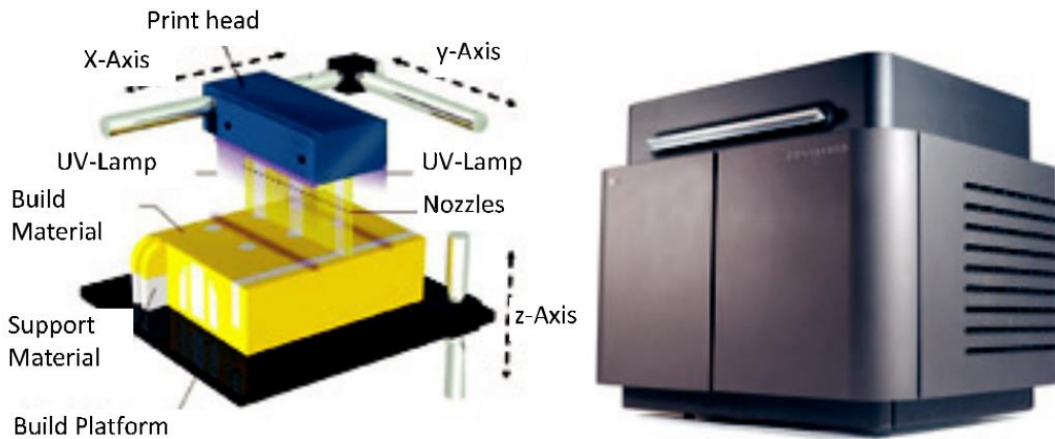


Fig. 1.10 Polymer jetting: scheme (left); two material machine Connex500 (right).

The parts need supports during the build process. The supports are generated automatically and build simultaneously by a second set of nozzles so that each layer consists either of build or of support material. Consequently, the supports are solid and consume a large amount of material. The support material can be washed out without leaving marks in a mostly automated post process. A typical part can be seen in Fig. 1.11, left.

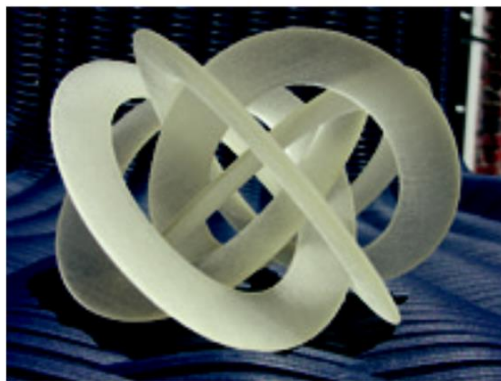


Fig. 1.11 Polymer jetting: structure (left); two-material wheel with elastic tire (right).

The process uses photosensitive monomers to create plastic parts. Materials are available in different colors and shore hardness. Using a proprietary technology called “Poly-Jet Matrix” together with a family of fabricators called “Connex”, parts can be made from two different materials that resemble two component injection molded parts (Fig. 1.11, right). This opens up the future possibility of composing multi-material parts. Typical parts are thin walled and detailed and show interior hollow structures.

1.4.4 Digital Light Processing

This variation of the photo polymerization process works with a commercial DLP projector as UV light source. It projects the complete contour of a cross-section of the actual layer and

initiates the solidification simultaneously. The process is commercialized under the name “Perfactory” by Envisiontec, Gladbeck, Germany.

The projector is mounted into the lower part of the machine body. The resin is kept in a reservoir made from glass sitting on the top of the projection unit. The actual cross section is projected from below on the lower surface of the resin. An upside-down arranged build platform (Fig. 1.12) dips into the resin from the top, leaving the space of one layer thickness between the transparent bottom and itself. After solidification of the layer, the platform is raised by the amount of one layer thickness, making space for the material of the subsequent layer. Due to the small reservoir, the process is designed for small parts. It allows quick material changes and the build needs supports.

A wide variety of photosensitive plastic materials are available, including biocompatible grades that can be used to make hearing aid housings or masters for dental prostheses.

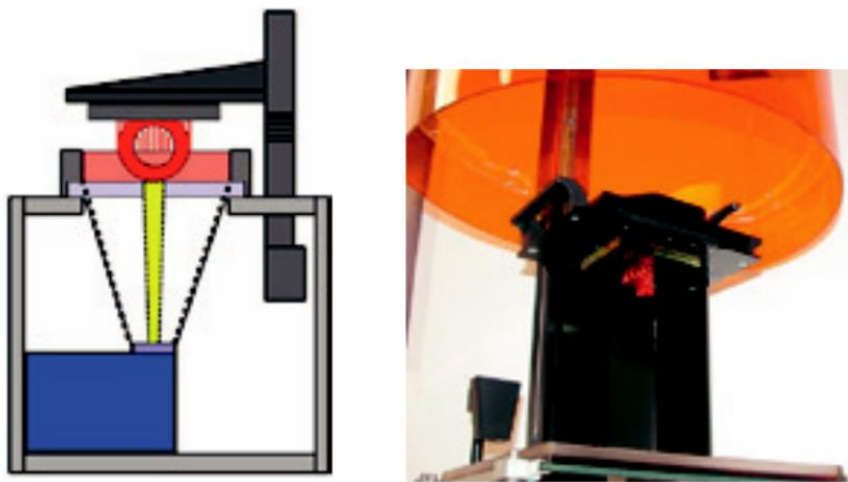


Fig. 1.12 Digital light processing, Perfactory, Envisiontec: scheme, cross-section and reservoir with glass bottom that represents the projection area (left) upside-down arranged build platform (with part).

1.4.5 Micro Stereolithography

There is a wide variety of processes to make parts in the micro-millimeter and even in the sub-micro-millimeter range (Fig. 1.13). Many of them are still under scientific development. Industrially applicable processes use laser stereolithography and mask-based systems, preferably for mass production of final micro parts. Especially if the build is offered as a service, proprietary materials are available. A commercial company that is specialized on customized materials and applications even in large series and which does not sell the machine is microTEC of Duisburg, Germany.

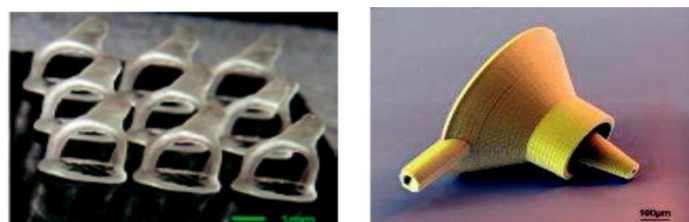


Fig. 1.13 Micro-stereolithography parts.

1.4.6 Sintering and Melting

The selective melting and re-solidification of thermoplastic powders is called laser sintering (also, depending on the manufacturer: selective laser sintering), laser fusing or laser melting. If an electron beam is used instead of a laser the process is called electron beam melting (EBM), and if the energy is provided by a radiator through a mask, it is called selective mask sintering.

Sintering processes in general do require neither bases to build the parts on nor supports to link the parts to the bases, because the loose powder surrounds and stabilizes the part during the build. While this is true for plastic processes, metal parts are an exception. They use bases and consequently supports as well, mainly to prevent the parts from warping during the build process.

1.4.6.1 Laser Sintering – Selective Laser Sintering (LS – SLS)

The term laser sintering or selective laser sintering is used preferably for machines that process plastics. They are commercialized by 3D Systems, Rock Hill, SC, USA and EOS GmbH, Munich, Germany.

The machines of both manufacturers, as well as the machine that processes metals are very similar. They consist of a build chamber to be filled with powder with a grain size of up to 50 μm and a laser scanner unit on top that generates the x-y contour. The bottom of the build chamber is designed as a movable piston that can be adjusted at any z-level (Fig. 1.14). The top of the powder bed defines the build area in which the actual layer is built. The whole build chamber is preheated to minimize laser power and completely flooded by shielding gas to prevent oxidation.

The laser beam contours each layer. The contour data are obtained from the slice data of each layer and directed by the scanner. Where the beam touches the surface, the powder particles are locally melted. The geometry of the melting spot is defined by the laser beam diameter and the traveling speed. While the beam travels further, the melted material solidifies by thermal conductivity into the surrounding powder. Finally, a solid layer is achieved.

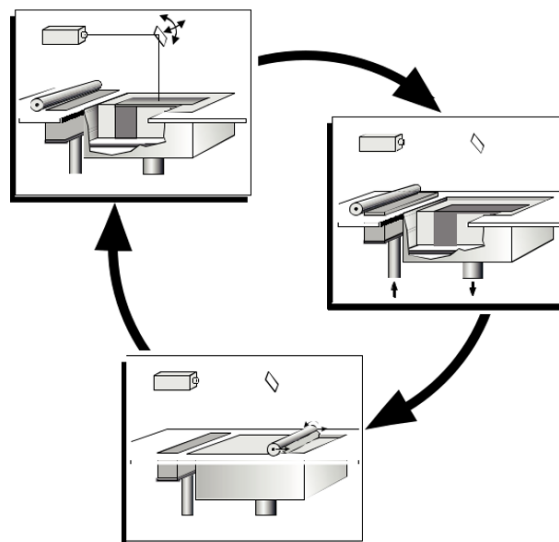


Fig. 1.14 Laser sintering and laser melting: scheme; melting and solidification of a single layer, lowering of the platform, recoating (clockwise from top left).

After solidification of one layer, the piston at the bottom is lowered by the amount of one layer thickness, thus lowering the whole powder cake including the semi-finished part. The emerging space on the top of the powder is filled with new powder taken from the adjacent powder feed chamber using a roller. The roller rotates counter-clock wise to its linear movement in order to spread the powder uniformly. This procedure is called recoating.

After recoating, the build process starts again and processes the next layer. The whole process continues layer by layer until the part is completed. In most cases, the top layer is made using a different scan strategy in order to improve its solidity.

After the build is finished and the top layer is processed, the whole part, including the surrounding powder, is covered by some layers of powder. This so-called powder cake has to be cooled down before the part can be taken off by removing the part from the surrounding powder. The cool-down can be done in the machine; however, cooling down in a separate chamber allows immediate beginning of a new build job.

Sintering allows the processing of all classes of materials: plastics, metals, and ceramics. The machines are basically very similar. They are either adapted to the different materials by software (and maybe minor hardware changes) or special versions of a basic machine design are adapted to process a specific class of materials. In this case, the recoating systems are specially designed for the materials to be processed; e.g., roller-based systems for plastic powders and hopper-type systems for plastic coated foundry sand. For metal processes wiper-type systems are used as well.

The extraction of the part from the powder (the so called “break out”) is typically done manually by brushing and low-pressure sand blasting. Semi-automatic, so-called “break out” stations facilitate the work and mark the trend to automated cleaning. Metal parts require the mechanical removal from the base and of the supports from the part which is time consuming and requires manual skills.

Plastic parts are often porous and need to be infiltrated. If required, they can be varnished and surface treated. Typically, metal parts are dense. They can be processed depending on the material, e.g., by cutting or welding.

Sintered parts made from plastic show properties close to plastic injection molded parts. They are either used as prototypes (Fig. 1.15, left) or as (direct manufactured) final parts (Fig. 1.15, right).

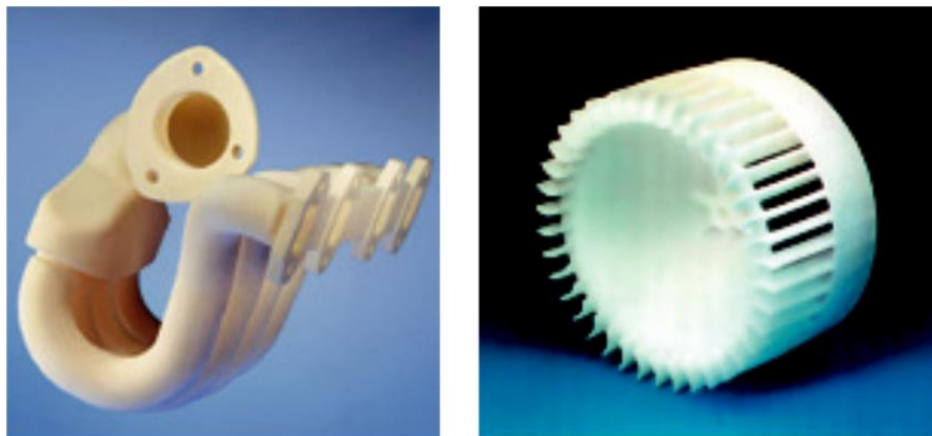


Fig. 1.15 Selective laser sintering, polyamide; exhaust gas device, prototype (left); fan, final product (right).

1.4.6.2 Laser Melting – Selective Laser Melting (SLM)

Laser melting basically is a laser sintering process as described earlier. It was developed in particular to process metal parts that need to be very (> 99%) dense. The laser melts the material completely. Therefore, it produces a local (selective) melting pool that results in a fully dense part after re-solidification. The process is generally called selective laser melting, SLM. There are some proprietary names as well such as “CUSING”, which is an acronym of “cladding” and “fusing”.

Today, most of the machines come from Germany: EOS-GmbH of Munich, Realizer-GmbH of Borchten, Concept Laser GmbH of Lichtenfels, and SLM-Solutions of Lübeck. In addition, 3D Systems, Rock Hill, SC, USA offers a re-branded system based on MTT machines, the predecessor of SLM Solutions. MTT, UK, now separated from its German branch, continues to design its own machine.

For almost all metal machines a wide variety of metals, including carbon steel, stainless steel, CoCr, titanium, aluminum, gold and proprietary alloys are available. Typically, metal parts are final parts and used as (direct manufactured) products or components of such products. Typical examples are the internally cooled cooling pin inserts for injection molds made from tooling steel in Fig. 1.16, left, and the micro cooler made from AlSi10Mg in Fig. 1.16, right.

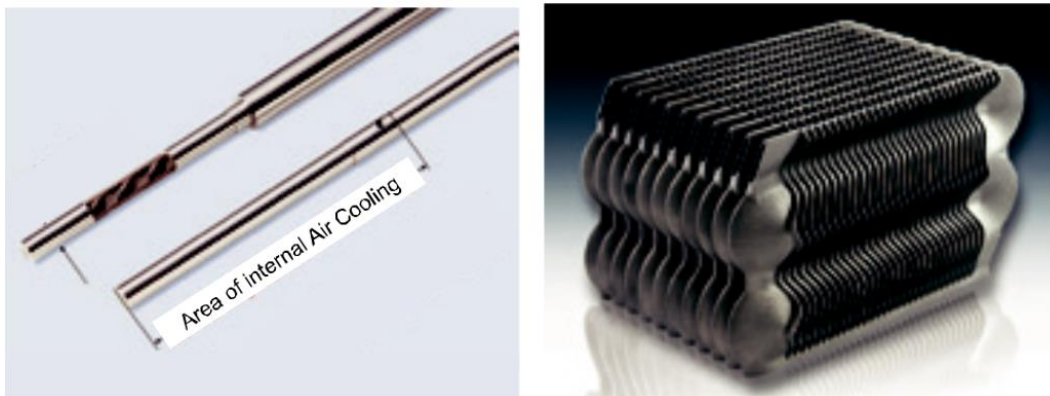


Fig. 1.16 Selective laser melting; Internally cooled pin for injection molds (left), micro cooler made from AlSi10Mg (right).

The machine designs are very similar to the plastic laser sintering machines. They use fiber lasers with a very good beam quality as well as sealed build chambers that can be evacuated or fed with shielding gas in order to handle inflammable materials such as titanium or magnesium. Build-in auxiliary heating devices help to prevent warping and distortion of the part.

Metal and ceramic micro sintering machines are close to market entry but still under development. Commercialization has been announced by EOS based on the machine development of 3D Micromac, Chemnitz, Germany. The typical layer thickness is in the range of 1–5 μm and the smallest wall thickness is > 30 μm . A fiber laser with a focus diameter

< 20 μm is used. As an example, a chess set is shown on Fig. 1.17. The tower's height is about 5.5 mm.



Fig. 1.17 Micro laser sintering, demonstrator chess set.

1.4.6.3 Electron Beam Melting

The local melting of the material can be achieved by an electron beam that replaces the laser. The procedure is then called electron beam melting, EBM. Because electron beam material processing requires a vacuum, a completely sealed construction is needed.

Arcam AB of Mölndal, Sweden presents a family of EBM machines dedicated to special applications, such as aerospace, medical, or tooling (Fig. 1.18).

The electron beam penetrates very deep and the set up allows a very high scan speed that can be used for preheating as well, therefore the process is very fast and works at elevated temperatures. As a result, stress and distortion are reduced and very good material properties can be achieved, according to the company.



Fig. 1.18 Electron beam melting (EBM): EBM System A2 (left); EBM scheme (right).

1.4.7 Extrusion – Fused Layer Modeling

The layer-by-layer deposition of pasty strings is called fused layer modeling. The process works with prefabricated thermoplastic material. Colored parts are obtained when colored material is used. Technically, FLM is an extrusion process, see Fig. 1.19. The parts need support during the build.

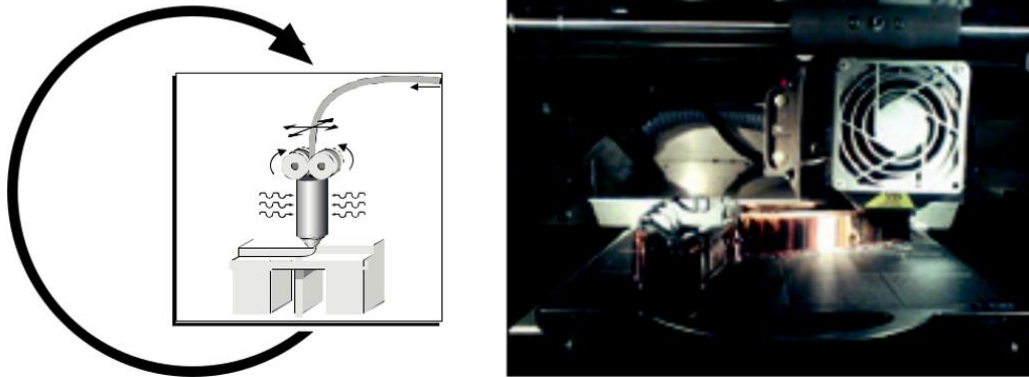


Fig. 1.19 Fused layer modeling extrusion process: scheme (left); build chamber with build platform, part in progress, print head (right).

1.4.7.1 Fused Deposition Modeling (FDM)

FDM is a registered, protected trade name for a fused layer process offered by Stratasys Company, Eden Prairie, MN, USA. Because it was the first commercialized FLM process worldwide, the name FDM is often used synonymously with FLM even as a generic name.

A FDM machine consists of a heated (app. 80 °C for ABS plastic processing) build chamber equipped with an extrusion head and a build platform. Consequently, the machine does not use a laser. The extrusion head provides the material deposition in the x-y area according to the contour of the actual layer. It is a plotter-type device.

The build material is a prefabricated filament that is wound up and stored in a cartridge from which it is continuously fed to the extrusion head. The cartridge has a build-in sensor that communicates with the material management system of the machine. In the head, the material is partly melted by an electric heating system and extruded through a nozzle that defines the string diameter that nearly equals the layer thickness.

Usually, string diameters range from 0.1 mm to 0.25 mm. The platform moves in z-direction and defines the layer thickness, as the material is squeezed on the top of the partly finished part. The process needs supports. They are made by a second nozzle that extrudes another plastic support material simultaneously with the build material.

The simultaneous processing of two materials indicates that the FLM process is basically capable of handling multi-material print heads. Therefore, the manufacture of multi-material parts can be expected in the future.

After deposition, the pasty string (of the build material as well as of the support material) solidifies by heat transfer into the preceding layer and forms a solid layer. Then the platform is lowered by the amount of one layer thickness and the next layer is deposited. The process repeats until the part is completed.

Typical part properties resemble those of plastic injection molded parts; however, they tend to show anisotropic behavior that can be reduced by properly adjusted build parameters. The parts are either used as concept models, functional prototypes, or as (direct manufactured) final parts.

1.4.8 Powder-Binder Bonding – Three-Dimensional Printing (Drop on Powder Processes)

The layer-by-layer bonding of powder particles in the range of 50 μm by selectively injecting a liquid binder into the top area of a powder bed is called “Three-Dimensional Printing – 3DP”. The process family is also called “Drop on Powder Processes”. The process was developed and registered by MIT in the early 1990s and licensed to Z-Corporation and others who commercialized it. Today, variations processing plastics, metals, or ceramics are commercially available. Most of them are two-step processes, requiring infiltration after the build. Some, especially metal processes, deliver a sort of green part that has to undergo thermal de-binding and sintering to achieve their final properties. As there are binders imaginable for any powder, the range of materials is almost infinite, including food and drug applications; however, only a small fraction is currently commercialized.

“Three-Dimensional Printing” or more frequently “3D Printing” became a synonym for all AM processes in general, thus being used as a generic term, because 3D printing resembles two-dimensional printing and therefore provides a very simple way to explain what AM is about. But the use of two identical terms with different meanings sometimes causes confusion. Therefore, especially beginners should avoid to mix the two meanings of this term.

1.4.8.1 Three-Dimensional Printing – Z-Corporation

The commercialized machines made by Z-Corporation, Burlington, MA, USA, work exactly according to the basic process. The process delivers a kind of green part that is dimensionally stable but needs infiltration to achieve solidity. The part remains in the powder bed until the build process is finished. It is stabilized by the surrounding powder and therefore does not require supports. As the binder can be colored, the parts can be colored as well. The company offers a family of 3D printers, most of which are capable of producing colored parts.

The lower part of the machine contains the build chamber and carries the powder. It is designed very much alike a laser sintering machine with a movable piston to adjust the layer and a roller for recoating. A plotter device with a commercial print head, as known from a 2-D office printer, is mounted on top of it. It travels over the build area and prints the binder onto the powder according to the actual contour. The particles forming the layer are bound, while the loose powder supports the part. In contrast to sintering, the process requires neither preheating nor shielding gas.

After solidification of one layer, the bottom piston is lowered by the amount of one layer thickness, thus lowering the whole powder cake including the semi-finished part. The emerging space on the top of the powder is filled with new powder taken from the adjacent powder feed chamber using a blade or a roller (recoating).

Today, starch-like powder and plaster-ceramic qualities are available to make parts and even shells for investment casting. As the binder can be colored, continuously colored parts can be made, in the same way, colored pictures are printed in 2D. The coloring even of texture-like designs is a unique selling point of this process.

After the top layer is processed the build is finished. Because this process works at room temperature, the powder cake shows room temperature and can be directly taken from the machine. The loose powder is removed by gently brushing and low-pressure air blasting.

Finally, the part needs infiltration to obtain durability. For this, wax or epoxy resin is used. As a result, the durability of the parts depends not only on the material but on the quality of the infiltration as well. Therefore, 3DP parts should not be used for structural testing.

Typical parts are concept models. They can be monochromatic or continuously colored (Fig. 1.20, top left and right). Z-printers are office friendly and easy to handle (Fig. 1.20, bottom).

The surface quality is rough compared to polymerization processes (Fig. 1.21, left) but can be improved significantly by manual post processing (Fig. 1.21, right).

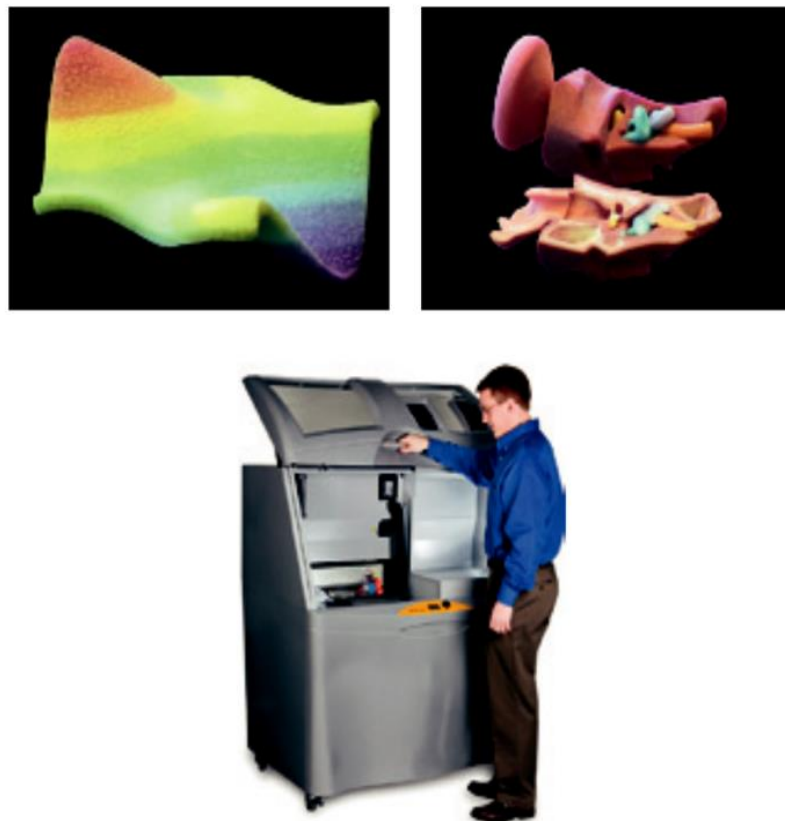


Fig. 1.20 Powder-binder process; colored parts (top left and right), machine ZPrinter450 (bottom).



Fig. 1.21 Powder-binder process; improved surface quality by manual finishing: part as from the machine (left) and after finishing (right).

1.4.8.2 Three-Dimensional Printing – Prometal

A variation of the basic process was licensed to the Ex-One LLC's Prometal Division, Irwin, PA, USA, that commercialized a metal printing and a sand-printing machine based on this principle.

The metal printing process makes metal and metal-ceramic parts by binding the powders via micro droplets. The process, run on a machine called R1, resembles the basic process, but uses a different recoating and leveling system and an additional heater to assure an even consistency of the powder bed and the part. A subsequent thermal process provides the part's strength and durability.

The sand-printing machine, commercialized as S-print by Prometal RTC, is part of a family of machines designed to produce complex cores from foundry sand. The reproducible manufacturing of complex cores increases the productivity of sand casting not just for prototype and test casting but also for production. The big machine is capable to feed a production line and must be regarded as a foundry machine. In Fig. 1.22, left, the S-print is displayed and Fig. 1.22, right, shows the actual top layer of the part during printing. The gantry that covers the print head can be seen partially on the very left.

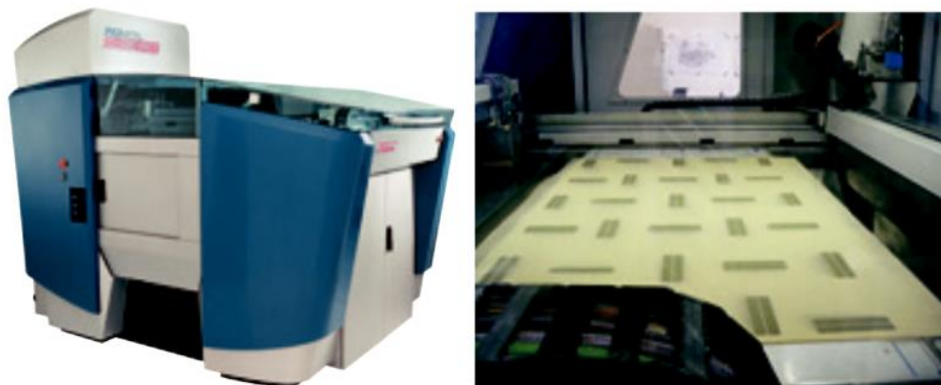


Fig. 1.22 Prometal foundry sand printer S-print (left); build chamber with print head-gantry at the very left and build area (right).

1.4.9 Layer Laminate Manufacturing (LLM)

The cutting of contours out of prefabricated foils or sheets of even layer thickness according to the sliced 3D CAD file and the subsequent bonding on the top of the preceding layer is called layer laminate manufacturing, LLM.

The foils or sheets can be made of paper, plastics, metal, or ceramics. A laser, a knife, or a milling machine can be used as a cutting device. The bonding of adjacent layers is done by glue, ultrasonic, soldering, or diffusion welding. Most of the processes just need one production step; a few require a post treatment such as sintering in a furnace.

The overall advantage of LLM processes is the fast build when massive parts are requested. The disadvantage is a huge amount of waste, depending on the geometry of the part.

1.4.9.1 Layer Laminate Manufacturing, Laminated Object Manufacturing (LOM)

The oldest and widely known AM LLM-process is the laminated object manufacturing (LOM). It was originally developed by Helisys, USA, which is now Cubic Technologies, Torrance, CA. This machine as well as a similar one, which was developed later by Kinergy, Singapore, is no longer produced. But there are a lot of these machines in the market and the company provides service, maintenance, and contract manufacturing. The build material is coiled paper of approximately 0.2 mm thickness. On its down face it is coated with glue which is activated by heat during the recoating process.

The machine consists of a build table that can be moved in z-direction and a mechanism to uncoil the paper, position it on the build table, and wind up the remaining paper on the opposite side. A laser does the cutting of the contour.

To build a part, the paper is positioned on the build table and fixed by a heated roller that activates the glue. The contour is cut by a plotter-type laser device that allows adjusting the cutting depth according to the paper thickness. Another frame-like laser cut defines the boundaries of the part. It leaves two paper stripes on each side of the part that enables the exceeding paper to be lifted and wound up by the second coil (Fig. 1.23). The material that fills the space between the contour and the frame remains within the part and supports it. It is cut into squares for easy removal of the waste material.

After the build process is finished, the block of paper, including the part and the support material is removed from the build platform. The frame and the squares that result in small blocks are removed and finally the part is obtained. The parts need varnishing to prevent delamination of the layers. Gear housings, which are typical parts, can be seen in Fig. 1.24.

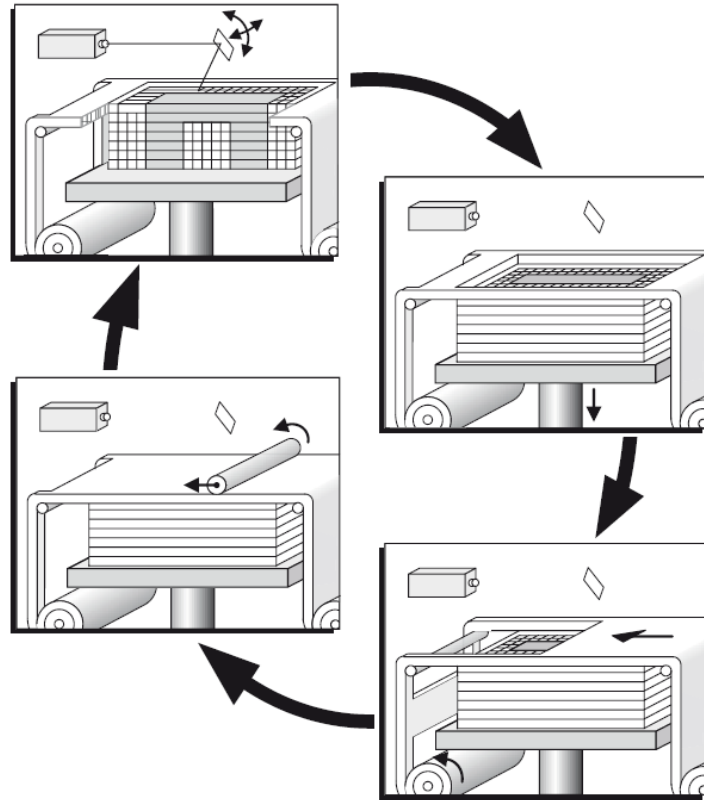


Fig. 1.23 Layer laminate manufacturing, laminated object manufacturing (LOM); scheme.

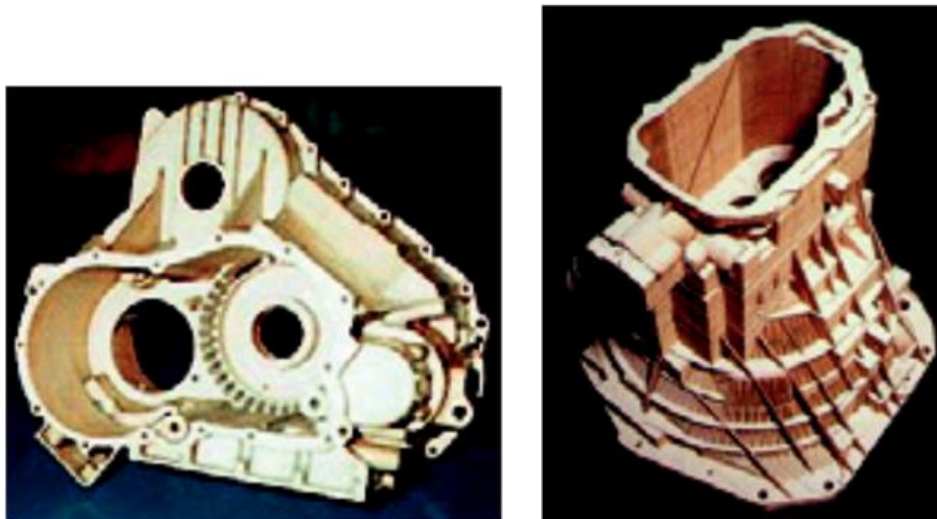


Fig. 1.24 Layer laminate manufacturing, paper lamination; gear housing.

1.4.9.2 Layer Laminate Manufacturing, Paper Lamination, MCOR Matrix

A variation of the paper lamination process was commercialized by Mcor Technologies, Ardee, Ireland. The contour is cut with a tungsten carbide drag blade instead of a laser. The process

is based on loose sheets of office paper (A4, 80 gsm) that is glued using standard white polyvinyl acetate (PVA) glue. As this glue tends to blister the paper, a special coating system based on micro drops was designed to overcome this problem. The drop density is lower in the area that does not belong to the part, which enables easy cleaning. The machine, called Matrix 300, works fast and delivers cheap models with a layer thickness of approx. 0.1 mm (Fig. 1.25, left). The parts can be colored if colored paper is used. To obtain the colored structure of the part, the paper must be filed manually in the right sequence (Fig. 1.25, right).

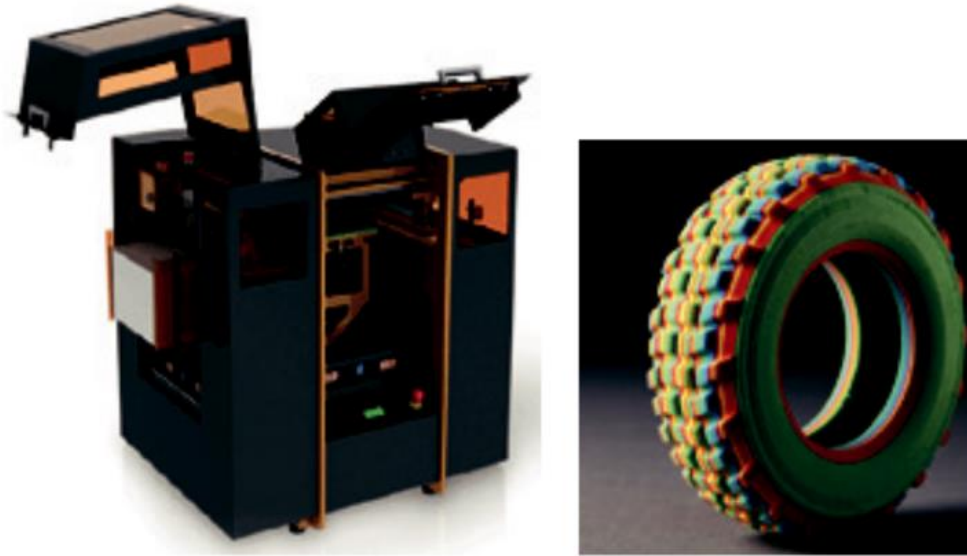


Fig. 1.25 Layer laminate manufacturing: paper lamination; MCOR Matrix 300 machine (left), colored part made from paper (right).

1.4.9.3 Layer Laminate Manufacturing, Plastic Laminate Printers

Although the term “laminate” is not dedicated to a special material, AM machines that work with PVC based plastic foils are called laminate printers. Originally developed and produced by Solidimension and shipped as SD300, identical machines as well as upgraded machines entered the market as Graphtec XD700 and Solido SD 300pro.

During the build, the contour of each layer is defined by a masking fluid and glue. Then the next layer is applied and fixed by the glue and the contour is cut using a build-in cutting plotter, see Fig. 1.26, left. Finally, a rigid plastic part surrounded by frame-like waste is obtained. The frames of each layer are alternating linked to the opposite edges of the preceding ones by glue as well. This allows easy peeling off of the resulting accordion-like waste structure. The rigid plastic parts perform very well, if their geometry meets the process requirements. As a typical part, a fan wheel can be seen in Fig. 1.26, right. Complex parts with interior hollow elements may cause problems.



Fig. 1.26 Layer laminate manufacturing; plastic laminate printers; machine (left); fan wheel made by the laminate Printer Solido SD 300 pro, PVC (right).

1.4.9.4 LLM Machines for Metal Parts

Most of the approaches to make metal parts use cutting and joining of sheet metals. The contours are either obtained from laser cutting or from milling. The sheets are joined by diffusion welding, powder welding, soldering, or mechanically by bolts. This kind of a semi-automated multi-step process is not a real AM process, although they are additive and layer oriented.

One of the rare real AM LLM machines is made by Solidica, MI, USA. The process is called ultrasonic consolidation. It is based on a traditional milling machine with an integrated ultrasonic (US) welding device that joins thin aluminum strips on top of the semi-finished part. After one layer is applied, its contour is milled and the next layer is joined, again by US. The process delivers completely dense aluminum parts that may contain integrated sensors that are placed into cavities made and sealed during the process. Further development enables the process not only to manufacture different materials including titanium, steel, copper, and nickel but also to realize combinations such as the Ti-Al structure shown in Fig. 1.27. As a result, Gradient-Modulus Energy Absorbing Material (GMEAM- Generally called „Graded Materials “-from: gradient modulus-, this material shows a defined variation of its properties within the parts made from it) can be manufactured, that shows a tremendous improvement in impact resistance.

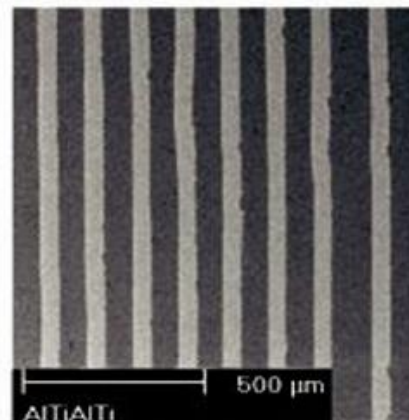


Fig. 1.27 Ultrasonic consolidation; UC-machine formation (left); Ti-Al high energy absorbing structure (right).

1.4.10 Other Processes: Aerosolprinting and Bioplotter

1.4.10.1 Aerosolprinting

A very interesting process with a high potential is called aerosolprinting. It was developed and launched as Maskles Mesoscale Materials Deposition (M3D) by Optomec, NM, USA.

A stream of very fine droplets (aerosols) is generated, loaded with ultra-fine particles with diameters in the nm range, and guided to the surface of a substrate (Fig. 1.28). Here, the aerosols are deposited according to a CAD designed pattern. The liquid phase is vaporized, leaving the particles in place. The particles may consist of any kind of functional inks, metals, ceramics, plastics, or even living cells. Depending on the kind of material, a post treatment by laser may be needed. Aerosolprinting is a very promising process for electronic devices as well as for tissue engineering.

As it is currently suitable only for 2½ D surface texturing and objects (at least now) and not for real 3D parts, some do not regard it a real AM process.

1.4.10.2 Bioplotter

One of the most unique selling points of AM will be multi-material processing. The 3D Bioplotter, which is a registered trademark of Envisiontec, Marl, Germany, allows to process a wide variety of materials from plastics, such as polyurethane or silicone, to bone materials such as hydroxyapatite, and drugs such as PCL (polycaprolactone) or materials such as collagen or fibrin for organ printing or soft tissue fabrication. Up to five materials can be processed using either a heated or a cooled dispenser unit that is operated by a 3-axis plotter. Depending on the material, the system uses different hardening processes such as precipitation, phase transition (liquid to solid), or two-component reaction. Some materials need post processing such as sintering.

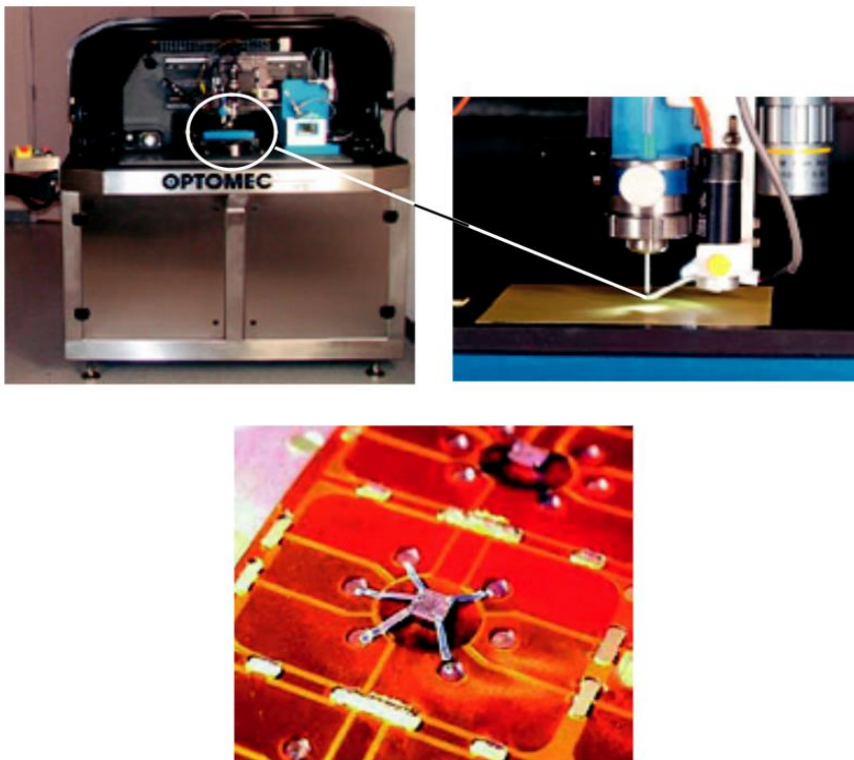
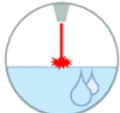



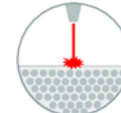
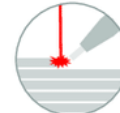



Fig. 1.28 Aerosolprinting, Maskles Mesoscale Materials Deposition (M3D); machine and deposition unit (top), surface structure for smart card (down).

1.4.11 Summary of AM Processes

To sum up, all AM categories and technologies, with the appropriate materials and their pros and cons, are given in the following table (Table 1.1).

Table 1.1 AM categories and technologies.

AM CATEGORY							
	Vat Photo-polymerisation	Material Extrusion	Material Jetting	Binder Jetting	Power Bed Fusion	Direct Energy Deposition	Sheet Lamination
TECHNOLOGIES	Stereolithography (SLA)	Fused Deposition Modeling (FDM) Contour Crafting	Polyjet / Inkjet Printing	Indirect Inkjet Printing (Binder 3DP)	Selective Laser Sintering (SLS) Direct Metal Laser Sintering (DMLS) Selective Laser Melting (SLM) Electron Beam Melting (EBM)	Laser Engineered Net Shaping (LENS) Electronic Beam Welding (EBW)	Laminated Object Manufacturing (LOM)
MATERIAL	Photopolymer Ceramics	Thermoplastics, Ceramic slurries, Metal pastes	Photopolymer, Wax	Polymer-, Metal- or Ceramic powder	Polymer-, Metal- or Ceramic powder	Metal powder or wire	Plastic film, Metallic sheet, Ceramic tape
PROS/CONS	+ High building speed + Good part resolution - Overcuring, scanned line shape - High cost for supplies and materials	- Inexpensive extrusion machine - Multi-material printing - Limited part resolution - Poor surface finish	+ Multi-material printing + High surface finish - Low-strength material	+ Full-color + Wide material selection - Require infiltration during post-processing - High porosities on finished parts	+ High Accuracy and Details + Fully dense parts + High specific strength & stiffness - Powder handling & recycling - Support and anchor structure	+ Repair of damaged/worn parts + Functionality graded material printing - Bad resolution - Expensive	+ High surface finish + Low cost - Decubing issues

1.5 Advantages of AM Processes

AM provides a unique ability to fabricate components with high variability and flexibility in geometrical features. It offers a path of fabricating some special components like light hollow contours or mold cavities with passages for internal cooling, etc. Great cost savings (more than 50% in general in aerospace/automobile industries) can be obtained by the use of the AM route for part fabrication as compared to the conventional methods of manufacturing. The time required to bring the component to market is greatly reduced by this route due to the enormous compaction of the design cycle in case of AM. Appreciable strength-to-weight ratio metallic parts can be fabricated since a high degree of freedom in design is permitted by the AM route. The quality of parts in terms of features and intricacy is highly improved. These

are environmentally friendly manufacturing methods for two main reasons: (1) tremendous reduction in scrap and wastage which can be attributed to its mode of operation and (2) reduced noise and pollution allowing them to be easily employed in office environments rather than specially designed workshops. Apart from these, there are numerous advantages of AM processes, some of which are summarized below [1]:

- Since the components are fabricated in a layered fashion so there is no requirement for tools and fixtures.
- The intricacy of the component has impact on the time and cost of the final AM product in contrast to the conventional manufacturing processes.
- Nesting/parallel processing of parts is possible by careful layout optimization.
- Tremendous reduction in the lead times for part fabrication results in considerable cost and time savings.
- Highly customized parts can be made easily by the AM route.
- Design and fabrication of functionally graded materials is very easy by the AM route and extremely economical as compared to conventional manufacturing techniques.
- Multiple setups for part fabrication are not required in almost all cases.
- Operator intervention work is greatly reduced to a supervisory level.
- AM processes are being highly responsive to dynamic manufacturing environment.
- Set-up/machine preparation time in case of AM processes is appreciably less as compared to that in conventional manufacturing.

Some other important advantages of AM include:

- Noise free
- Can be operated from the comfort of home or office
- Offers an excellent and impressive spectrum of applications
- Can form process chains when suitably combined with other conventional/unconventional manufacturing processes
- Lesser time for products to reach markets for customer end use
- Reduced material wastage owing to non-occurrence of mistakes
- Lesser costs owing to appreciable manufacturing savings
- Improved qualities
- Parts with complex and intricate geometries can be obtained
- Tools, molds or punches not required.

1.6 Challenges of AM Processes

Despite remarkable progress in the domain of AM, a variety of aspects like production speeds, build scale economies, precision, quality, raw materials, communication interfaces, etc. need attention to fully explore the potential of AM. Apart from the benefits stated in the previous section, AM is faced with multiple issues that restrict its use in a few application areas. The AM challenges are summarized as [1]:

- Non-optimal build speeds

- Relatively less accuracy
- Decision regarding optimal part orientation
- Restricted choice of raw materials and resulting material properties
- Poor surface finish
- Pre-processing and post-processing requirements
- High system cost chiefly owing to limited buyers
- Anisotropic behavior of AM fabricated parts
- Occurrence of stair-stepping phenomenon
- Need for optimal layer thickness selection
- Need of support structures
- Poor structural strength of parts fabricated via AM techniques.

1.7 Pros and Cons of AM with Respect to Conventional Manufacturing Techniques (CMTs)

In comparison to traditional manufacturing processes, AM offers numerous advantages, some of which are discussed here [1], [2].

- Part Flexibility

In AM techniques, there is minimal need for post-processing and also no constraints on tooling, so that complex geometrical shapes can be successfully obtained. In other words, in AM, part functionality is not sacrificed on the grounds of ease of manufacturing as is done in conventional manufacturing. Thus, for complex geometrical shapes, AM offers more suitability as compared to CMTs. Also, the cost of products with increased complexity remains the same in AM techniques which sharply increases in CMTs, as shown in Diagram 1.1. Further, functional properties can be easily obtained in parts fabricated via AM techniques, which altogether opens up newer avenues for novel designs and innovations in manufacturing.

- Waste Prevention

AM techniques utilize a layer-by-layer additive process for developing parts/components thereby reducing material wastage, which is a major issue in subtractive manufacturing processes where a large amount of material is removed during machining.

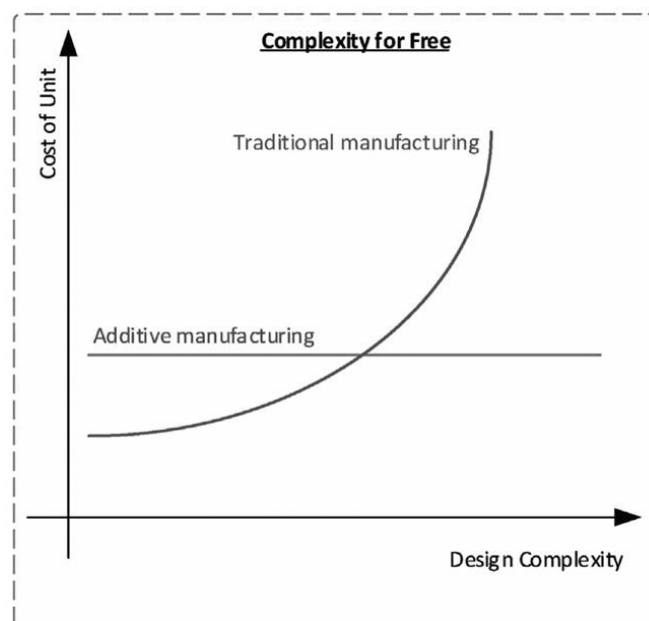


Diagram 1.1 AM Complexity for Free

- Production Flexibility

AM techniques require less costly set-up and do not require tooling and fixturing. Owing to this, AM techniques are economical and are suitable for small batch production. The properties of a fabricated part depend on the process and raw materials instead of operator skills. In addition, issues of production bottlenecks and line balancing are eliminated as AM techniques can produce complex shapes in a single piece.

- Process Running Cost

Most of the subtractive manufacturing techniques need substantial labor, money and time for preparing fixtures, tools, molds, machine set-up, etc. owing to which the running cost per product is high. On the other hand, in the absence of tooling requirements and presence of shorter product development cycle, the running cost per product in AM techniques is small.

- Probability of Change

New product/design development via traditional manufacturing techniques can be expensive, owing to many trial experiments and consequent time consumption. In contrast, AM offers freedom to design at negligible cost. Once a prototype is designed/developed by varying the CAD data, actual production can be performed. During AM, no extra cost in the form of retooling is involved.

Despite several benefits of AM techniques over traditional manufacturing processes, they present some challenges which are discussed below.

- Start-up Investment

Owing to the high cost of AM modelers and the complex set-ups required during installations, the start-up investment is higher in the case of AM machines. However, conventional machines can be bought and set up at much lower prices than their AM counterparts.

- Mass Production

During the production process, AM is less efficient in developing products at large scale as compared to traditional manufacturing. This can be seen from Diagram 1.2 which shows that the initial product cost in AM is less and almost remains the same with an increase in production scale. This is mainly due to the slow deposition rates and built capacity constraints in AM. On the other hand, the initial product cost in conventional processes is very high but reduces with an increase in scale of production.

- Raw Material

With the recent innovations in AM processes such as selective laser sintering (SLS), laser beam machining (LBM), etc. it becomes quite possible to process metallic components via 3D printing. However, some metal alloys still cannot be worked upon, or their output characteristics are poor. Thus, the range of raw materials in AM techniques is relatively smaller. In comparison to AM, traditional manufacturing processes are well established and can process almost all types of materials.

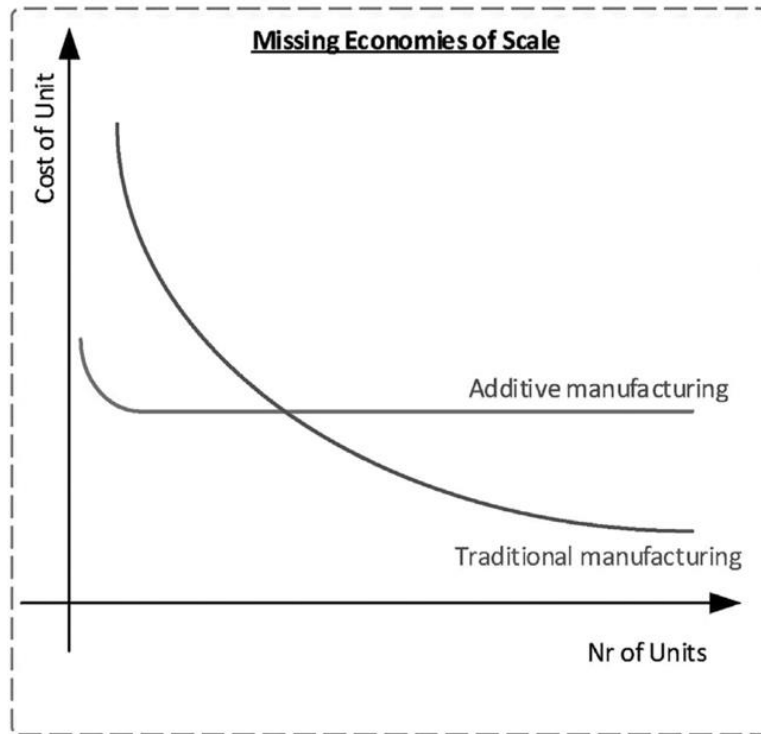


Diagram 1.2 AM Missing Economies of Scale.

1.8 AM Materials

AM raw materials can be of varied forms, including sheet, filament, paste, ink, gas, wire and powder. Materials like polymers, ceramics, composites, metals, alloys, functionally graded, smart, hybrid, etc. are widely utilized AM raw materials. The material compatibility of different AM techniques is given in the Table 1.2, below:

Table 1.2 Material compatibility of different AM techniques.

Popular AM techniques	Polymers	Metals	Ceramics	Composites
SLA	✓			✓
MJM	✓			✓
FDM	✓			
EBM		✓		
SLS	✓	✓	✓	✓
DMLS		✓		
LOM	✓	✓	✓	✓
UAM		✓		
LMD		✓		✓

1.9 Defects in AM Parts

Despite the tremendous research progress in AM technology, some newly developed AM processes, especially MAM (Metal Additive Manufacturing) processes, are at their early stage and the relationship of basic processing parameters with microstructure and other properties is not fully understood. In the absence of optimized process parameters and material combinations, defects occur which result in poor mechanical properties of fabricated components. The subsequent sections present a brief overview of common defects for different materials and AM techniques.

1.9.1 Balling Phenomena

Balling is basically a phenomenon which occurs when the wetting of the underlying surface is not produced by the liquid material. This leads to a rough, bead-shaped scan track that reduces surface finish and increases pore formation. Such types of defects generally occur in laser sintering- based AM techniques. A typical example of balling phenomena is depicted in Fig. 1.29.

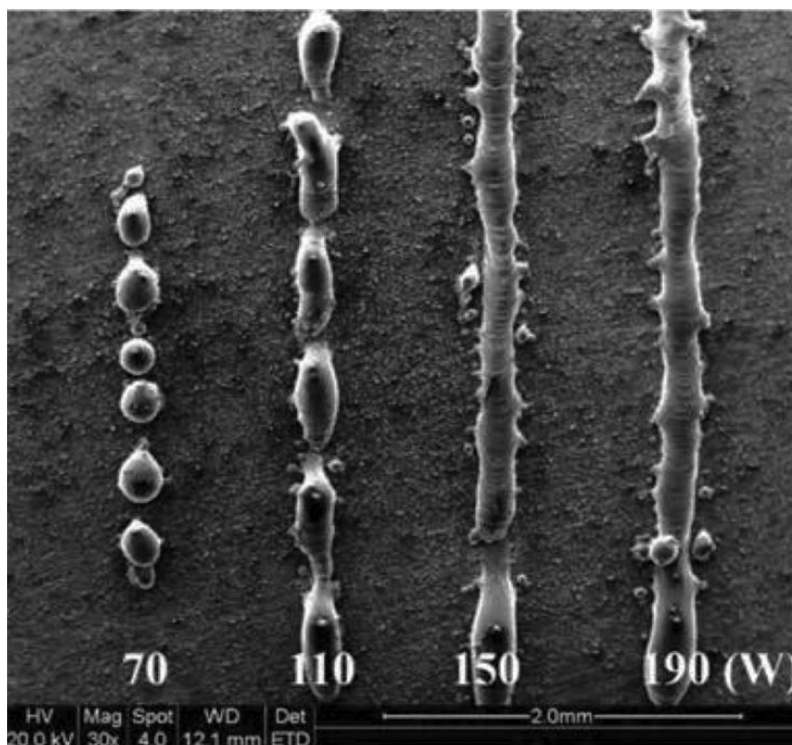


Fig. 1.29 Illustration of Balling Phenomena during SLM Process.

1.9.2 Porosity Defects

Porosity and voids are commonly occurring flaws in AM parts, as the most utilized binding mechanisms are governed by changes in temperature under the action of capillary and gravity forces in absence of external force. The major reasons behind the porosity or voids defects are: (1) repeated formation of keyholes resulting in formation of voids; (2) entrapment of

gases which results in microscopic pores in powder particles when they are atomized; (3) inadequate penetration of current layer of melting pool into previous layer or the substrate. Defects like keyholes induced porosity, absence of fusion pores and porosity due to gases are shown in Fig. 1.30. Keyhole porosity is small in size and generally less than 100 μm .

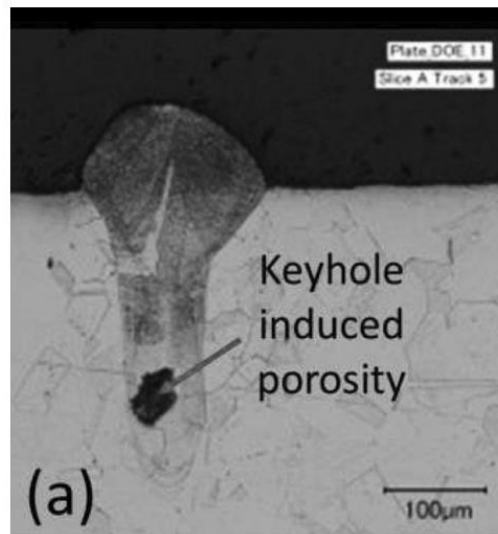


Fig. 1.30 Keyhole Porosity Defect.

1.9.3 Cracks

Crack defect is another main problem in AM parts which generally occurs in fusion-based AM techniques. During fusion-based AM techniques, metallic powders experience rapid melting and solidifications. Due to the rapid cooling rate, a high temperature gradient and subsequently large thermal residual stresses are generated in the fabricated part. The combination of large residual stresses and high temperature gradient result in initiation of cracks. Cracks are mostly prominent along grain boundaries.

This occurrence is most common along the boundary of grains and is chiefly due to temperature variations owing to different rates of contraction for each layer, i.e., substrate, solidifying and deposited layers. Liquation cracking is another defect and is mostly observed in a mushy/partially melted zone which experiences tensile force leading to liquid films acting as cracking points. Various other cracks can be similarly explained. These cracks are either appreciably long or relatively small. The process of delamination occurs when the layers separate mutually in the event of residual stress at the layer interface being more than the alloy's yield strength.

1.9.4 Distortion

Distortion is a kind of defect in AM parts which mainly originates due to the stresses developed in the material caused by the change in volume during shrinkage. Diagram 1.3 shows some typical distortion defects [1].

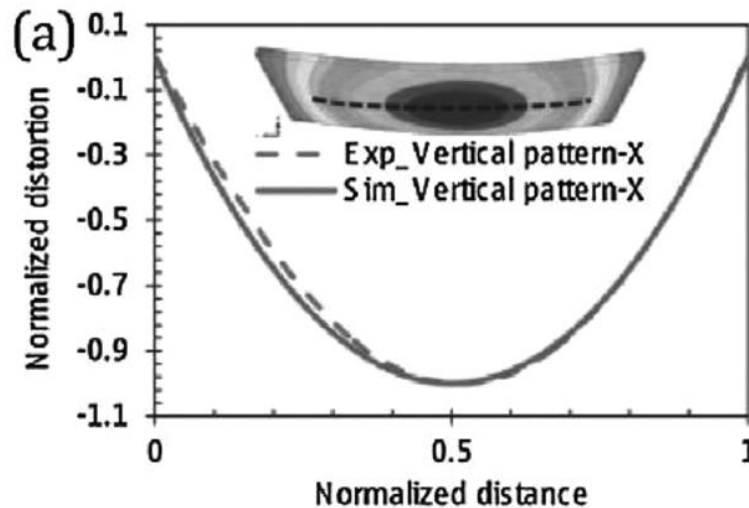


Diagram 1.3 Typical Distortion Defect in AM Parts in SLM Processed Steel.

1.9.5 Stair-stepping effect

The stair-stepping effect is another common limitation in the AM process due to layer-by-layer manufacturing methodology. This hampers the surface quality of the parts along the built direction especially for inclined and curved surfaces. Increasing layer thickness has a significant effect on poor surface finish of the parts. The stair-stepping effect is quantified using Total Waviness of the parts. The selection of proper build direction and process parameters is important for reducing the stair-stepping effect. Fig. 1.31 presents the stair-stepping effect in Laser AM [5].

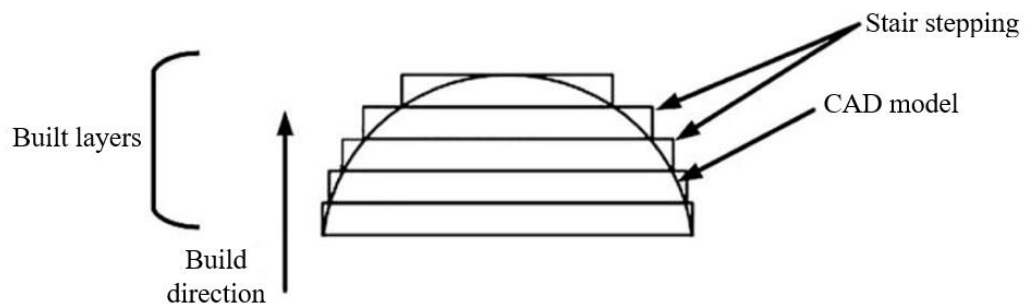


Fig. 1.31 Stair-stepping effect.

Nowadays with the advancement in the materials, AM is being used in different application areas. Surface finish in AM is highly variable due to variable staircase formation during layer upon layer part fabrication process. Post-finishing operations have an important role in improving the surface finish of AM build parts. Part fabrication through (AM) process followed by finishing on the different setup is known as post-finishing operation. A general technique for surface finish improvement is typically done through the use of milling machine with customized or standard mill cutters, which machine the staircase of an AM build parts to

reduce the roughness of the surface during post-finishing operation. Since post-finishing operation are performed after fixturing the AM parts on a different setup, this induces location error due to which staircases are not removed properly. This results in a non-uniform surface generation in finished parts.

As a result of this, additive manufacturing and material removal process must be used on the same setup as an integrated finishing operation for solving the issue of location error. In integrated finishing operation, not only the lead time reduces but also location errors problem is minimized.

To overcome the above disadvantages, in this research work, a new technique of post-finishing is proposed. This technique designed and developed a selective melting tool; first to eliminate the effect of the location error which is induced by fixturing the part for finishing process on the different setup. To selectively and adaptively heating of build edge profile, proposed post-finishing operation provides forced closed follower mechanism and heating arrangements to the finishing tool. Then it provides non-rotational linear feed rate to the heated tool to fill the neighbouring valley through the softened material which is piled up near the border of a heated tool [2].

1.10 Post-processing of laser additive manufacturing (LAM) parts

Post-processing varies according to the AM technique. Discussing each and every post-processing technique is really extensive and out of this paper's interest. However, an example of LAM post-processing is given here, as LAM is the main focus of this study.

Specifically, the bulk and surface properties as well as geometry achieved in LAM-built material are influenced by distortions due to heating, partially melted powders, solidified melt droplets and surface variations brought by the laser movement and processing strategy. Thus, deposited surface roughness, dimensional accuracy and properties are inadequate for many industrial applications. Therefore, a certain amount of post-processing is required for LAM components.

The first stage of post-processing is soon after the part is built. In the PBF process, the fabricated component will be enclosed by powder material and this loose or unfused powder is removed during post-processing. In PBF, support structures may be generated based on the geometry and are to be removed by cutting. In addition to this, PBF and PFD processes require removal of part from the substrate. This is usually done with wire electrical discharge machining or a saw.

The next stage of post-processing depends on the application. This can be surface finish enhancement, aesthetic enhancements, property enhancements and so on. Surface finish enhancements have been done using conventional subtractive manufacturing techniques such as computer numerical control (CNC) milling and polishing, glass blasting, or ultrasonic machining. Recently, post-processing of LAM components was performed using laser-based techniques such as laser shock peening (LSP), laser finishing and laser annealing (LA). The components built using LAM are inherited with tensile residual stress on the surface due to rapid heating and cooling during material processing. Thus, LSP, an advanced surface

engineering process, introduces compressive residual stresses into materials, thereby improving product life through increased resistance to many surface-related failures, such as wear and corrosion. LSP on LAM fabricated IN718 showed significant improvement in mechanical properties such as hardness, corrosion and wear resistance by 27%, 70% and 77%, respectively. LSP studies on LAM fabricated NiTi and TiNiCu-based shape memory alloys showed changes in the surface morphology such as increment in surface roughness and decrement in lots of peak structures. The microstructures were closely bonded, and there were no cracks formed on the surface due to LSP. The X-ray diffraction (XRD) graphs showed amorphization of the samples and broader peak width is observed after LSP. Differential Scanning Calorimetry (DSC) graphs also show that compositions were capable of producing peaks, in both a heating and cooling curve. Further, LA was performed to overcome the problem of amorphization and recrystallize the formed samples. The increase in grain size of all samples was visible with Atomic Force Microscopy (AFM) and XRD results. The DSC graphs showed peaks formed in them after LA. Thus, combination of LSP and LA is an exceptional combination of two advanced techniques for post-processing of LAM components. Femtosecond laser was employed for removing extra material, reducing surface roughness and improving the geometrical quality of complex micro-scale topology features, such as holes with a higher aspect ratio. A significant reduction in the surface roughness was observed. It can be concluded that femtosecond laser radiation is suitable for post-processing of thermal sensitive parts with complex features due to high spatial sensitivity and controlled energy input.

Post-processing heat treatment is also applied for LAM components to adopt the properties of the components to the working conditions or to reduce the thermal stress induced. Thus, the desired microstructure and mechanical properties for service conditions can be achieved by various heat treatment procedures. These treatments alter the grain size, grain orientation, porosity and mechanical properties. Relieving of internal stress is another aspect associated with heat treatment. As discussed earlier, LAM components have residual internal stress due to a high thermal gradient. Thus, annealing is performed on LAM components for reducing the internal residual stresses. Solution treatment and ageing procedures are common for precipitation-hardened materials, such as nickel-based super alloys. Solution treatment helps in dissolving the undesirable phases, while aging enables the formation and growth of precipitation phases. These processes are usually done sequentially. The processing conditions and time for solution treatment should be properly selected for dissolving the precipitates. Once the solution treatment is done, aging is carried out to increase the hardness of the material. The standard heat treatment procedures for Inconel 718 are as follows:

1. Solution treatment (980°C, 1 h/air cooling) and double aging (720°C, 8 h/furnace cooling at 55°C/h to 620°C, 8 h/air cooling)
2. Homogenisation treatment (1080°C, 1.5 h/air cooling) and solution treatment (980°C, 1 h/air cooling) and double aging (720°C, 8 h/furnace cooling at 55°C/h to 620°C, 8 h/air cooling).

Another well-known solution that is used for experimental reasons, in order to examine porosity and microstructure of Ti-alloys, is the Keller's reagent solution [6], which consists of:

- 95 ml water,
- 2.5 ml HNO₃,
- 1.5 ml HCl,
- 1.0 ml HF.

The hot isostatic pressing (HIP) process has been extensively used in the healing defects such as cavities, voids and hot cracking. Enhancement and reduction of the scatter in the mechanical properties was observed as compared to an untreated sample. This can be attributed to the ability of HIP to heal the bulk and surface defects. Since HIP involves high pressure and temperature, fracture surfaces of the cracks were closed mechanically by the high temperature creep, then bonded together, and finally diffusion homogenized.

Property enhancements can be done with non-thermal techniques, such as shot peening. Shot peening is a mechanical surface treatment technique in which small balls are impacted on the surface of a component. The repeated impacts of the balls induce compressive residual stress and refine the microstructure. This helps in delaying the crack initiation and hinders the crack propagation. Thus, the mechanical properties and microstructure can be tailored as per the requirement by shot peening. Infiltration is another post-processing technique used in laser-sintered components. Porous LS part is heated in contact with the infiltrant to a temperature at which the infiltrant is melted and will soak into the part through capillary action. The infiltrant solidifies on cooling and produces the final part. The significant attention is on the ability of the infiltrant to wet the solid preform and form the dense solid. The strength of the structure after infiltration is a function of the time period of infiltration [5].

1.11 AM Applications

AM processes constitute an important class of manufacturing technology advancement. There is a huge spectrum of applications of additively manufactured parts which can chiefly be attributed to the development and improvement of AM processes. AM is particularly suitable for applications in producing complex shaped geometrical components as compared to conventional manufacturing techniques. From their initial applications as visualization tools, the innovation of AM parts has witnessed tremendous growth and diversity. The applications of AM processes have almost reached each industrial sector, which mainly includes aerospace, defense, marine, automotive, medical, retail sector, etc. [1]

The most important AM applications are given below [7]:

1.11.1 Artistic

Artistic applications of 3D metal printing are leading the way toward exploration of entirely new designs, shapes and processes. Some of these capture the essence of freeform, emotional design. A design and part by Bathshiba Sculpture LLC is one example, shown in Fig. 1.32.



Fig. 1.32 3D printed metal sculpture.

As software and material become cheaper, artistic access to solid free form design tools will allow a further expansion into the world of emotional design. As music, color, video, and other forms of dynamic audio and visual 2D art can evoke emotional response or inspirational experience, so will 3D virtual reality (VR) headsets and the 3D VR experience. Capturing moments of 3D VR and bringing them back to the physical world will be enabled by AM. This will include kinetic artwork and parts that change in time within the local environment of use.

3D printing machines designed for precious metals⁵ feature a powder management process developed for the jeweler and watchmaking industries, ensuring full accountability of the valuable powders and providing quick metal changeover through a cartridge-based system. The 3D metal printing machines used to create jewelry can be smaller and relatively less expensive than machines used to print automotive and aerospace parts. Artwork and jewelry do not require the same levels of certification and control needed by aerospace, automotive and medical devices, therefore making jewelry an attractive market for additive processing. Artistic designs that cannot be produced in metal by any other method are made possible while using less material and streamlining the production of custom made-to-order pieces. Hollow structures with internal supports allow the fabrication of larger pieces with the desired strength but without the weight or cost of a solid piece. AM systems such as shown in Fig. 1.33a feature small build volumes ideal for the rapid fabrication of small pieces such as jewelry while minimizing the total volume of precious metal powder stock. They use a small laser focal spot sizes, providing excellent detailed resolution, allowing the creation of fine features and structures, as shown in Fig. 1.33b and c.

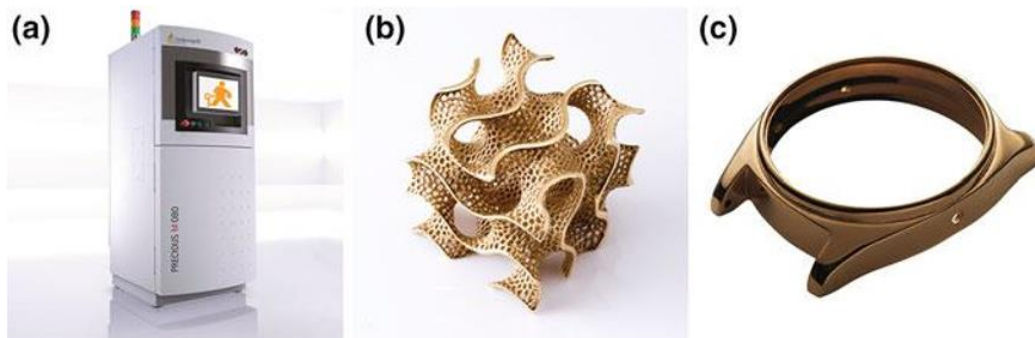


Fig. 1.33 a) Direct Metal Laser Sintering machine for jewelry, b) Sculptural design printed in gold, c) 3D printed gold watchcase.

1.11.2 Personalized

Renishaw and Empire Cycle teamed up to build the first design of the titanium bicycle as described in an article from Engineering and Technology magazine, “First 3D printed bike enters record books,” by Alex Kalinauckas. Fig. 1.34 shows the frame components as-fabricated in sections within the AM machine build volume. Fig. 1.35 shows the assembled frame with wheels and additional bicycle components. Technology demonstrations such as this highlight the ability to produce personalized designs out of specialty and lightweight materials such as titanium. Complex shapes with lightweight internal strengthening structures

and flowing organic forms allow the combination of engineering and artistic features to produce unique one of a kind individualized object.

3D scanning and printing is now commonly used in the fabrication of custom-fit hearing aids and other such personal devices. Although currently made in polymers, the hearing aid example shows the potential for 3D scanning and printing to disrupt market places and radically change products made specifically for you. Mass produced items have the appeal of low cost but in some cases the benefit of a customized item made specifically for you will offer the greatest value. As scanning and digital definition of our bodies becomes common place, every human-to-object interface holds the potential for customization. As an example, a mobile app may be used to order a personalized piece of jewelry. Personalized rings with the initials of a loved one, can be printed in various precious metals as shown in Fig. 1.36. Custom made and personalized items, such as golf club heads, are being produced by Ping. Although out of the price range for many, these types of items can infer personal taste and passion for the sport, as well as status (Fig. 1.37). Any sport, personal item or household fixture with a high- end market can be a target of innovative and unique designs made possible using AM metal.



Fig. 1.34 Titanium bike frame as-built using AM.



Fig. 1.35 Titanium bike frame as assembled.



Fig. 1.36 Personalized jewelry.



Fig. 1.37 Custom golf club head.

1.11.3 Medical

“Disruptive” applications for AM are beginning to emerge into the manufacturing mainstream. One such application is that of dental devices, where small custom-fit crowns and dental implants are disrupting the historic methods for the fabrication of these components. Fig. 1.38 shows dental crowns and bridges produced by direct metal laser sintering (DMLS). In one example, an EOS M 100 DMLS machine fuses Cobalt Chrome SP2 alloy, a medical material using a certified and qualified process. Small lot size, high precision and high value products such as these are seeing wide adoption.



Fig. 1.38 Additively manufacturing dental hardware.

Another application soon to be widely realized is metal medical implants, as certifications for medical use are being approved for human use in the European Union (EU) and US. Over 50,000 medical devices have been implanted for the medical industry as produced by the electron beam melting (EBM) additive manufacturing process alone. The benefits provided by AM are those of rapid production of personalized fit items for direct use, such as for implants, or secondary uses, such as drill guides and fixtures using the patient's own medical imaging to create 3D models anatomically matched devices. The accuracy of direct AM parts is sufficient for these applications, while the surface finish or porous structures offer advantages for bone ingrowth. These complex engineered surfaces are cleaned and sterilized offering a biological fixation intended to replace cemented fixation to optimize the implant–host interface. Fig. 1.39 shows a 3D printed titanium cranial implant on a 3D printed skull model.

Materials offering sufficient strength and biocompatibility are those currently used in medical devices, such as cobalt chrome and titanium alloys, which are easily fabricated using AM. Specialty metals such as tantalum may also see wider use in AM produced devices or AM deposited surfaces. Such medical devices command a high price and fit well within the build volume of powder bed fusion processes.



Fig. 1.39 Titanium skull implants.

1.11.4 Aerospace

Lockheed Martin and Sciaky have demonstrated the use of AM for the creation of a titanium propulsion tanks using EBAM, as shown in Fig. 1.40. In this case, the EBAM process is used to create a rough blank shape that can later be machined into a shape that would otherwise need to be formed by obtaining commercially available titanium plate, pressing into shape, then machining. Pressing would require a forming punch and die and a large hydraulic press. Vessels of various sizes would require a costly punch and die for each shape.

Fig. 1.41 show a full-scale rocket engine part 3D printed out of copper by NASA. The additively manufactured part is designed to operate at extreme temperatures and pressures and demonstrates one of the advanced technologies NASA is evaluating for use in fabricating parts

for the mission to the planet Mars. In another application, Aerojet Rocketdyne has fabricated and demonstrated the hot-fire testing of a rocket engine thrust chamber made using AM deposition of a copper alloy. Fig. 1.42 shows a liquid oxygen/gaseous hydrogen rocket injector assembly, built using additive manufacturing technology, being hot-fire tested at NASA Glenn Research Center. The potential reduction in fabrication lead times and costs provides strong motivation for evaluating the AM technology. Space and aerospace applications require strict procedures and certification for processes and components. Significant saving may be realized in the reduction of the number of certified parts and processes, such as joining, used to produce a component. The reduction in weight can result in significant savings during the launch into space escaping the gravity well of earth or fuel saving during commercial aircraft flights. The reduction in material waste during fabrication of expensive specialty materials such as nickel-based alloys or titanium is also an important factor in justifying the use of additive manufacturing. Additional benefits in system efficiency and environmental factors such as noise and emissions may also be realized.

In a business case study, the Airbus Group EADS Innovations performed an eco-assessment analysis as applied to a standard Airbus A320 nacelle hinge bracket, shown in Fig. 1.43 and strove to include detailed aspects of the overall lifecycle: from the supplier of the raw powder metal, to the equipment manufacturer EOS, to the end-user, Airbus Group Innovations. An entire lifetime assessment contrasted costs and savings of each method along the entire manufacturing chain from cradle to grave, indicating a lifetime cost saving primarily due to reduced weight (titanium versus steel, lightweight design).



Fig. 1.40 Titanium propulsion tank.



Fig. 1.41 Copper rocket nozzle.



Fig. 1.42 Testing of an additive manufactured rocket nozzle.

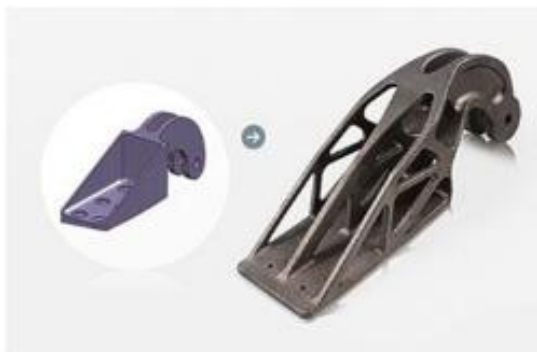


Fig. 1.43 A design for AM meeting lightweight target.

EOS and Airbus Group Innovations Team (now the EADS Innovation Works) cites another study associated with the weight reduction benefits of AM designs with respect to energy consumption and the reduction of CO₂ emissions by nearly 40% over the full lifecycle of a conventionally cast steel aircraft bracket in comparison to an additive manufactured direct metal laser sintered titanium bracket with optimized topology. A savings of 25% in the reduction of titanium scrap and a possible weight savings of 10 kg per aircraft was also cited.

1.11.5 Automotive

Formula 1 race car design teams are benefitting from the design freedom and rapid prototype/testing to speed fabrication cycles to gain competitive advantage off the track. In these cases, cost is a secondary consideration while weight reduction and design freedom are paramount. These sorts of critical application components, made of plastics, metals, or composites are not subject to the same testing and certification constraints as commercial man-rated components, thus providing a high-performance test bed for these components. As they say, racing improves the breed and this applies to the materials, designs, methods, and machines here as well. Such applications provide a proving ground for AM technologies, although the success stories and detailed methods will be tightly held as company confidential information. A steering knuckle part for a race car fabricated by DMLS is shown in Fig. 1.44. Two additional examples include a light twin-walled drive shaft and brake disks that are 25% lighter, with better cooling. Fig. 1.45 shows an AM printed piston for automotive application. While the big attraction of AM metal processing of automotive parts remains rapid prototyping of functional test parts, the production of specialty and hard to find parts, such as those used in vintage automotive restoration is actively being pursued. Mass production of automotive parts is out of reach of current direct metal AM processes but AM methods starting with a CAD model and resulting in a metal part such as by producing a sand mold or plastic pattern is gaining wider acceptance.



Fig. 1.44 Race car steering knuckle produced by DMLS.



Fig. 1.45 AM produced automotive piston.

Casting of large complex components can be realized by directly 3D printing a sand mold and then casting a part in metal can save development time, allowing for multiple design iterations during the prototyping cycle. Fig. 1.46 shows a silica sand casting mold used to cast a Formula 1 race car transmission housing using aluminum alloy A356. ExOne provides a case study where a batch size of five castings were produced at the cost of 1500 € per part compared a lot cost of 15,000 €–20,000 € using conventional patterns, tools and lost foam casting methods. This demonstrates that 3D printing technology can make sense for certain small lot size casting applications.



Fig. 1.46 Binder Jet produced silica sand mold for casting an aluminum Formula 1 transmission housing.

1.11.6 Industrial Applications Molds and Tooling

Mold inserts can benefit from complex conformal cooling channels to speed the molding process and improve part quality. Fig. 1.47 provides a view of a model part revealing complex cooling channels made possible by 3D printing (right view) and the outer surface of the part produced by the DMLS process in a finished and polished condition (left view). A case study by GPI Prototype & Mfg. Services of the actual part, shows it was still in use after 190,000 shots resulting in a productivity increase of 48%. Applications such as these place an additional reliance on the computer-aided engineering analysis of potential designs to fully optimize the benefit of AM processing. In addition to conformal cooling, AM metal processing may be used to repair or modify existing tooling to extend the life or increase the performance of existing parts.

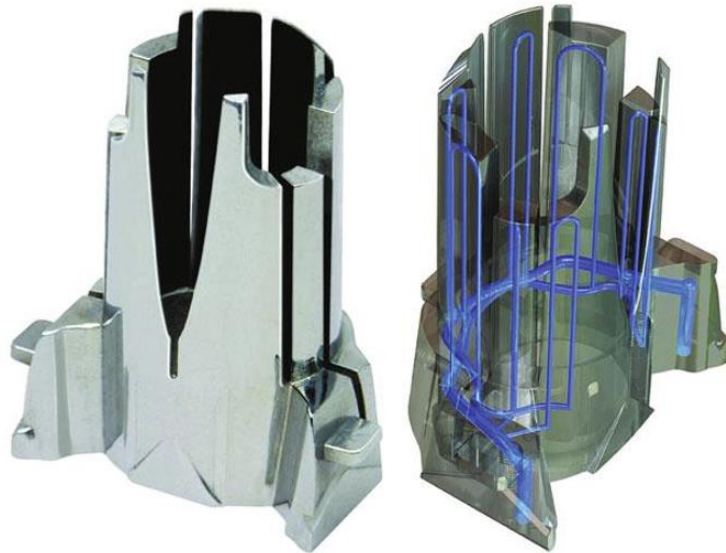


Fig. 1.47 DMLS fabricated part and model showing internal conformal cooling channels.

1.11.7 Remanufacture and Repair

Maintenance, repair or overhaul applications can benefit from direct energy deposition to apply coating for original parts or for repair.

Fig. 1.48 shows such an example where a forging tool for a connecting rod has been coated using the directed energy deposition (DED) process. To overcome the heat checking and wear damages during forging, the tool was built using low-cost steel and a high-temperature Co-based alloy was applied in the heat checking areas. In contrast to the mechanical bonding of the chemical vapor deposition (CVD) and physical vapor deposition (PVD) and thermal spray coatings, DED material is bonded to the base steel and can withstand the thermal and fatigue loading of the forging process without chipping of the coating material. DED built hard facing material was about 6 mm thick to sustain severe forging pressure and also allow for machining of the tool multiple times. DED applied tools had four times longer life over conventional tooling and resulted in significant cost savings while reducing downtime. In another example,

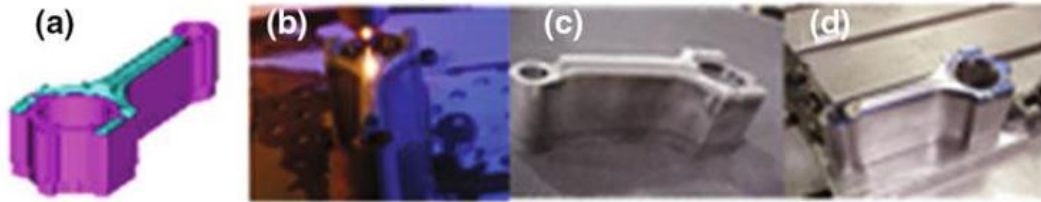


Fig. 1.48 Case study by DM3D Technology of a forging tool modified with cobalt-based alloy coating using the DMD process; a) CAD model showing tool base and DMD coating, b) DMD process in action, c) MD deposited tool, d) finish machined tool.

Optomec demonstrates repairing an impeller blade using laser beam directed energy deposition (Fig. 1.49).

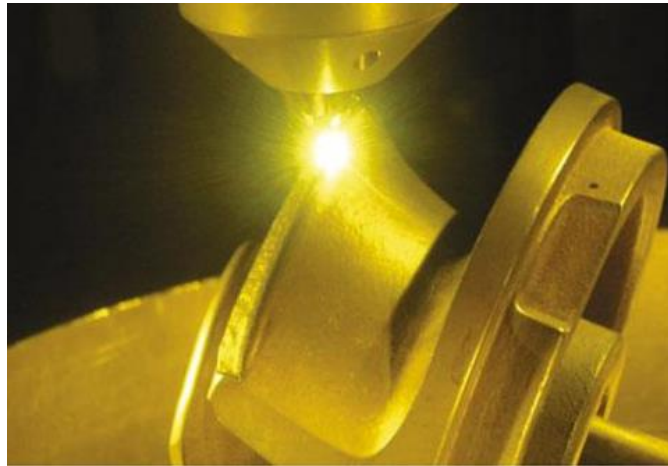


Fig. 1.49 Directed Energy Deposition Repair of Impeller Pump.

1.11.8 Scanning and Reverse Engineering

Scanning technology can use laser or photographs to capture an object's shape and use reverse engineering software to recreate a model of the object. That model can be used to 3D print plastic patterns or sand molds of direct to metal parts.

Geomagic, owned by 3D Systems, provides hardware and software solutions to allow 3D scanning and the creation of 3D models to be used in original and reverse engineering applications. One example, in Fig. 1.50, demonstrates the ability to scan motorcycle engine parts, process the point cloud data into a model that can be features and assembled into a 3D model that can also be used to 3D print a plastic or metal component. The software can interface with professional level computer-aided design (CAD) software such as Catia, Solidworks, etc.



*Fig. 1.50 Directed Energy Deposition Repair of Impeller Pump
Example of scanned parts to CAD model.*

1.11.9 Construction

In the construction industry, construction components or the entire buildings can be printed using this technology. The recent growth of building information modelling (BIM) may facilitate greater use of 3D printing. 3D printing allows faster and more accurate and complex construction by lowering labor costs and wastage. It also enables construction in dangerous environments like space where humans cannot work safely.

The printer prints the building blocks from melted plastic or metal. The building blocks that are printed, are used to form component parts that can be arranged together like Lego to create a complete building.

Metal can be used and structures like bridges can be printed. Huge 3D printers are used to do this kind of jobs. Even the printing time is also very less, it is claimed that a house was printed in less than 20 hours.

3D printing in this industry is helpful in constructions in areas such as off-Earth habitats like on the Moon or Mars (Fig. 1.51).



Fig. 1.51 A view of 3D printed house.

1.11.10 Defense

In military and defense manufacturing, customized equipment is vital and deadlines are non-negotiable. In such an industry 3D printing gives freedom for the government and manufactures, to design a single end-use part or to build complex and precise prototypes. 3D printing enables design teams to rapidly produce high-quality precise and realistic prototypes, which has moving parts at relatively less cost when it compared to other traditional machining process. It can also reduce the outsourcing costs. The team can manufacture a part then and there when it is required. 3D printed parts have less weight and high strength which increase efficiency of the objects and reduces its carbon footprint.

During disasters, shelters can be printed on site. Special blend of cement is used in printing the walls of these shelters, which has strength greater than conventional walls [2].

1.12 AM Forecast

Forecast is an essential tool, which helps industries plan their resources and shape their business strategies. For researchers and government organizations, forecasting provides an idea on the present status and future scenarios of technology and business for investment decisions. It also helps researchers to understand futuristic technology developments and actions required therein.

An AM forecast is given by Sriram V. et al. [2], where the data were collected from reports on AM revenues and 3D printer units sold for a complete understanding of the important factors, which helped in correlating the quantities. The factors considered are mainly year-wise revenues generated for AM products, equipment and AM material, AM service revenue, units of personal and industrial AM sold, etc. The objective has been to forecast the direct parts as percentage of overall AM market (Diagram 1.4, up), the percentage of increase in AM parts used in each industry (Diagram 1.4, down) and the number of industrial metal AM units to be deployed for the next 10 years (Diagram 1.5).

The data and the forecast are given below (Table 1.3, Diagram 1.4, Diagram 1.5):

Table 1.3 AM market remarks.

Company name	Imp Remarks
Siemens	Predicts that 3D printing will be 50% cheaper and up to 400% faster in the next five years. Siemens is also predicting the global market for 3D printing will reach €7.7B (\$8.3B) by 2023
Boeing	Already installed over 200 different types of flying production parts on 16 different aircraft
GE aviation	Designed an entirely new nozzle that integrates 18 separate parts into one. The new nozzle is 25% lighter and 5 times more durable
3D systems	Sales into design and manufacturing increased 27% from 2013 to 2014, growing to \$609.8 M in sales. Sales into healthcare increased 80%, from \$71.7 M in 2013 to \$129.3 M in 2014. The consumer segment of 3D systems business grew by 26% in the last year, from \$34.8 M in 2013 to \$43.8 M in 2014
Gartner	Prototyping (24.5%), product development (16.1%) and innovation (11.1%) are three most common reasons for companies to pursue printing
PwC	PwC estimates 67% of manufacturers are already using 3D printing. Of these, 28.9% are exploring how 3D printing can be optimally integrated into their production processes. 24.6% are using 3D printing for prototyping

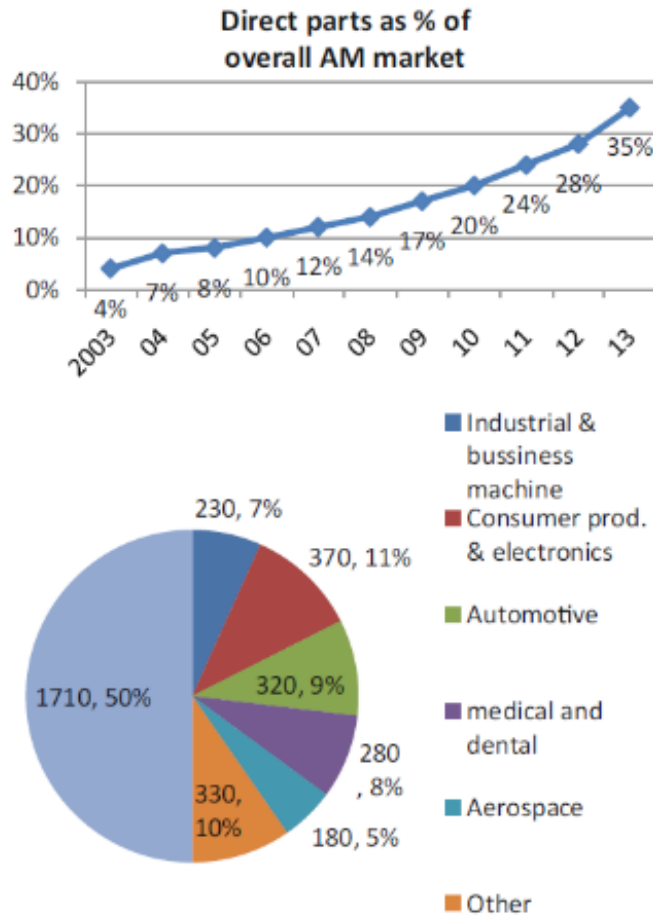


Diagram 1.4 AM market growth.

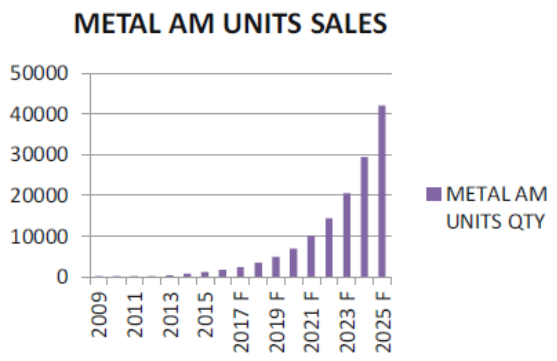


Diagram 1.5 Metal AM units sales and forecast F.

2. Selective Laser Melting (SLM)

2.1 Definition

Selective laser melting (SLM) is an additive manufacturing (AM) technique to produce complex three-dimensional parts through solidifying successive layers of powder materials on the basis of a CAD model. SLM is associated with complete melting of the powder material rather than sintering or partial melting of the powder particles which is the dominant mechanism in the selective laser sintering (SLS) process.

2.2 SLM Basic Mechanism

Fig. 2.1 shows a schematic layout of the SLM process. In this process (carried out under a protective atmosphere), a metal base plate is used to anchor the part during the building process. A layer of powder (most commonly from metals) is spread on top of the base plate and is subsequently melted by a laser beam projected from above. The laser scans the powder bed according to the shape defined in a CAD file (that has been sliced into many different layers). After each layer has been scanned, the powder bed is moved down over a distance of one layer thickness, followed by an automated leveling system that distributes a new layer of powder. The laser then melts a new cross-section. The process is repeated to form the desired solid metal part (comprised of hundreds or possibly thousands of thin layers).

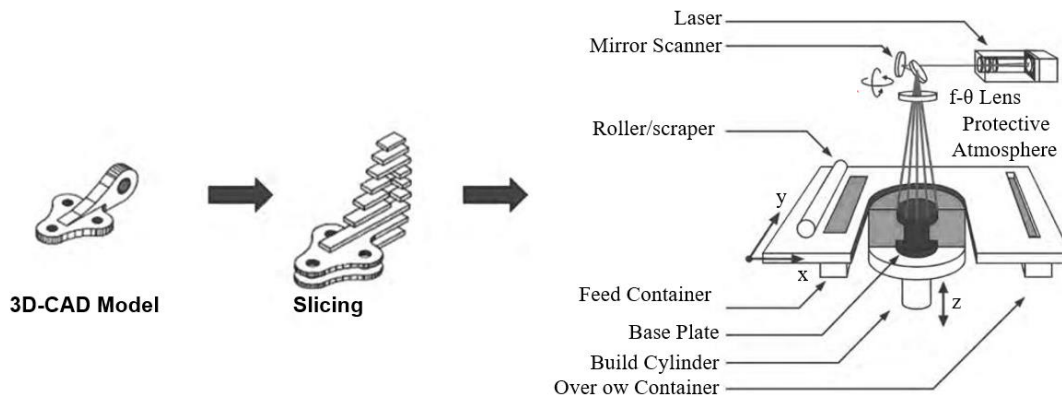


Fig. 2.1 Schematic diagram of the SLM process.

2.3 SLM Advantages and Disadvantages

Many advantages are associated with the SLM process, including (1) high density and strength of the parts; (2) negligible waste of material (unused powders can be recycled); (3) possibility of producing complicated shapes (e.g., a steel mold with curved internal cooling channels, which is common to other AM methods); (4) ability to process a wide variety of metals and their mixtures (due to the powder-based nature of SLM); and (5) no need for any distinct binders or melt phases, so the process can directly produce single material parts (e.g., steel, Ti, or Al alloys), rather than first producing a composite green part that requires such secondary processing steps as debinding (Debinding is a secondary step to remove the binding additives from the green compacts) and furnace sintering (as done with some other AM methods).

Selective laser melting is a newly developed process faced with various challenges. For example, SLM suffers from melting pool instabilities leading to imperfections such as low-quality down-facing surfaces, greater upper-surface roughness, and the risk of internal pores. The resulting coarse and grainy surface finish may require a secondary machining or polishing process. Additionally, high temperature gradients in SLM increase the risk of delamination and distortion due to large thermal or residual stresses. From an economical aspect, the high cost of a high-power laser source, long processing times, and a small palette of available materials are the main obstacles. Despite these challenges, SLM is increasingly becoming a competitive manufacturing alternative.

2.4 SLM Machine and Equipment

2.4.1 Basic Units and Process Layout

An SLM machine consists of three main units: (1) laser and scanner system, (2) controller system, and (3) build chamber. The laser (Fig. 2.2A) consists of an elongated cavity with two mirrors at its ends in which light oscillates back and forth between the mirrors. Between the mirrors, there is a light-amplifying medium, where stimulated emission occurs. The mirrors guide the light back into the amplifying medium repeatedly for continued growth of the developing beam. After amplification, the emissions pass through a partially transmitting mirror. The resultant beam is then guided to enter a scanning system. Most laser scanner systems use a galvano scanner (In a galvano scanner, two electromechanical actuators rotate two mirrors -deflecting the laser beam in the x and y directions-, in response to electric current flowing through their coils in a magnetic field) to steer the laser beam, as shown in Fig. 2.2B. The scanner guides the beam through focusing optics (to further focus the beam) to scan any desired geometry on the powder bed (Fig. 2.2B). In addition to the machine, the scanning is automated and controlled via a dedicated controller and computer unit.

Scanning the powder bed is carried out in a secured container called the build chamber (see Fig. 2.3). The build chamber is designed to provide an inert/protective atmosphere (using mostly N_2 or Ar gas circulation) and contains a build stage (Fig. 2.4). The build stage is a platform to hold the build cylinder (in which the base plate is mounted), the feed cylinder (holding the powder), the elevator systems (to bring the powder level up/down), and the coating system (to uniformly distribute a thin powder layer onto the base plate).

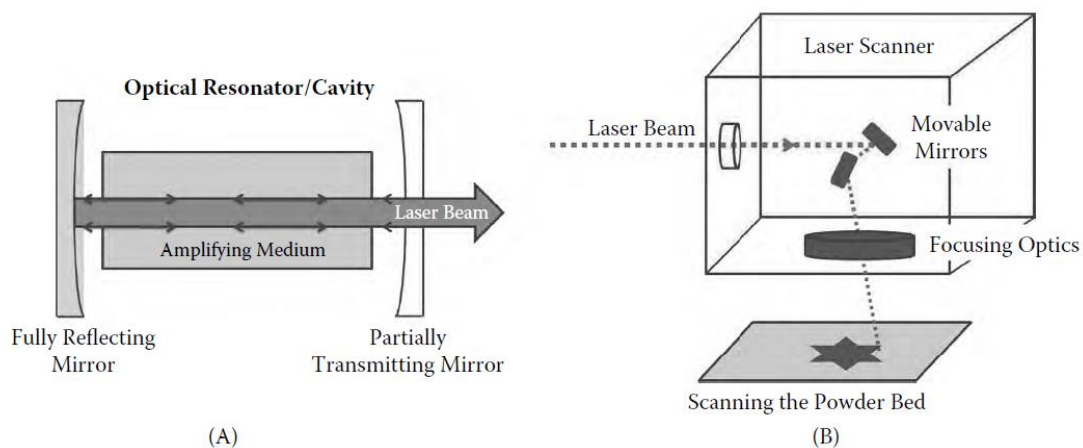


Fig. 2.2 Simplified schematic of a typical (A) laser and (B) scanner system.

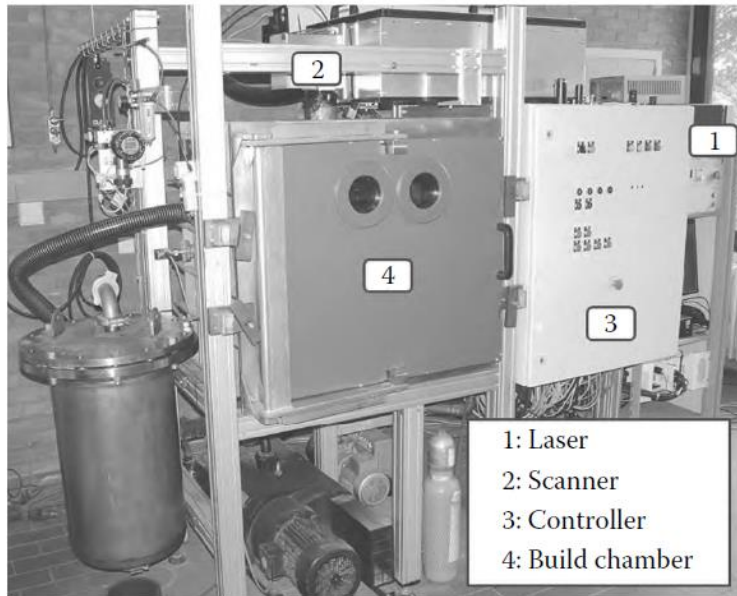


Fig. 2.3 In-house SLM machine developed at KU Leuven.

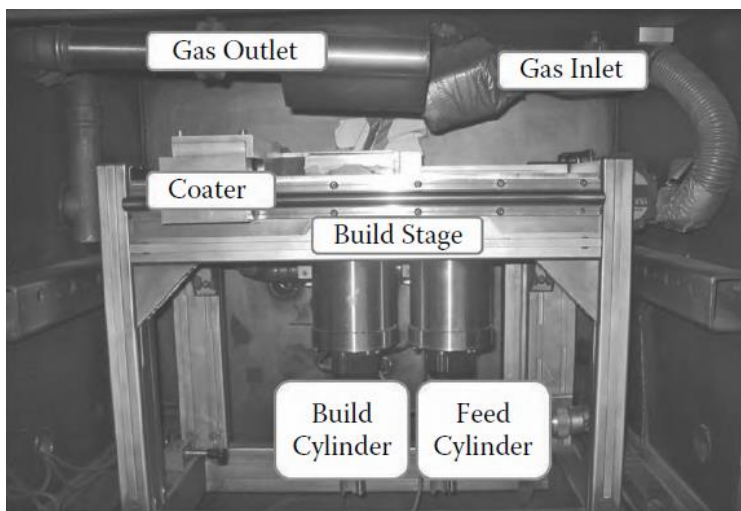


Fig. 2.4 An example of a SLM machine build chamber at KU Leuven.

2.4.2 Preheating Stage

To increase the efficiency of the SLM process or to improve the quality of manufactured parts (in case of specific alloys), a preheating system may be incorporated in the SLM machine. This can be done by heating the base plate in order to mitigate the temperature gradient between the base plate and the top layers. Fig. 2.5 shows an overview of a heating module. The heating element itself (labeled 2 in Fig. 2.5) is installed underneath the building platform and enclosed by insulation material. The temperature of the base plate can be monitored by a thermocouple probe. A proportional and integral control loop (PI-controller) controls the

power to the heating element to achieve the desired temperature on the base plate within a range of $\pm 2^{\circ}\text{C}$ [8].

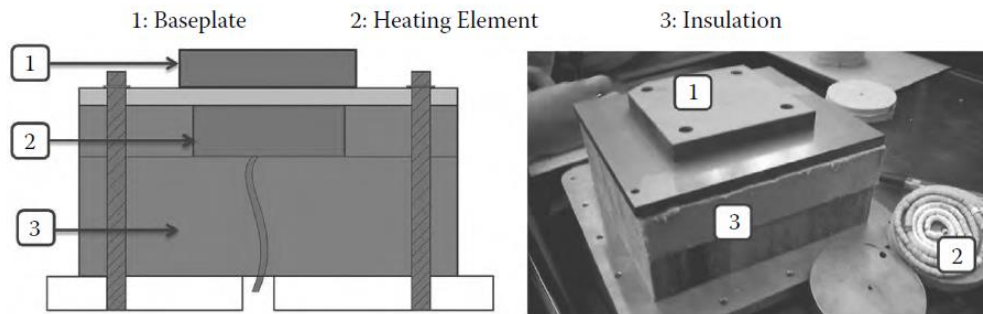


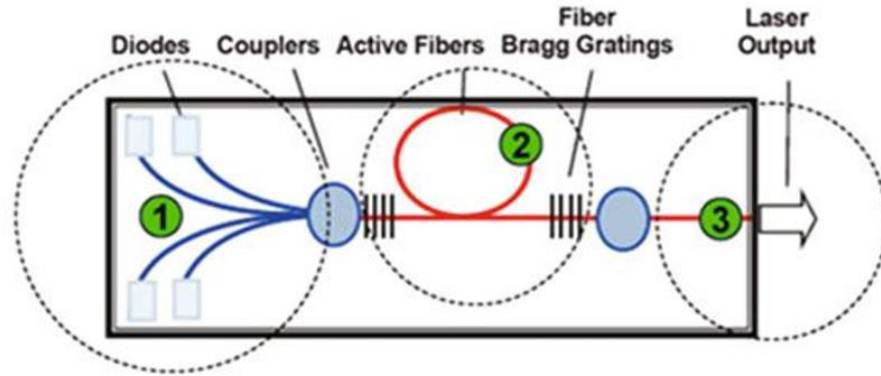
Fig. 2.5 A customized preheating system developed by KU Leuven.

2.5 SLM Physical Phenomena

2.5.1 Laser beam

The invention of the laser more than a half century ago was a technical milestone in physics that has found applications across a wide spectrum of material processing. Lasers, powerful enough to melt metal, were developed early on and found wide application in laser cutting as early as the 1970s, although equipment costs focused uses to high value, high payback production operations. Although the prices have dropped considerably, high-powered lasers used for AM systems can still cost hundreds of thousands of dollars.

Lasers generate a high energy density beam of photons and can be transmitted and focused to produce a small spot size of energy capable of melting and vaporizing metal. Laser equipment can generate beam powers of thousands of watts and focus to beam spot sizes of fractions of a millimeter. These small spot sizes can result in very small melting pools capable of melting at very high travel speeds on the order of many meters per second. There is a wide range of laser technology used in AM with names such as Nd:YAG, disk lasers, and direct diode lasers, but this discussion will focus on the newer fiber laser technology because most AM systems now use fiber lasers due to their reliability, compact size, and low maintenance. The basic principle of a fiber laser is shown in Fig. 2.6. Optical pump diodes are coupled onto an active laser fiber with a special reflective coating and Bragg gratings that reflect the laser light back-and-forth, along the length of the fiber, to create a coherent beam of light at the output of the laser. Beam delivery is often accomplished using additional optical fibers that provide a durable, flexible, fully enclosed beam path for delivery and containment of the light energy. These fibers are safety interlocked to shut down the system in the event of a breach of the delivery fiber. Final beam delivery includes optical elements and lenses to condition and focus the beam after it leaves the optical fiber. Manipulation of the beam is often accomplished by magnetically driven mirrors or CNC motion.



- ① **Pump diode modules** pump the light radiation into the active fiber
- ② **Optical active fiber** with a doped core (ytterbium) and couble cladding, where the pumped light excites the core
- ③ **Transport optical fiber** bringing out the power from the module

Fig. 2.6 Fiber laser principal.

The laser beam is directed toward the work and focused at or near the part surface at power densities sufficient to achieve the desired degree of melting. Laser energy impinging on the workpiece is either reflected away or absorbed into the part or filler material creating heating and melting. Laser absorption or reflection may be significantly different for different metals.

Without getting into the complexity of laser material interactions, it is important to note that different metals will absorb or reflect laser energy differently, such as titanium versus copper. Aluminum or silver have very low absorption coefficients while titanium has relatively higher absorption. The type or wavelength of laser energy affects the absorption as well. Yb:YAG fiber lasers will pass through quartz optical elements, such as the window of an inert processing chamber, a focusing lens or within a quartz fiber. In comparison, a CO₂ laser wavelength will couple with and melt quartz making it impossible to transmit using a fiber and difficult to deliver into an AM processing chamber.

In addition to the material and wavelength absorption dependence, the absorption of laser energy by melted metal is often much greater than for solid metal. Plumes of vaporized metal or plasma can form above a melting pool, absorbing laser energy and preventing it from reaching the melting pool. If that is not enough, the pressure of the rapidly expanding cloud of vaporized metal and superheated gas can create a depression in the melting pool trapping laser energy and further enhancing absorption. This depression often called a keyhole creates a vapor cavity that may extend deeply into the metal. This keyhole mode of melting (Fig. 2.7) can produce deep penetration but also may create defects such as porosity, spatter (also balling) or entrapped voids. These transitions in absorption and melting between heating, conduction melting, keyhole melting and plume formation can be very abrupt and can result from very small changes in laser power, travel speed, focal spot size changes, or other minor

process disturbances. In AM processing, powder size, and layer thickness can also have an effect.

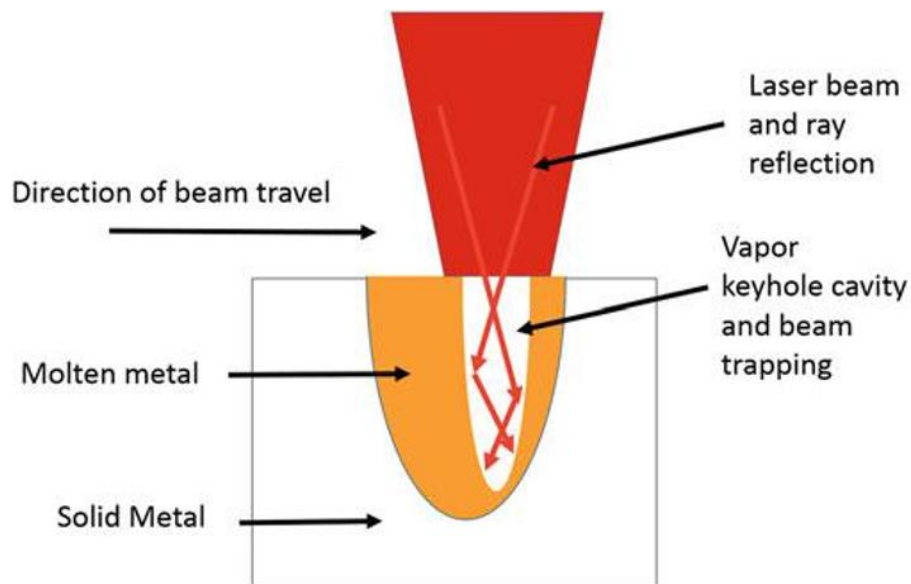


Fig. 2.7 Laser keyhole vapor cavity.

As mentioned earlier, laser absorption increases upon melting and may be of sufficient energy to preferentially vaporize low melting point constituents of an alloy, such as aluminum, magnesium or lithium, thus changing the chemistry of the deposit. Vaporized metal may redeposit upon surfaces within the build chamber or nearby optical components. The dynamics of laser material interactions are extremely complex (solid, liquid, gas and sometimes plasma) and may be sources for process instability [9].

2.5.2 The Melting Pool

The many physical effects that occur during SLM processes influence the process stability and the final component quality. Identifying and understanding these phenomena and their interplay are crucial for successful manufacturing.

During heating, the powder bed is irradiated by a laser, whereby the photon is transformed into thermal energy by absorption. Photons are generally absorbed within the first nanometers at the surface of the material. In contrast to opaque continuous material, the powder bed allows for deep penetration due to multiple reflections at the particle surface. The absorbed thermal energy is distributed depending on the relative density and reflectivity of the powder bed within the top powder layers.

Thermal radiation, thermal convection, and evaporation of volatile elements cause a heat loss, which depend on the surface temperature of the material. During SLM, heat convection between the material and the shielding gas occurs. Due to heat conduction, the absorbed thermal energy is further distributed into the material, and temperature peaks at the surfaces

are reduced. This effect depends mainly on the thermal diffusivity of the material and the sintering grade of the powder bed.

If preheating is applied, the base temperature of the powder bed is elevated, simplifying melting and reducing temperature gradients during manufacturing. If the preheating temperature is higher than the sintering temperature of the material, the single powder particles get interconnected by small sinter necks. These pre-sintered powder particles act as support structures during the subsequent manufacturing and increase the thermal and electrical conductivity.

During processing, the material melts and forms a melting pool. Convection depends on viscosity and is driven by external forces like gravity, buoyancy, surface tension, capillarity, Marangoni effects, and evaporation pressure. Depending on the process and the material, these phenomena have different impacts. The melting pool lifetime is commonly short, viscosities are low, and gravity plays a minor role compared with the roles of the other forces. Thermal expansion induces buoyancy and exerts thermal stresses. The high surface tension in combination with the wetting ability of metals results in a smooth surface for stable melting pools. In contrast, unstable melting pools are split up, and the surface tension causes the formation of single melt balls. Marangoni forces induce fluid motion away from the temperature peak in the center of the melting pool and increase heat transport. Due to high melting pool temperatures, the material evaporates, and the resulting recoil pressures additionally drive the fluid motion. Especially in SLM processes, these pressures cause the so-called keyhole formation, in which the laser beam penetrates into the material up to certain layer thicknesses, forming a vapor capillary. Selective evaporation of volatile elements additionally changes the local and global material composition.

After melting and consolidation of the material, the temperature decreases, and the material solidifies. Material shrinkage during solidification induces stresses in the surrounding material that can partially relax during successive layer processing. The residual stresses inside the component are the main reason for distortions.

Depending on the temperature gradients and the processing temperature, a certain microstructure evolves. Due to the layer-wise manufacturing, repeated heat treatment of the heat-affected zone around the melting pool may change the microstructure by solid-state phase transformations.

In the last step, a new powder layer is applied. Its characteristics are influenced primarily by the powder properties and the previous layer surface. High flowability of the powder, depending on powder properties such as surface topology, size distribution, and shape, is necessary to achieve high relative density of the powder bed [10].

Specifically, the characteristics of the melting pool are given below [11]:

- Melting pool temperature: The maximum temperature significantly increases with a general increase in laser or linear energy density, but it slightly decreases with an increase in laser scanning speed.

- Temperature gradient: The temperature gradient in the melting pool increases linearly with an increase in the applied laser power. The temperature gradient is more pronounced in materials with low thermal conductivity.
- Melt lifetime: The liquid lifetime is the duration from the time powder particles in the local region start to melt until they eventually solidify. It is found to increase with an increase in the laser power and a decrease in the laser scanning speed.
- Melting pool dimensions: The melting pool dimensions including length, width and depth increase with an increase in laser power. However, the melting pool length increases and the width of the melting pool decreases with an increase in laser scanning speed.
- Melt viscosity: The viscosity of a melt decreases with an increase in linear energy density as a result of the increase in the melting pool temperature. Dynamic viscosity should be balanced so that its low enough that the melting pool can be spread properly on a formerly processed layer and high enough to prevent balling phenomena.
- Melt flow: Mass transfer in the melting pool occurs as a result of the thermocapillary flow; Marangoni convection occurs as the result of surface tension gradient. The direction of the melt flow is determined by the sign of the surface tension gradient of the melt, as shown schematically in Fig. 2.8. A shallow and broad melting pool is produced if the flow is radially outward when $\frac{d\gamma_{LV}}{dT} < 0$ (as for pure metals and many alloys), as in Fig. 2.8(a). A narrow/deep melting pool is formed if the flow is radially inward when $\frac{d\gamma_{LV}}{dT} > 0$ (as for alloys containing a sufficiently large number of surface-active elements), as shown in Fig. 2.8(b). Surface tension at the edge of a melting pool can be dramatically reduced by surface oxidation during SLM of iron and tungsten; this changes the sign of the surface tension gradient and the melt flow from the cooler melt at the edge (lower relative surface tension due to oxidation) toward the area near the center of the melting pool (higher surface tension). The velocity of the melt flow increases with an increase in laser scanning speed and powder layer thickness, which results in melt splashing at high laser scanning speeds.

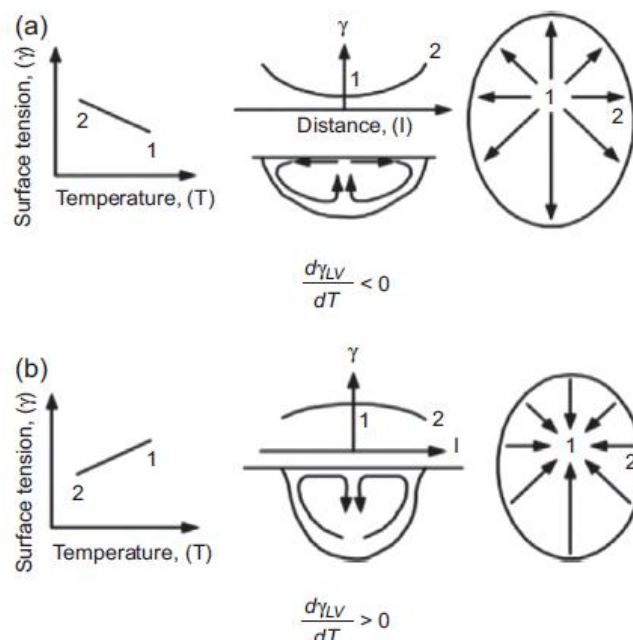


Fig. 2.8 Schematic illustration of the effect of the surface tension gradient on Marangoni convection in a melting pool; a) $\frac{d\gamma_{LV}}{dT} < 0$, b) $\frac{d\gamma_{LV}}{dT} > 0$; 1 represents the center of the melting pool, 2 represents the edge of the melting pool.

- Stability of the melting pool: A melting pool is stable at a range of scanning speeds for a given laser power. The range of the stable zone increases with an increase in laser power, and it becomes narrower for materials with a higher thermal conductivity at a given laser power and layer thickness. The melting pool stability is critical for the quality of SLM-fabricated parts; melting pool instability results in an irregular and/or discontinuous track, which leads to high surface roughness and volumetric porosity due to balling in the fabricated parts.
- Hydrodynamic instability of a melt is driven by the Marangoni effect and becomes increasingly important with an increase in the Laser Energy Density (LED) because of a relatively high laser power or a low scanning speed.
- Capillary (Rayleigh) instability of a melt occurs when the total surface of the melting pool is larger than that of a sphere with the same volume and when the viscosity is too low.
- Balling: Balling is a phenomenon where the melted track shrinks and breaks up into a row of spheres to reduce the surface energy by the surface tension if the melted material does not wet the underlying substrate. The balling effect can lead to high surface roughness and porosity in the as-built parts, and it might even jeopardize the powder-laying process if the size of the balls is large enough to obstruct the movement of the paving roller. An ellipsoidal ball with a diameter of about 500 μm is detrimental to the quality of the SLM-processed part. However, spherical balls with a diameter of about 10 μm have no obvious detrimental effect on the quality of the SLM-processed part.
- Sputtering: Sputtering is caused by overheating the melting pool, and the intensity of sputtering increases with an increase in input energy density. Liquid droplet and non-melted powder particles around the melting pool are expelled by the recoil pressure generated on the melting pool as the result of the melt evaporating. The sputter caused by melt expulsion is spherical and much larger than the particle size of the feed powders. Oxides, a few micrometers in size on the sputter surface, are the result of the oxidation of the most volatile elements in the alloys that are enriched on the surface of the sputters. The sputter caused by the expulsion of non-melted particles is also known as a satellite and has a microstructure similar to that of the feed powder alloy.

Balling is attributed to (1) the capillary instability of a melting pool; (2) hydro-dynamic instability driven by the Marangoni effect; (3) splashing of the melting pool as a result of a high melting pool surface temperature, a high velocity of the melt flow and a turbulent liquid solidification front; (4) high oxygen content in the atmosphere due to deteriorated wettability at the interface, with the oxidation of the melting pool and the increasing tendency to the larger radially inward Marangoni flow caused by the larger positive value of the surface tension gradient of liquid, with higher dissolved oxygen content in iron and tungsten; (5) rapid solidification before the melt is properly spread, driven by capillary flow when processing materials with high thermal conductivity, such as tungsten; and (6) lack of contact between the melted powder and the substrate because of insufficient melting of substrate.

Balling occurs as a result of capillary instability (Fig. 2.9) to reduce the surface free energy. Therefore, it is critical to control the ratio of the length of the melt to the width of the melt to meet:

$$\frac{l}{d} < 2.1 \quad (1)$$

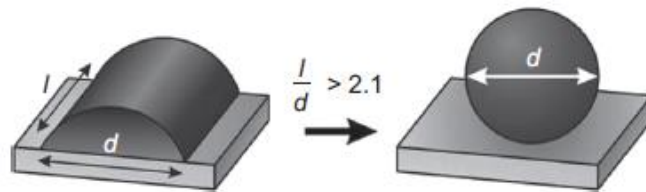


Fig. 2.9 Balling caused by capillary instability as a half cylinder transitioning to a sphere, depending on the dimensions of the melt pool.

$$\frac{l}{d} < \frac{\pi}{\sqrt{2}} \sqrt{\frac{2\theta(2+\cos 2\theta)-3\sin 2\theta}{\theta(1+\cos 2\theta)-\sin 2\theta}} \quad \text{when } \theta > \frac{\pi}{2} \quad (2)$$

where θ is the contact angle. Hence optimal laser processing parameters are required to make the length-to-width ratio of the melting pool as small as possible in order to eliminate the balling effect.

Balling can be eliminated to a certain extent with surface remelting provided by a second laser scan and proper selection of laser exposure time to achieve a balanced viscosity. The density of SLM-processed parts can be improved by laser surface remelting after the first scan [11].

To sum up, the basic physical phenomena that take place in an SLM melting pool are visualized in Fig. 2.10, left:

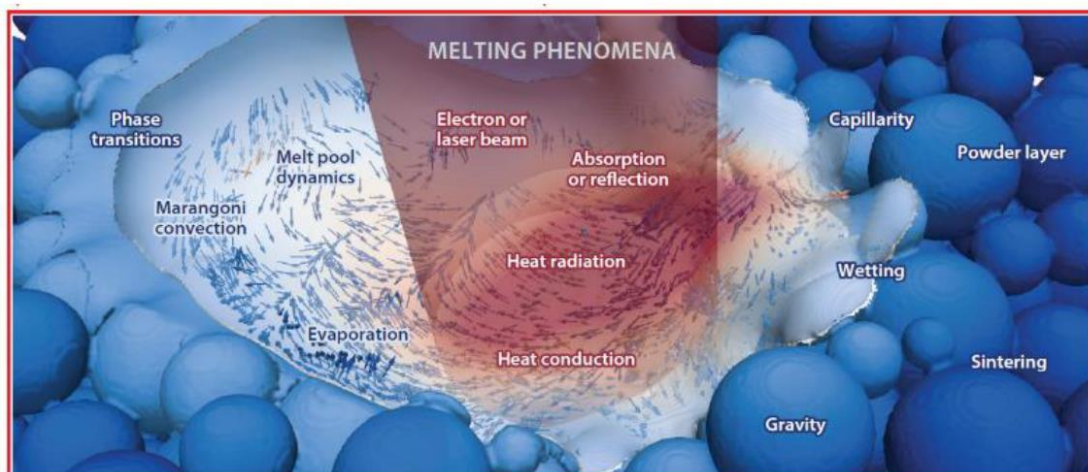


Fig. 2.10 Physical phenomena in SLM (left) and EBM (right).

2.6 Processing Aspects

2.6.1 Starting Powder

The apparent density of the powder, which influences the final density of the SLM parts, depends on the powder size, shape, and size distribution (an example is shown in Fig. 2.11). Generally, packing of spheres leads to a higher density than other shapes. The spherical particles with smooth surfaces may also improve the powder flowability and deposition. Moreover, finer powders may result in a higher apparent density (to some extent), indicating a higher final density and mechanical properties. For mono-sized spheres, the highest obtainable packing density is theoretically 74%. However, the apparent powder density can be increased by mixing different powder sizes (see Fig. 2.11B). In fact, finer particles can fill the voids between the larger powders and subsequently increase the powder density. It is worth mentioning that higher packing density may also increase the cooling/solidification rate (by increasing the thermal conductivity), resulting in finer microstructural features. Higher mechanical properties may be achieved from these finer microstructural features.

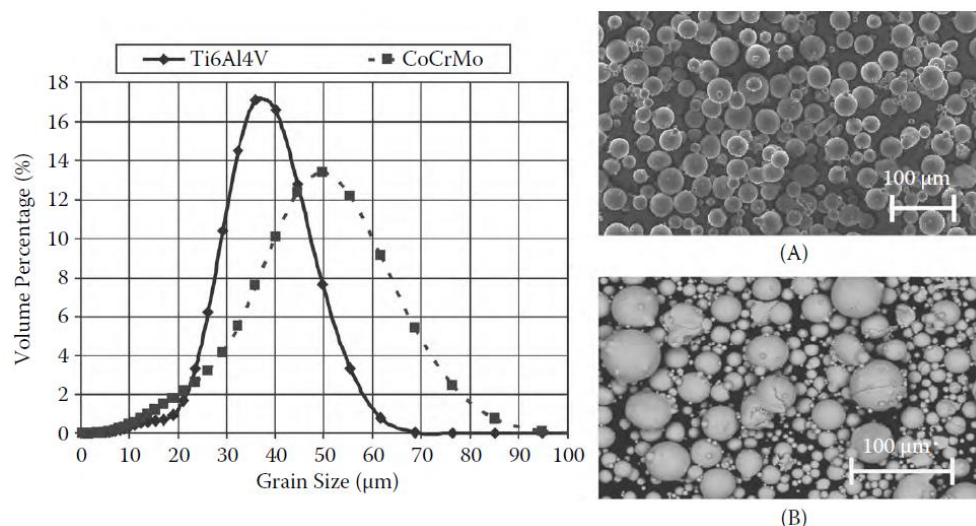


Fig. 2.11 Powder size distribution and micrographs of (A) titanium and (B) cobalt chromium powder.

2.6.2 Input Parameters (Laser Power, Scanning Speed, Layer Thickness, Scan Line Spacing)

The SLM process is set by adjusting various parameters. An optimal combination of laser power, scanning speed, powder layer thickness, and scan line spacing (also known as hatch spacing) is required to minimize the potential defects (by achieving optimal melting pools) and to produce high-quality parts. In order to improve the precision, an offset (about the radius of the laser beam) can be applied. A fill contour can also be used for a higher precision or an improved outer boundary quality (Fig. 2.12). The effect of the process parameters can be combined and presented as the energy density, which is an engineering parameter representing the energy delivered to a unit volume of powder material. This is achieved by combining the laser power, scanning speed, scan line spacing (or hatch spacing), and layer thickness as shown below [12]:

$$VED' = \frac{P}{vst} \left(\frac{J}{mm^3} \right) \quad (3)$$

or

$$VED = \frac{P}{vD_b t} \left(\frac{J}{mm^3} \right) \quad (4)$$

Where:

VED or VED' = volumetric energy density $\left(\frac{J}{mm^3} \right)$,

P = laser power (W),

v = scanning speed $\left(\frac{mm}{s} \right)$,

s = scan line spacing (mm),

t = layer thickness (mm).

D_b = laser beam diameter (mm).

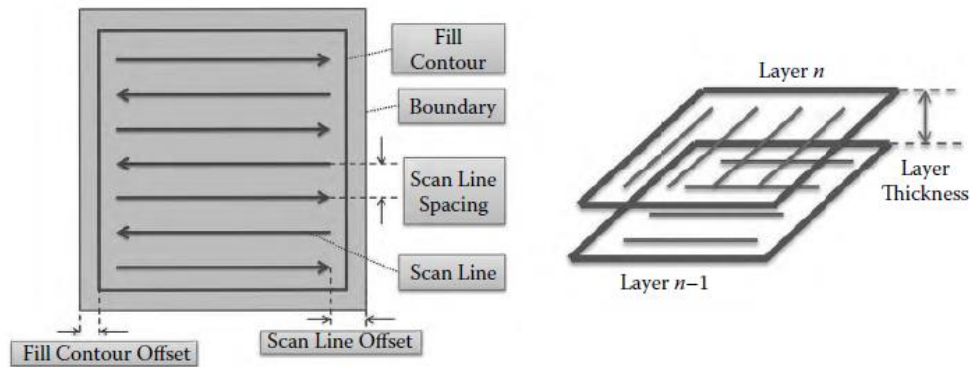


Fig. 2.12 Schematic representation of scanning parameters that can be altered to improve quality. Boundary parameters (e.g. scan line offset, fill contour) increase precision and the quality of the borders.

Accordingly, increasing the laser power and decreasing the scanning speed, scan line spacing, or layer thickness increases the laser energy density.

2.6.3 Scanning Strategies

Different scanning strategies (Fig. 2.13) affect the thermal history during the SLM process and consequently alter the material properties, including density, thermal and residual stress, and microstructure. It has been reported, for example, that an alternating scanning strategy (rotating the scanning direction in each layer) improves the density of Ti6Al4V parts. The scanning strategy also influences the residual stresses and can be modified to mitigate quality issues such as warpage, cracks, and delamination.

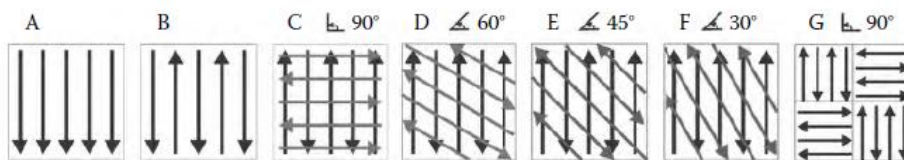


Fig. 2.13 Schematic examples of possible scanning strategies: (A) unidirectional, (B) bidirectional, (C-F) alternating bidirectional (with different angles at 90°, 60°, 45° and 30°) and (G) chessboard scanning strategy.

2.6.4 Laser Remelting and Laser Erosion

In SLM, the surface roughness is an important parameter of the overall quality of the part. A number of surface modification technologies are commonly applied after the SLM process, including mechanical methods (abrasive sandblasting and machining), chemical processes (acid etching and oxidation), and thermal processes (plasma spraying). Because these methods are applied after SLM, they require removing the part from the building platform. This increases the overall production time, precision errors, and final cost; however, SLM itself can be directly used to improve the surface quality through a controlled laser remelting of the surface. For example, Fig. 2.14 shows a successful laser remelting experiment to smoothen the surface without the use of any secondary treatment. This surface improvement can be attributed to the surface shallow melting mechanism. In this mechanism, melting a thin material layer fills valley in between the peaks and removes aggregated spheres of particles.

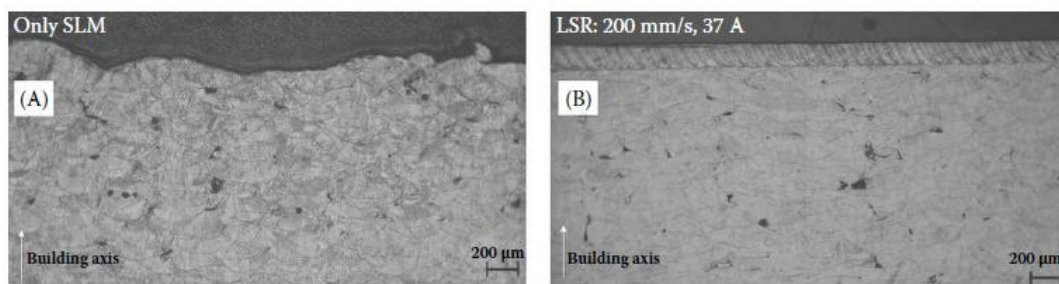


Fig. 2.14 Surface quality enhancement of 316L stainless steel with laser remelting: (A) before laser remelting and (B) after laser remelting with 200 mm/s scanning speed and 95W laser power.

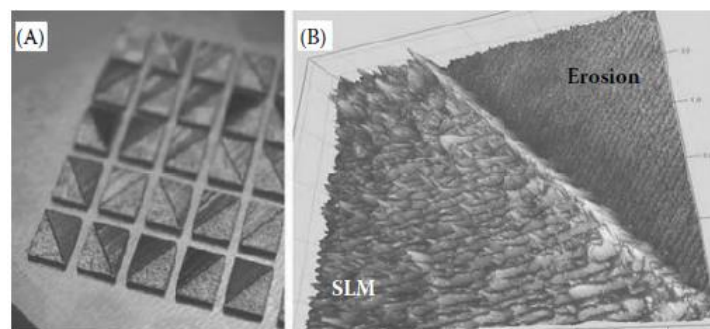


Fig. 2.15 The surface quality before and after laser erosion of the SLM surface.

Another technique to directly manipulate the surface of SLM products (using the SLM machine) is to evaporate the material by using an incident laser beam (pulse laser is usually needed). This is called selective laser erosion (SLE) and is employed to improve the surface (Fig. 2.15) or even to engrave a desired geometry on additive layers. In this method, the laser beam can be narrowed to a dozen micrometers, allowing for very small internal radii and fine details, thus giving SLE the capability of micromachining. The main challenge is to achieve an appropriate adjustment when many parameters are involved. The parameters may include scanning speed, pulse frequency, laser power, scan spacing, and number of eroded layers. Fig. 2.16 demonstrates an application of combining SLM and SLE to produce small internal and

external features. Although SLM alone is limited to achieving holes or engravings below 400 to 500 μm , SLE of additive layers allows very precise evaporation of material to make features as small as 50 μm (Fig. 2.16). Therefore, these techniques can be combined, such that dense additive layers are first made using SLM and then the hollow features can be eroded in each layer, to achieve the narrowest holes and engravings.

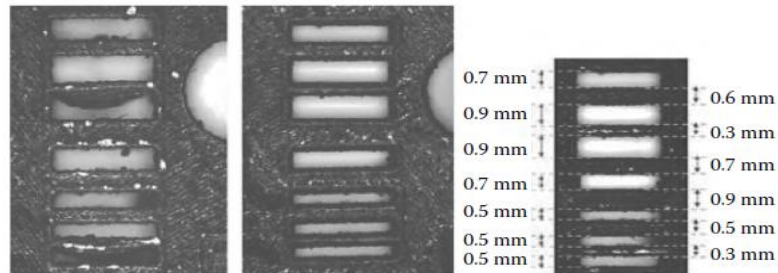


Fig. 2.16 Comparison of the slits/ribs made by SLM without erosion and made by SLM combined with SLE (after every layer) with nominal widths of the slits and ribs on the right.

2.6.5 Single Track Scans

Single tracks (Fig. 2.17) can be used to explore the shape of the melting pool. The generated knowledge is a shortcut to assessing the processing windows (i.e., the successful range of scanning speeds and laser powers) for SLM of a specific material. The following factors are considered to evaluate the quality of a single track:

- Being uninterrupted (see Fig. 2.17A,B for examples of good and bad tracks), preventing pores and irregularities
- Controlled penetration (into the layer below), demonstrating good wetting and bonding to the previous layer (Fig. 2.17C)
- Controlled height for building up layers of good height (Fig. 2.17C)
- Optimum connection angle of about 90° between the scan track and the layer below (Fig. 2.17C), which enhances the dimensional accuracy and density and minimizes the required overlap between adjacent scan tracks [8].

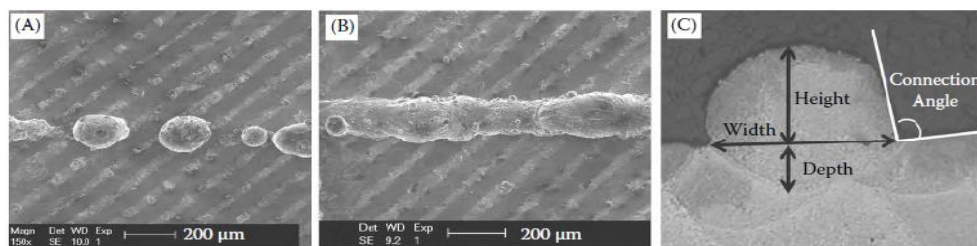


Fig. 2.17 Important factors in single track experiments: (A) bad/interrupted track from top view, (B) good/continuous track from top view and (C) side view factors demonstrated on a good track.

2.7 SLM Potential Defects

Similar to welding processes, residual stresses are produced in SLM-processed parts as a result of high temperature gradients, large amounts of thermal expansion and shrinkage or non-

uniform plastic deformation during the heating and cooling cycle. The substantial shrinkage of the moving melting pool during cooling and solidification is constrained by the cooler underlying previously processed layers.

The thermal shrinkage rate for a given powder material increases with an increase in laser power or a decrease in laser scanning speed.

An SLM-built part is under tension, and the maximum stress is located at the surface of the part and can reach the yield stress, as shown in Diagram 2.1. The final residual stress increases with the number of layers that have been built.

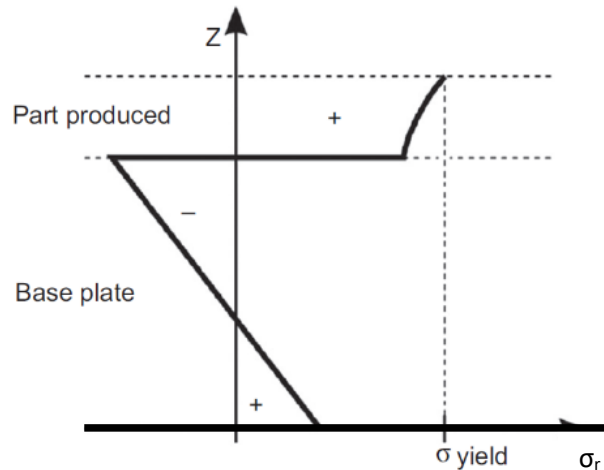


Diagram 2.1 Distribution of residual stresses in a base plate and built part along the building direction.

Residual stresses result in:

- Part distortion.
- Cracking.
- Delamination of the part.

Crack density is more significantly dependent on laser power because the temperature profile is more strongly dependent on laser power than laser scanning speed; hence steeper temperature gradients produced at higher laser powers result in an increase in the magnitude of thermal stress and therefore increase hot cracking.

Because the average residual stress in the laser scanning direction is about two times higher than the stress in the direction perpendicular to the laser scanning direction, residual stresses can be reduced by shortening the scan track using an island/checkerboard scanning strategy. More homogeneous stress distribution can be achieved by changing the stress anisotropy from one layer to the next, scanning with a rotating scan pattern.

Rescanning by the laser beam with the lower energy density is reported to effectively stop crack propagation during SLM fabrication, probably as a result of part distortion.

Distortion caused by internal stresses can be reduced by using elemental powders instead of a pre-alloyed powder. The in-situ alloying of two or more elemental powdered materials during manufacturing can lower the solidification temperature by forming various combinations of eutectic/hypoeutectic/hypereutectic alloys. The processed alloy is able to remain in a semi-solid or stress-reduced state throughout the build with the assistance of powder bed being preheated at the elevated temperature. Much longer overhangs without support can be built using a mixture of elemental powders.

Residual stresses and distortion of the SLM-processed part can be reduced by applying (1) stress relief heat treatment, (2) re-scanning by the laser beam and (3) increasing in the powder bed temperature. However, residual stresses are not always disadvantageous; the retention of a reasonable level of residual stress in SLM-processed parts favors enhanced hardness.

Defects such as porosity, lack of fusion and cracks are often produced in additively manufactured materials. These defects adversely affect the properties and performance of these materials because the defects reduce the part density and act as stress risers. The defects include:

- **Gas pores:** Gas pores are formed by trapped gases and are normally spherical. The gas pores are inherited from a gas-atomized powder or moisture on the powder particle surface and the dissolved hydrogen in the powder, which are the primary contributors to the formation of porosity in SLM-processed aluminum alloys. These are not significant contributors to the porosity of SLM-processed Ti6Al4V samples since the porosity depends on the processing parameters.
- **Keyhole pores:** Keyhole pores are produced by the collapse of a steep and deep melting pool that is formed at the start/end points of the scan tracks or when the linear energy density is too high.
- **Incomplete melting or lack of fusion:** Some unmelted particles can be trapped inside the pores if the energy is insufficient to melt all the powder, which has a statistically geometric shape. This type of defect is located at the interlayers and is also known as an elongated pore. The plane of this type of defect is perpendicular to the build direction.
- **Unstable melting pool:** Irregular pores can be formed at low laser scanning speeds as a result of hydrodynamic instability of the melting pool at a high energy density and because of melt flow instability at a high laser scanning speed. The instability of melt flow during SLM is attributed to the Marangoni force and recoil pressure produced by the evaporation of the melting pool. The instability of melt flow, which increases with an increase in laser scanning speed and powder layer thickness, results in small liquid droplets splashing onto the solid built surface.
- **Lack of overlap:** Intra-layer porosity is produced as a result of the large hatching space.

Porosity or relative density in the SLM-fabricated part is strongly dependent on linear energy density. The velocity of gaseous bubbles in the melting pool increases with an increase in linear energy density and reaches a maximum value at an optimal LED at which the highest density of the part is achieved. Further increases in linear energy density result in the

formation of a rotational pattern of the flow vortex, which tends to entrap gaseous bubbles and reduce their velocity. This leads to the formation of high porosity in the consolidated parts.

Four melting zones have been defined on a laser power versus laser scanning speed map for SLM of Ti6Al4V: 'fully dense' (zone I), 'over-melting' (zone II), 'incomplete melting' (zone III) and 'over-heating' (zone OH), as shown in Diagram 2.2(a). Defects in the samples produced in zone II have a spherical shape, whereas the morphology of defects in the samples produced in zone III are irregular.

At a laser power, the density decreases/porosity increases with an increase in laser scanning speed, as shown in Diagram 2.2(c).

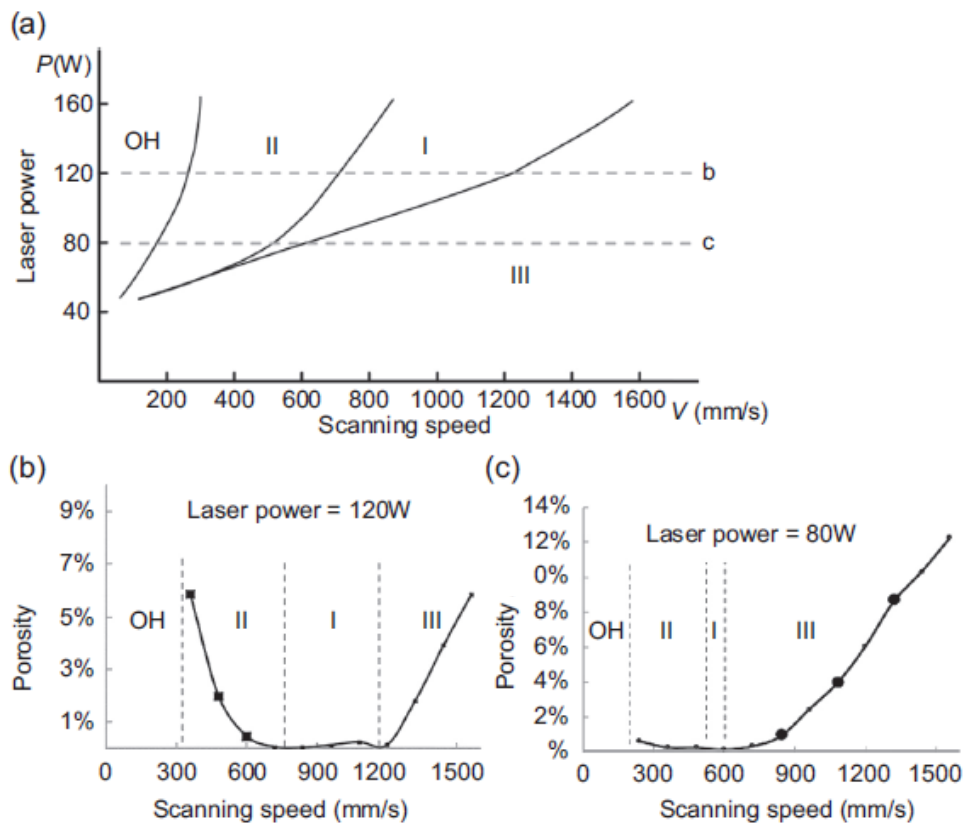


Diagram 2.2 (a) Four zones on a laser power versus laser scanning speed map, (b-c) Graphs of the dependence of porosity on laser scanning speed at two levels of laser power in selective laser melting- fabricated Ti6Al4V.

It has been reported that the density of the SLM-fabricated part (ρ) increases with an increase in energy density (E_p), as described by:

$$\rho = C_1 - C_2 e^{-KE_p} \quad (5)$$

where C_1, C_2, K are constants.

However, significant density variations can be found at the same level of energy density (as shown in Diagram 2.3) because some combinations of laser power and laser scanning speed may cause (1) incomplete melting of powder; (2) instability of the melting pool; (3) overheating of the powders and (4) balling effects. At the same energy density level of $120 \frac{J}{mm^3}$, the density of the additively manufactured part increases with an increase in laser power and laser scanning speed and reaches a maximum value at the laser power of 165W; a further increase in laser power results in a slight reduction in density. The porosity produced at the combination of higher laser power and higher scanning speed is smaller and more circular in shape and is attributed to the balling effect and high thermal stress cracking, whereas the porosity produced at the combination of lower laser power and lower scanning speed is filled with unmelted powders because of insufficient melting. However, the balling effect has also been observed in a sample that was produced at a low laser power and scanning speed [8], [11].

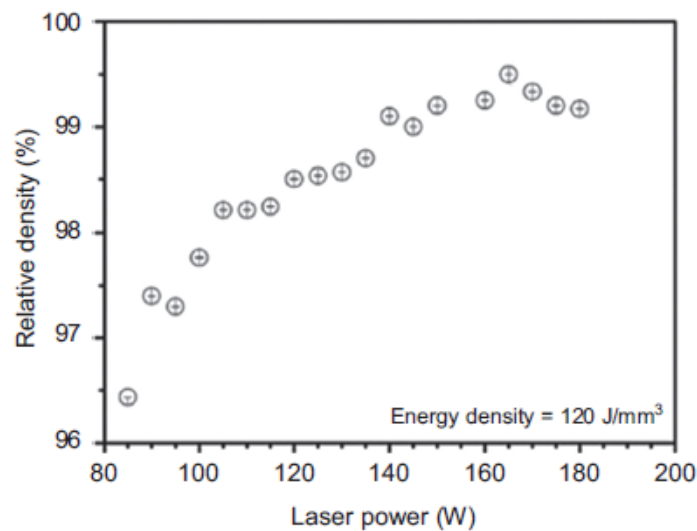


Diagram 2.3 Effect of laser power on the relative density of selective laser melting- fabricated commercially pure titanium at a constant energy density of $120 J/mm^3$.

2.8 Microstructural features

The microstructure of additively manufactured alloys is significantly different from that of conventionally processed alloys because of the fast and directional cooling achieved during the additive manufacturing processing. Several significant characteristics of additively manufactured alloys via laser-based process are summarized in this section.

2.8.1 Texture

Because of the unidirectional heat transfer and cooling (heat is primarily conducted away vertically through the previously built part to the platform), a strong morphological and crystallographic texture has been observed in columnar structures in Ti6Al4V, nickel superalloys, 1Cr18Ni9Ti stainless steel, NiCr alloy, AlSi10Mg, CoCrMo steel and Al-12Si (AlSi12)

processed by layer-based additive manufacturing processes. The columnar structures are the elongated grains that grow across the layers in the direction roughly parallel to the build direction because of the epitaxial grain growth at the partially remelting grains on the previously solidified layers and directional solidification.

The dominant $\{100\}$ texture in the direction of grain growth is developed in SLM-processed Inconel alloy as the result of the preferential $\{100\}$ growth direction of cubic crystals, which results in the columnar structure shown in Fig. 2.18.

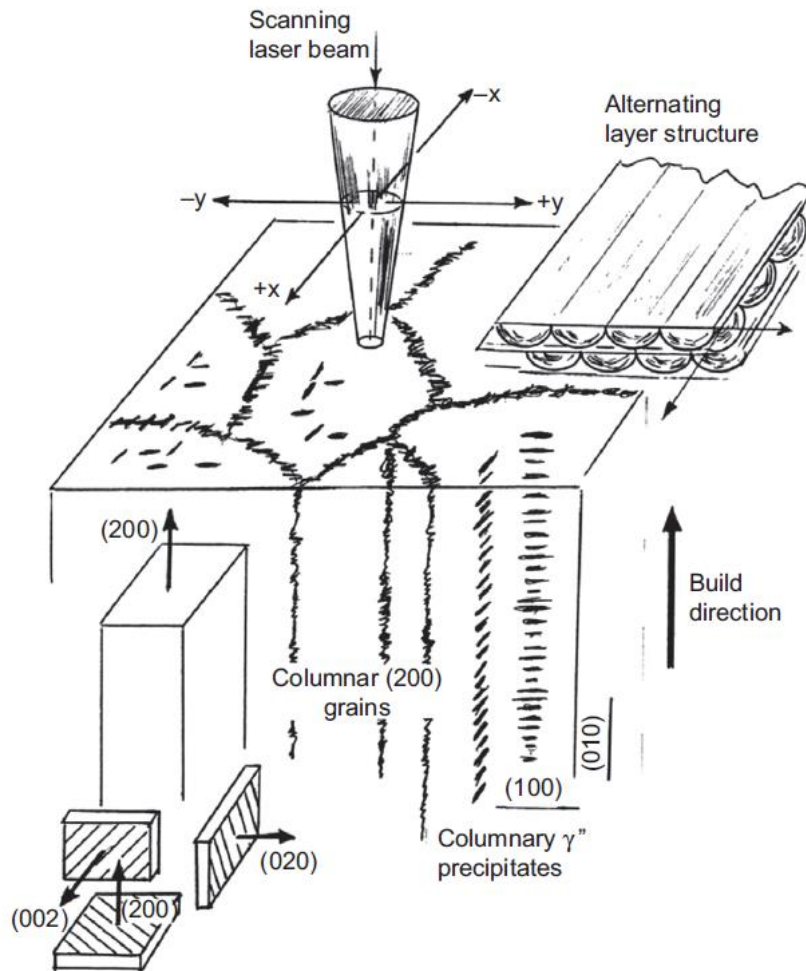


Fig. 2.18 Schematic illustration of columnar γ grains formed by unidirectional solidification, γ'' precipitate arrays and the melting pool/ layer structure in Inconel 718 processed by selective laser melting.

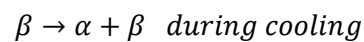
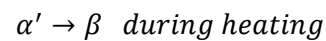
In the SLM-processed Ti6Al4V, the average length of prior β grains is in the order of millimeters. This shows that prior β grains grow through tens of layers along a direction tilted at an angle about 20 degrees from the build direction (z-axis). The inclined angle is attributed to the rotation of the scan direction in each layer. The acicular martensite α' laths, characterized by high vanadium content and a high dislocation density, are primarily orientated at inclinations of about 45 and 90 degrees to the build direction.

The texture can be changed by applying different laser-scanning strategies. A reduction in texture can be achieved by rotating a 90-degree laser scanning vector between the two adjacent layers or rotating the scanning vector within one layer (the checkerboard or island scanning method).

2.8.2 Non-equilibrium microstructure

An out-of-equilibrium microstructure is normally produced in the SLM process as a result of a high cooling rate. The cooling rate in the SLM process is approximated within the range of 10^3 - 10^8 K/s which is fast enough to fabricate bulk metallic glass for certain alloy compositions.

Very fine acicular martensite (α') is normally obtained in SLM-processed Ti6Al4V and commercially pure titanium (cpTi) as a result of the phase transformation $\beta \rightarrow \alpha'$ at a high cooling rate. In addition to defects, the hard and brittle nature of metastable martensite is partially attributed to the higher strength and lower ductility of SLM-processed Ti6Al4V compared with conventionally forged/annealed Ti6Al4V parts in which stable/ductile alpha (α) plus beta (β) phases are produced. However, $\alpha + \beta$ phases have been reported in SLM-processed Ti6Al4V with appropriate energy input and double laser scanning on each layer as a result of the in-situ decomposition of the martensite α' phase induced by heating and cooling during the build of the subsequent layers caused by the following phase transformations [11]:



3. SLM State-Of-The-Art

Both experimental and theoretical papers, that try to estimate or predict the melting pool geometry, are presented below:

Zhang Z. et al. [13] developed a 3D heat-transfer finite element model for Laser Powder-Bed Fusion (LPBF) for accurately predicting melting pool dimensions and surface features. Eight heat source models (Fig. 3.1, Table 3.1) were used for the numerical modeling of LPBF and can be categorized as 1) geometrically modified group (GMG); and, 2) absorptivity profile group (APG). Experiments were carried out to validate the simulation results. All the eight heat source models lead to over 40% shallower melting pools compared with the experiments (for the experiments, a Stainless Steel 17-4PH powder was used).

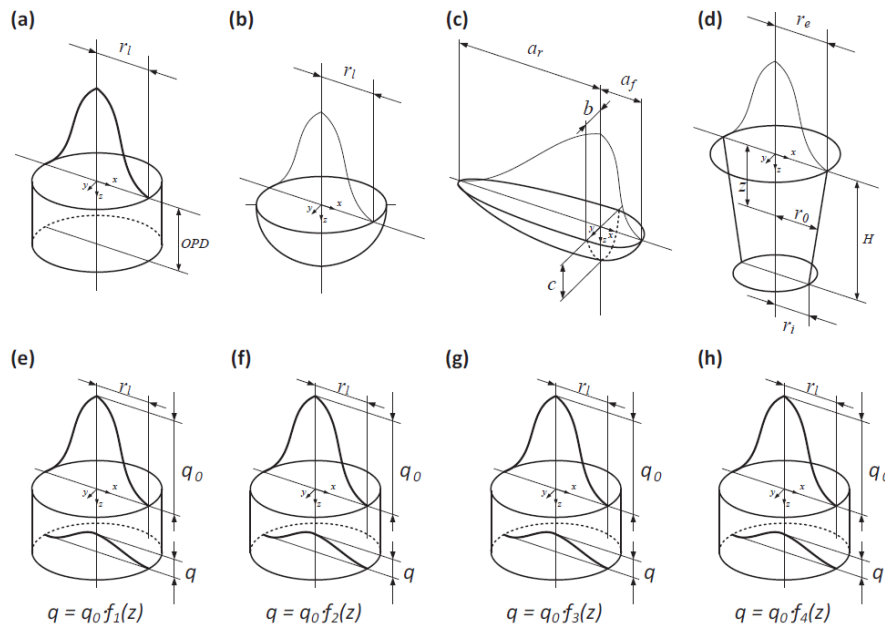


Fig. 3.1 The schematic of the heat source models, (a) cylindrical shape; (b) semi-spherical shape; (c) semi-ellipsoidal shape; (d) conical shape; (e) radiation transfer method; (f) ray-tracing method; (g) linearly decaying method; (h) exponentially decaying method.

Table 3.1 Summary of mathematical representations of laser beam heat sources.

GMG1	Cylindrical shape	$I(x, y, z) = \frac{\beta \cdot P}{S \times \alpha_{OPD} \times OPD}$
GMG2	Semi-spherical shape	$I(x, y, z) = \frac{2^{5/2} \beta P}{\pi^{3/2} r_l^3} \exp\left[-2 \frac{x^2 + y^2 + z^2}{r_l^2}\right]$
GMG3	Semi-ellipsoidal shape	$I_f(x, y, z) = f_f \cdot \frac{2^{5/2} \beta P}{\pi^{3/2} a_f b c} \exp\left[-2 \left(\frac{x^2}{a_f^2} + \frac{y^2}{b^2} + \frac{z^2}{c^2}\right)\right]$ $I_r(x, y, z) = f_r \cdot \frac{2^{5/2} \beta P}{\pi^{3/2} a_f b c} \exp\left[-2 \left(\frac{x^2}{a_f^2} + \frac{y^2}{b^2} + \frac{z^2}{c^2}\right)\right]$
GMG4	Conical shape	$I(x, y, z) = \frac{6\beta \cdot P}{\pi H (r_0^2 + r_e r_l + r_l^2)} \exp\left[-2 \frac{x^2 + y^2}{r_0^2}\right], \quad r_0 = r_e + \frac{z}{H}(r_e - r_l)$
APG1	Radiation transfer equation method	$I(x, y, z) = \frac{2P}{\pi r_l^2} \exp\left[-2 \frac{x^2 + y^2}{r_l^2}\right] \left(-\eta \frac{dq}{dz}\right)$ $q = \frac{\eta a_s}{(4\gamma - 3)D} \left\{ (1 - \gamma^2) \exp[-\lambda] \cdot \left[(1 - a_s) \exp[-2a_s \xi] + (1 + a_s) \exp[2a_s \xi] \right] \right.$ $\left. - (3 + \gamma \exp[-2\lambda]) \times \left\{ [1 + a_s - \gamma(1 - a_s)] \exp[2a_s(\xi - \lambda)] \right. \right.$ $\left. \left. + [1 - a_s - \gamma(1 + a_s)] \exp[2a_s(\xi + \lambda)] \right\} \right\}$ $\frac{-3(1 - \gamma)(\exp[-\xi] - \gamma \exp[\xi - 2\lambda])}{4\gamma - 3}$
APG2	Ray-tracing method	$I(x, y, z) = \frac{2P}{\pi r_l^2} \exp\left[-2 \frac{x^2 + y^2}{r_l^2}\right] \frac{d\theta}{dz}$
APG3	Linearly decaying equation	$I(x, y, z) = \frac{2P}{\pi r_l^2} \exp\left[-2 \frac{x^2 + y^2}{r_l^2}\right] f(z), \quad f(z) = \beta \cdot \frac{z}{H} \left(1 - \frac{z}{H}\right)$
APG4	Exponentially decaying equation	$I(x, y, z) = \frac{2P}{\pi r_l^2} \exp\left[-2 \frac{x^2 + y^2}{r_l^2}\right] f(z), \quad f(z) = \beta \cdot \frac{1}{H} \exp\left[-\frac{ z }{H}\right]$

In order to improve the model performance, a mathematical model with varied anisotropically enhanced thermal conductivity and varied absorptivity was proposed and applied to the heat transfer simulation with the exponentially decaying heat source (APG4).

The main conclusions are listed as follows:

1. The expressions of varied anisotropically enhanced thermal conductivity and varied absorptivity were linear algebraic equations. Good agreement between the simulation and the experimental results was derived. The averaged error of melting pool width and depth are 2.9% and 7.3%, respectively.
2. The proposed heat transfer model has been further validated by the surface features, track stability and ripple angle. For the track stability, the predicted results are in good agreement with the experimental results. In addition, the simulated ripple angles are within the range of experimental results.

Lee K. et al. [14] developed a novel hybrid heat source model considering the different absorption mechanisms for porous and dense state materials, and an effective absorptivity is adapted to the proposed model to analyze the melting mode transition. The proposed model can predict the melt pool characteristics including the melt pool dimensions and the melting modes in the selective laser melting (SLM) process. The problem is formulated using the heat transfer equation considering the phase transition and the degree of consolidation based on the phase-field approach. The single-track scans of 316 L stainless steel for both the non-powder case and the powder case are simulated to validate the model and the obtained results are in good agreement with the experimentally measured melt pool dimensions (mean error within 6%). Furthermore, the melting modes (conduction and keyhole) can be distinguished based on the predicted melt pool morphology and the degree of vaporization with the proposed model, which provides insight to define the optimized process boundary. It is also found that the keyhole mode melting is more sensitive to the change of the process parameter than the conduction mode melting.

However, during the melting process of SLM, a certain amount of volume shrinks due to the void fraction of the powder layer. The location of the surface then gets lower after the void is filled by the molten material. This volume shrinkage affects the morphology of the generated melting pool because it affects the heat conduction in the surrounding powder layer. Furthermore, the applied heat flux for each material point changes due to the variation of the distance from the center of the laser beam. The proportion of volume shrinkage of the powder layer is generally equivalent to the initial porosity of powder. To consider the volume shrinkage in the simulation, a simplified method is used in this study which is deactivating the shrunk element. After the powder layer is molten, the shrunk volume (Fig. 3.2) is treated as an empty space with zero conductivity in the simulation.

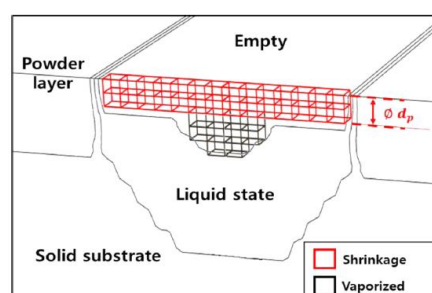


Fig. 3.2 Volume shrinkage due to the initial porosity of powder layer and material removal due to evaporation.

The main conclusions that can be drawn from the study are summarized as follows:

1. The analysis results show that the model achieved good agreement (mean error within 6% for both the case without powder and the case with powder) when compared to the experimentally measured melt pool dimensions. The predicted melting modes based on the melt pool morphologies are also in good agreement with the experimental results.
2. The different characteristics of the two melting modes (conduction and keyhole) are discussed in the process optimization point of view with the degree of intense heating. It is concluded that the keyhole mode melting is not preferred in terms of energy efficiency and is more sensitive to the change of the laser power.
3. The performance of the proposed hybrid heat source model is also compared with the conventional heat source models. The result shows that the combination of the volumetric and the surface heat fluxes contributes to more realistic results considering the different absorption mechanisms of the porous and dense materials.

Gu D. et al. [15] provide multiscale modeling and corresponding experimental verification of the SLM processing of metals, alloys, and metal matrix composites, including an aluminum (Al)-based alloy (AlSi10Mg), a nickel (Ni)-based super-alloy (Inconel 718), and ceramic particle-reinforced Al-based and Ni-based composites. SLM of metals typically involves multiscale coordinated control principles, including microstructure development during SLM processing (the microscale), the laser absorption and melting behavior of powder particles (the mesoscale), and the stress and deformation of SLM-processed structures (the macroscale).

Multiscale computational numerical modeling has become an essential tool in predicting the thermodynamic and kinetic mechanisms of the SLM process, and thereby efficiently shortening the process optimization cycle of SLM-fabricated parts. In addition, the quantitative data acquired from the numerical modeling provide insight into the scientific problems existing in SLM processing. The basic conclusions of the present study are as follows:

1. Using mesoscale modeling and simulation, it was determined that for the SLM process of an Al-alloy powder at a relatively high scanning speed or a low laser power, the balling phenomenon, which is a typical metallurgical defect of SLM, tended to occur under the activity of excessive shrinkage of the liquid track in both the transverse and radial directions.
For the SLM of a Ni-alloy powder, when a relatively low laser power was applied, porosity was distinctly presented both on the top surface and on the cross-section of the SLM-processed composites, due to the reduced surface tension of the liquid and the weakened migration of the melt between the current track and the neighboring solidified track.
2. Using microscale simulation and understanding, it was determined that for the SLM process of AlN/AlSi10Mg nanocomposites, the thermal behavior, thermal-capillary convection, and pressure distribution in the vicinity of the AlN reinforcing particles were sensitive to the SLM processing parameters. Due to the combined effect of the

convection vortex, the capillary force, and the gravity force, the pressure difference and centripetal force acted on the AlN reinforcing particle, promoting sufficient rearrangement of the AlN particles. A novel regular distribution of AlN reinforcing particles in a ring-like structure was obtained within the finally solidified composites under the optimized laser energy density. For the SLM of WC/Inconel 718 composites, under the radiation from a high-energy laser beam, an in situ chemical reaction occurred between the WC particles and the Inconel 718 matrix, leading to the formation of a gradient interface with $(W, M)C_3$ ($M = Ni, Cr, Fe$) carbide. The formation of the gradient interface between the reinforcing particles and the matrix decreased the tendency of crack and pore formation and improved the bonding coherence at the interface.

3. Using macroscale modeling, the thermal mechanical coupling effect and the residual stress distribution within an SLM-fabricated Al-alloy part were studied. SLM processing of the current track efficiently provided a preheating effect for the untreated neighboring powder bed and, meanwhile, provided the annealing effect for the adjacent SLM-processed tracks. The combined effect of self-preheating and self-annealing significantly alleviated the residual stress within SLM parts. The residual stress located at the start and finish sides of the scanning track was much lower than that located in other positions of the track. The residual stress distribution of the SLM-processed layer varied along the depth of the layer. In the bottom of the scanned layer, the residual stress located at the start/ finish side increased to the maximum values.

Pang S. et al. [16] investigate the coupled keyhole and weld pool dynamics during deep penetration laser welding with a comprehensive sharp interface keyhole welding model. The coupling of transient keyhole evolution, heat transfer and weld pool dynamics was simulated. The major findings of the present theoretical modelling study are listed below:

1. The frequency of keyhole depth variation is shown to be in agreement with the experimental values of keyhole oscillations, and the amplitude of keyhole depth variation could qualitatively reflect the porosity content of the final weld bead.
2. Under certain low heat input welding conditions, the ablation recoil pressure could withstand the restoring effect of the surface tension and fluid flow pressure exerted on the keyhole wall, and a deep penetration laser welding process with a stable and collapse-free keyhole could be obtained. Under this condition, the fluid flow directions of the weld pool near the keyhole wall are upwards and approximately parallel to the keyhole wall.
3. The processes of three-dimensional periodical keyhole oscillation and bubble formation in the laser welding process of an unstable keyhole could be well simulated by the present sharp interface model. The mechanisms of keyhole instability are found to be closely associated with hump behaviour on the keyhole wall. The welding speed and surface tension are shown to be closely related to the formation of humps on the keyhole wall. The effects of recoil pressure, surface tension and impacting

- pressure of fluid flow periodically drive the humps downwards, collapse the keyhole and may lead to the formation of pores near the central parts or tips of the keyhole.
4. Significant different weld pool dynamics during laser welding with an unstable keyhole are found by comparing with the fluid flow in a welding process with a stable keyhole.
 5. Several characteristic flow patterns in the weld pool during laser welding with an unstable keyhole, including the sideways flows around the keyhole, the upward flows along the rear keyhole wall, the rapid downward flows near the keyhole wall, inner vortex flows behind the bottom part of the blind keyhole as well as a type of periodical wavy flow on the weld pool surface, are successfully predicated by the present model and found to qualitatively agree with x-ray transmission imaging experiments.
 6. The transient keyhole dynamics plays a very important role in some of the characteristic flow patterns of the weld pool; therefore, modelling the keyhole and weld pool in a self-consistent way is of significance to understand the physics of laser welding.
 7. Since many important flow patterns are closely related to the effects of recoil pressure, surface tension and impacting pressure of fluid flow, it is essential to incorporate these effects into a hydrodynamic keyhole welding model of laser welding.

Khairallah S. et al. [17] demonstrate the effect of the recoil pressure and Marangoni convection in laser powder bed fusion (L-PBF) of 316L stainless steel and how denudation, spattering, and pore defects emerge and become part of a laser bed-fusion process. The physics processes involved are intimately coupled to each other since they all have a strong dependence on the temperature.

While radiation cooling scales as T^4 , the evaporative cooling is more efficient at limiting the peak surface temperature because of its exponential dependence on T . This has a strong effect on the magnitude of the recoil pressure since the latter also grows exponentially with the temperature. The recoil force overcomes the surface tension, which opposes the compressive effect of the recoil force, and therefore creates the depression and material spatter. Upon cooling below the boiling point, the surface tension takes over and causes pores to form upon depression wall collapse. The surface tension effects dominate in the transition region where a strong flow (Marangoni effect) takes place. This flow helps with cooling of the depression, creating the denudation zone, pulling in adjacent particles and creating side pores close to partially melted particles. Eventually the transition zone thins out due to the melt flow breaking up and forming the tail-end region. The latter is subject to irregular flow that is short lived due to the drop in temperatures and solidification.

Deep and narrow depressions should be avoided in order to decrease pore formation due to depression collapse. One should also note that, upon changing direction along a scan track, the laser intensity should be decreased otherwise, extra heat deposited could lead to a deep and narrow depression, which collapses and forms pores. An appropriate scan vector overlap can increase the densification by eliminating partially melted and trapped particles and any

associated shallow lateral pores. Also, a gentle ramping down of the laser power can prevent end-of-track pores and side surface roughness.

Volpp J. et al. [18] present an analytical model of the keyhole including multiple reflections in a subroutine during laser deep penetration welding. The influence of spatial laser intensity profiles on the resulting keyhole geometry can be shown by observing keyhole shapes resulting from a Gaussian-like and a top hat distribution. Calculation results show that different spatial laser intensity distributions lead to similar keyhole shapes due to similar energy distributions on the keyhole walls after multiple reflections but to different radial pressure gradients. The top hat distribution leads to higher pressure gradient values leading to higher back pressure to the quasi-static state and presumably to a more unstable process. Experiments for measuring keyhole diameters in different depths are conducted to estimate keyhole shapes after welding Aluminum Alloy 6082 using tungsten inlays. Measured and modeled keyhole shapes show similar tendencies.

D. Dai et. al in [19] carry out the simulation of the melting pool dynamics changing from the heat conduction to the keyhole-mode of SLM-processed TiC/AlSi10Mg parts, using a finite volume method (FVM) and the following conclusions can be drawn:

1. The melting pool depth, namely laser penetration ability, gradually increases and reaches a comparable fixed depth and then fluctuates as the SLM process proceeds. The depth of the melting pool is controlled by the conduction of heat and the resultant recoil pressure caused by the evaporation of the metal as the SLM process proceeds.
2. There is a significant difference in the fluctuation behavior of the melting pool using different protective atmospheres. It seems that Ar protective atmosphere has the stabilization ability to significantly decrease the keyhole melting pool fluctuation (Diagram 3.1) and, therefore a dense SLM-processed part will be obtained (Diagram 3.2).

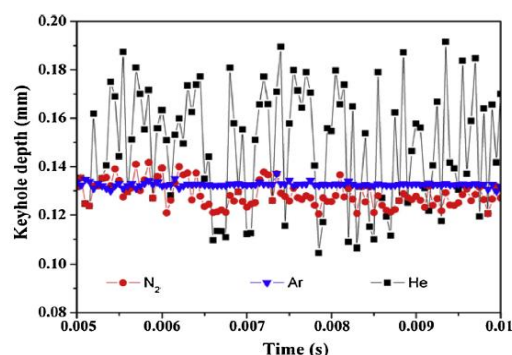


Diagram 3.1 Typical melting pool depth variation curves during keyhole-mode SLM process using different protective atmospheres.

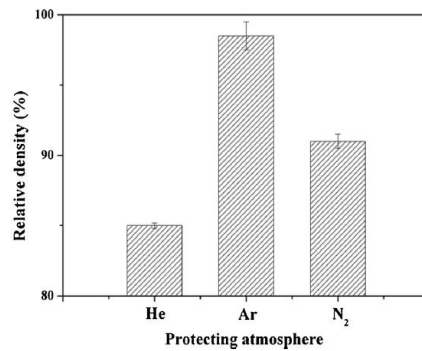


Diagram 3.2 Relative density obtained in the SLM- processed part using different protective atmospheres.

3. The applied protective atmosphere plays a crucial role in determining the surface quality of the SLM-processed part. For the application of Ar protective atmosphere, a stable-state of the melting pool depth combined with a uniform recoil pressure forced on the free surface of the melting pool is typically produced, leading to the formation of a sound surface morphology.
4. The surface quality and relative density are experimentally obtained and have a good accordance with the results predicted by the simulation. The physical issues considered in the mathematical model are completely general. Therefore, the SLM physical model established in this paper is completely suitable for other powder system.

Le T. et al. [20] utilize a three-dimensional thermal-fluid FVM model to examine the effects of the inverse Marangoni flow induced by the sulfur concentration of SS316 powder on the dimensions of the melt-pool formed during SLM processing. The simulations have employed a volumetric heat source with a Gaussian distribution and have evaluated the laser absorptivity of the powder bed by means of mesoscopic ray-tracing simulations. In addition, the surface tension gradient, which governs the direction and magnitude of the Marangoni flow, has been approximated as a function of the sulfur concentration using a simple linear regression approach. The major findings of this study can be summarized as follows:

1. The sulfur level of SS316 metal powder plays a critical role in governing the fluid flow behavior of the melted metal within the melt-pool during SLM processing. In particular, for a higher sulfur level (>60 ppm), the Marangoni flow changes from an outward radial direction to an inward radial direction; thereby resulting in a deeper and narrower melt-pool. Furthermore, the occurrence of inverse Marangoni flow inside the melt-pool sweeps the gas bubbles away from the solidification front, and therefore lowers the porosity of the scanning track.
2. The present simulation model focuses specifically on the effects of inward Marangoni convection. In other words, it ignores the volume shrinkage and the recoil pressure. Consequently, in comparing the simulation results for the melt-pool dimensions with

the experimental results, the simulation model overestimates the melt-pool depth in the conduction mode and underestimates the melt-pool depth in the keyhole mode.

Miyagi M. et al. [21] carried out in situ observation of the laser-melting portion using X-rays under various laser-melting conditions for austenitic stainless steel.

The keyhole depth and width increases, and the fluctuation in keyhole depth tends to decrease as the laser power increases. The fluctuation in keyhole depth tends to increase when no shielding gas is applied.

The inclination angle of the keyhole decreases as the laser traverse speed becomes higher than the keyhole-formation speed, keyhole width increases and the keyhole opening expands.

As the defocus distance increases, the inclination of the keyhole decreases, and the fluctuation in keyhole depth tends to increase.

Heeling T. et al. [22] present a 3D numerical model for the selective laser melting process that allows a detailed look into the process dynamics at comparably low calculation effort (coarse mesh). It combines a finite difference method with a combined level set volume of fluid method for the simulation of the process and starts with a homogenized powder bed in its initial configuration. The model uses a comprehensive representation of various physical effects like dynamic laser power absorption, buoyancy effect, Marangoni effect, capillary effect, evaporation, recoil pressure and temperature dependent material properties. It is validated for different process parameters using cubic samples of stainless steel 316L and nickel-based superalloy IN738LC. The results show the significance of evaporation and its related recoil pressure for a feasible prediction of the melting pool dynamics. Furthermore, a possible way to reduce the times and costs for material qualification by using the simulation model to predict possible process parameters and therefore to reduce the necessary experimental effort for material qualification to a minimum is shown.

Wang H. et al. [23] have developed a coupled thermal-mechanical-fluid model to reveal the microscale dynamic evolution of metal powders, particularly for Ti-6Al-4V, during laser irradiation. Using different laser powers, layer thicknesses, and hatch spacings, they have systematically compared powder evolutions in two typical processing modes – conduction mode and keyhole mode. There is only one circular flow in the longitudinal section of the melting pool in the conduction model, while two circular flows present in the keyhole mode (Fig. 3.3).

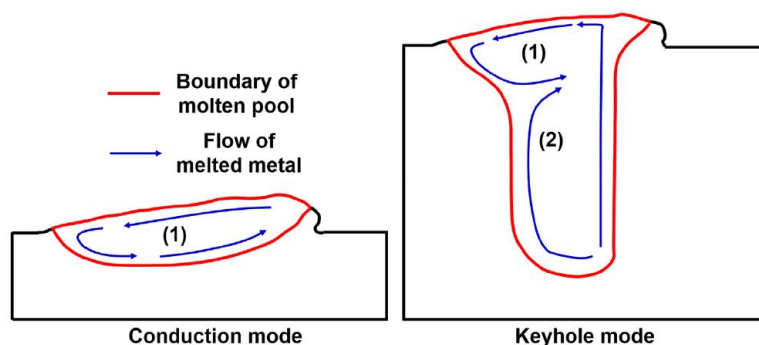


Fig. 3.3 Schematics of the circular flows in two typical modes. The red line represents the boundary of the melting pool, while the blue arrow represents the flow of melted metal. Metal in the melting pool flows along the direction of the arrow, keeping the balance of heat and mass.

Gravity drives the melted metal to fill the gaps between the powders and contributes to the formation of the molten pool. The simulation results demonstrate that a larger printable powder layer thickness is achieved in the keyhole mode than that in the conduction mode. The thermal distribution during the multiple-track melting in the conduction mode is more uniform than that in the keyhole mode, leading to more uniform resulting microstructure. This study presents opportunities to control the microstructure and defects at the microscale of the AM products by modulating processing parameters and switching between conduction and keyhole modes.

However, the limitation of this study lies on the fact that the evaporation process of the metal is not considered in the simulation. Thus, the dynamic formation of the keyhole can't be clarified.

King W. et al. [24] identify, through the analysis of single-track experiments, the existence of, and conditions for, keyhole-mode melting in metal additive manufacturing of Stainless Steel 316L. Specifically:

1. The utility of using the normalized enthalpy to combine the effects of power, speed, and beam size was validated experimentally. The relationship is useful up to the keyhole threshold. Beyond the threshold, the normalized enthalpy does not include the additional physics that exists in keyhole formation. However, the normalized enthalpy is a reasonable scaling to allow data from different powers, speeds, and beam sizes to be viewed in the same context. The normalized enthalpy can be used to identify the keyhole threshold from experiments but appears to be missing some physics particularly with regard to the dependence of melting pool depth on beam size in the conduction mode.
2. There is a threshold for transition from conduction mode laser melting to keyhole mode that depends on power, speed, and beam size for a powder layer thickness of 50 μm that can be expressed in terms of the normalized enthalpy, $\Delta H/h_s \approx (30 \pm 4)$. The threshold is expected to depend on layer thickness and possibly powder size distribution. However, for powder sizes and layer thicknesses typically used in laser powder bed fusion, we have experimental evidence from related work that the change in the threshold will be within the error bar.
3. The threshold for keyhole mode melting can be used to help identify the optimum region in power, speed, and beam size space for a good quality additively manufactured part because going far below the threshold results in insufficient melting and going too far above results in an increase in voids due to keyhole mode melting.

Caprio L. et al. [25] present a methodology for the estimation of the melting pool penetration depth in the SLM process. The monitoring system devised relies upon the measurement of melting pool surface oscillations through reflections of a secondary probe light (Fig. 3.4)

captured by means of a high-speed camera (Fig. 3.5). An image processing algorithm and signal analysis procedure have been developed in order to extract an indicator representative of the oscillation frequency of melting pool surface waves (Fig. 3.6).

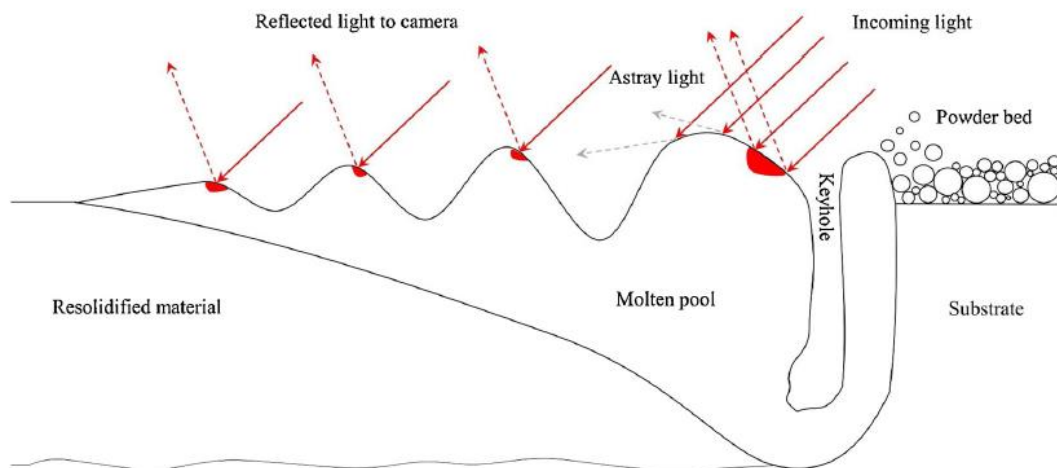


Fig. 3.4 Schematic representation of a transversal view of the melting pool during the LPBF.

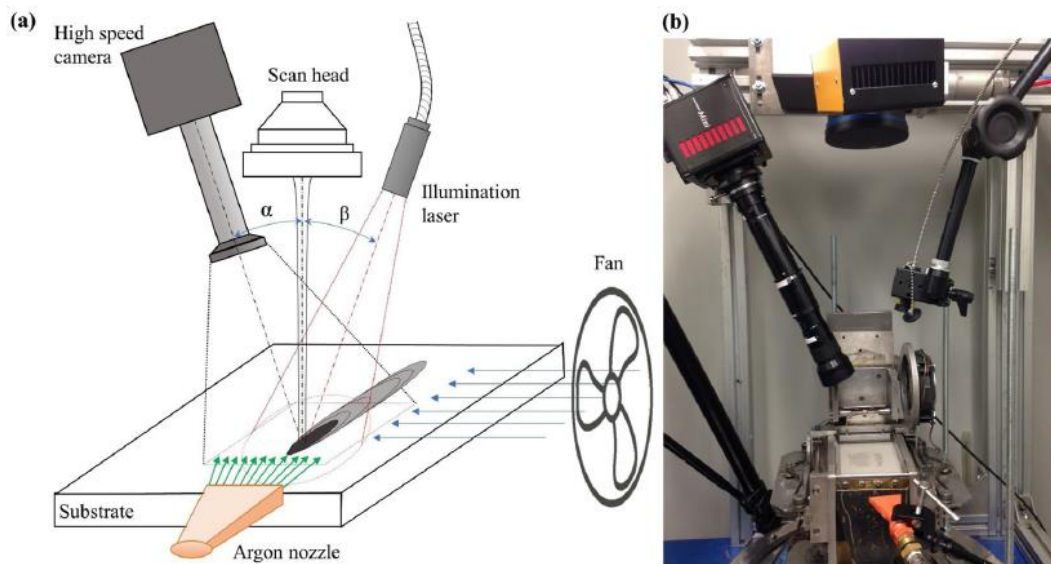


Fig. 3.5 Experimental setup (a) schematic representation and (b) effective realisation.

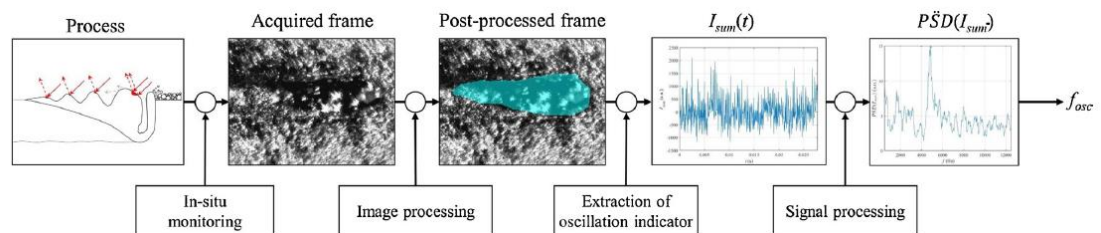


Fig. 3.6 Block diagram of the methodological approach developed.

Melting pool surface oscillations ranging from 3.5 kHz to 5.5 kHz were measured. At higher levels of emission power, the oscillation frequency of the melting pool decreased and may be directly correlated to an increase in melting pool mass and penetration depth. At constant process parameters, oscillation frequency did not show statistical difference between bead-on-plate and SLM experiments (Stainless Steel 316L was the material). Both processes showed analogous trends with shallower melting pools at increasing values of the oscillation frequency.

Proof of concept testing of the devised methodology was conducted with both bead-on-plate material remelting and SLM single track experiments. The monitoring equipment was designed and implemented in order to have sufficient spatial and temporal resolution as well as to obtain sufficient resolution in the frequency domain for the signal analysis procedure.

Bertoli U. et al. [12] discuss the use of Volumetric Energy Density (VED) as a key parameter for SLM of 316L stainless steel. It was shown that:

1. The results confirm that decreasing VED to values below 100 J/mm^3 by either decreasing laser power or increasing scan speed led to a degradation of track shape that ultimately enters the balling regime. Furthermore, tracks deposited with sufficiently high VED values (e.g., 242 J/mm^3), obtained with increasing laser power and speed, show a transition from the continuous regime to the irregular and balling regimes.
2. VED can effectively capture track width evolution. At the lowest VED values (e.g., 48 J/mm^3), the track width reaches its minimum value, approaching the laser spot size ($55 \mu\text{m}$).
3. Depending on the peak temperature, SLM can be carried out in conduction or keyhole mode. In keyhole mode, vaporization of the metal is achieved and the strong recoil pressure creates a deep melting pool with high depth/width ratio and can lead to keyhole porosity. VED is not an appropriate metric to quantify melting pool depth and the threshold between conduction and keyhole.
4. VED is generally a thermodynamic quantity and is therefore not able to capture the complex physics such as Marangoni flow, hydrodynamic instabilities and recoil pressure that drive heat and mass transport in different portions of the melting pool and that, in the end, will dictate final track morphology.

Qi T. et al. [26] investigate the melting mode transition and the characteristics between the keyhole and the conduction mode. According to the research results, following conclusions can be drawn:

1. Depending on the process parameters, three kinds of melting mode, e.g., keyhole mode, transition mode and conduction mode can be found in SLM-processed Al7050 alloy. When the defocusing distance and other process parameters keep constant, the melting mode varies from keyhole to conduction with the increase of scanning speed

from 100 to 1200 mm·s⁻¹. The mode changes from the conduction to transition at the higher speeds, while it transforms from the transition to keyhole at the lower speeds (Fig. 3.7).

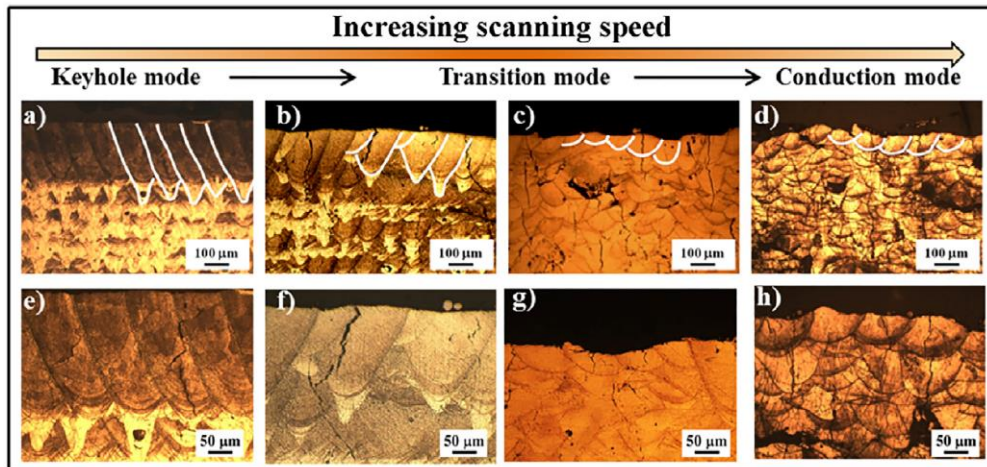


Fig. 3.7 Metallographic images on vertical section of samples with scanning speed of a,e) 100 mm/s; b,f) 250 mm/s; c,g) 850 mm/s; d,h) 900 mm/s.

- When scanning speed and other process parameters keep constant, with the defocusing distance decreasing from 2.5 mm to -2 mm, the melting mode changes from conduction mode, transition mode, keyhole mode to conduction mode in turn (Fig. 3.8).

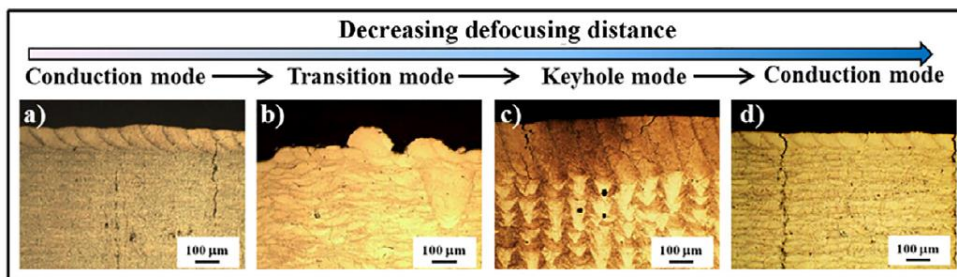


Fig. 3.8 Metallographic images on vertical section of samples with constant scanning speed of 150 mm/s and defocusing distances of: a) 2.5 mm; b) 0 mm; c) -1.5 mm; d) -2 mm.

- The surface under keyhole mode shows metallic luster, while the surface under conduction mode shows dull black. This is caused by the fact that the oxygen content on the surface under keyhole mode is much lower than that under conduction mode.
- Three types of cracks appear in sequence with the melting mode. The crack growth is along the grain boundary. The crack density under keyhole mode is much lower than that under conduction mode due to fine and irregular grains under keyhole mode. The account of cracks of the SLM-processed samples increases when the scanning speed increases.

5. Due to the changing of the thermal gradient and growth rate from border to centerline of the melting pool, the solidification morphology is different between the two melting modes. Moreover, under keyhole mode the convection effects occupy the dominant position on the bottom of the melting pool, resulting in the formation of V-shaped striations along the flow pattern.
6. The nano-hardness of melting pools under conduction mode is slightly higher and more uniform than those under keyhole mode due to the high evaporation of Zn and Mg elements under keyhole mode. The nano-hardness in different regions of the melting pools under keyhole mode is not uniform. The nano-hardness on the bottom is higher than that from other regions.

Zhang D. et al. [27] establish a three-dimensional finite element model including laser penetration and Marangoni effect and use it to study thermofluidic field in the melting pool and its influence on the shape of the melting pool during selective laser melting of Inconel 718 alloy. The following conclusions can be drawn:

1. A heat source considering the characteristics of thermal physical properties of powder bed with porosity and multi-reflection of powder bed to laser beam was implemented in simulation, which results were in agreement with the practice;
2. Marangoni effect driven by surface tension during SLM process makes fluid flow state in melting pool mainly an outward convection (namely Marangoni coefficient $\partial\gamma/\partial T$ is negative);
3. The effects of convective and conductive heat flux on melting pool shape were investigated during SLM process with fixed-point heat source. The results showed that the convective heat flux in melting pool is dominant, which is one order magnitude larger than conductive one, and accelerates flow rate of the melt in the weld, benefits to heat transfer. The convective heat flux makes the melting pool wider and the conductive heat flux makes comparably the melting pool deeper and wider;
4. The effects of convective and conductive heat flux on melting pool shape were investigated during SLM process with a moving heat source. The results showed that thermofluidic field of melting pool and the effects of convective and conductive heat flux on melting pool shape were same as that with fixed-point heat sources.
5. The effects of heat accumulation on heat flux and melting pool shape were investigated during SLM process with a moving heat source different comparing with fixed-point heat source. The process of multiple scanning with moving heat source led to heat accumulation, which increases the magnitude of convection and conduction heat flux, and the length, width and depth of the weld.

However, the evaporation process hasn't been taken into account in the model and the effect of heat accumulation on the melting pool shape and grain morphology with different scanning strategies isn't explored.

Papazoglou E. et al. [28] present a complete and robust methodology for modeling the evolution and final shape of melting pool, as well as other thermal phenomena occurring during conduction mode SLM process. At first the effective absorption coefficient of the laser beam incident is calculated using the Fresnel equations, taking into account the multiple scattering that the laser beam undergoes as it interacts with the powder material. For the melted phase of the material, the absorption coefficient was determined based on the electron-phonon dominated optical conductivity and the Drude theory. Then, the thermo-physical properties of the powder bed were calculated; in order to determine the thermal conductivity of the powder bed, the Zehner and Schlünder model was used, while for the other material properties, analytical relations from the literature were adopted, both temperature and phase-dependent. The convection coefficient was calculated based on the Nusselt number, according to the process parameters. Moreover, the energy loss due to ablated material was estimated, while the latent heats of melt and evaporation were taken into consideration. Finally, a moving volumetric Gaussian heat source was used, to simulate the laser beam.

Three simulations were run, for different volumetric energy densities, and the simulation results were compared and validated with experimental ones. The melting pool shape, and its geometrical characteristics were calculated, the total heat losses owing to material ablation, radiation and convection were estimated, as well the heating and cooling rates. In brief, from the described study it was deduced that:

1. The absorption coefficient of the powder bed, while the material remains in a solid state, and taking into consideration the multiple scatterings of the laser beam, was calculated as 58.66%. The coefficient increases gradually as the material melts, reaching up to 82%.
2. In numerical models of the SLM process, thermo-physical properties of the powder bed have to be calculated in respect to the powder characteristics, as they significantly differ from those of the solid material. Specifically, the thermal conductivity of the powder bed was found to be an order of magnitude lower than this of the solid material.
3. The melting pool formation, as well the track shape can be simulated by the presented model with a significant degree of accuracy. For different VED values, the track acquires different geometrical characteristics. For VED value of 97 J/mm^3 a uniform melting pool was formed, while for 81 J/mm^3 , the melted pool developed ellipsoid formations and instabilities. For a VED value of 48 J/mm^3 , the melting pool was narrow, with a small zone of ellipsoid formations connected to the track. The above results were in line with experimental findings.
4. The nominal depth and width of the melting pool were estimated and it was found that they were in accordance with the experimentally measured values.
5. The heat losses due to material ablation are the highest, followed by the radiation losses which are almost constant, while the convection losses are, in all cases, considerably low.

6. From the obtained results, it is found that temperature rates of the order of 106 K/s occur during the SLM process at the time when laser beam is turned off, being in agreement with the relative literature.

Conclusion:

Keyhole mode has been studied extensively for laser welding ([16], [18]). However, bibliography is limited for SLM-processed keyhole mode. SLM specific papers ([12], [13], [15], [20], [22], [25], [27], [28]) focus more on the melting pool and the conductive mode dynamics, rather than the keyhole dynamics.

Moreover, the limited SLM-keyhole specific papers study the keyhole effect only via indexes and coefficients (such as normalized enthalpy) ([24]) or with models that don't take into consideration the very important phenomenon of metal evaporation ([17], [19], [23]), which leads to inaccurate results.

The materials used in the most papers above are Stainless Steel, Al- alloys and Ni- alloys. Very few studies ([23]), use Ti- alloys (such as Ti6Al4V) in their keyhole simulations. Furthermore, the most simulations consider constant values for the material properties, whereas the truth is that these properties have a strong dependance on temperature ([22], [28]).

In order to reduce the gap or the limitations of the existing bibliography, this diploma thesis studies the keyhole effect for SLM- processed Ti6Al4V (with temperature-dependent material properties), taking into account the heat transfer and metal evaporation phenomena that take place.

4. Model and Simulation

In the current study, a model to simulate and predict the SLM melting pool geometrical characteristics is developed. The aim is to attain accurate and realistic results by using a general method, which avoids the extensive utilization of semi-empirical coefficients or complex and case driven heat source models. In specific, a heat transfer finite element model coupled with deformed geometry was developed. The heat transfer consists the main core of almost every SLM simulation, while the deformed geometry was adopted in order to model and simulate the material ablation during SLM. Material ablation and the consequent enthalpy transfer during SLM is a key mechanism which significantly impact the melting pool characteristics, however it is often neglected or modeled partly. For certain machining conditions combinations, namely where keyhole is formed, this material ablation is crucial in forming that particular melting pool geometry, hence, it should be considered and modeled. Moreover, a number of additional features have been adopted. Material thermophysical properties are temperature dependent and distinct for the porous and the bulk material, while the latent heats of phase transformation, melting and vaporization were also taken into account. Furthermore, the heat losses due to convection and radiation have been also calculated and considered, whilst, the mass and enthalpy loss due to ablation was modeled simultaneously by the utilization of deformed geometry limiting that way the model's DOFs. Finally, the validation of the proposed model was done through comparison with experimental results acquired by the literature, a blind type testing methodology that is extensively adopted by similar studies.

4.1 Model Description

4.1.1 Size and Shape

The model used for the simulations is a 3D-geometry rectangular block (Fig. 4.1) with the following dimensions:

- Width: $W= 1\text{mm}$ or 1.5mm
- Depth: $D= 0.25\text{mm}$
- Height: $H=0.3\text{mm}$

Specifically, 0.27mm is the height of the substrate layer and $30\mu\text{m}$ is the height of the powder layer.

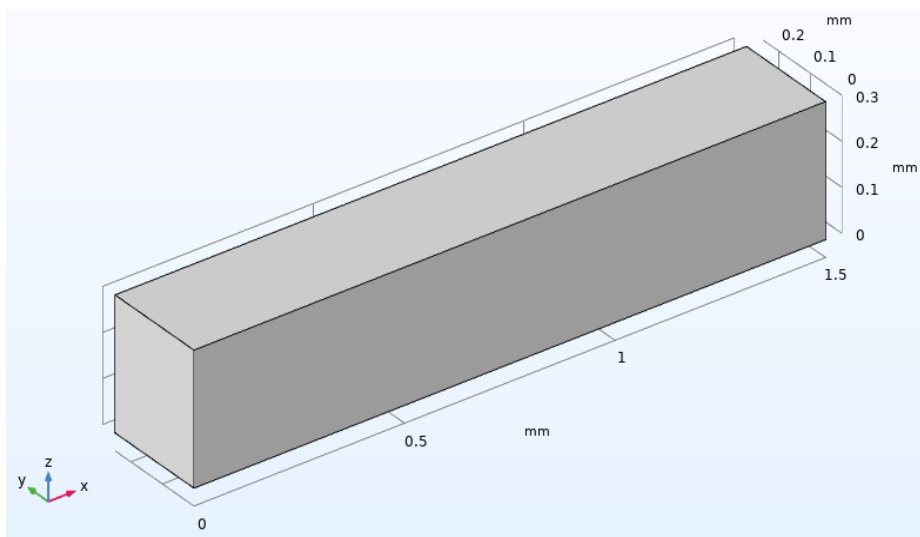


Fig. 4.1 The model used in the simulation.

4.1.2 Position

The initial point O (0,0,0) of the coordinate system is placed at the front-bottom-left corner of the block given in Fig. 4.1.

4.2 Material Properties

In this study, the model utilizes three “materials”, which are the following:

- N₂ (the shielding gas),
- Bulk Ti6Al4V,
- Porous medium (combination of Ti6Al4V and N₂).

Moreover, all the material properties are temperature-dependent.

4.2.1 N₂ Properties

In [29], the values of nitrogen density, specific heat capacity, viscosity, thermal conductivity and thermal expansion coefficient, for different temperatures are given (Table 4.1).

Table 4.1 N₂ properties.

T (K)	ρ (kg/m ³)	Cp (KJ/kg K)	μ (μPa s)	k (W/m K)	β (1/K)
Temperature	Density	Specific Heat Capacity	Viscosity	Thermal Conductivity	Thermal Expansion Coefficient
200	1.7108	1.0429	12.947	0.01824	0.005
300	1.1421	1.0408	17.84	0.0262	0.003333333
400	0.8538	1.0459	21.98	0.03335	0.0025
500	0.6824	1.0555	25.7	0.03984	0.002
600	0.5687	1.0756	29.11	0.0458	0.001666667
700	0.4934	1.0969	32.13	0.05123	0.001428571
800	0.4277	1.1225	34.84	0.05609	0.00125
900	0.3796	1.1464	37.49	0.0607	0.001111111
1000	0.3412	1.1677	40	0.06475	0.001
1100	0.3108	1.1857	42.28	0.0685	0.000909091
1200	0.2851	1.2037	44.5	0.07184	0.000833333

In this study, it is considered that for temperatures below 200K, the value of the property is constant and equals to the value of the same property for 200K. Furthermore, values for temperatures above 1200K, are constant and equal to the values of 1200K.

With interpolation to the data above, the following piecewise temperature-functions are calculated for the above properties (Diagram 4.1, Diagram 4.2, Diagram 4.3, Diagram 4.4):

$$N_2 \text{ density: } \rho_{N_2}(T) \left(\frac{kg}{m^3} \right) = \begin{cases} 1.7108, & 0 \leq T(K) \leq 200 \\ 3.048 \cdot 10^{-12} \cdot T^4 - 1.105 \cdot 10^{-8} \cdot T^3 + 1.521 \cdot 10^{-5} \cdot T^2 - 0.009876 \cdot T + 3.007, & 200 \leq T(K) \leq 1200 \\ 0.2851, & 1200 \leq T(K) \leq 10000 \end{cases} \quad (6)$$

With R²=0.9997.

$$N_2 \text{ heat capacity: } Cp_{N_2}(T) \left(\frac{J}{kgK} \right) = \begin{cases} 1042.9, & 0 \leq T(K) \leq 200 \\ 1.844 \cdot 10^{-10} \cdot T^4 - 8.533 \cdot 10^{-7} \cdot T^3 + 0.001322 \cdot T^2 - 0.6131 \cdot T + 1128, & 200 \leq T(K) \leq 1200 \\ 1203.7, & 1200 \leq T(K) \leq 10000 \end{cases} \quad (7)$$

With R²=0.9997.

$$N_2 \text{ viscosity: } \mu_{N_2}(T)(Pa \cdot s) = \begin{cases} 12.947 \cdot 10^{-6}, & 0 \leq T(K) \leq 200 \\ -4.72 \cdot 10^{-18} \cdot T^4 + 2.246 \cdot 10^{-14} \cdot T^3 - 4.531 \cdot 10^{-11} \cdot T^2 + 6.599 \cdot 10^{-8} \cdot T + 1.541 \cdot 10^{-6}, & 200 \leq T(K) \leq 1200 \\ 44.5 \cdot 10^{-6}, & 1200 \leq T(K) \leq 10000 \end{cases} \quad (8)$$

With $R^2=1$.

$$N_2 \text{ thermal conductivity: } k_{N_2}(T) \left(\frac{W}{mK} \right) = \begin{cases} 0.01824, & 0 \leq T(K) \leq 200 \\ -4.006 \cdot 10^{-15} \cdot T^4 + 1.837 \cdot 10^{-11} \cdot T^3 - 5.027 \cdot 10^{-8} \cdot T^2 + 0.0001006 \cdot T + 8.439 \cdot 10^{-5}, & 200 \leq T(K) \leq 1200 \\ 0.07184, & 1200 \leq T(K) \leq 10000 \end{cases} \quad (9)$$

With $R^2=1$.

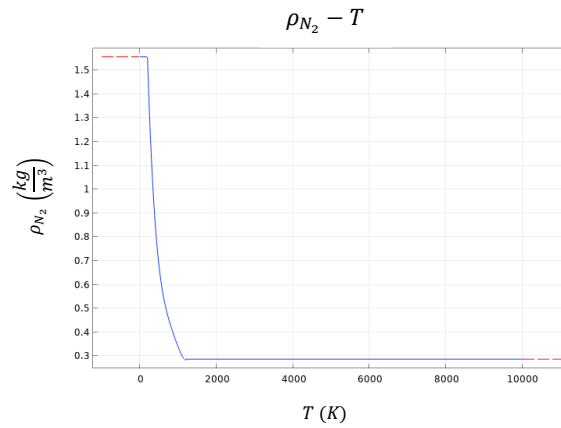


Diagram 4.1 Nitrogen density to temperature.

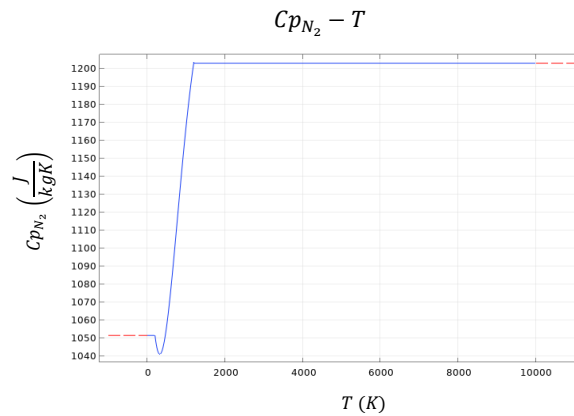


Diagram 4.2 Nitrogen heat capacity to temperature.

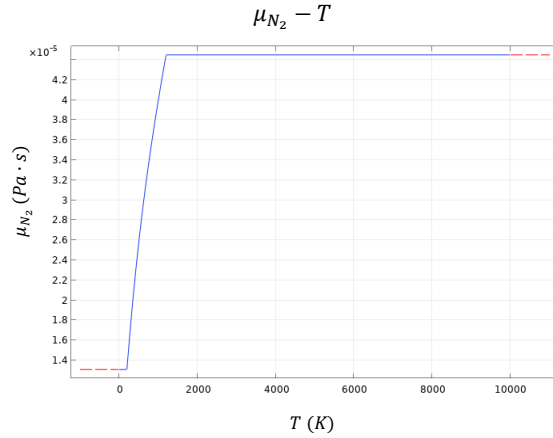


Diagram 4.3 Nitrogen viscosity to temperature.

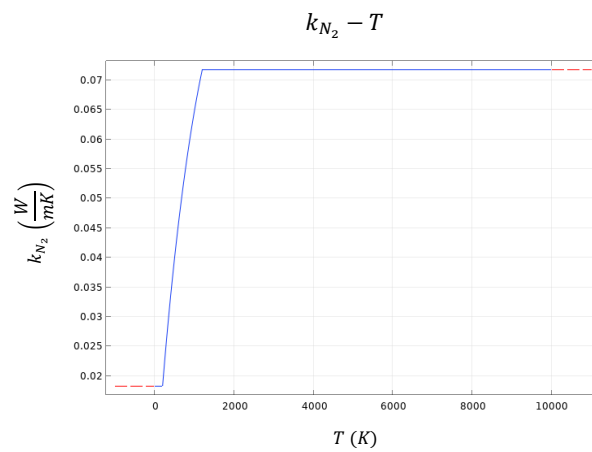


Diagram 4.4 Nitrogen thermal conductivity to temperature.

All the other properties and characteristic numbers of N_2 , can be calculated as analytic functions of the above piecewise functions. Specifically (Diagram 4.5),

$$N_2 \text{ thermal expansion coefficient: } \beta_{N_2}(T) \left(\frac{1}{K} \right) = \frac{1}{T} \quad (10)$$

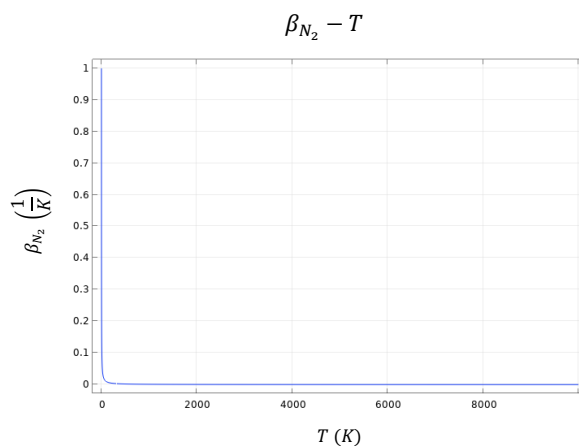


Diagram 4.5 Nitrogen thermal expansion coefficient to temperature.

Moreover, in [30], the formulas for the dimensionless Prandtl (Pr), Grashof (Gr), Rayleigh (Ra) and Nusselt (Nu) numbers are given. Eventually, and the Convective Heat Transfer Coefficient of nitrogen (h_{N_2}) can be calculated. Specifically (Diagram 4.6, Diagram 4.7, Diagram 4.9, Diagram 4.8, Diagram 4.10),

$$Pr(T) = \frac{c_{p_{N_2}}(T) \cdot \mu_{N_2}(T)}{k_{N_2}(T)} \quad (11)$$

$$Gr(T) = \frac{g \cdot \rho_{N_2}^2(T) \cdot \beta_{N_2}(T) \cdot (T - T_\infty) \cdot L^3}{\mu_{N_2}^2(T)} \quad (12)$$

where:

- $g \left(\frac{m}{s^2}\right)$ is the gravity acceleration.
- $T_\infty (K)$ is the ambient temperature.
- $L (m)$ is a characteristic length of the specimen. It must be chosen carefully, so that $10^4 \leq Ra \leq 10^7$.

In this study, $g = 9.81 \frac{m}{s^2}$, $T_\infty = 293.15K$, $L = 0.1m$, so:

$$Gr(T) = \frac{9.81 \cdot \rho_{N_2}^2(T) \cdot \beta_{N_2}(T) \cdot (T - 293.15) \cdot 0.1^3}{\mu_{N_2}^2(T)} \quad (13)$$

$$Ra(T) = Gr(T) \cdot Pr(T) \quad (14)$$

$$Nu(T) = 0.54 \cdot Ra^{1/4}(T) \quad (15)$$

$$h_{N_2}(T) = \frac{Nu(T) \cdot k_{N_2}(T)}{L} \quad (16)$$

In this study, $L = 0.1m$, as referred above, so:

$$h_{N_2}(T) = \frac{Nu(T) \cdot k_{N_2}(T)}{0.1} \quad (17)$$

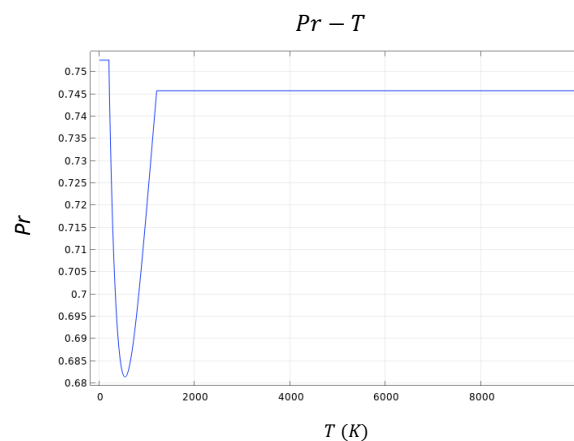


Diagram 4.6 Nitrogen Prandtl number to temperature.

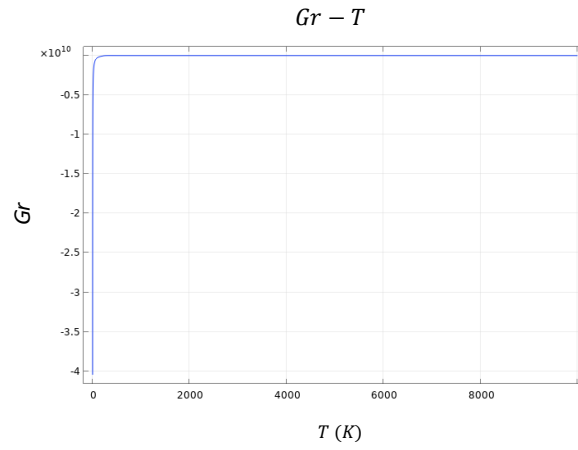


Diagram 4.7 Nitrogen Grashof number to temperature.

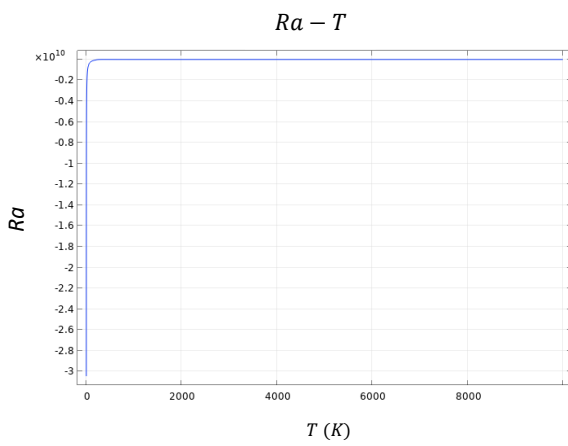


Diagram 4.9 Nitrogen Rayleigh number to temperature.

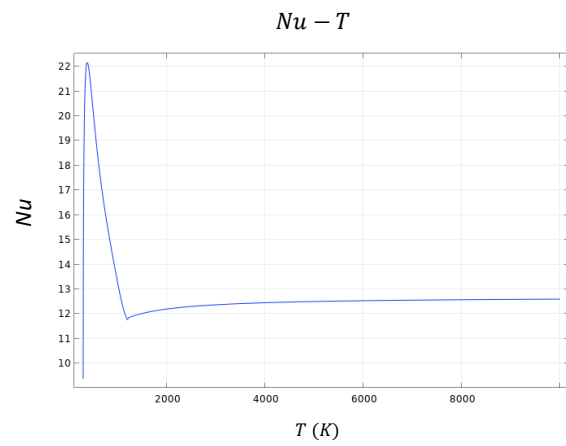


Diagram 4.8 Nitrogen Nusselt number to temperature.

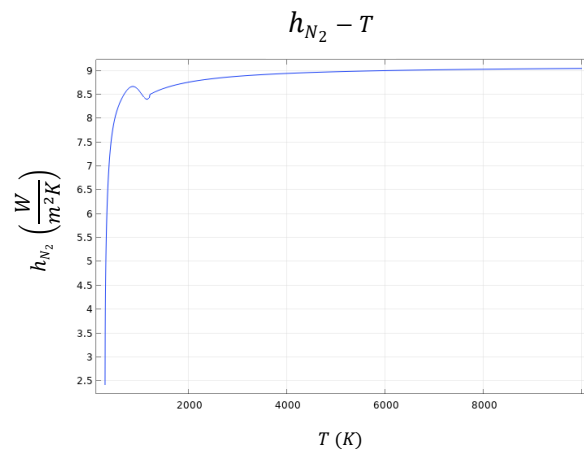


Diagram 4.10 Nitrogen convective heat transfer coefficient to temperature.

4.2.2 Bulk Ti6Al4V properties

Ti6Al4V consists of four phases: α , β , liquid and gas. The transitional temperatures are:

- $T(\alpha \rightarrow \beta) = 1268.15K$
- $T(\text{liquid}) = 1923.15K$
- $T(\text{gas}) = 3315K$

Ti6Al4V properties are temperature-dependent. For each property and for each phase, a different polynomial fit.

In [31], values for the Ti6Al4V properties for different temperatures are given (Table 4.2).

Table 4.2 Bulk Ti6Al4V properties.

θ (degrees C)	T(K)	ρ (kg/m ³)	Cp(J/kgK)	k(W/mK)
Temperature	Temperature	Density	Thermal Heat Capacity	Thermal conductivity
25	298.15	4420	546	7
100	373.15	4406	562	7.45
200	473.15	4395	584	8.75
300	573.15	4381	606	10.15
400	673.15	4366	629	11.35
500	773.15	4350	651	12.6
600	873.15	4336	673	14.2
700	973.15	4324	694	15.5
800	1073.15	4309	714	17.8
900	1173.15	4294	734	20.2
995	1268.15	4282	753	22.7
996	1269.15	4282	641	19.3
1100	1373.15	4267	660	21
1200	1473.15	4252	678	22.9
1300	1573.15	4240	696	23.7
1400	1673.15	4225	714	24.6
1500	1773.15	4205	732	25.8
1600	1873.15	4198	750	27
1650	1923.15	4189	759	28.4
1651	1924.15	3920	831	33.4
1700	1973.15	3886	831	34.6

With interpolation of the above data, for each interval $[0, 1268.15K]$, $[1268.15K, 1923.15K]$, $[1923.15K, 3315K]$, $[3315K, 10000K]$, the temperature-dependent piecewise functions of Ti6Al4V properties are calculated. It is considered that the polynomials for $[1923.15K, 1973.15K]$ are applied and at the $[1973.15K, 3315K]$ interval. For temperatures above 3315K, the values of the properties are constant and equal to the corresponding values of 3315K.

Specifically, the bulk Ti6Al4V properties are described by the following piecewise functions (Diagram 4.11, Diagram 4.12, Diagram 4.13):

$$\text{Bulk Ti6Al4V density: } \rho_{Ti6Al4V}(T) \left(\frac{kg}{m^3} \right) = \begin{cases} -0.1419 \cdot T + 4461, & 0 \leq T(K) \leq 1268.15, \text{ with } R^2 = 0.9993 \\ -0.1427 \cdot T + 4463, & 1268.15 \leq T(K) \leq 1923.15, \text{ with } R^2 = 0.9958 \\ -0.6939 \cdot T + 5255, & 1923.15 \leq T(K) \leq 3315, \text{ with } R^2 = 1 \\ 3081.0113, & 3315 \leq T(K) \leq 10000 \end{cases} \quad (18)$$

Bulk Ti6Al4V heat capacity: $C_{p_{Ti6Al4V}}(T) \left(\frac{J}{kgK} \right) =$

$$\begin{cases} 0.215 \cdot T + 483, & 0 \leq T(K) \leq 1268.15, \text{ with } R^2 = 0.9994 \\ 0.1802 \cdot T + 412.4, & 1268.15 \leq T(K) \leq 1923.15, \text{ with } R^2 = 1 \\ -1.567 \cdot 10^{-15} \cdot T + 831, & 1923.15 \leq T(K) \leq 3315, \text{ with } R^2 = 1 \\ 831, & 3315 \leq T(K) \leq 10000 \end{cases} \quad (19)$$

Bulk Ti6Al4V thermal conductivity: $k_{Ti6Al4V}(T) \left(\frac{W}{mK} \right) =$

$$\begin{cases} 0.0157 \cdot T + 1.257, & 0 \leq T(K) \leq 1268.15, \text{ with } R^2 = 0.976 \\ 0.01274 \cdot T + 3.492, & 1268.15 \leq T(K) \leq 1923.15, \text{ with } R^2 = 0.9847 \\ 0.02449 \cdot T - 13.72, & 1923.15 \leq T(K) \leq 3315, \text{ with } R^2 = 1 \\ 67.4616, & 3315 \leq T(K) \leq 10000 \end{cases} \quad (20)$$

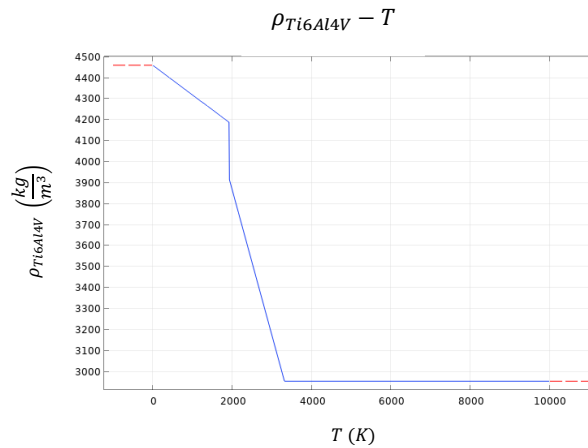


Diagram 4.11 Bulk Ti6Al4V density to temperature.

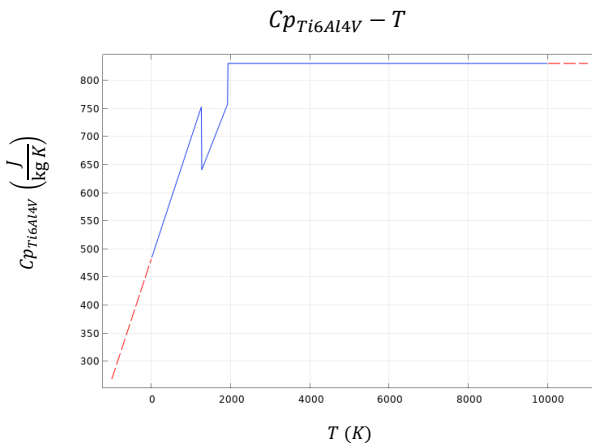


Diagram 4.12 Bulk Ti6Al4V heat capacity to temperature.

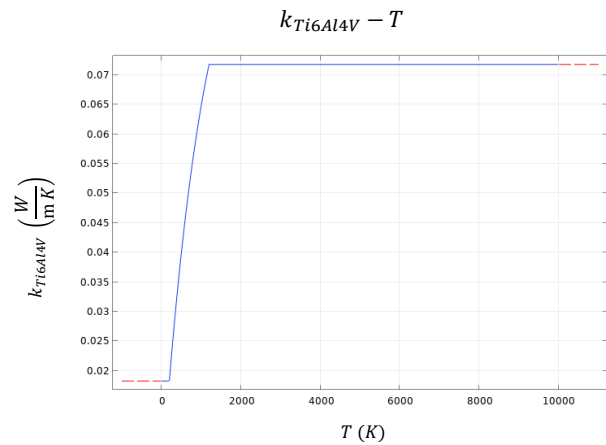


Diagram 4.13 Bulk Ti6Al4V thermal conductivity to temperature.

Another, very important, parameter for SLM is emissivity. Emissivity (ϵ) is the ratio of the radiance of an object or surface to the radiance of a blackbody (Planckian radiator) at the same temperature. It is therefore dimensionless and can assume values between 0 and 1 for

thermal radiators at equilibrium. Spectral emissivity $\epsilon(\lambda)$ is the emissivity at a given wavelength. If a radiator is neutral with respect to wavelength, with a constant spectral emissivity less than unity, it is called a graybody [32].

In [33] and for Ti6Al4V, emissivity is a function of both wavelength and temperature (Table 4.3).

Specifically,

Table 4.3 Emissivity as function of wavelength and temperature.

Wavelength (μm)	Linear fit
1.5	$1.1 \cdot 10^{-3}T - 0.634$
1.6	$1.14 \cdot 10^{-3}T - 0.658$
1.7	$1.26 \cdot 10^{-3}T - 0.744$
1.8	$1.35 \cdot 10^{-3}T - 0.832$
1.9	$1.53 \cdot 10^{-3}T - 0.991$
2	$1.69 \cdot 10^{-3}T - 1.780$
2.1	$1.56 \cdot 10^{-3}T - 0.975$
2.2	$1.56 \cdot 10^{-3}T - 0.970$

In order to calculate the functions above as only-temperature functions (Diagram 4.14), the process below is followed:

All the linear functions above are like:

$$c_1(\lambda) \cdot T + c_2(\lambda) \quad (21)$$

So, Table 4.4 can be created:

Table 4.4 Values of c_1 and c_2 for different wavelengths.

Wavelength λ (μm)	$c_1(\lambda(\mu\text{m}))$	$c_2(\lambda(\mu\text{m}))$
1.5	$1.1 \cdot 10^{-3}$	-0.634
1.6	$1.14 \cdot 10^{-3}$	-0.658
1.7	$1.26 \cdot 10^{-3}$	-0.744
1.8	$1.35 \cdot 10^{-3}$	-0.832
1.9	$1.53 \cdot 10^{-3}$	-0.991
2	$1.69 \cdot 10^{-3}$	-1.780
2.1	$1.56 \cdot 10^{-3}$	-0.975
2.2	$1.56 \cdot 10^{-3}$	-0.970

A linear interpolation to the c_1 data, gives that:

$$c_1(\lambda(\mu\text{m})) = 0.8083 \cdot 10^{-3} \cdot \lambda - 0.09667 \cdot 10^{-3}, \text{ with } R^2 = 0.8269 \quad (22)$$

A linear interpolation to the c_2 data, gives that:

$$c_2(\lambda(\mu\text{m})) = -0.8576 \cdot \lambda + 0.6386, \text{ with } R^2 = 0.8275 \quad (23)$$

In this study, $\lambda = 1.080 \mu m$, so $c_1(1.080) = 0.0007763$ and $c_2(1.080) = -0.2876$.

Eventually, $\varepsilon_{Ti6Al4V}(T) = 0.0007763 \cdot T - 0.2876$. For temperatures below 800K, emissivity is constant and equals to the emissivity of the 800K. For temperatures above 1000K, emissivity is constant and equals to the emissivity of the 1000K.

So,

$$\varepsilon_{Ti6Al4V}(T) = \begin{cases} 0.1782, & 0 \leq T(K) \leq 800 \\ 0.0007763 \cdot T - 0.2876, & 800 \leq T(K) \leq 1000 \\ 0.7493, & 1000 \leq T(K) \leq 10000 \end{cases} \quad (24)$$

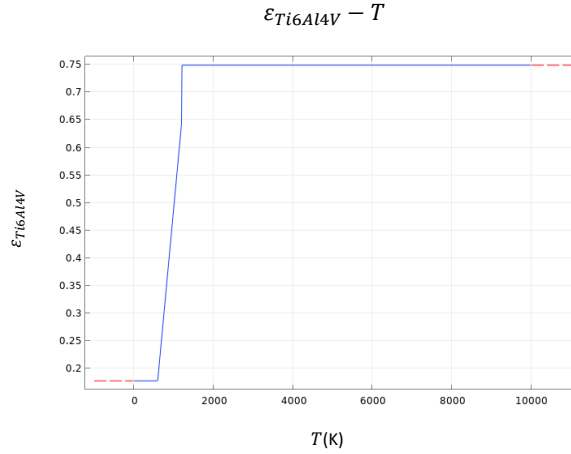


Diagram 4.14 Bulk Ti6Al4V emissivity to temperature.

4.2.3 Porous Ti6Al4V

In this study, it is assumed that for SLM, the Ti6Al4V powder has abruptly the same porosity as the 316L powder. From [34], the average of apparent and tapped density for powder 316L is 4.695 g/cm^3 . On the other hand, from [31], the density of the bulk 316L is 7.950 g/cm^3 .

So, the porosity (φ) for 316L equals to:

$$\varphi(316L) = 1 - \frac{4.695}{7.950} = 0.41$$

In this study, it can be assumed that the porosity of the Ti6Al4V powder is:

$$\varphi(Ti6Al4V) = 0.45$$

However, porosity is applied only for temperatures below melting point (1923.15K). Above the melting point there is no porosity. Furthermore, in order to have a smooth transition from 0.45 to 0 porosity (for computational reasons), it is assumed that in the [1923.15, 1933.15] interval the porosity reduces linearly. Specifically, for Ti6Al4V powder (Diagram 4.15),

$$\varphi(T) = \begin{cases} 0.45, & 0 \leq T(K) \leq 1923.15 \\ -0.045 \cdot T + 86.99175, & 1923.15 \leq T(K) \leq 1933.15 \\ 0, & 1933.15 \leq T(K) \leq 10000 \end{cases} \quad (25)$$

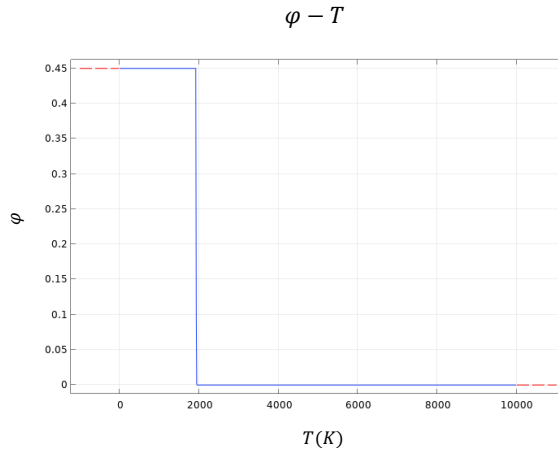


Diagram 4.15 Powder porosity to temperature.

This porosity means that for temperatures below melting point, the powder consists of 55% (=1- $\varphi_{Ti6Al4V}$) bulk Ti6Al4V and 45% N_2 (shielding gas). This idea is used in order to calculate the porous density and the porous heat capacity via the mixture rule. Specifically (Diagram 4.16, Diagram 4.17),

$$\rho_{powder}(T) = \varphi(T) \cdot \rho_{N_2}(T) + (1 - \varphi(T)) \cdot \rho_{Ti6Al4V}(T) \quad (26)$$

$$Cp_{powder}(T) = \varphi(T) \cdot Cp_{N_2}(T) + (1 - \varphi(T)) \cdot Cp_{Ti6Al4V}(T) \quad (27)$$

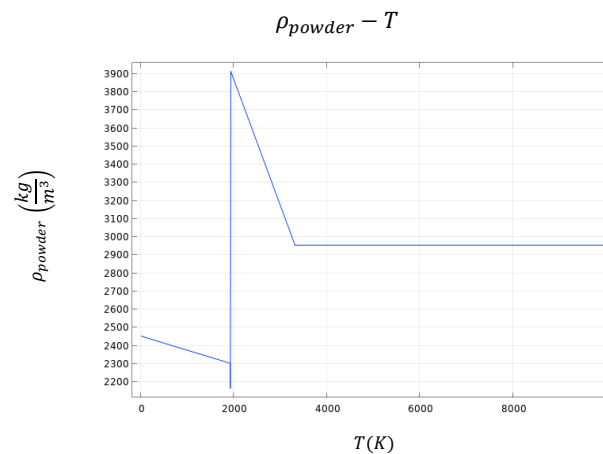


Diagram 4.16 Powder density to temperature.

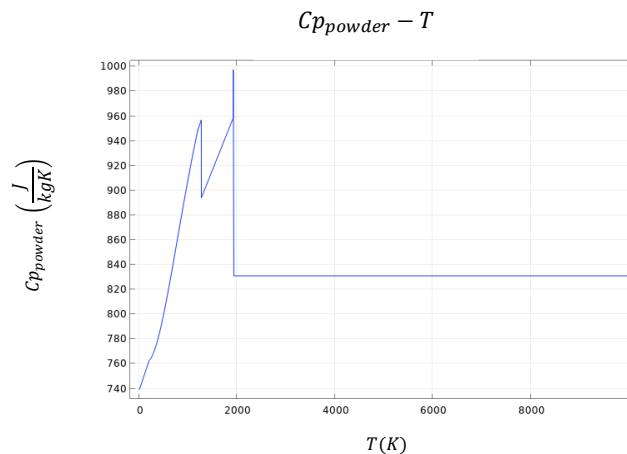


Diagram 4.17 Powder heat capacity to temperature.

In order to calculate the porous emissivity and the porous thermal conductivity, the process described in [35] is followed.

The emission of radiation to ambient from a hot porous surface, such as the powder bed, can be assumed to be caused by emission from the heated particles and emission from the cavities in the powder bed, all at the same temperature. Although the walls of the cavities are made of the same particles, the emissivity of the hole is a function of its geometry. The hole emissivity is always higher than that of the material comprising the cavity. Consequently, it is expected that the emissivity of the powder is higher than that of the solid and it follows the expression:

$$\varepsilon_{powder}(T) = A_H(T)\varepsilon_H(T) + (1 - A_H(T))\varepsilon_{Ti6Al4V}(T) \quad (28)$$

Where:

$\varepsilon_H(T)$ is the emissivity of the hole. It is described by the expression:

$$\varepsilon_H(T) = \frac{\varepsilon_{Ti6Al4V}(T) \left[2 + 3.082 \left(\frac{1-\varphi(T)}{\varphi(T)} \right)^2 \right]}{\varepsilon_{Ti6Al4V}(T) \left[1 + 3.082 \left(\frac{1-\varphi(T)}{\varphi(T)} \right)^2 \right] + 1} \quad (29)$$

A_H is the area fraction of the surface that is occupied by the radiation-emitting holes. It is described by the expression:

$$A_H(T) = \frac{0.908\varphi^2(T)}{1.908\varphi^2(T) - 2\varphi(T) + 1} \quad (30)$$

Because $\varepsilon_{Ti6Al4V}(T)$ changes only into the interval $800 \leq T(K) \leq 1000$, so and the $\varepsilon_{powder}(T)$ only changes into the same interval.

For this reason, for temperatures 800, 900, 1000K, the values of $A_H(T)$, $\varepsilon_H(T)$ and $\varepsilon_{powder}(T)$ are calculated and presented in Table 4.5.

Table 4.5 Calculation of $A_H(T)$, $\varepsilon_H(T)$ and $\varepsilon_{powder}(T)$ for different temperatures.

Temperature (K)	$A_H(T)$	$\varepsilon_H(T)$	$\varepsilon_{powder}(T)$
800	0.3780	0.7676	0.4976
900	0.3780	0.8217	0.5663
1000	0.3780	0.8632	0.6303

With interpolation of the $\varepsilon_{powder}(T)$ data and given that for temperatures below 800K or above 1000K, $\varepsilon_{powder}(T)$ is constant and equals to $\varepsilon_{powder}(800K)$ or $\varepsilon_{powder}(1000K)$, accordingly, the $\varepsilon_{powder}(T)$ function (Diagram 4.18), eventually, is:

$$\varepsilon_{powder}(T) = \begin{cases} 0.4977, & 0 \leq T(K) \leq 800 \\ -5.181 \cdot 10^{-13} \cdot T^4 + 2.248 \cdot 10^{-9} \cdot T^3 - 3.782 \cdot 10^{-6} \cdot T^2 + 0.003515 \cdot T - 0.8322, & 800 \leq T(K) \leq 1000, \text{ with } R^2 = 1 \\ 0.6302, & 1000 \leq T(K) \leq 10000 \end{cases} \quad (31)$$

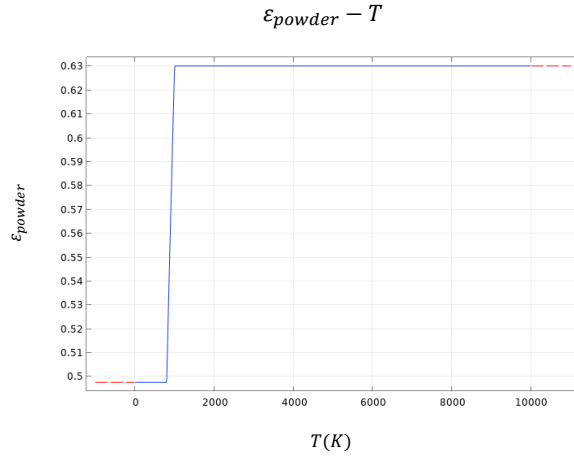


Diagram 4.18 Powder emissivity to temperature.

Moreover, the thermal conductivity for powder is calculated by the following equation:

$$\begin{aligned} \frac{k_{\text{powder}}(T)}{k_{N_2}(T)} &= (1 - \sqrt{1 - \varphi}) \left(1 + \frac{\varphi k_R(T)}{k_{N_2}(T)} \right) + \\ &+ \sqrt{1 - \varphi} \left\{ (1 - \Phi) \left[\frac{2}{1 - \frac{B k_{N_2}(T)}{k_{Ti6Al4V}(T)}} \left(\frac{B}{\left(1 - \frac{B k_{N_2}(T)}{k_{Ti6Al4V}(T)} \right)^2} \left(1 - \frac{k_{N_2}(T)}{k_{Ti6Al4V}(T)} \right) \ln \left(\frac{k_{Ti6Al4V}(T)}{B k_{N_2}(T)} \right) - \frac{B+1}{2} - \right. \right. \right. \\ &\left. \left. \left. \frac{B-1}{1 - \frac{B k_{N_2}(T)}{k_{Ti6Al4V}(T)}} + \frac{k_R(T)}{k_{N_2}(T)} \right) + \Phi \frac{k_{\text{contact}}(T)}{k_{N_2}(T)} \right\} \end{aligned} \quad (32)$$

Where:

$k_{\text{powder}}(T) \left(\frac{W}{mK} \right)$ is the effective thermal conductivity of the powder bed.

$k_R(T) \left(\frac{W}{mK} \right)$ is the thermal conductivity part of the powder bed owing to radiation, denoted by Damköhler's equation below:

$$k_R(T) = \frac{4\varepsilon_{\text{powder}}(T)\sigma_B T^3 x_R}{1 - 0.132\varepsilon_{\text{powder}}(T)} \quad (33)$$

Where:

$\sigma_B = 5.67 \times 10^{-8} \frac{W}{m^2 K^4}$ is the Stefan-Boltzmann constant.

x_R (m) is the median particle diameter of the powder. In this study, $x_R = 30 \times 10^{-6} m$.

Φ is the flattened surface fraction of particle in contact with another particle; $\Phi = 0$ when there is no contact for the particles; $\Phi = 1$ when there is complete particle contact. In this study, it is considered that $\Phi = 0.0003$.

B is the deformation parameter of the particle; $B = 1$ when the particle surface is that of a sphere; $B < 1$ when it is a prolonged needle; $\infty > B > 1$ when it is a barrel-like body; B may be approximately calculated from the porosity φ of the powder bed:

$$B \approx 1.25 \left(\frac{1-\varphi}{\varphi} \right)^{\frac{10}{9}} \quad (34)$$

In this study, $\varphi = 0.45$, so $B = 1.5622$.

$k_{contact}(T) \left(\frac{W}{mK} \right) = 18\Phi k_{Ti6Al4V}(T)$, for $\Phi < 0.0003$; $k_{contact}(T)$ is near to $k_{Ti6Al4V}(T)$ in value only when Φ is greater than 0.01. In this study, $\Phi = 0.0003$, so it is considered that:

$$k_{contact}(T) = 0.00054 k_{Ti6Al4V}(T) \quad (35)$$

Using the equation above, thermal conductivity for powder is calculated for temperatures 100, 200, ..., 2000K. The results are given in the Table 4.6 below:

Table 4.6 Calculation of $k_{powder}(T)$ for different temperatures.

Temperature (K)	$k_{powder}(T) \left(\frac{W}{mK} \right)$
100	0.1532
200	0.1713
300	0.2420
400	0.3075
500	0.3686
600	0.4258
700	0.4793
800	0.5295
900	0.5770
1000	0.6218
1100	0.6636
1200	0.7026
1300	0.7041
1400	0.7161
1500	0.7278
1600	0.7394
1700	0.7510
1800	0.7626
1900	0.7743
2000	0.8176

With interpolation to the data above:

$$k_{powder}(T) = 2.131 \cdot 10^{-13} \cdot T^4 - 8.811 \cdot 10^{-10} \cdot T^3 + 9.916 \cdot 10^{-7} \cdot T^2 + 0.0001841 \cdot T + 0.1183,$$

with $R^2 = 0.9986$

However, melted or evaporated powder has no porosity, so for temperatures above 1923.15K, $k_{powder}(T) = k_{Ti6Al4V}(T)$.

Eventually (Diagram 4.19),

$$k_{powder}(T) \left(\frac{W}{mK} \right) = \begin{cases} 2.131 \cdot 10^{-13} \cdot T^4 - 8.811 \cdot 10^{-10} \cdot T^3 + 9.916 \cdot 10^{-7} \cdot T^2 + 0.0001841 \cdot T + 0.1183, & 0 \leq T(K) \leq 1923.15 \\ 0.02449 \cdot T - 13.72, & 1923.15 \leq T(K) \leq 3315 \\ 67.4616, & 3315 \leq T(K) \leq 10000 \end{cases} \quad (36)$$

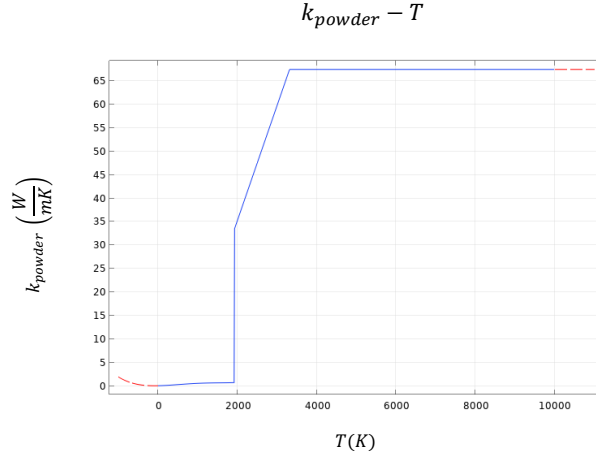


Diagram 4.19 Powder thermal conductivity to temperature.

4.2.4 Model's material properties

The model used in this study consists of 0.27mm of solid Ti6Al4V substrate and 30 μ m of Ti6Al4V powder on top of the solid substrate. In the solid substrate, the bulk Ti6Al4V properties are applied, whereas in the powder, the Ti6Al4V porous properties are applied. So, the combined properties of the full model are functions of temperature, but also and of the model height (expressed on the z-coordinate) and are given below:

$$\rho_{model}(T) \left(\frac{kg}{m^3} \right) = \begin{cases} \rho_{Ti6Al4V}(T), & 0 \leq z(mm) \leq 0.27 \\ \rho_{powder}(T), & 0.27 \leq z(mm) \leq 0.30 \end{cases} \quad (37)$$

$$Cp_{model}(T) \left(\frac{J}{kgK} \right) = \begin{cases} Cp_{Ti6Al4V}(T), & 0 \leq z(mm) \leq 0.27 \\ Cp_{powder}(T), & 0.27 \leq z(mm) \leq 0.30 \end{cases} \quad (38)$$

$$k_{model}(T) \left(\frac{W}{mK} \right) = \begin{cases} k_{Ti6Al4V}(T), & 0 \leq z(mm) \leq 0.27 \\ k_{powder}(T), & 0.27 \leq z(mm) \leq 0.30 \end{cases} \quad (39)$$

4.2.5 Phase Change

This node is used to specify the properties of a phase change material according to the apparent heat capacity formulation, when modeling heat transfer in solids, fluids and porous media. In this formulation, latent heat is included as an additional term in the heat capacity. Specifically,

$$\left\{ \begin{array}{l} \rho(T) = \rho_{model}(T) \\ C_p(T) = \left(\sum_{j=1}^{Nphases} \theta_j C_{p_{model},j}(T) \right) + \left(\sum_{j=1}^{Nphases-1} L_{j \rightarrow j+1} \frac{d\alpha_{m,j \rightarrow j+1}}{dT} \right) \\ \alpha_{m,j \rightarrow j+1} = \frac{1}{2} \frac{\theta_{j+1} - \theta_j}{\theta_j + \theta_{j+1}} \\ k(T) = \sum_{j=1}^{Nphases} \theta_j k_{model,j}(T) \\ \sum_{j=1}^{Nphases} \theta_j = 1 \end{array} \right. \quad (40)$$

Where:

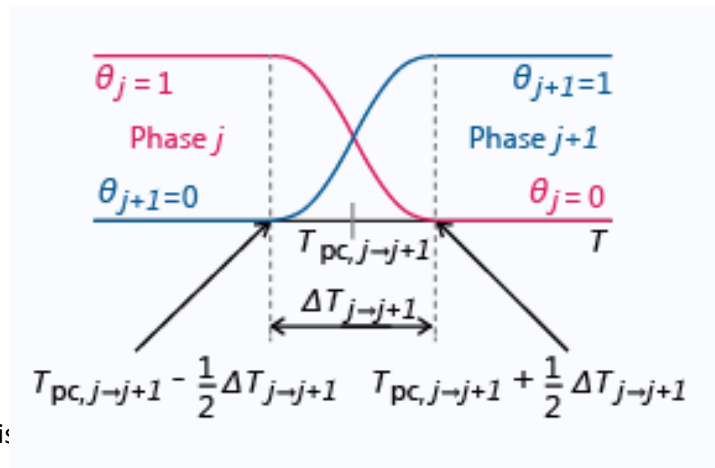
$Nphases$ is the number of phases of the material. In this study, for Ti6Al4V, $Nphases = 4$. Specifically, the phases are: α , β , the liquid phase and the gas phase.

$\rho(T) \left(\frac{kg}{m^3} \right)$ is the model density, which considers the latent heat and the phase change properties of Ti6Al4V.

$C_p(T) \left(\frac{J}{kg \cdot K} \right)$ is the model heat capacity at constant pressure, which considers the latent heat and the phase change properties of Ti6Al4V.

$k(T) \left(\frac{W}{m \cdot K} \right)$ is the model thermal conductivity, which considers the latent heat and the phase change properties of Ti6Al4V.

The parameters for the definition of the transition temperature intervals are described with the following Diagram 4.20:



Each transition is:

een:

Diagram 4.20 Phase change parameters.

$T_{pc,j \rightarrow j+1} - \frac{\Delta T_{j \rightarrow j+1}}{2}$ and $T_{pc,j \rightarrow j+1} + \frac{\Delta T_{j \rightarrow j+1}}{2}$, releasing a total heat per unit volume equal to $L_{j \rightarrow j+1}$.

The Phase change temperature between phase j and phase j+1, $T_{pc,j \rightarrow j+1}$, should be set to define the center of the j-transition interval. In this study, $T_{pc,1 \rightarrow 2} = 1268.15K$ ($\alpha \rightarrow \beta$), $T_{pc,2 \rightarrow 3} = 1923.15K$ (*melting temperature*), $T_{pc,3 \rightarrow 4} = 3315K$ (*evaporation temperature*).

The Transition interval between phase j and phase j+1, $\Delta T_{j \rightarrow j+1}$, should be set to define the width of the j-transition interval. In this study, $\Delta T_{1 \rightarrow 2} = \Delta T_{2 \rightarrow 3} = \Delta T_{3 \rightarrow 4} = 10K$.

The Latent heat from phase j and phase j+1, $L_{j \rightarrow j+1}$, should be set to define the latent heat per unit mass released during the j-phase transition. In this study, $L_{1 \rightarrow 2} = 48 \frac{kJ}{kg}$, $L_{2 \rightarrow 3} = 282 \frac{kJ}{kg}$, $L_{3 \rightarrow 4} = 10382 \frac{kJ}{kg}$. The calculations to find out the latent heats are demonstrated in the 'Deformed Geometry' section.

The material properties of phase j are valid when $T < T_{pc,j \rightarrow j+1} - \frac{\Delta T_{j \rightarrow j+1}}{2}$, while the material properties of phase j+1 hold for $T > T_{pc,j \rightarrow j+1} + \frac{\Delta T_{j \rightarrow j+1}}{2}$. Within the transitional interval ($T_{pc,j \rightarrow j+1} - \frac{\Delta T_{j \rightarrow j+1}}{2} < T < T_{pc,j \rightarrow j+1} + \frac{\Delta T_{j \rightarrow j+1}}{2}$), there is a "mushy zone" with mixed material properties.

4.3 Physical Model Governing Equations

4.3.1 Heat Transfer in Solids

The heat equation to model heat transfer in solids is given below:

$$\begin{cases} \rho(T)C_p(T)\frac{\partial T}{\partial t} + \nabla \cdot \mathbf{q}(T) = Q(T) \\ \mathbf{q}(T) = -k(T)\nabla T \text{ (Fourier's law)} \end{cases} \quad (41)$$

With the following material properties, fields and sources:

$\mathbf{q}(T)$ ($\frac{W}{m^2}$) is the heat flux vector, so $\mathbf{q}(T) = \mathbf{q}_{LB}(T) + \mathbf{q}_{conv}(T) + \mathbf{q}_{rad}(T)$ (these heat fluxes are analyzed in following sections).

$Q(T)$ ($\frac{W}{m^3}$) is the heat rate per unit volume. In this study, $Q(T) = 0$.

4.3.2 Initial Condition

The initial value of the temperature T is room temperature, 293.15 K (20°C).

4.3.3 Boundary Condition

Heat transfer symmetry is used here as boundary condition and it means that there is no heat flux across the boundary.

The equation that describes this boundary condition is given below:

$$-\mathbf{n} \cdot \mathbf{q} = 0 \quad (42)$$

Where \mathbf{n} is the perpendicular vector of the boundary surface.

In this study, y-plane is the boundary surface, in order to reduce at half the model dimensions and eliminate the computational time.

4.3.4 Deposited Beam Power

The heat source model brought by narrow beams, such as a laser beam, to a given boundary, is given by the following equation:

$$-\mathbf{n} \cdot \mathbf{q}_{LB} = P_o \cdot f(\mathbf{O}, \mathbf{e}) \frac{|\mathbf{e} \cdot \mathbf{n}|}{\|\mathbf{e}\|} \quad (43)$$

Where:

$\mathbf{q}_{LB} \left(\frac{W}{m} \right)$ is the heat flux due to the laser.

P_o (W) is the deposited beam power.

\mathbf{e} is the beam orientation vector.

\mathbf{O} (m) is the beam origin point.

$f(\mathbf{O}, \mathbf{e})$ is the beam distribution type function.

4.3.4.1 Surface perpendicular vector \mathbf{n}

The laser beam is applied on the top surface of the model, so \mathbf{n} , in these simulations, is perpendicular to the z-plane.

4.3.4.2 Deposited Beam Power P_o

Deposited beam power is given below:

$$P_o = a \cdot P \quad (44)$$

Where:

a is the material absorptivity.

P (W) is the laser power.

Fundamentals of transmission, absorption and reflection:

When radiant flux is incident upon a surface or medium, three processes occur: transmission, absorption and reflection. Fig. 4.2 shows the ideal case, where the transmitted and reflected components are either specular or perfectly diffuse. Fig. 4.3 shows the transmission and reflection for actual surfaces.

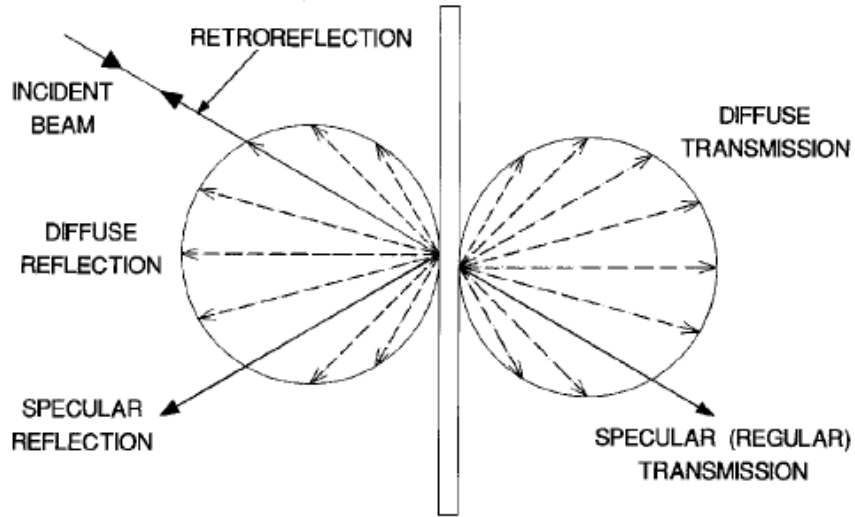


Fig. 4.2 Idealized reflection and transmission.

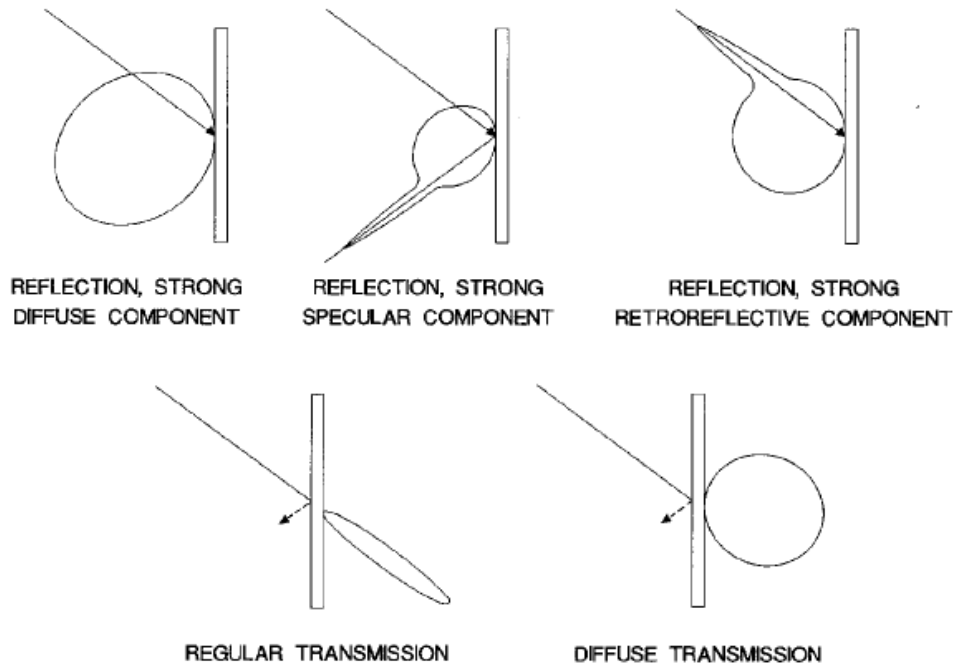


Fig. 4.3 Actual reflection and transmission.

Transmission (τ) is the term used to describe the process by which incident radiant flux leaves a surface or medium from a side other than the incident side, usually the opposite side.

Absorption (α) is the process by which incident radiant flux is converted to another form of energy, usually heat. Absorption is the fraction of incident flux that is absorbed.

Reflection (ρ_f) is the process where a fraction of the radiant flux incident on a surface is returned into the same hemisphere whose base is the surface and which contains the incident radiation. The reflection can be specular (in the mirror direction), diffuse (scattered into the entire hemisphere), or a combination of both [32].

However, during SLM, the radiant flux isn't incident upon a flat surface, but upon the spheres of the metal powder. The absorptivity of the spheres is noticeably higher than the normal-incidence value. This enhancement is due to multiple scattering. So, in the powder, a ray can scatter repeatedly, leading to additional absorption relative to the case of a flat surface. The scattering of multiple rays is demonstrated in Fig. 4.4 and Fig. 4.5 [36].

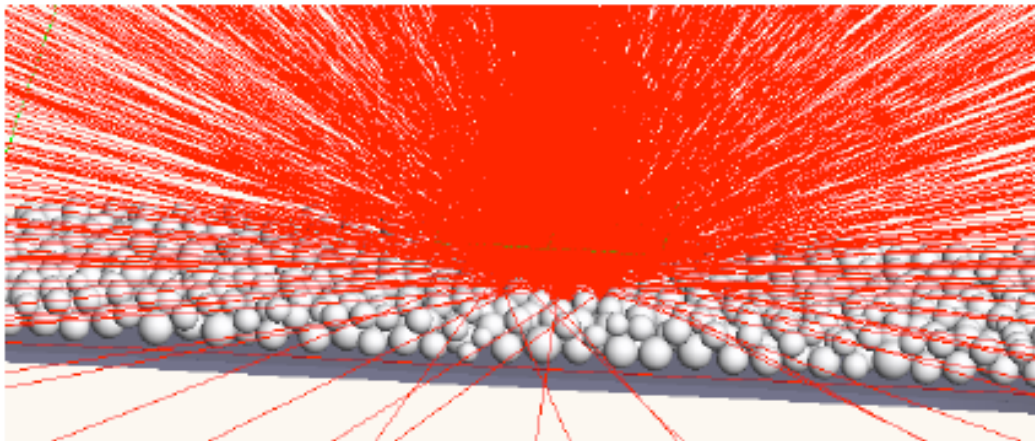


Fig. 4.4 Reflected rays during illumination of a realistic array.

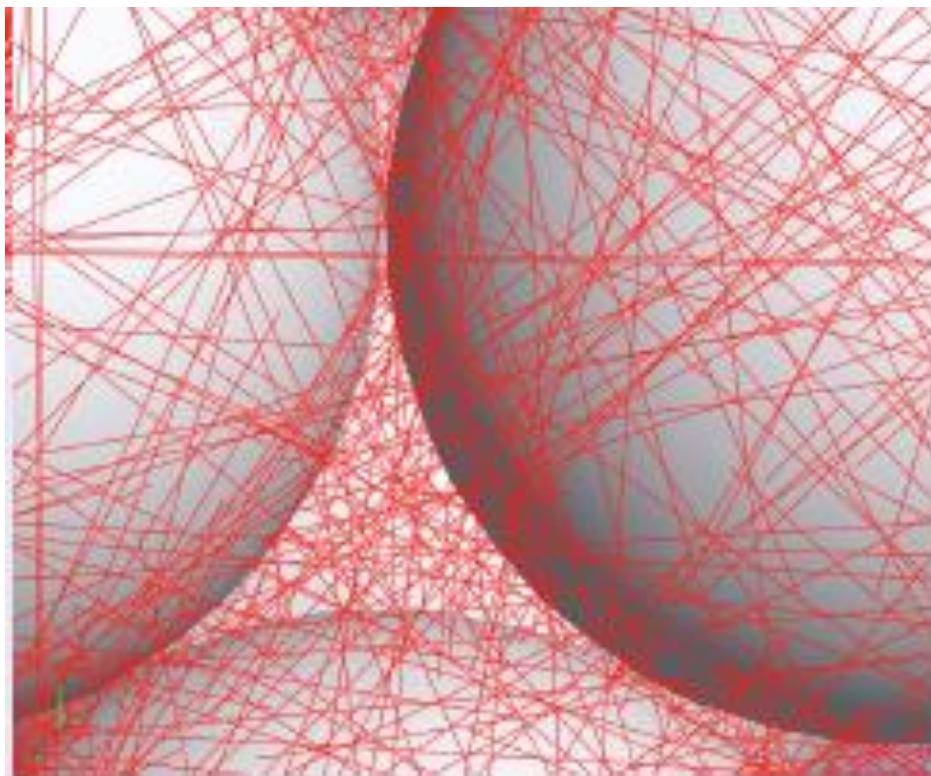


Fig. 4.5 Detail showing multiple scattering from spheres.

In this study, the absorbance coefficient for Ti6Al4V is considered constant and equals to 0.77, according to [37].

4.3.4.3 Beam orientation vector e

The laser beam is downwards so, $e = [0 \ 0 \ -1]$.

4.3.4.4 Beam origin point O

The laser beam is moving on the x-direction, so the x-coordinate of O must be time-dependent. Moreover, the laser beam shouldn't start from or end to the edges of the model, because this often leads to computational errors. In this study, the x-coordinate of the starting point of the laser beam is 0.25[mm].

So, the time-dependent x-coordinate of O , is given below:

$$O_x = 0.25(mm) + v\left(\frac{mm}{s}\right) \cdot t$$

Where $v\left(\frac{m}{s}\right)$ is the laser scanning speed.

On y-direction, the laser beam is moving on the y=0-line of the model, so $O_y = 0 \text{ mm}$. Furthermore, the laser beam is incident upon the top surface of the model, so $O_z = 1 \text{ mm}$.

To sum up:

$$O = \left(0.25(mm) + v\left(\frac{mm}{s}\right) \cdot t, \ 0(mm), \ 1(mm)\right) \quad (45)$$

4.3.4.5 Beam distribution type function $f(O, e)$

In this study, the laser beam intensity is modeled as a gaussian distribution, so:

$$\begin{cases} f(O, e) = \frac{1}{2\pi\sigma^2} e^{-\frac{d_g^2}{2\sigma^2}} \\ d_g = \frac{\|e \times (x - O)\|}{\|e\|} \end{cases} \quad (46)$$

Where:

σ (m) is the standard deviation of the gaussian distribution.

x (m) is the position, where the laser beam intensity is calculated via the gaussian distribution.

d_g (m) is the distance demonstrated in Fig. 4.6, below:

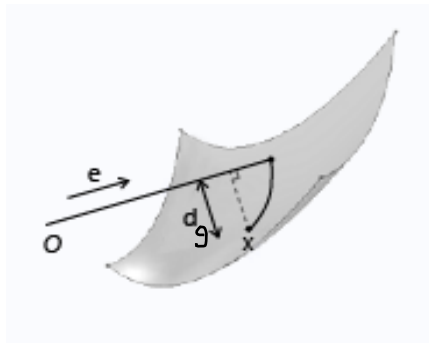


Fig. 4.6 Demonstration of distance d_g .

4.3.4.6 Standard deviation σ

The beam diameter or beam width of a laser beam is the diameter along any specified line that is perpendicular to the beam axis and intersects it. Since beams typically do not have sharp edges, the diameter can be defined in many different ways. One of the most common definitions of the beam width is 4σ . This is the laser beam definition considered in this study. The beam width can be measured in units of length at a particular plane perpendicular to the beam axis.

In this study a 4σ - laser beam with a $100\mu\text{m}$ diameter is used, as demonstrated in Fig. 4.7:

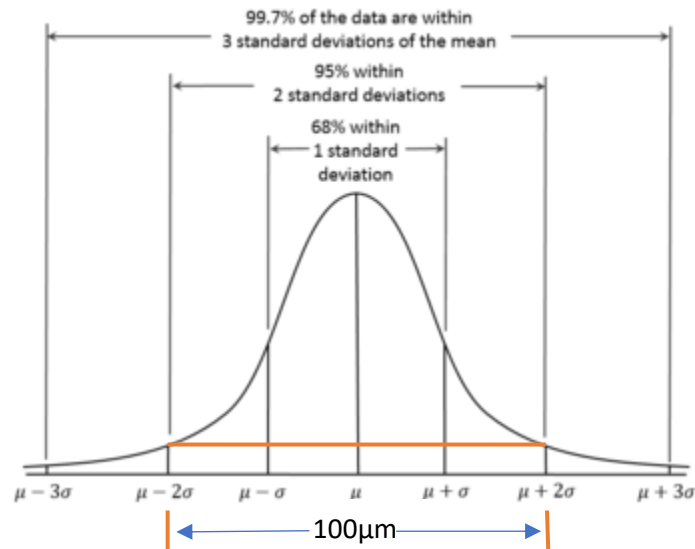


Fig. 4.7 Laser beam gaussian distribution.

So, from Fig. 4.7, $\sigma = \frac{\text{laser beam diameter}}{4} = \frac{100\mu\text{m}}{4} = 25\mu\text{m}$.

4.3.5 Convective heat flux

Convection occurs between the shielding gas (in this study is N_2) and all the surfaces of the model. Convective heat flux (q_{conv}) is given below:

$$\mathbf{n} \cdot \mathbf{q}_{conv} = h_{N_2} \cdot (T_\infty - T) \quad (47)$$

4.3.6 Surface-to-Ambient Radiation

This node accounts for radiation from model boundaries to the ambient. The net inward heat flux (q_{rad}) from surface-to-ambient radiation is:

$$-\mathbf{n} \cdot \mathbf{q}_{rad} = \varepsilon_{powder}(T) \sigma_B (T_\infty^4 - T^4) \quad (48)$$

4.4 Deformed Geometry

4.4.1 Deformed Geometry vs Moving Mesh

Mesh deformation can be set up in two different ways, depending on the intended behavior of the model: either the deformation represents a fundamental change in the shape of the geometry, or it represents the shape change induced by deformation of solid materials. The former is referred as Deformed Geometry and the latter as Moving Mesh functionality. Technically, the difference is that Deformed Geometry functionality deforms the material frame mesh relative to the geometry frame mesh, while Moving Mesh functionality deforms the spatial frame mesh relative to the material frame mesh. Both types of deformation can be used at the same time, one on top of the other.

When using Deformed Geometry functionality, the material does not follow the change in shape. Deformation of the geometry boundaries therefore corresponds to addition or removal of material. When using Moving Mesh features, solid materials follow the mesh deformation and deform in the same way as the mesh. Fluids and gases, however, are added or removed so as to always fill the current shape of the domain. Any effects of compression or expansion must be introduced explicitly into the equations.

Deformed Geometry features are used to study the behavior of different shapes of an original object. In a model with Deformed Geometry, the material never follows a perturbation of the shape. The total mass of the first shape is not the same as the mass for the second, perturbed geometry. Any deformation can be regarded as removal or addition of material.

Moving Mesh features are used to study how a solid object deforms as the results of physical load, and how fluids in adjacent domains react to displacement of the domain boundaries. In a model with Moving Mesh, a solid material follows the mesh deformation. A movement of a boundary can therefore be regarded as bending or punching the original object. Undeformed and deformed solid objects have the same mass, but the total amount of fluid in a domain whose boundaries deform can change.

4.4.2 Deforming Domain

A deforming domain node specifies that the shape of the selected domains of the model should be governed by the domain boundaries, which are in turn controlled either by explicit deformed mesh boundary condition nodes, or by implicit continuity constraints requiring that a deforming domain must follow the shape of adjacent domains, or stay fixed if there is no adjacent domain. Explicit boundary conditions take precedence over implicit constraints.

In the interior of the domains, the mesh is controlled by a smoothing equation.

4.4.3 Smoothing

There are four types of mesh smoothing: Laplace, Winslow, Hyperelastic and Yeoh.

To see how these smoothing methods differ, let x and y be the spatial coordinates of the spatial frame, and let X and Y be the reference coordinates of the material frame.

- Laplace smoothing: In the static case, it solves the equation:

$$\frac{\partial^2 x}{\partial X^2} + \frac{\partial^2 x}{\partial Y^2} = 0 \quad (49)$$

and in the transient case, it solves the equation:

$$\frac{\partial^2 \frac{\partial x}{\partial t}}{\partial X^2} + \frac{\partial^2 \frac{\partial x}{\partial t}}{\partial Y^2} = 0 \quad (50)$$

Similar equations hold for the y coordinate.

- Winslow smoothing: The following equation is solved:

$$\frac{\partial^2 X}{\partial x^2} + \frac{\partial^2 X}{\partial y^2} = 0 \quad (51)$$

Similar equations hold for the Y coordinate. Equivalently, X and Y satisfy Laplace equations as functions of the x and y coordinates.

- Hyperelastic smoothing: The hyperelastic smoothing method searches for a minimum of a mesh deformation energy inspired by neo-Hookean materials:

$$W_{mesh} = \int_{\Omega} \frac{\nu}{2} (I_1 - 3) + \frac{\kappa}{2} (J - 1)^2 dV \quad (52)$$

Where ν and κ are artificial shear and bulk moduli, respectively, and the invariants J and I_1 are given by:

$$\begin{cases} J = \det(\nabla_X x) \\ I_1 = J^{-2/3} \text{tr}((\nabla_X x)^T \nabla_X x) \end{cases} \quad (53)$$

- Yeoh smoothing: The Yeoh smoothing method is also inspired by hyperelastic materials, in this case the three-term Yeoh hyperelastic model, which is a generalization of a neo-Hookean material. It uses a strain energy of the form:

$$W_{mesh} = \frac{1}{2} \int_{\Omega} C_1 (I_1 - 3) + C_2 (I_1 - 3)^2 + C_3 (I_1 - 3)^3 + \kappa (J - 1)^2 dV \quad (54)$$

Where κ is an artificial bulk modulus, as above, while C_1 , C_2 and C_3 are other artificial material properties. The values of C_1 and C_3 are by default 1 and 0, respectively. The value of C_2 controls the nonlinear stiffening of the artificial material under deformation. As C_2 increases, mesh transformations do not transmit easily through the mesh. As C_2 reduces, mesh transformations transmit easily through the mesh.

The Laplace smoothing is the cheapest option in terms of computations because it is linear and uses one equation for each coordinate direction, which are not coupled to each other. However, there is no mechanism in Laplace smoothing that prevents inversion of elements. Therefore, this method is most suitable for small deformations in a linear regime — for example, when computing the sensitivity of some quantity to virtual deformations around the initial shape.

The Winslow, hyperelastic, and Yeoh smoothing methods are increasingly nonlinear and create a single coupled system of equations for all coordinate directions, which makes them more expensive to solve. They also share the theoretical property that continuous solutions to these equations always have positive volume everywhere. Unfortunately, this is not necessarily true for the discrete finite element solutions. In addition, a positive volume is not sufficient for maintaining element quality.

In compression, the three nonlinear methods show similar behavior, while in extension, the Winslow smoothing tends to allow elements to be stretched too far. The main difference

between the simpler Hyperelastic method and the more advanced Yeoh model is that the latter responds to element distortion by sharply increasing the stiffness of distorted elements. This, to some extent, prevents further distortion in those regions and effectively acts to spread the mesh deformation more evenly over the domain, away from moving boundaries.

Yeoh smoothing generally produces the best results and allows the largest displacement of boundaries before mesh elements become inverted. However, because of its strong nonlinearity, it can cause convergence problems, in particular for the time-dependent and segregated solvers.

In this study, a Hyperelastic smoothing type mesh, according to [38], is used.

4.4.4 Symmetry

A symmetry node is applied on flat boundaries of deforming domains, in order to prevent boundary nodes from moving out of the plane. This allows the mesh to move tangentially to the symmetry plane, but not in its normal direction.

In this study, symmetry is applied to all the surfaces of the model, except from the top surface.

4.4.5 Prescribed Normal Mesh Velocity

The Prescribed Normal Mesh Velocity node specifies the velocity of the boundary in the current normal direction. In this study, Prescribed Normal Mesh Velocity is applied on the top surface of the model and expresses the velocity that the nodes with temperature over 3315K “evaporate”. In this study, it is considered that evaporation velocity for temperatures over 6000K is constant and equals to the evaporation velocity of 6000K. Specifically,

$$\mathbf{v}_n = \begin{cases} -V_{evap}(T, \beta_R), & 0 < T(K) \leq 6000 \\ -V_{evap}(6000K, \beta_R), & T(K) > 6000 \end{cases} \quad (55)$$

Where:

$\mathbf{v}_n \left(\frac{m}{s}\right)$ is the prescribed normal mesh velocity.

“-“ in front of V_{evap} function means that the “evaporated” nodes “disappear” from the mesh.

$V_{evap}(T, \beta_R) \left(\frac{m}{s}\right)$ is the velocity that the nodes with temperature over 3315K “evaporate” and is calculated according to [39], as follows:

Total mass flux from the metal surface due to the evaporation can be expressed as:

$$\begin{cases} V_{evap}(T, \beta_R) = \frac{1}{\rho(T)} (1 - \beta_R) \left(\frac{m}{2\pi k_B T}\right)^{\frac{1}{2}} p_{sat}(T) \\ p_{sat}(T) = p_0 e^{\left(\frac{mL_v}{k_B T_v} \left(1 - \frac{T_v}{T}\right)\right)} \quad (\text{saturated vapor pressure at a temperature } T, \text{ expressed with the Clausius - Clapeyron's relation}) \end{cases} \quad (56)$$

Where:

p_0 (Pa) is the ambient pressure. In this study, $p_0 = 1.01 \cdot 10^5$ Pa.

$k_B = 1.380649 \cdot 10^{-23} \frac{J}{K}$ is the Boltzmann constant.

T_v (K) is the boiling point. In this study, $T_v = 3315K$.

β_R is the ratio of the atoms that recombine to the surface to the atoms that evaporate from the melt surface.

$m \left(\frac{kg}{atom} \right)$ is the mass per atom of metal. It is calculated by the following procedure:

- The atomic mass numbers of Ti, Al and V are found. Specifically, $A_{Ti} = 47.867 \frac{g}{mol}$, $A_{Al} = 26.981539 \frac{g}{mol}$, $A_V = 50.9415 \frac{g}{mol}$.
- The weighted average atomic mass number of Ti6Al4V is calculated. Specifically, $A_{Ti6Al4V} = \frac{6A_{Ti} + 4A_{Al} + A_V}{11} = 40.55178691 \frac{g}{mol}$.
- The mass per atom of Ti6Al4V is calculated as following:

$$m = \frac{A_{Ti6Al4V}}{N_A} \quad (46)$$

Where $N_A = 6.0221407 \cdot 10^{23} \frac{atoms}{mol}$ is the Avogadro number.

Eventually, $m = 6.733782641 \cdot 10^{-23} \frac{g}{atom}$.

$L_v \left(\frac{J}{kg} \right)$ is the Ti6Al4V latent heat of vaporization. In this study, $L_v \left(in \frac{kJ}{mol} \right) = \max\{L_v^{Ti}, L_v^{Al}, L_v^V\} = \max\left\{421 \frac{kJ}{mol}, 293.4 \frac{kJ}{mol}, 0.452 \frac{kJ}{mol}\right\} = 421 \frac{kJ}{mol}$. Moreover, Ti6Al4V molar mass is: $M_{Ti6Al4V} = 6 \cdot A_{Ti} + 4 \cdot A_{Al} + A_V = 446.069656 \frac{g}{mol}$. So, $L_v = \frac{421 \frac{kJ}{mol}}{446.069656 \frac{g}{mol}} = 10.38178665 \frac{kJ}{g} = 10.38178665 \frac{J}{kg}$.

For $T=3330, 3340, \dots, 5000K$ and $\beta_R=0.1, 0.2, \dots, 1$, the $V_{evap}(T, \beta_R)$ values are calculated into the following Table 4.7:

Table 4.7 Calculation of $V_{evap}(T, \beta_R)$ for different temperatures and β_R .

Temperature (K)	β_R									
	0.1	0.2	0.3	0.4	0.5	0.6	0.7	0.8	0.9	
3330	0.01526	0.01356	0.01187	0.01017	0.00848	0.00678	0.00509	0.00339	0.0017	0
3340	0.01595	0.01417	0.0124	0.01063	0.00886	0.00709	0.00532	0.00354	0.00177	0
3350	0.01666	0.01481	0.01296	0.01111	0.00926	0.0074	0.00555	0.0037	0.00185	0
3360	0.0174	0.01547	0.01353	0.0116	0.00967	0.00773	0.0058	0.00387	0.00193	0
3370	0.01817	0.01615	0.01413	0.01211	0.01009	0.00807	0.00606	0.00404	0.00202	0
3380	0.01897	0.01686	0.01475	0.01264	0.01054	0.00843	0.00632	0.00421	0.00211	0
3390	0.01979	0.01759	0.0154	0.0132	0.011	0.0088	0.00666	0.0044	0.0022	0
3400	0.02065	0.01836	0.01606	0.01377	0.01147	0.00918	0.00688	0.00459	0.00229	0
3410	0.02154	0.01915	0.01676	0.01436	0.01197	0.00957	0.00718	0.00479	0.00239	0
3420	0.02247	0.01997	0.01747	0.01498	0.01248	0.00998	0.00749	0.00499	0.0025	0
3430	0.02342	0.02082	0.01822	0.01551	0.01301	0.01041	0.00781	0.0052	0.0026	0
3440	0.02441	0.0217	0.01899	0.01628	0.01356	0.01085	0.00814	0.00543	0.00271	0
3450	0.02544	0.02261	0.01979	0.01696	0.01413	0.01131	0.00848	0.00565	0.00283	0
3460	0.02651	0.02356	0.02062	0.01767	0.01473	0.01178	0.00884	0.00589	0.00295	0
3470	0.02761	0.02454	0.02147	0.0184	0.01534	0.01227	0.0092	0.00613	0.00307	0
3480	0.02875	0.02555	0.02236	0.01917	0.01597	0.01278	0.00958	0.00639	0.00319	0
3490	0.02993	0.0266	0.02328	0.01995	0.01663	0.01333	0.00998	0.00665	0.00333	0
3500	0.03115	0.02769	0.02423	0.02077	0.01731	0.01384	0.01038	0.00692	0.00346	0
3510	0.03242	0.02881	0.02521	0.02161	0.01801	0.01441	0.01081	0.0072	0.0036	0
3520	0.03372	0.02998	0.02623	0.02248	0.01874	0.01499	0.01124	0.00749	0.00375	0
3530	0.03508	0.03118	0.02728	0.02338	0.01949	0.01559	0.01169	0.00779	0.0039	0
3540	0.03647	0.03242	0.02837	0.02432	0.02026	0.01621	0.01216	0.00811	0.00405	0
3550	0.03792	0.03371	0.02949	0.02528	0.02107	0.01685	0.01264	0.00843	0.00421	0
3560	0.03942	0.03504	0.03066	0.02628	0.0219	0.01752	0.01314	0.00876	0.00438	0
3570	0.04096	0.03641	0.03186	0.02731	0.02276	0.0182	0.01365	0.0091	0.00455	0
3580	0.04256	0.03783	0.0331	0.02837	0.02364	0.01891	0.01419	0.00946	0.00473	0
3590	0.0442	0.03929	0.03438	0.02947	0.02456	0.01965	0.01473	0.00982	0.00491	0
3600	0.04591	0.04081	0.03571	0.0306	0.0255	0.0204	0.0153	0.0102	0.0051	0
3610	0.04766	0.04237	0.03707	0.03178	0.02648	0.02118	0.01589	0.01059	0.0053	0
3620	0.04948	0.04398	0.03848	0.03299	0.02749	0.02199	0.01649	0.011	0.0055	0
3630	0.05135	0.04565	0.03994	0.03423	0.02853	0.02282	0.01712	0.01141	0.00571	0
3640	0.05328	0.04736	0.04144	0.03552	0.0296	0.02368	0.01776	0.01184	0.00592	0
3650	0.05528	0.04914	0.04299	0.03685	0.03071	0.02457	0.01843	0.01228	0.00614	0
3660	0.05734	0.05097	0.04459	0.03822	0.03185	0.02548	0.01911	0.01274	0.00637	0
3670	0.05946	0.05285	0.04624	0.03964	0.03303	0.02643	0.01982	0.01321	0.00661	0
3680	0.06164	0.0548	0.04795	0.0411	0.03425	0.0274	0.02055	0.0137	0.00685	0
3690	0.0639	0.0568	0.0497	0.0426	0.0355	0.0284	0.0213	0.0142	0.0071	0
3700	0.06622	0.05887	0.05151	0.04415	0.03679	0.02943	0.02207	0.01472	0.00736	0
3710	0.06862	0.061	0.05337	0.04575	0.03812	0.0305	0.02287	0.01525	0.00762	0
3720	0.07109	0.06319	0.05529	0.04739	0.03949	0.0316	0.0237	0.0158	0.0079	0
3730	0.07363	0.06545	0.05727	0.04909	0.04091	0.03273	0.02454	0.01636	0.00818	0
3740	0.07625	0.06778	0.05931	0.05083	0.04236	0.03389	0.02542	0.01694	0.00847	0
3750	0.07895	0.07018	0.06141	0.05263	0.04386	0.03509	0.02632	0.01754	0.00877	0
3760	0.08173	0.07265	0.06357	0.05448	0.0454	0.03632	0.02724	0.01816	0.00908	0
3770	0.08459	0.07519	0.06579	0.05639	0.04699	0.03759	0.0282	0.0188	0.0094	0
3780	0.08753	0.0778	0.06808	0.05835	0.04863	0.0389	0.02918	0.01945	0.00973	0

3790	0.09056	0.0805	0.07044	0.06037	0.05031	0.04025	0.03019	0.02012	0.01006	0
3800	0.09368	0.08327	0.07286	0.06245	0.05204	0.04163	0.03123	0.02082	0.01041	0
3810	0.09688	0.08612	0.07535	0.06459	0.05382	0.04306	0.03229	0.02153	0.01076	0
3820	0.10018	0.08905	0.07792	0.06679	0.05566	0.04453	0.03339	0.02226	0.01113	0
3830	0.10357	0.09207	0.08056	0.06905	0.05754	0.04603	0.03452	0.02302	0.01151	0
3840	0.10706	0.09517	0.08327	0.07138	0.05948	0.04758	0.03569	0.02379	0.0119	0
3850	0.11065	0.09835	0.08606	0.07377	0.06147	0.04918	0.03688	0.02459	0.01229	0
3860	0.11434	0.10163	0.08893	0.07622	0.06352	0.05082	0.03811	0.02541	0.0127	0
3870	0.11813	0.105	0.09188	0.07875	0.06563	0.0525	0.03938	0.02625	0.01313	0
3880	0.12202	0.10846	0.0949	0.08135	0.06779	0.05423	0.04067	0.02712	0.01356	0
3890	0.12602	0.11202	0.09802	0.08401	0.07001	0.05601	0.04201	0.028	0.014	0
3900	0.13013	0.11567	0.10121	0.08675	0.07229	0.05784	0.04338	0.02892	0.01446	0
3910	0.13435	0.11942	0.10449	0.08957	0.07464	0.05971	0.04478	0.02986	0.01493	0
3920	0.13869	0.12328	0.10787	0.09246	0.07705	0.06164	0.04623	0.03082	0.01541	0
3930	0.14314	0.12723	0.11133	0.09542	0.07952	0.06362	0.04771	0.03181	0.0159	0
3940	0.14771	0.1313	0.11488	0.09847	0.08206	0.06565	0.04924	0.03282	0.01641	0
3950	0.1524	0.13547	0.11853	0.1016	0.08467	0.06773	0.0508	0.03387	0.01693	0
3960	0.15721	0.13975	0.12228	0.10481	0.08734	0.06987	0.0524	0.03494	0.01747	0
3970	0.16216	0.14414	0.12612	0.1081	0.09009	0.07207	0.05405	0.03603	0.01802	0
3980	0.16723	0.14865	0.13006	0.11148	0.0929	0.07432	0.05574	0.03716	0.01858	0
3990	0.17243	0.15327	0.13411	0.11495	0.09579	0.07663	0.05748	0.03832	0.01916	0
4000	0.17776	0.15801	0.13826	0.11851	0.09876	0.07901	0.05925	0.0395	0.01975	0
4010	0.18324	0.16288	0.14252	0.12216	0.1018	0.08144	0.06108	0.04072	0.02036	0
4020	0.18885	0.16786	0.14688	0.1259	0.10491	0.08393	0.06295	0.04197	0.02098	0
4030	0.1946	0.17298	0.15136	0.12973	0.10811	0.08649	0.06487	0.04324	0.02162	0
4040	0.2005	0.17822	0.15594	0.13367	0.11139	0.08911	0.06683	0.04456	0.02228	0
4050	0.20655	0.1836	0.16065	0.1377	0.11475	0.0918	0.06885	0.0459	0.02295	0
4060	0.21274	0.1891	0.16547	0.14183	0.11819	0.09455	0.07091	0.04738	0.02364	0
4070	0.21909	0.19475	0.17041	0.14606	0.12172	0.09737	0.07303	0.04889	0.02434	0
4080	0.2256	0.20053	0.17547	0.1504	0.12533	0.10027	0.0752	0.05013	0.02507	0
4090	0.23226	0.20646	0.18065	0.15484	0.12904	0.10323	0.07742	0.05161	0.02581	0
4100	0.23909	0.21253	0.18596	0.1594	0.13283	0.10626	0.0797	0.05313	0.02657	0
4110	0.24609	0.21874	0.1914	0.16406	0.13671	0.10937	0.08203	0.05469	0.02734	0
4120	0.25325	0.22511	0.19697	0.16883	0.14069	0.11255	0.08442	0.05628	0.02814	0
4130	0.26058	0.23163	0.20267	0.17372	0.14477	0.11581	0.08686	0.05791	0.02895	0
4140	0.26809	0.2383	0.20851	0.17873	0.14894	0.11915	0.08936	0.05958	0.02979	0
4150	0.27578	0.24513	0.21449	0.18385	0.15321	0.12257	0.09193	0.06128	0.03064	0
4160	0.28364	0.25213	0.22061	0.18909	0.15758	0.12606	0.09455	0.06303	0.03152	0
4170	0.29169	0.25928	0.22687	0.19446	0.16205	0.12964	0.09723	0.06482	0.03241	0
4180	0.29993	0.26661	0.23328	0.19995	0.16663	0.1333	0.09998	0.06665	0.03333	0
4190	0.30836	0.2741	0.23984	0.20557	0.17131	0.13705	0.10279	0.06852	0.03426	0
4200	0.31698	0.28176	0.24654	0.21132	0.1761	0.14088	0.10566	0.07044	0.03522	0
4210	0.3258	0.2896	0.2534	0.2172	0.181	0.14448	0.1086	0.0724	0.0362	0
4220	0.33483	0.29762	0.26042	0.2232	0.18601	0.14811	0.11161	0.07441	0.0372	0
4230	0.34405	0.30582	0.2676	0.22937	0.19114	0.15291	0.11468	0.07646	0.03823	0
4240	0.35349	0.31421	0.27493	0.2356	0.19638	0.1571	0.11783	0.07855	0.03928	0
4250	0.36313	0.32278	0.28244	0.24209	0.20174	0.16139	0.12104	0.0807	0.04035	0
4260	0.37299	0.33155	0.29011	0.24866	0.20722	0.16577	0.12433	0.08289	0.04144	0
4270	0.38307	0.34051	0.29794	0.25538	0.21282	0.17025	0.12769	0.08513	0.04256	0
4280	0.39337	0.34966	0.30596	0.2						

With interpolation to the data above and for $T > 3315K$,

$$V_{evap}(T, \beta_R) = -27.91 + 0.02325T + 27.91\beta_R - 6.501 \cdot 10^{-6}T^2 - 0.02325T\beta_R + 7.696 \cdot 10^{-13}\beta_R^2 + 6.109 \cdot 10^{-10}T^3 + 6.501 \cdot 10^{-6}T^2\beta_R - 2.987 \cdot 10^{-16}T\beta_R^2 - 7.238 \cdot 10^{-14}\beta_R^3 - 6.109 \cdot 10^{-10}T^3\beta_R + 3.05 \cdot 10^{-20}T^2\beta_R^2 + 6.115 \cdot 10^{-18}T\beta_R^3 + 5.808 \cdot 10^{-15}\beta_R^4$$

So, eventually,

$$V_{evap}(T, \beta_R) = \begin{cases} 0, & T < 3315K \text{ or } \beta_R = 1 \\ -27.91 + 0.02325T + 27.91\beta_R - 6.501 \cdot 10^{-6}T^2 - 0.02325T\beta_R + 7.696 \cdot 10^{-13}\beta_R^2 + 6.109 \cdot 10^{-10}T^3 + 6.501 \cdot 10^{-6}T^2\beta_R - 2.987 \cdot 10^{-16}T\beta_R^2 - 7.238 \cdot 10^{-14}\beta_R^3 - 6.109 \cdot 10^{-10}T^3\beta_R + 3.05 \cdot 10^{-20}T^2\beta_R^2 + 6.115 \cdot 10^{-18}T\beta_R^3 + 5.808 \cdot 10^{-15}\beta_R^4, & T \geq 3315K \text{ and } \beta_R \neq 1 \end{cases} \quad (57)$$

The diagram that describes the above function is given below (Diagram 4.21):

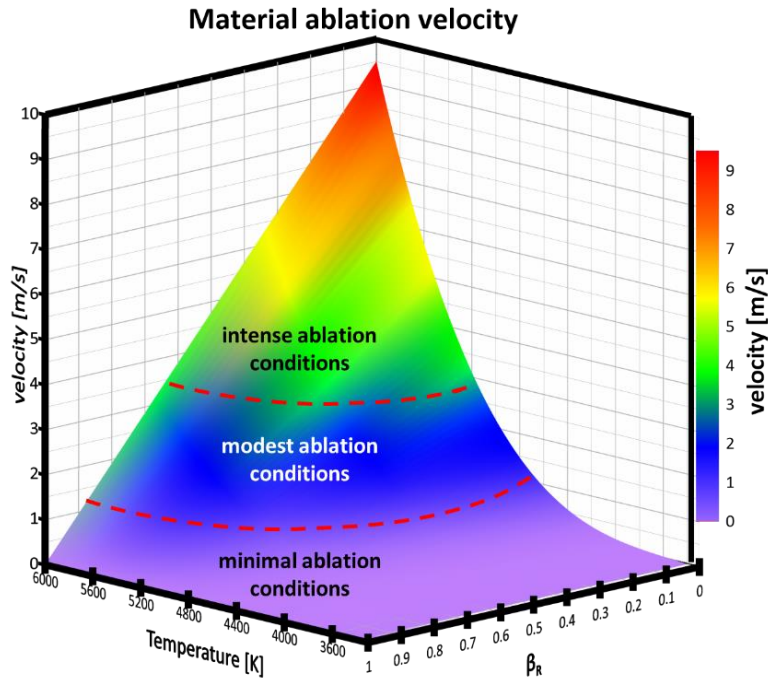


Diagram 4.21 V_{evap} as function of temperature and β_R .

The velocity of each mesh element is visualized in Fig. 4.8:

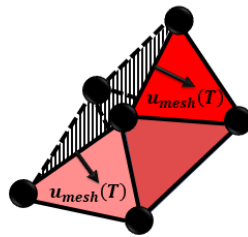


Fig. 4.8 Visual representation of mesh element velocity.

4.5 Numerical Computation:

4.5.1 Mesh

The Finite-Element-Method (FEM) has become the most popular mesh-based numerical method for the calculation of structural and thermal models and therefore also for physical phenomena as residual stresses and distortions during the AM process. The main idea behind the FEM is that a complex geometry can be discretized in a finite number of much simpler objects, the elements. Those elements form a mesh representing the actual geometry reduced to a finite number of unknowns. The finite number of unknowns leads to a finite number of equations to be solved, either in an explicit or implicit way. Explicit methods can run into numerical instability, if the time step is too large. However implicit solutions might fail to converge for heavily non-linear calculations.

Simulations of the additive manufacturing process are split into two separate systems. A thermal and a mechanical simulation. These simulations can run simultaneously as coupled calculation or in sequence as uncoupled calculations. Coupled simulations are more accurate, but at the same time more computationally expensive. As input for both systems material properties, the parts geometry, which later has to be meshed, as well as initial and boundary conditions have to be specified. At the moment there are two different meshing options:

4.5.1.1 Cartesian meshing

Cartesian or voxel meshing is the most commonly used mesh type for current additive manufacturing simulations. The mesh consists of cubes (voxels) with a, for the whole model consistent, specified size. This leads to a layered mesh, which is necessary to mimic the part generation in layers like in powder bed fusion processes using element birth and death. Due to the voxel elements with identical edge length on each side of the cube, the representation of the geometry is only an approximation. Depending on the size of the elements, tiny features are either not expressed in detail, leading to an inaccurate simulation, or the computational cost of the simulation model highly increases. In order to cope with the inaccurate representation of the geometry using hexahedron elements, a so-called projection factor is used. This factor ranges from zero to one and describes the level of representation with zero as no adaption of the elements. With an increasing value of the factor, the elements get more and more distorted to fit the actual geometry of the part. The resulting skewness and uneven aspect ratio lead to a worse element quality. Nevertheless, more accurate simulation results are possible using this meshing method. Cartesian meshes can use linear, quadratic or even higher polynomial approaches. The hexahedron shaped elements then have eight (linear) or twenty (quadratic) nodes per element.

4.5.1.2 Tetrahedral meshing

Its aim is to simplify the representation of the small detailed geometry of AM parts without increasing the level of complexity of the model. The tetrahedral shape of the elements allows the meshing algorithm to achieve a better fitting mesh with only small element distortions. Despite the higher number of elements in the simulation model using this meshing method, accurate results can be achieved in less time than with Cartesian meshes.

The tetrahedron shaped elements of a tetrahedral mesh commonly have five (linear approach) or ten (quadratic approach) nodes per element. As there are less nodes per element than with the hexahedron shaped ones, more elements are required to reach the same result accuracy [40].

The following parameters control the tetrahedral mesh element size:

- Maximum element size: This parameter limits the allowed element size.
- Minimum element size: This parameter is used to specify the minimum allowed element size. This value is used to prevent the generation of many elements around small curved parts of the geometry. If some details of the geometry are smaller than the minimum element size, the mesh will contain elements of a smaller size in order to resolve the geometry.
- Maximum element growth rate: This parameter is used to determine the maximum rate at which the element size can grow from a region with small elements to a region with larger elements. The value must be greater or equal to one. For example, with a maximum element growth rate of 1.5, the element size can grow by at most 50% (approximately) from one element to another.
- Curvature factor: This parameter is used to determine the size of boundary elements compared to the curvature of the geometric boundary (that is, the ratio between the boundary element size and the curvature radius). The curvature radius multiplied by the curvature factor, which must be a positive scalar, gives the maximum allowed element size along the boundary. A smaller curvature factor gives a finer mesh along curved boundaries.
- Resolution of narrow regions: This parameter is used to control the number of layers of elements that are created in narrow regions (approximately). The value must be a non-negative scalar. A higher value gives a finer mesh in narrow regions. If the value of this parameter is less than one, the mesh generator might create elements that are anisotropic in size in narrow regions.

In this study, a tetrahedral mesh is used. In order to reduce computational time this mesh consists of two sub-meshes, one finer (at the top surface of the model) and one coarser (at the rest model). Specifically, the element sizes of each sub-mesh are given below:

- Finer mesh:
 - Maximum element size: 0.025mm
 - Minimum element size: 0.015mm
 - Maximum element growth rate: 1.3
 - Curvature factor: 0.9
 - Resolution of narrow regions: 0.4
- Coarser mesh:
 - Maximum element size: 0.0905mm
 - Minimum element size: 0.0192mm
 - Maximum element growth rate: 1.4
 - Curvature factor: 1

- Resolution of narrow regions: 0.3

Visually, the mesh used in this study is given in the following Fig. 4.9:

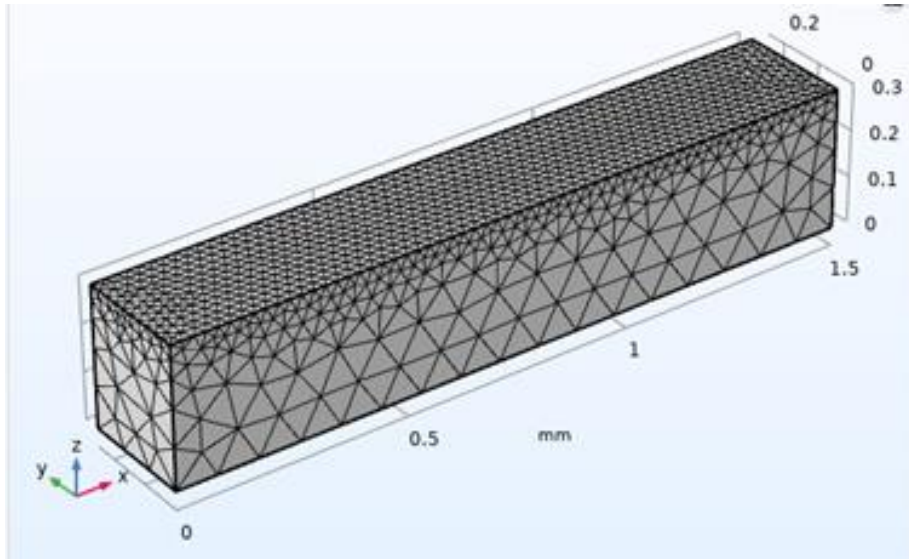


Fig. 4.9 The mesh used in the simulation.

The interaction of the mesh with the laser beam is visualized in Fig. 4.10:

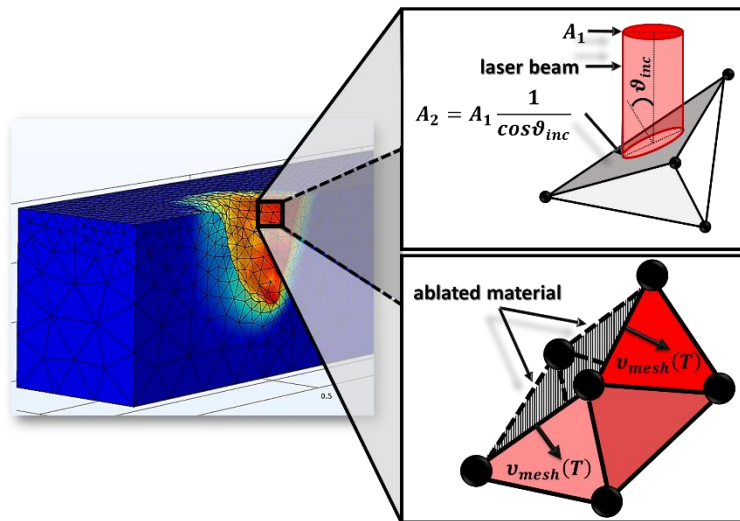


Fig. 4.10 Visual representation of the laser beam interaction with the mesh elements.

4.5.2 Mesh Refinement

In the keyhole mode, there is a large mesh deformation, which leads some elements to fall below the minimum element size value, resulting in singularity or inverted element errors. In order to handle these errors, a mesh refinement occurs in this study. Mesh refinement at the deformed area can not only bring out the geometrical characteristics of the deformation site but also perform a highly realistic simulation of the deformation process [41].

4.5.3 Study

The simulation occurs for a length appropriate to reach the steady state. The maximum length is 1mm, starting from 0.25mm and ending to 1.25mm (according the x-coordinate) of the 1mm or 1.5mm specimen.

To sum up, the full model is visualized in Fig. 4.11:

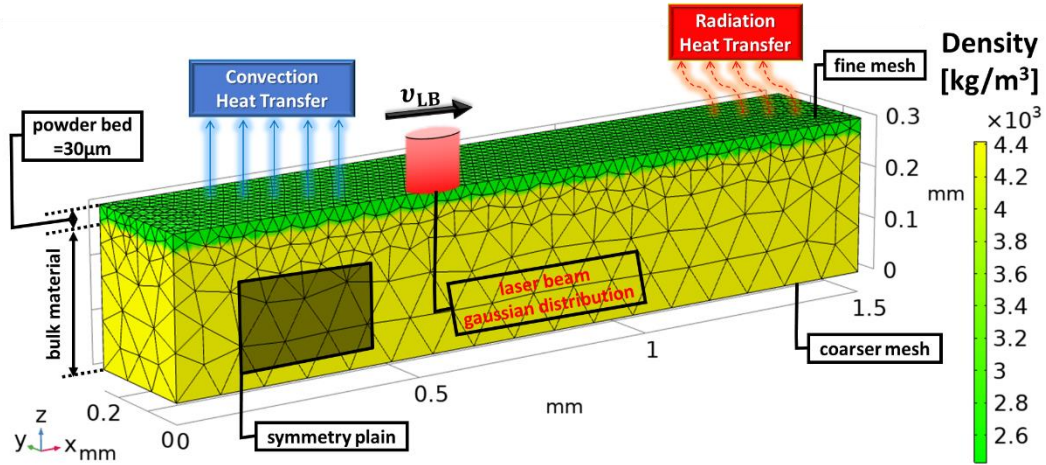


Fig. 4.11 Visual representation of the full model used in the simulation.

4.5.4 Visual Representation

In the end of the simulation and in order to present the solution of all time steps at once, the following mathematical equation is applied:

$$T_{max} = nojac \begin{cases} T, & T > T_{max} \\ T_{max}, & T \leq T_{max} \end{cases} \quad (58)$$

Where T_{max} (K) is the maximum temperature of each element.

This equation means that if the temperature at the previous time step is greater than T_{max} , set T_{max} equal to temperature. Otherwise, leave T_{max} unchanged. The nojac() operator is needed, in order to prevent the contribution of this equation to the Jacobian (the system) matrix.

Over this mathematical equation, the following filter: $T > 1923.15K$ is applied, so that only the melting pool of all time steps is shown in the visual representation of the simulation's results. Finally, these results are mirrored by the $y=0$ plane, so that the whole melting pool is appeared.

4.5.5 Results Validation

The results of this simulation were validated with the experimental results estimated by Dilip J. et al. [42].

5. Results and Discussion

5.1 Basic physical fundamental mechanisms used for the analysis of the results

Some very useful theoretical and experimental fundamental mechanisms are given below, in order to help with the understanding of the results analysis:

5.1.1 Conduction mode vs transition mode vs keyhole mode

Depending on processing conditions, SLM is known to have two operational regimes: conduction mode and keyhole mode. Heat conduction is the dominant heat transfer mechanism for conduction mode melting, whereas heat convection is the dominant heat transfer mechanism for keyhole mode melting. In addition, there exists a transition mode, which lies between the conduction and keyhole mode, wherein the dominance of conduction or convection depends upon the processing conditions. When the power density is lower than a certain threshold value, heat conduction is the dominant heat transfer mechanism, particularly for determining the depth of the melting pool created; this regime is called the conduction mode of laser melting. The cross section of melting pools created in conduction mode is generally semicircular (i.e. the melt pool depth is lesser than or equal to its half-width). The vaporization of metals in conduction mode melting is considered to be negligible. In contrast, keyhole mode melting is observed when the energy density exceeds a threshold value such that a deep vapour cavity forms within the molten metal due to intense localized heating and vaporization of alloying element. In keyhole mode of laser melting, the depth of the molten pool is controlled by the recoil momentum pressure (also known as recoil pressure) generated by the vaporization of the melt pool materials. Convective heat transfer (due to thermo-capillary convection, also known as Bénard–Marangoni convection) is the dominant mode of heat transfer within the melting pool. The top region of a keyhole mode melting pool resembles an hourglass and is wide due to the radially outward Marangoni flow, whereas the bottom of the melt pool is narrow and resembles the shape of a keyhole. The melt pool depth in keyhole mode laser melting is typically greater than the half-width of the melt pool defined at the top of a given melting pool [43].

5.1.2 Definition of melting pool steady-state

In conduction mode, where balling and discontinuities may occur, the steady state is more time or track length dependent. Specifically, for the 50W-1200mm/s, a track length of 1.5mm was used, which was sufficient for the observation of all the phenomena and characteristics of the melting pool.

On the other hand, the keyhole melting pool steady state is considered to be the combination of the evaporation steady state and the heat transfer steady state. Usually, the evaporation steady state comes first and is defined by the formation of a horizontal “evaporation” line (Fig. 5.1).

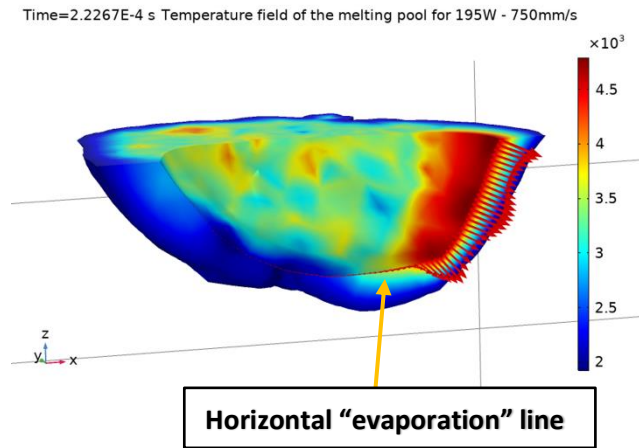


Fig. 5.1 The keyhole evaporation steady state.

The heat transfer steady state is defined by the formation of a "tail" behind the laser source (Fig. 5.2).

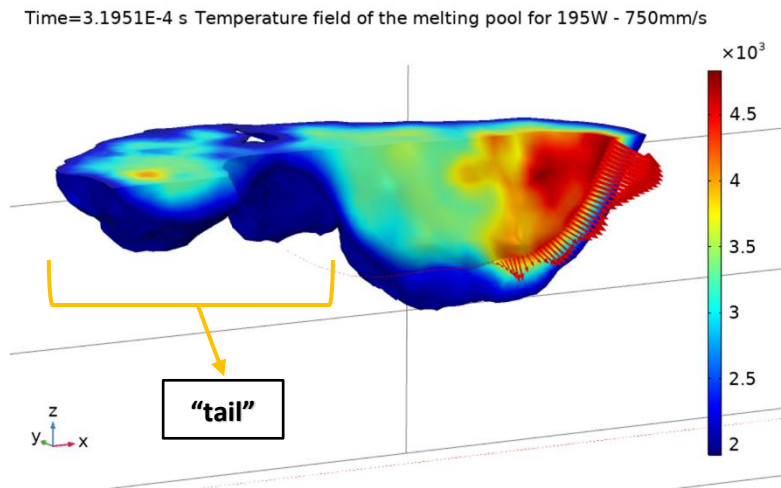


Fig. 5.2 The keyhole heat transfer steady state.

5.1.3 The β_R determination

In this study, the trial-and-error method used to determine the β_R coefficient, so for each set of processing parameters, five to six simulations, approximately, have been run, in order to find out the correct value, which leads to results that resemble the experimental ones. Moreover, the accuracy of this value is limited to the first decimal, as the target of this study is to propose a fast way to predict the width and depth of the melting pool, without an extensive need for calibration.

5.2 Simulation results and discussion

The results of this simulation were validated with the experimental results estimated by Dilip J. et al. [42].

Table 5.1 Simulation results

Laser power (W)	Scanning speed (mm/s)	VED (J/mm ³)	β_R	Depth error (%)	Width error (%)
50	1000	13.88	1	-10%	8.47%
195	750	86.66	0.55	-15%	-16%
195	500	130	0	-1.7%	-14.6%

In Table 5.1, depth error and width error have been calculated according to the following formulas:

$$\text{Depth error (\%)} = \frac{\text{Experimental depth} - \text{Simulation depth}}{\text{Experimental depth}} \quad (59)$$

$$\text{Width error (\%)} = \frac{\text{Experimental width} - \text{Simulation width}}{\text{Experimental width}} \quad (60)$$

From Table 5.1, it can be observed that the simulation results are in a good agreement with the experimental data, as the error in all the cases is below 16%. These errors occur, mainly, because of the consideration that the absorbance coefficient is constant and equals to 0.77. In reality, as discussed in section 4.3.5.2, the absorbance coefficient is temperature dependent and is calculated via the Fresnel equations and the Drude theory [28]. However, Fresnel equations and Drude theory, insert nonlinearity, leading to a complex model with high computational cost and time. For this reason, the temperature dependence of the absorbance coefficient, in this study, is ignored. Secondly, another reason which may lead to the errors is the difference between the theoretical material properties, given in [29], [31] and the real properties of the material used in the experiment.

Another very important observation from Table 5.1 is the relation between VED and β_R (see Diagram 5.1, Diagram 5.2). Specifically, as the VED increases, the β_R decreases and vice versa. This phenomenon can be explained according to the ablation theory. When VED increases, which means that the laser power increases and/or the scanning speed decreases, a bigger area of the model reaches or exceeds the Ti6Al4V evaporation temperature (3315K), so there is a bigger mass ablation. Bigger mass ablation means that less atoms (which were evaporated) recombine to the surface of the model. This low atom recombination is modeled in the simulation as a low β_R .

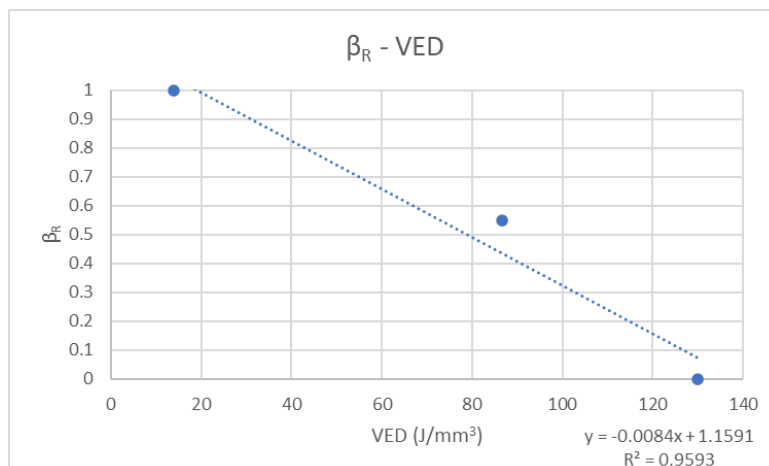


Diagram 5.1 Linear relation between β_R and VED.

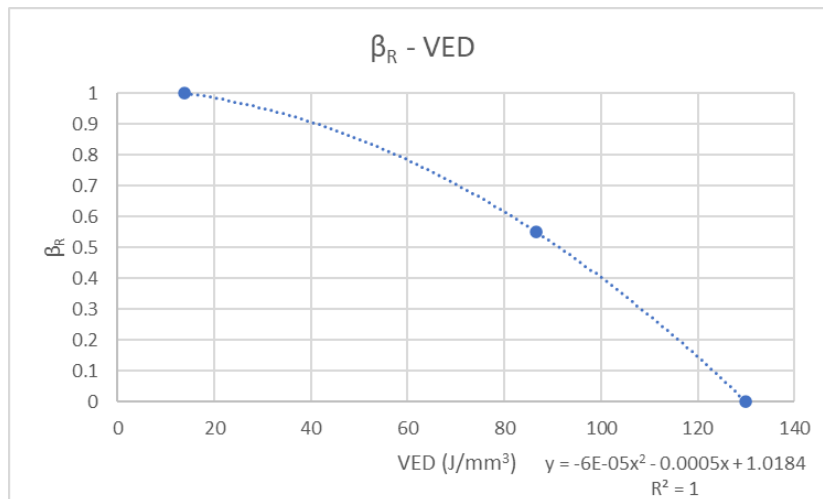


Diagram 5.2 2nd-polynomial relation between β_R and VED.

The VED and β_R values are an indication that a polynomial relation between VED and β_R could exist. Linear (Diagram 5.1) and 2nd-polynomial (Diagram 5.2) relations are proposed above. However, the only three VED and β_R values are not enough to give an accurate tendency line, so further investigation is required to ensure which specific relation exists.

5.3 Comparison between simulation and experimental results

In Fig. 5.3, a direct comparison between experimental and simulation results occurs. It is observed that all the simulation results are in a good agreement with the experimental data, as they all have a less than 16% error.

The 50W-1200mm/s represents a conduction mode simulation, whereas the 195W-750mm/s and the 195W-500mm/s represent the keyhole mode.

In conduction mode, the cross section of the melting pool is generally semicircular. The vaporization of metals in conduction mode melting is considered to be negligible. In the specific case of 50W-1200mm/s, the melting is improper, because balling and discontinuities appear and no bonding with the substrate exists.

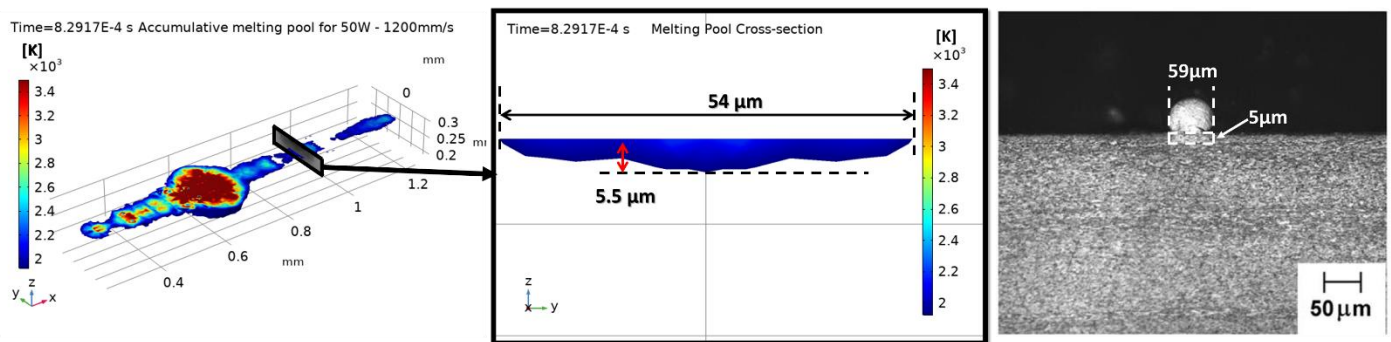
Balling is a phenomenon where the melted track shrinks and breaks up into a row of spheres to reduce the surface energy by the surface tension if the melted material does not wet the underlying substrate. The balling effect can lead to high surface roughness and porosity in the as-built parts, and it might even jeopardize the powder-laying process if the size of the balls is large enough to obstruct the movement of the paving roller. Balling, in this simulation, is attributed to splashing of the melting pool as a result of a high melting pool surface temperature and to lack of contact between the melted powder and the substrate because of insufficient melting of substrate [42].

The balling effect could happen for two main reasons. One is the formation of the balls due to inadequate laser energy input with little liquid content. And the other due to melting pool splashes induced by high scanning speed. Consequently, the laser power and scanning speed have a direct influence on balling effect [37].

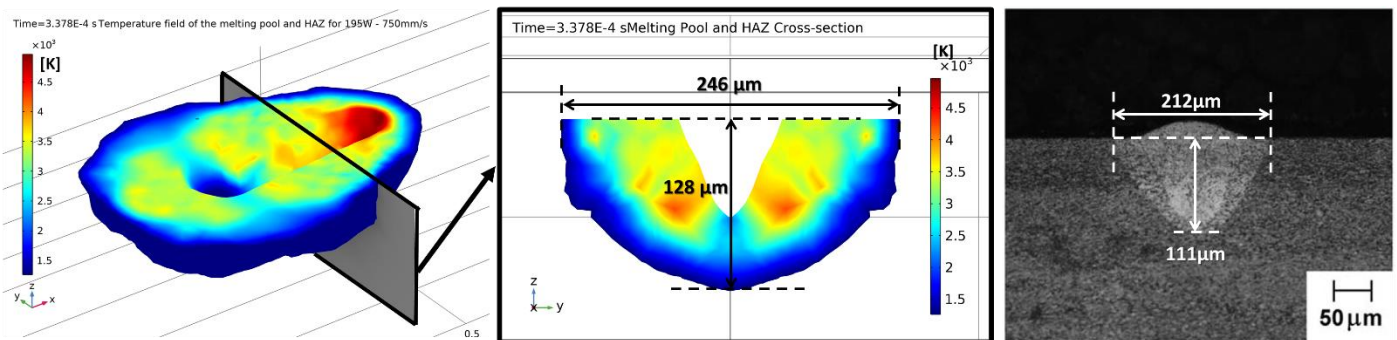
It has been reported that higher scanning speed leads to an increasing length to diameter ratio in a melting pool. Such a melting pool with length to diameter ratio greater than π will cause balling effect. The balling effect can be characterized by the break-up of the melting pool into balls, which degrades surface integrity of the final components. Therefore, to achieve the optimal surface integrity, the range of the optimal scanning speed is limited by the balling effect. It has also been reported that a higher laser power can expand the range for the optimal speed [44].

In Fig. 5.3, balling appears (in both experimental and simulation results) spherical in shape and bulging upwards which is a result of the aforementioned mechanism.

50W – 1200mm/s (VED=13.88 J/mm³) and recombination factor $\beta_R=1$



195W – 750mm/s (VED= 86.66 J/mm³) and recombination factor $\beta_R=0.55$



195W – 500mm/s (VED= 130 J/mm³) and recombination factor $\beta_R=0$

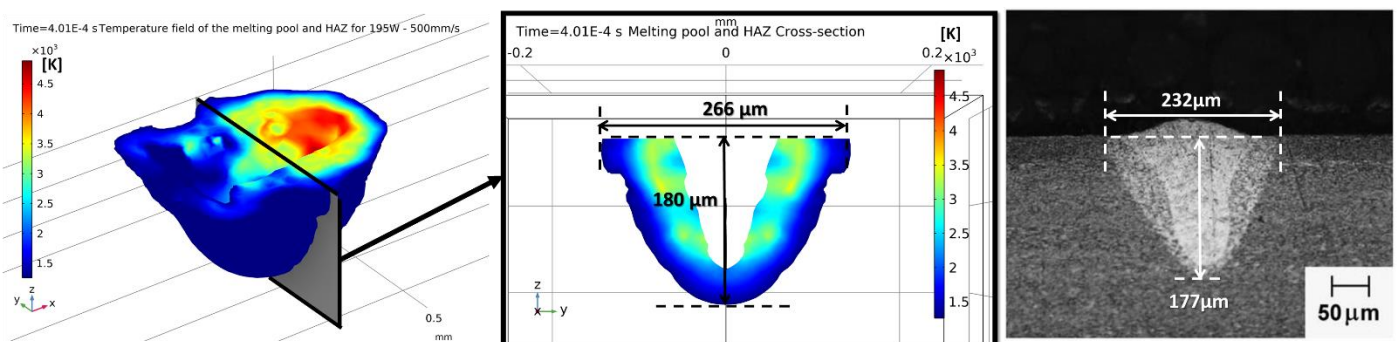


Fig. 5.3 Comparison between simulations and experiments.

When such a set of parameters is applied to fabricate the bulk parts, it may result in a significant amount of porosity.

Moreover, the discontinuities (Fig. 5.3, experimental and simulation results of 50W-1200mm/s) are evident that the laser power is insufficient to melt the powder since the laser scans at a faster rate, hence lower energy input [45].

Furthermore, as observed in Fig. 5.3 for 50W-1200mm/s, the depth of the melting pool is below $6\mu\text{m}$ for the experimental and the simulation results, which is lower than the powder height ($30\mu\text{m}$), so the new layer created cannot be bonded with the substrate layer.

All in all, the significance of this case study is to prove that the model used in this simulation is useful not only to predict the width and depth of the melting pool, but also to predict and the possible defects that each set of processing parameters may appear.

In keyhole mode a deep vapour cavity forms within the molten metal due to intense localized heating and vaporization of alloying element. In keyhole mode, the depth of the melting pool is controlled by the recoil pressure generated by the vaporization of the melting pool materials. The top region of a keyhole mode melting pool is wide, whereas the bottom of the melt pool is narrow creating a V-shape. The V-shape of the 195W-750mm/s and 195W-500mm/s resembles the experimental ones, accordingly, so the model proposed in this study can accurately enough predict the geometry of the keyhole.

Moreover, it can be observed that for constant laser power, the depth of the melting pool increases when the scanning speed decreases. That happens because for low scanning speeds, each region of the model is affected for more time from the laser power, so the temperature of each region goes higher, affecting and the deeper layers. This increase of the depth for low scanning speeds is also predicted by the simulation of this study.

In SLM material addition takes place due to layer-by-layer melting and solidification of a thin layer of spread powder. In this process, the laser beam also re-melts some portion of the layers beneath to ensure good bonding between the layers. The solidification of the alloy begins with the formation of a β nucleus, and the pre-existing β grains partially undergo melting and serve as heterogeneous sites for nucleation. Thus, newly formed β will grow epitaxially in the build direction or opposite to the heat extraction. In close similarity to the weld solidification, the solidifying β grains tend to orient towards the moving heat source (laser beam), resulting in a slightly tilted grain structure. Further, the β grain orientation in the deposit highly depends on the laser power, scanning strategy and scan speed applied. They define the amount of time available for the melt to solidify at any particular instance of time. The solidified high-temperature β (bcc) phase is unstable at lower temperatures and will transform to a metastable phase, martensitic α' (hcp) phase. Hence, the final resultant microstructure will have coarse columnar grains, which are highly oriented towards the build direction with martensite α' inside the grains. Due to the inherent layer-by-layer deposition method, as a new layer is being deposited a narrow region (heat affected zone) close to the melt pool boundary will reach temperatures above the transformation temperature ($995\text{ }^\circ\text{C}$), and martensite (α') transforms back to the high-temperature β phase. As the laser beam

traverses away, the high-temperature β phase, under faster cooling conditions will transform to martensite (α'). The martensite formed from re-heating of primary martensite (α') to β phase and transformed back to martensite will be from here on referred to as α' (secondary) and the heat affected regions (areas colored in blue in Fig. 5.4) result in α' (tertiary). In other words, as the build progresses, the layers will experience multiple thermal cycling effects which lead to the formation of alternate areas of martensite α' (primary), α' (secondary) and α' (tertiary) in the entire part. Diagram 5.3 illustrates the evolution of microstructure in the selective laser melted Ti6Al4V alloy. Although it is difficult to draw a clear line between the three martensites (α' (primary), α' (secondary) and α' (tertiary)) in the as-built part microstructures it is important to understand the microstructural evolution of the alloy during the SLM process. In summary, the part will have preferentially-oriented epitaxial grains with high aspect ratio, with martensite [42].

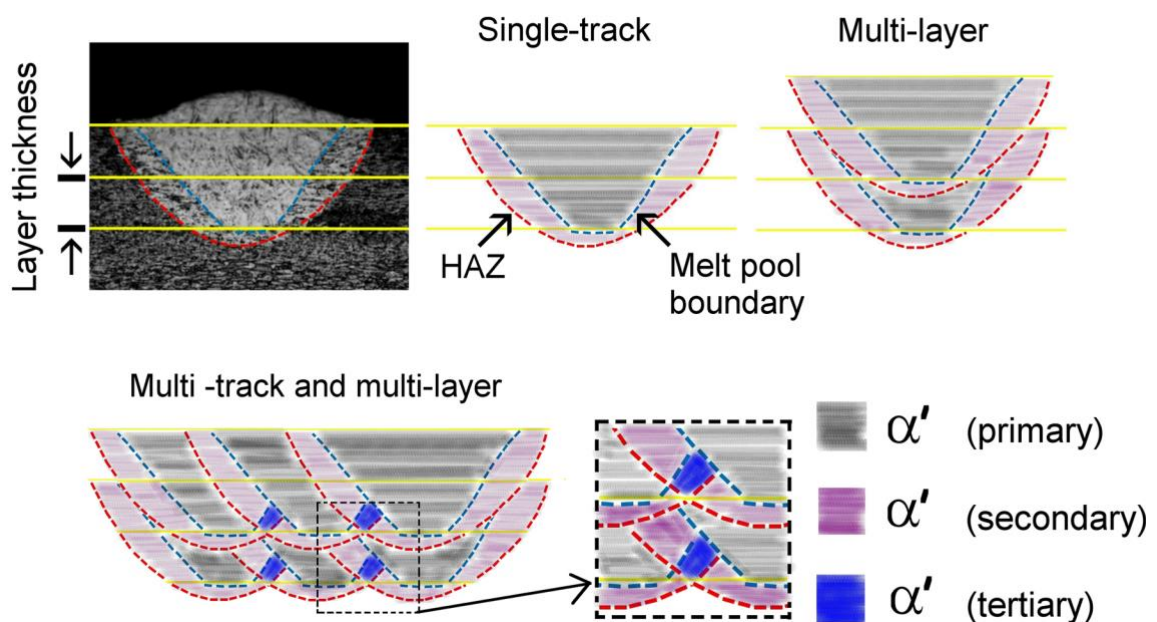


Fig. 5.4 A schematic illustration of microstructural evolution in a single-track, multi-layer, and multi-track, multi-layer Ti-6Al-4V SLM deposit

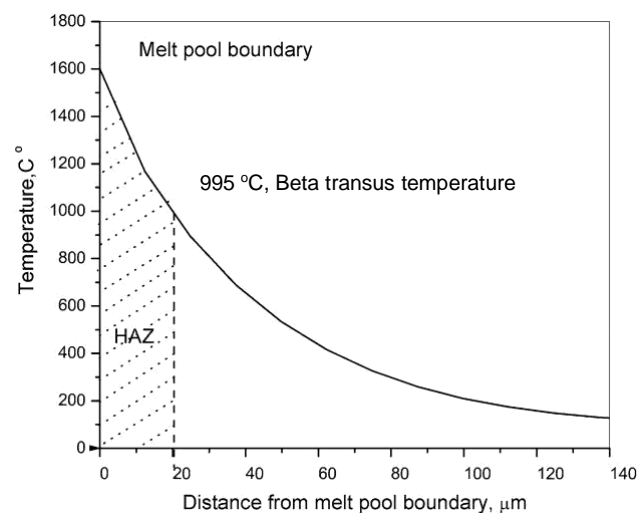


Diagram 5.3 Plot of thermal cycle of the melt pool boundary during deposition of a single track of Ti-6Al-4V alloy in SLM

In this diploma thesis, only single tracks are studied, so the martensite α' (tertiary) is given only theoretically in Fig. 5.4 and does not appear in the simulation or the experimental results of Fig. 5.3. On the other hand, α' (primary) and α' (secondary) are visible in both the simulation and experimental results, which resemble to each other, accordingly, which means that the model developed in this study can accurately predict the melting pool microstructure of the SLM-processed Ti6Al4V.

5.4 50W-1200mm/s analysis

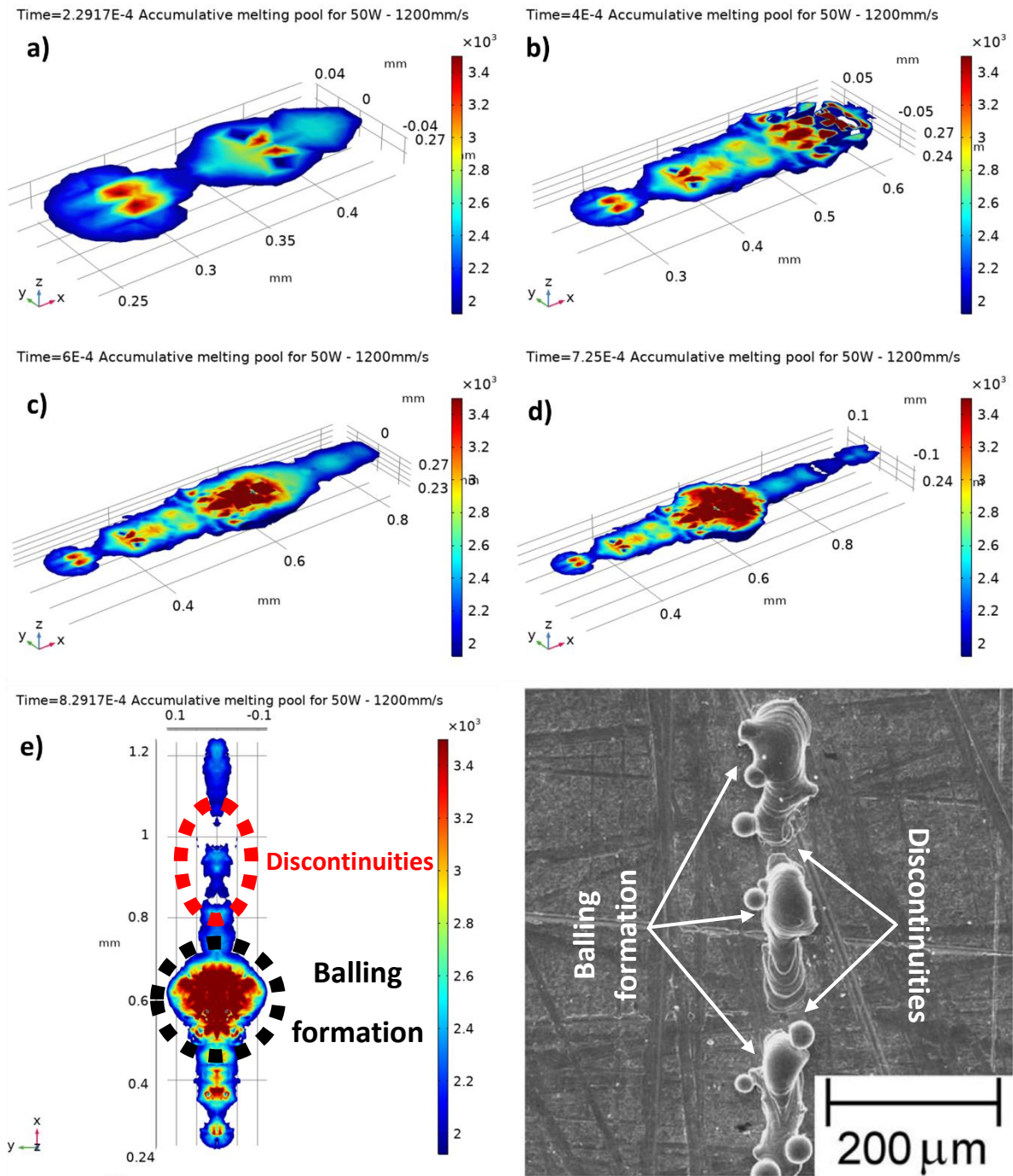


Fig. 5.5 50W-1200mm/s melting pool evolution.

Given that the set of the parameters used in this case (50W-1200mm/s) is invalid, the melting pool is irregular even from the beginning of the process (Fig. 5.5a). The width and depth of the melting pool and the temperature distribution in the molten material are rather unstable. For this reason, at Fig. 5.5b, the fragmentation of the melting pool occurs which leads to the accumulation of more heat in the center of the molten material. This accumulated heat leads to very high temperatures in this region, which results in the excessive enlargement of the depth and width of this area (Fig. 5.5c) and eventually, at the balling formation (Fig. 5.5d). However, at the same time with the balling formation, the laser melts a “new area” in front of the balling, with constant depth and width, which is evident of the steady state (Fig. 5.5c). Nevertheless, because of the high scanning speed-to-laser power ratio, this steady state is very difficult to be maintained and immediately discontinuities start to appear (Fig. 5.5d). Lastly, in Fig. 5.5e, a direct comparison of the experimental and the simulation defects occurs, which proves the ability of the model to predict possible irregularities.

5.5 195W-750mm/s analysis

In the beginning of the process, the laser “digs” the material in order to create the keyhole, so the mass ablation velocity is only downwards (Fig. 5.6a). As the keyhole increases, the velocity gets more diagonal, in order not only to dig the material, but also to move the keyhole forwards (Fig. 5.6b, c). Once the evaporation steady state is reached, the velocity has mainly a horizontal direction, which means that the digging stops (and the depth of the melting pool does not change) and the keyhole only moves forwards (Fig. 5.6d, e). Furthermore, in this state, the velocity is evenly distributed to the forward side wall of the keyhole, because by this time the laser comes very close to this region. Finally, when and the heat transfer steady state is reached, so the model is fully steady, the velocity continues to be mainly horizontal (Fig. 5.6f). However, here the velocity is not evenly distributed, but the ablation is greater to the upper part of the side wall than to the lower parts. This happens because by this time, the laser has overtaken this region and the laser power cannot reach the whole side wall. It is also useful to observe that a small downwards velocity is developed to the abrupt edges that have been remained on the bottom of the keyhole. This means that the SLM system tries by its own to dig and correct any abrupt defects, leading to a smooth keyhole surface. In Fig. 5.6g the fully mirrored model is given, where the martensite α' (primary) and α' (secondary) regions are visible.

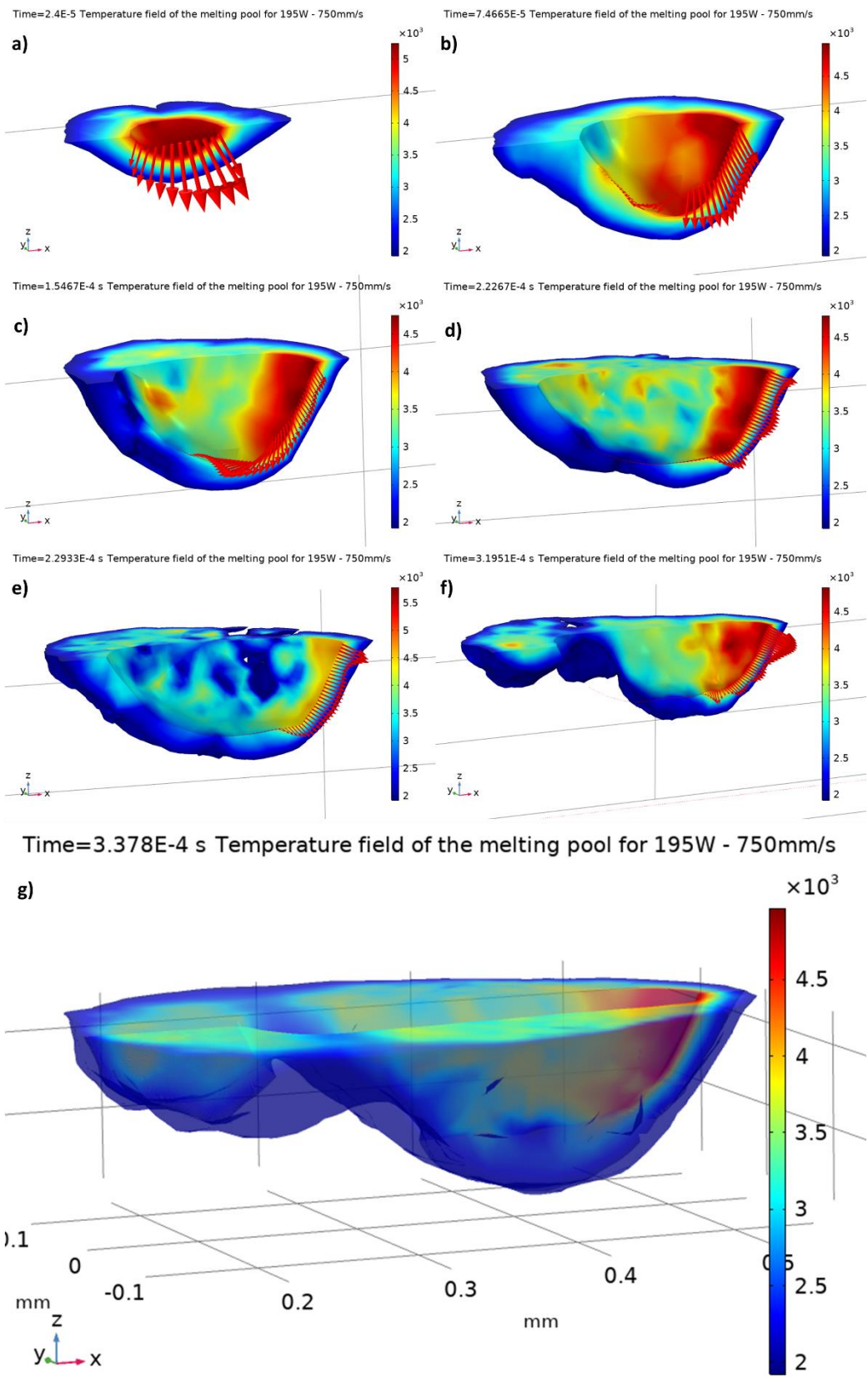


Fig. 5.6 195W-750mm/s keyhole evolution.

5.6 195W-500mm/s analysis

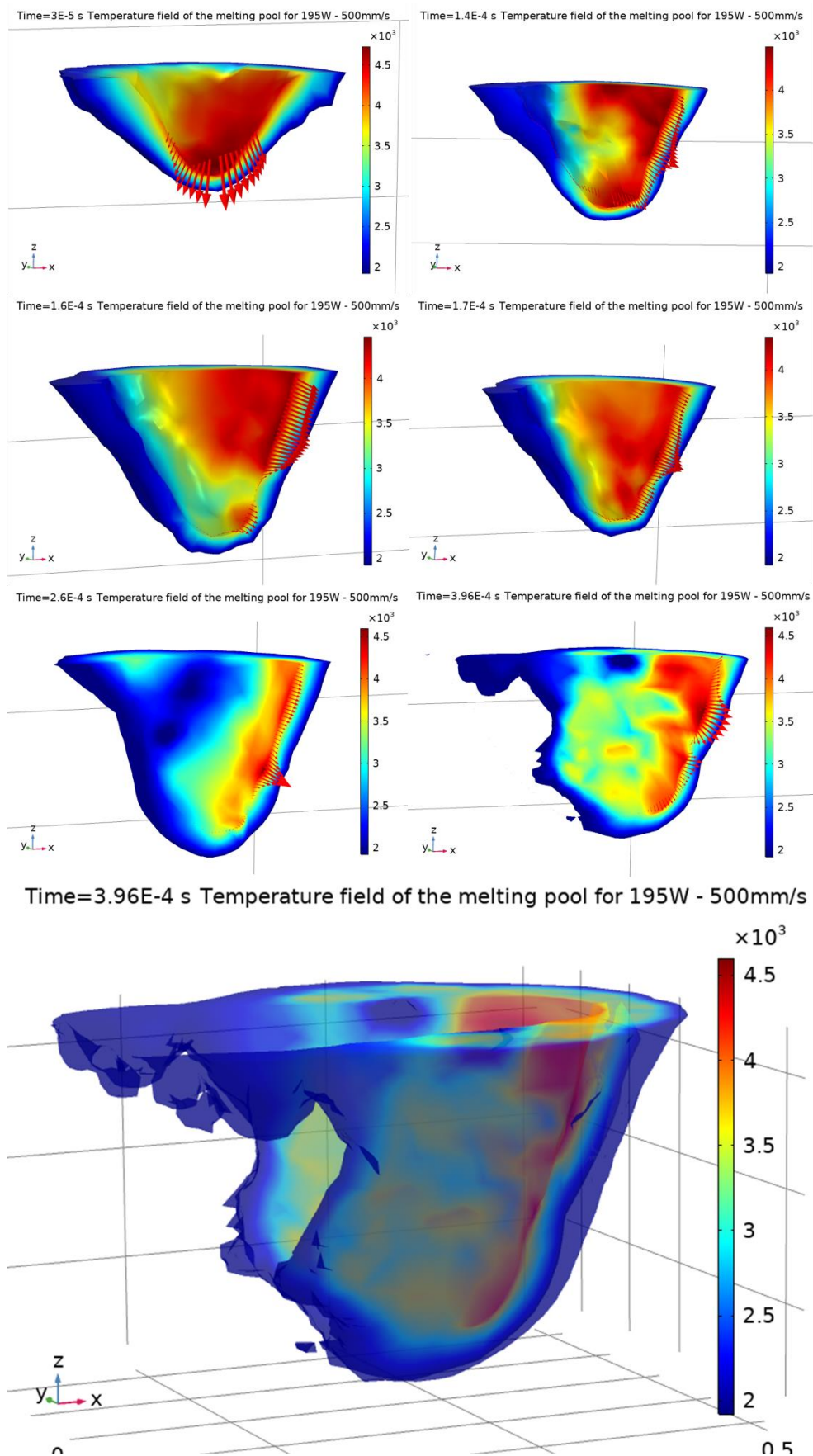


Fig. 5.7 195W-500mm/s keyhole evolution.

In the beginning of the process, the laser “digs” the material in order to create the keyhole, so the mass ablation velocity is only downwards (Fig. 5.7a). As the keyhole increases, the velocity gets more diagonal, in order not only to dig the material, but also to move the keyhole forwards (Fig. 5.7b). Once the evaporation steady state is reached, the velocity has mainly a horizontal direction, which means that the digging stops (and the depth of the melting pool does not change) and the keyhole only moves forwards (Fig. 5.7c, d, e). Furthermore, in this state, the velocity is evenly distributed to the forward side wall of the keyhole, because by this time the laser comes very close to this region. However, this even distribution is disrupted in a small abrupt region and then appears again after this region (Fig. 5.7c). Taking a closer look to this region, an approximately 90° edge is observed, where the surface of the side wall in this region is vertical (parallel to z-axis). As a result, the free surfaces of the mesh elements of this region of the side wall are also vertical, which means that these mesh elements can only be tangent to the periphery of the “laser cylinder” and they are never intersected by the laser beam. Moreover, the periphery of the laser cylinder has no power (due to the Gaussian distribution of the laser intensity), so there is no heat transfer in this region (Fig. 5.8). In order to move this region forwards, this abrupt edge should firstly be digged. When this region is digged (Fig. 5.7d, e) the horizontal velocity developed there is greater than the velocity of the rest side wall, in order for this region to catch up with the forward move of the rest side wall. Finally, when and the heat transfer steady state is reached, so the model is fully steady, the velocity continues to be mainly horizontal (Fig. 5.7f). However, here the velocity is not evenly distributed, but the ablation is greater to the upper part of the side wall than to the lower parts. This happens because by this time, the laser has overtaken this region and the laser power cannot reach the whole side wall. It is also useful to observe that even at the full steady state, an abrupt edge in the middle of the side wall can be developed, which disrupts the horizontal velocity of this region till it is digged. In Fig. 5.7g the fully mirrored model is given, where the martensite α' (primary) and α' (secondary) regions are visible.

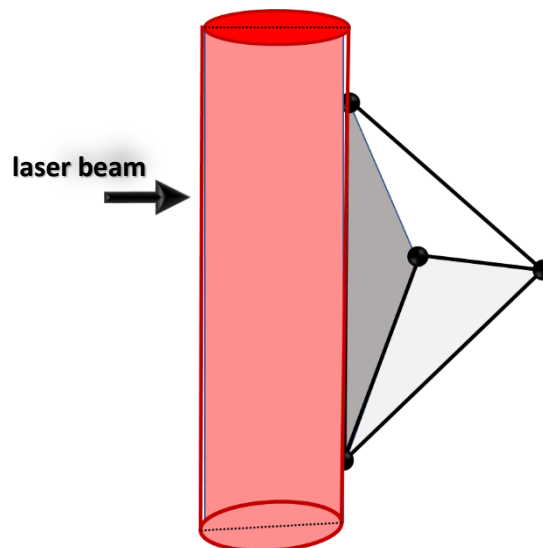


Fig. 5.8 There is no interaction between the laser beam and the vertical surface of a mesh element.

5.7 Percentage reduction of maximum power intensity

Laser intensity ($\frac{W}{mm^2}$) is defined as the laser power per surface unit.

When a laser beam with an initial beam area A_1 is incident to a surface, then the laser beam area that “contacts” the surface is given by the following relation:

$$A_2 = A_1 \frac{1}{\cos \vartheta_{inc}} \quad (61)$$

Where A_1 , A_2 and ϑ_{inc} are described by Fig. 5.9:

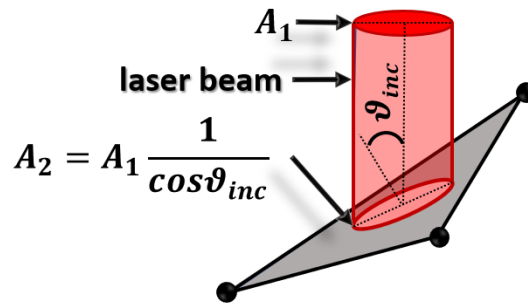


Fig. 5.9 Laser beam “contacts” a surface.

As observed by (61), for $\vartheta_{inc} = 0$, where the surface is horizontal (which represents the initial surface that is incident to the laser beam), $A_2 = A_1$. On the other hand, when $0^\circ < \vartheta_{inc} < 90^\circ$ (which represents the inclination of the keyhole surface), $A_2 > A_1$. Of course, as the keyhole becomes deeper, the inclination increases, so the A_2 increases and the laser intensity decreases.

This phenomenon is quantified in Diagram 5.4:

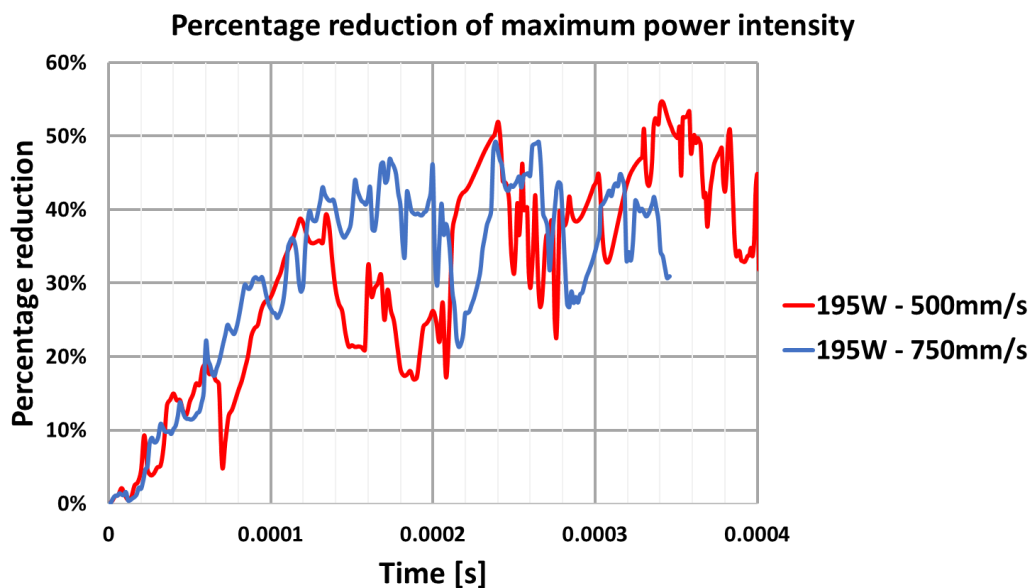


Diagram 5.4 Percentage reduction of maximum power intensity.

In the beginning, where the keyhole becomes deeper and deeper, the percentage reduction of maximum laser intensity increases. When keyhole reaches a steady state, and its depth does not change, the percentage reduction of maximum laser intensity oscillates around a constant value.

5.8 Material removal rate

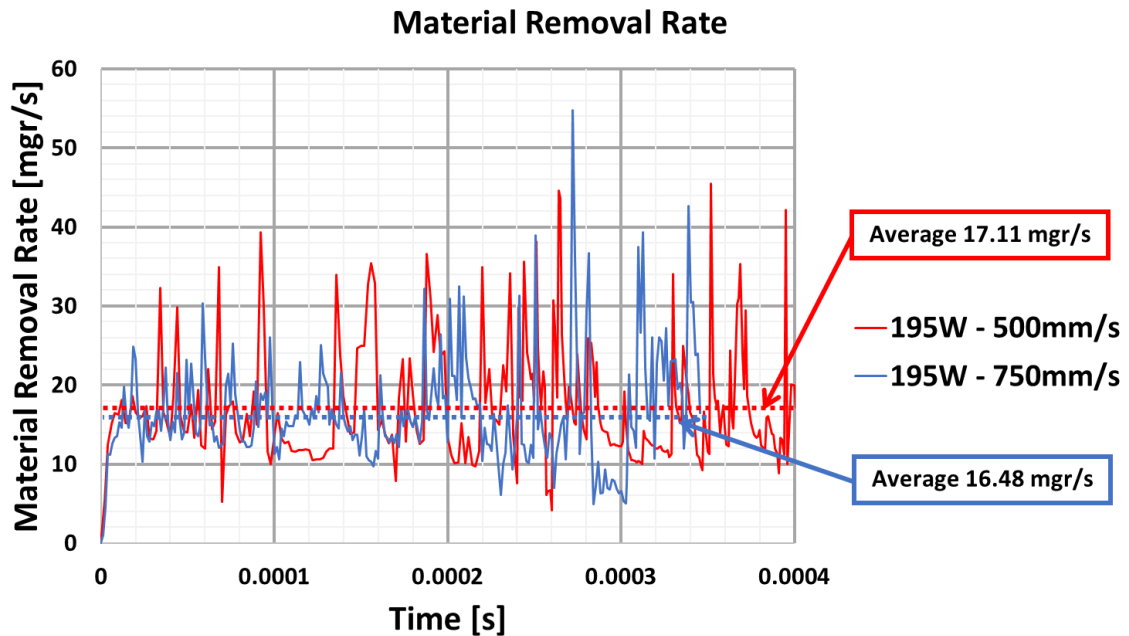


Diagram 5.5 Material removal rate.

As observed in Diagram 5.5, material removal rate is not constant, but it depends on the relative position between the laser beam and the melting pool. Specifically, the peaks of the diagram represent the moments when the laser beam is over the melted material (material with temperatures over 1923.15K) increasing further the temperature of this region, which increases the evaporation of the material. On the other hand, the lows of the diagram represent the moments when the laser beam moves forwards to a “new” solid region (with temperatures below 1923.15K). In this case the material needs to be melted, firstly, so the evaporation rate here is lower.

Moreover, for constant laser power and scanning speed, the values of the material removal rate seem to be independent from the keyhole depth and width. On the other hand, for same laser powers and different scanning speeds the average material removal rate changes. Specifically, for lower scanning speeds, more heat is absorbed by each region of the model, so the temperature increases more and more mass is ablated. This leads to greater average material rate in 195W-500mm/s than in 195W-750mm/s.

6. Conclusions

In this study, a heat-transfer model is developed in order to predict the width and the depth of SLM-processed Ti6Al4V single tracks with temperature dependent properties, using only one unknown coefficient which needs calibration. Material evaporation and mass ablation, via the mesh deformation, have also been included in order to simulate the keyhole effect. The simulations done are the following: a) 50W-1200mm/s (conduction mode), b) 195W-750mm/s (keyhole mode), c) 195W-500mm/s (keyhole mode).

The results showed that:

- The predicted width and depth in all the cases above are in a good agreement with the experimental data from bibliography, as the errors are all below 16%.
- The high scanning speed-to-laser power ratio used in conduction mode leads to invalid bulk parts with defects, such as balling and discontinuities. However, the model proposed in this study is able to predict these irregularities.
- In keyhole mode, the material evaporation is included and the mass ablation is predicted. Furthermore, the model proposed in this study is able not only to predict the width and depth of the keyhole, but also to simulate the martensite α' (primary) and α'' (secondary) regions.

Future research

In order to reduce the computational time and cost, this model does not include fluid dynamics, such as melting pool flow and Marangoni effect, thus the collapse of the keyhole side walls inside the cavity, when the keyhole starts to cool, cannot be predicted. So, for a future research, the present model could be complemented with fluid dynamics, in order to fully simulate the SLM process.

References

- [1] T. Srivastava, M.; Rathee, S.; Maheshwari, S.; Kundra, *Additive Manufacturing Fundamentals and Advancements*. CRC Press; Taylor & Francis Group.
- [2] L. Jyothish Kumar, P. M. Pandey, and D. I. Wimpenny, *3D printing and additive manufacturing technologies*. 2018.
- [3] H. Wang, Y. Fu, M. Su, and H. Hao, "A novel method of indirect rapid prototyping to fabricate the ordered porous aluminum with controllable dimension variation and their properties," *J. Mater. Process. Technol.*, vol. 266, no. 2, pp. 373–380, 2019, doi: 10.1016/j.jmatprotec.2018.11.017.
- [4] A. Gebhardt, *Understanding Additive Manufacturing*. 2011.
- [5] L. Jyothish Kumar *et al.*, *Additive Manufacturing: Applications and Innovations*, vol. 10, no. 3. 2018.
- [6] G. Vander Voort, "Metallographic etching of aluminium and its alloy." pp. 1–49, 2006, [Online]. Available: <https://www.google.co.kr/%5Cnpapers3://publication/uuid/EDC9CDCA-8112-413D-80E6-1FF029414226>.
- [7] Z. Prevorovsky, J. Krofta, and J. Kober, *NDT in additive manufacturing of metals*, vol. 2017-Octob. 2017.
- [8] M. LaMonica, *Additive Manufacturing-Innovations, Advances, and Applications*, vol. 116, no. 3. 2013.
- [9] J. Milewski, *Additive Manufacturing of Metals From Fundamental Technology to Rocket Nozzles, Medical Implants, and Custom Jewelry*. 2017.
- [10] M. Markl and C. Körner, "Multiscale Modeling of Powder Bed-Based Additive Manufacturing," *Annu. Rev. Mater. Res.*, vol. 46, no. April, pp. 93–123, 2016, doi: 10.1146/annurev-matsci-070115-032158.
- [11] M. Brandt, *Laser Additive Manufacturing Materials, Design, Technologies and Applications*. Elsevier Ltd., 2017.
- [12] U. Scipioni Bertoli, A. J. Wolfer, M. J. Matthews, J. P. R. Delplanque, and J. M. Schoenung, "On the limitations of Volumetric Energy Density as a design parameter for Selective Laser Melting," *Mater. Des.*, vol. 113, pp. 331–340, 2017, doi: 10.1016/j.matdes.2016.10.037.
- [13] Z. Zhang *et al.*, "3-Dimensional heat transfer modeling for laser powder-bed fusion additive manufacturing with volumetric heat sources based on varied thermal conductivity and absorptivity," *Opt. Laser Technol.*, vol. 109, no. July 2018, pp. 297–312, 2019, doi: 10.1016/j.optlastec.2018.08.012.
- [14] K. H. Lee and G. J. Yun, "A novel heat source model for analysis of melt Pool evolution in selective laser melting process," *Addit. Manuf.*, vol. 36, no. August, p. 101497, 2020, doi: 10.1016/j.addma.2020.101497.

- [15] D. Gu, C. Ma, M. Xia, D. Dai, and Q. Shi, "A Multiscale Understanding of the Thermodynamic and Kinetic Mechanisms of Laser Additive Manufacturing," *Engineering*, vol. 3, no. 5, pp. 675–684, 2017, doi: 10.1016/J.ENG.2017.05.011.
- [16] S. Pang, L. Chen, J. Zhou, Y. Yin, and T. Chen, "A three-dimensional sharp interface model for self-consistent keyhole and weld pool dynamics in deep penetration laser welding," *J. Phys. D: Appl. Phys.*, vol. 44, no. 2, 2011, doi: 10.1088/0022-3727/44/2/025301.
- [17] S. A. Khairallah, A. T. Anderson, A. Rubenchik, and W. E. King, "Laser powder-bed fusion additive manufacturing: Physics of complex melt flow and formation mechanisms of pores, spatter, and denudation zones," *Acta Mater.*, vol. 108, pp. 36–45, 2016, doi: 10.1016/j.actamat.2016.02.014.
- [18] J. Volpp and F. Vollertsen, "Analytical modeling of the keyhole including multiple reflections for analysis of the influence of different laser intensity distributions on keyhole geometry," *Phys. Procedia*, vol. 41, pp. 460–468, 2013, doi: 10.1016/j.phpro.2013.03.102.
- [19] D. Dai and D. Gu, "Effect of metal vaporization behavior on keyhole-mode surface morphology of selective laser melted composites using different protective atmospheres," *Appl. Surf. Sci.*, vol. 355, pp. 310–319, 2015, doi: 10.1016/j.apsusc.2015.07.044.
- [20] T. N. Le and Y. L. Lo, "Effects of sulfur concentration and Marangoni convection on melt-pool formation in transition mode of selective laser melting process," *Mater. Des.*, vol. 179, p. 107866, 2019, doi: 10.1016/j.matdes.2019.107866.
- [21] M. Miyagi and J. Wang, "Keyhole dynamics and morphology visualized by in-situ X-ray imaging in laser melting of austenitic stainless steel," *J. Mater. Process. Technol.*, vol. 282, no. October 2019, p. 116673, 2020, doi: 10.1016/j.jmatprotec.2020.116673.
- [22] T. Heeling, M. Cloots, and K. Wegener, "Melt pool simulation for the evaluation of process parameters in selective laser melting," *Addit. Manuf.*, vol. 14, pp. 116–125, 2017, doi: 10.1016/j.addma.2017.02.003.
- [23] H. Wang and Y. Zou, "Microscale interaction between laser and metal powder in powder-bed additive manufacturing: Conduction mode versus keyhole mode," *Int. J. Heat Mass Transf.*, vol. 142, p. 118473, 2019, doi: 10.1016/j.ijheatmasstransfer.2019.118473.
- [24] W. E. King *et al.*, "Observation of keyhole-mode laser melting in laser powder-bed fusion additive manufacturing," *J. Mater. Process. Technol.*, vol. 214, no. 12, pp. 2915–2925, 2014, doi: 10.1016/j.jmatprotec.2014.06.005.
- [25] L. Caprio, A. G. Demir, and B. Previtali, "Observing molten pool surface oscillations during keyhole processing in laser powder bed fusion as a novel method to estimate the penetration depth," *Addit. Manuf.*, vol. 36, no. March, p. 101470, 2020, doi: 10.1016/j.addma.2020.101470.
- [26] T. Qi, H. Zhu, H. Zhang, J. Yin, L. Ke, and X. Zeng, "Selective laser melting of Al7050 powder: Melting mode transition and comparison of the characteristics between the

- keyhole and conduction mode," *Mater. Des.*, vol. 135, pp. 257–266, 2017, doi: 10.1016/j.matdes.2017.09.014.
- [27] D. Zhang, P. Zhang, Z. Liu, Z. Feng, C. Wang, and Y. Guo, "Thermofluid field of molten pool and its effects during selective laser melting (SLM) of Inconel 718 alloy," *Addit. Manuf.*, vol. 21, no. 100, pp. 567–578, 2018, doi: 10.1016/j.addma.2018.03.031.
- [28] E. L. Papazoglou, N. L. Karkalos, and A. P. Markopoulos, "A comprehensive study on thermal modeling of SLM process under conduction mode using FEM."
- [29] V. Holman, *Heat Transfer (10th edition)*, vol. 15, no. 3. 1999.
- [30] J. R. Zhuang, Y. T. Lee, W. H. Hsieh, and A. S. Yang, "Determination of melt pool dimensions using DOE-FEM and RSM with process window during SLM of Ti6Al4V powder," *Opt. Laser Technol.*, vol. 103, pp. 59–76, 2018, doi: 10.1016/j.optlastec.2018.01.013.
- [31] K. C. Mills, *Recommended Values of Thermophysical Properties for Selected Commercial Alloys*. 2002.
- [32] M. Bass, E. Stryland, D. Williams, and W. Wolfe, *Handbook of Optics- Devices, Measurements and Properties*, Second. McGraw-Hill, 1377.
- [33] L. Li, K. Yu, K. Zhang, and Y. Liu, "Study of Ti-6Al-4V alloy spectral emissivity characteristics during thermal oxidation process," *Int. J. Heat Mass Transf.*, vol. 101, pp. 699–706, 2016, doi: 10.1016/j.ijheatmasstransfer.2016.05.069.
- [34] J. Yan, Y. Zhou, R. Gu, X. Zhang, W. M. Quach, and M. Yan, "A comprehensive study of steel powders (316L, H13, P20 and 18Ni300) for their selective laser melting additive manufacturing," *Metals (Basel)*, vol. 9, no. 1, 2019, doi: 10.3390/met9010086.
- [35] S. S. Sih and J. W. Barlow, "The prediction of the emissivity and thermal conductivity of powder beds," *Part. Sci. Technol.*, vol. 22, no. 4, pp. 427–440, 2004, doi: 10.1080/02726350490501682.
- [36] C. D. Boley, S. A. Khairallah, and A. M. Rubenchik, "Modeling of powder absorption in additive manufacturing," *Opt. InfoBase Conf. Pap.*, no. June, pp. 10–12, 2014, doi: 10.1364/cleo_at.2014.am1l.5.
- [37] E. Mirkoohi, D. E. Seivers, H. Garmestani, and S. Y. Liang, "Heat source modeling in selective laser melting," *Materials (Basel)*, vol. 12, no. 13, pp. 1–18, 2019, doi: 10.3390/ma12132052.
- [38] M. Courtois *et al.*, "The numerical challenges in multiphysical modeling of laser welding with arbitrary Lagrangian-Eulerian method," *COMSOL Conf.*, no. 1, p. 8, 2018.
- [39] K. Hirano, R. Fabbro, and M. Muller, "Study on temperature dependence of recoil pressure near the boiling temperature - Towards better modeling and simulation," *ICALEO 2012 - 31st Int. Congr. Appl. Lasers Electro-Optics*, no. December 2017, pp. 678–684, 2012, doi: 10.2351/1.5062526.
- [40] P. Cirp, S. Weber, J. Montero, M. Bleckmann, K. Paetzold, and A. Siadat, "Study of Layered Tetrahedral and Cartesian meshing in Additive Manufacturing Simulation A

- new methodology to analyze the functional and physical architecture of Cartesian meshing in Additive Manufacturing Simulation Web,” *Procedia CIRP*, vol. 91, pp. 522–527, 2020, doi: 10.1016/j.procir.2020.02.209.
- [41] L. Qi, C. Guo-Dong, and W. Shu-Zhen, “Softness-based adaptive mesh refinement algorithm for soft tissue deformation,” *BioSystems*, vol. 191–192, no. February, 2020, doi: 10.1016/j.biosystems.2020.104103.
- [42] J. J. S. Dilip *et al.*, “Influence of processing parameters on the evolution of melt pool, porosity, and microstructures in Ti-6Al-4V alloy parts fabricated by selective laser melting,” *Prog. Addit. Manuf.*, vol. 2, no. 3, pp. 157–167, 2017, doi: 10.1007/s40964-017-0030-2.
- [43] S. Patel and M. Vlasea, “Melting modes in laser powder bed fusion,” *Materialia*, vol. 9, no. November 2019, 2020, doi: 10.1016/j.mtla.2020.100591.
- [44] Y. Fu, C.;Guo, “3-Dimnsional Finite Element Modeling of Selective Laser Melting Ti6Al4V Alloy,” p. 283, 1386.
- [45] J. J. S. Dilip, M. A. Anam, D. Pal, and B. Stucker, “A short study on the fabrication of single track deposits in SLM and characterization,” *Solid Free. Fabr. 2016 Proc. 27th Annu. Int. Solid Free. Fabr. Symp. - An Addit. Manuf. Conf. SFF 2016*, pp. 1644–1659, 2016.



ΕΘΝΙΚΟ ΜΕΤΣΟΒΙΟ ΠΟΛΥΤΕΧΝΕΙΟ
ΣΧΟΛΗ ΜΗΧΑΝΟΛΟΓΩΝ ΜΗΧΑΝΙΚΩΝ

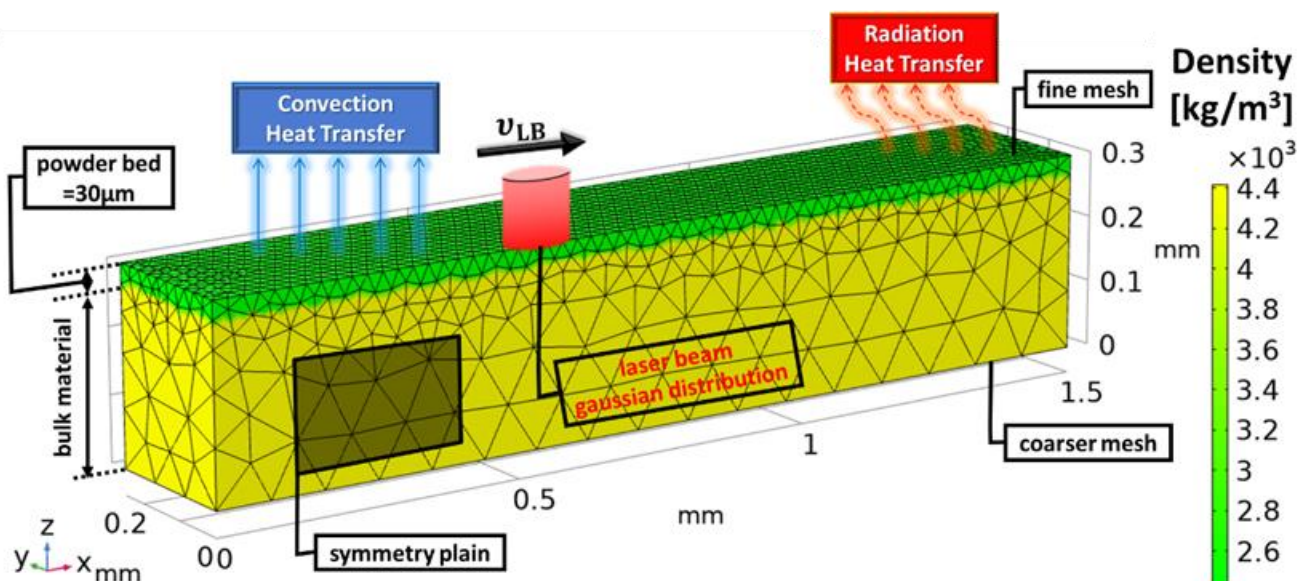
Εκτεταμένη περίληψη διπλωματικής εργασίας στα Ελληνικά

Μελέτη και μοντελοποίηση της μετάβασης από conduction σε keyhole μορφή κατά τη διάρκεια της SLM κατεργασίας

(Study and modeling of the transition from conduction to keyhole mode during SLM process)

Βασιλική Ε. Αλεξοπούλου (02116097)

2020-2021



Τομέας: Τεχνολογίας των Κατεργασιών

Επιβλέπων: Α. Μαρκόπουλος, Αν. Καθηγητής, ΕΜΠ

Εισαγωγή στις Προσθετικές Κατεργασίες (ΠΚ)

Οι ΠΚ παρουσιάζουν ραγδαία εξέλιξη τις τελευταίες δεκαετίες. Ξεκίνησαν από τους Kodama (1980), Hull (SLA, 1987), Deckard (SLS, 1987) και Crump (FDM, 1989) και στη συνέχεια υιοθετήθηκαν εξελίχθηκαν από μεγάλες εταιρείες, όπως EOS GmbH, Helisys, Z Corp, Object Envision Tec και EBW/Exone.

Όλες οι ΠΚ περιλαμβάνουν οχτώ βήματα: 1) Δημιουργία CAD μοντέλων, 2) μετατροπή των αρχείων CAD σε αρχεία .stl, 3) μεταφορά των αρχείων .stl στην μηχανή ΠΚ, 4) ρύθμιση των παραμέτρων της μηχανής, 5) κατασκευή τεμαχίου, 6) εξαγωγή τεμαχίου από την μηχανή ΠΚ, 7) φινιρίσμα τεμαχίου, 8) εφαρμογή του τεμαχίου.

Οι ΠΚ διακρίνονται σε άμεσες και έμμεσες διεργασίες. Άμεσες είναι οι διεργασίες που οδηγούν σε τελικά προϊόντα, ενώ έμμεσες είναι οι διεργασίες που οδηγούν σε παραγωγή καλουπιών, τα οποία εν συνεχεία χρησιμοποιούνται για άλλες κατεργασίες. Μια άλλη διάκριση είναι: ταχεία προτυποποίηση, ταχεία παραγωγή και ταχεία κατασκευή εργαλείων. Με την ταχεία προτυποποίηση δημιουργούνται μοντέλα, που χρησιμοποιούνται για εποπτικούς λόγους, για επίδειξη κάποιας δομής ή μηχανής ή για τον έλεγχο συγκεκριμένων ιδιοτήτων σε μικρότερη κλίμακα. Με την ταχεία παραγωγή κατασκευάζονται τελικά προϊόντα, ενώ με την ταχεία κατασκευή εργαλείων, παράγονται εργαλεία με ιδιαίτερα σχήματα και μορφολογίες.

Η βασική αρχή πάνω στην οποία στηρίζονται όλες οι ΠΚ είναι η δημιουργία τεμαχίων σε στρώσεις και η ένωση κάθε στρώσης με τις γειτονικές της. Σήμερα, υπάρχουν πάνω από 100 είδη μηχανών ΠΚ, οι οποίες επεξεργάζονται μέταλλα, πλαστικά, κεραμικά σε μορφή σκόνης, φύλλων, λάστιχων.

Όλες οι ΠΚ μπορούν να χωριστούν στις εξής οικογένειες κατεργασιών: 1) Πολυμερισμός (η επιλεκτική στερεοποίηση υγρών μονομερών γίνεται από ακτινοβολία UV), 2) Στερεολιθογραφία (δίνει τεμάχια με καλή ποιότητα επιφανείας και εξαιρετικές λεπτομέρειες, πραγματοποιείται μέσω του πολυμερισμού υγρού μονομερούς από ακτίνα λέιζερ UV και χρησιμοποιείται στην παραγωγή τεμαχίων με λεπτότοιχες διατομές), 3) Εκτύπωση πολυμερών (πραγματοποιείται με πολυμερισμό φωτοευαίσθητων υγρών μονομερών από πιεζοηλεκτρική εκτυπωτική κεφαλή που αποτελείται από δύο UV λάμπες που κινούνται ταυτόχρονα και μπορεί να δώσει τεμάχια που αποτελούνται από πολλά διαφορετικά υλικά), 4) Κατεργασία ψηφιακού φωτός (είδος φωτοπολυμερισμού που χρησιμοποιεί προτζέκτορα DLP ως πηγή φωτός UV, η ρητίνη αποθηκεύεται σε γυάλινη δεξαμενή στην κορυφή και η προβολή γίνεται από κάτω προς τα πάνω), 5) Κατεργασίες σύντηξης και τήξης (ευρεία κατηγορία που περιλαμβάνει την Επιλεκτική Σύντηξη με Λέιζερ -SLS-, την Επιλεκτική Τήξη με Λέιζερ -SLM- και την Τήξη με Ακτίνα Ηλεκτρονίων -EBM-), 6) Εξώθηση- Εκτύπωση συντηγμένων επιπέδων (το υλικό έχει μορφή νήματος και είναι αποθηκευμένο σε φυσίγγια, το πιο γνωστό είδος είναι η Εκτύπωση Συντηγμένης Εναπόθεσης -FDM-), 7) Κατεργασία σκόνης με συνδετική ουσία (κάθε στρώση σκόνης ενώνεται με τις γειτονικές της μέσω υγρής συνδετικής ουσίας, η κατεργασία αυτή έχει επικρατήσει να λέγεται Τρισδιάστατη Εκτύπωση -3D Printing-), 8) Κατεργασία στρώσεων φύλλων (χρησιμοποιούνται φύλλα μετάλλων, πλαστικού ή χαρτιού), 9) Άλλες κατεργασίες (εκτύπωση με χρήση αεροζόλ, εκτύπωση βιολογικών υλικών).

Συνοπτικά, όλες οι ΠΚ δίνονται παρακάτω (Πίνακας 1):

Πίνακας 1 Κατηγορίες και τεχνολογίες των ΠΚ.

AM CATEGORY							
	Vat Photo-polymerisation	Material Extrusion	Material Jetting	Binder Jetting	Power Bed Fusion	Direct Energy Deposition	Sheet Lamination
TECHNOLOGIES	Stereolithography (SLA)	Fused Deposition Modeling (FDM) Contour Crafting	Polyjet / Inkjet Printing	Indirect Inkjet Printing (Binder 3DP)	Selective Laser Sintering (SLS) Direct Metal Laser Sintering (DMLS) Selective Laser Melting (SLM) Electron Beam Melting (EBM)	Laser Engineered Net Shaping (LENS) Electronic Beam Welding (EBW)	Laminated Object Manufacturing (LOM)
MATERIAL	Photopolymer Ceramics	Thermoplastics, Ceramic slurries, Metal pastes	Photopolymer, Wax	Polymer-, Metal- or Ceramic powder	Polymer-, Metal- or Ceramic powder	Metal powder or wire	Plastic film, Metallic sheet, Ceramic tape
PROS/CONS	+ High building speed + Good part resolution - Overcuring, scanned line shape - High cost for supplies and materials	- Inexpensive extrusion machine - Multi-material printing - Limited part resolution - Poor surface finish	+ Multi-material printing + High surface finish - Low-strength material	+ Full-color + Wide material selection - Require infiltration during post-processing - High porosities on finished parts	+ High Accuracy and Details + Fully dense parts + High specific strength & stiffness - Powder handling & recycling - Support and anchor structure	+ Repair of damaged/worn parts + Functionality graded material printing - Bad resolution - Expensive	+ High surface finish + Low cost - Decubing issues

Τα βασικά πλεονεκτήματα των ΠΚ είναι:

- Ευκολία στην παραγωγή εξατομικευμένων προϊόντων.
- Δυνατότητα επεξεργασίας όλων των υλικών.
- Απαιτείται μόνο μία μηχανή για την παραγωγή του τελικού προϊόντος (σε αντίθεση με τις συμβατικές κατεργασίες).
- Είναι αθόρυβες.
- Μπορούν να πραγματοποιηθούν από την άνεση του γραφείου ή του σπιτιού.
- Μειωμένη σπατάλη υλικού.
- Κατασκευή τεμαχίων με σύνθετες γεωμετρίες.
- Δεν απαιτούνται καλούπια, εργαλεία, κοπτικά.

Τα βασικά μειονεκτήματα των ΠΚ είναι:

- Χαμηλότερες ταχύτητες κατασκευής.
- Χαμηλή ποιότητα επιφανείας.
- Απαιτείται προ-επεξεργασία και μετά-επεξεργασία.
- Ανισοτροπική συμπεριφορά των ΠΚ-τεμαχίων.

- Παρουσία της ατέλειας σκαλοπατιού (stair-stepping).
- Χαμηλότερη αντοχή.

Οι βασικές ατέλειες των ΠΚ είναι:

- Σφαιρικές ατέλειες (balling).
- Πόροι
- Ρωγμές
- Παραμόρφωση επιφάνειας.
- Φαινόμενο σκαλοπατιού.

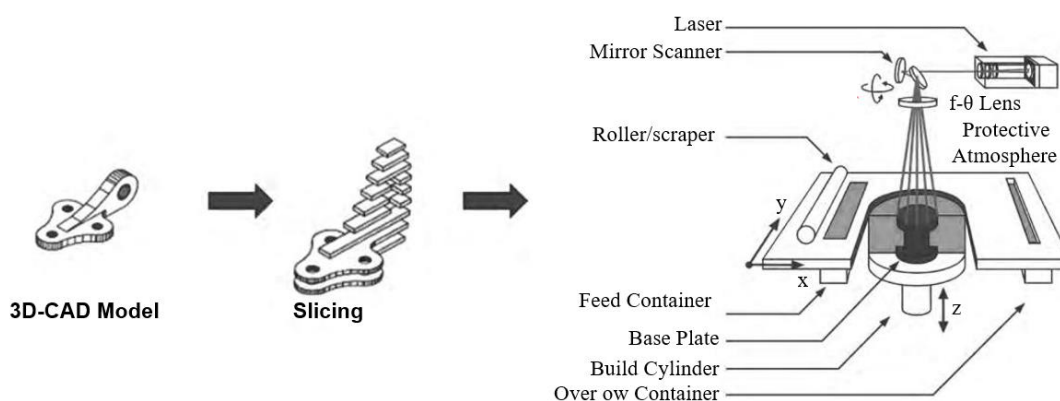
Οι ΠΚ έχουν εφαρμογή σε πολλούς τομείς:

- Καλλιτεχνικές κατασκευές.
- Παραγωγή εξατομικευμένων προϊόντων.
- Ιατρική (οδοντιατρική, ορθοπεδική).
- Αεροδιαστημική.
- Αυτοκίνηση.
- Καλούπια, εργαλεία για τη βιομηχανία.
- Οικοδομικά, αμυντικά έργα.

Επιλεκτική Τήξη με Λείζερ (SLM)

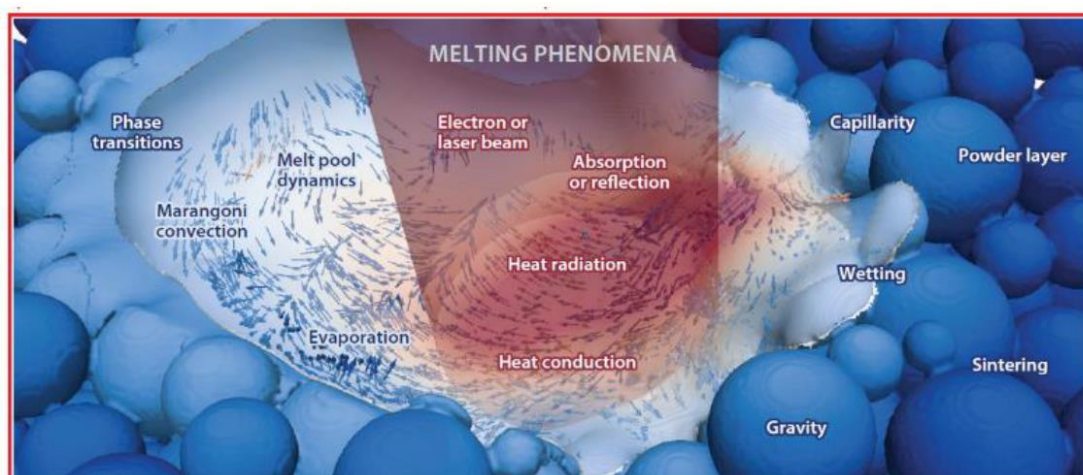
Η SLM είναι ένα είδος ΠΚ που παράγει σύνθετα τρισδιάστατα τεμάχια μέσω της στερεοποίησης διαδοχικών στρώσεων σκόνης, με βάση ένα CAD μοντέλο. Η SLM σχετίζεται με ολική τήξη της σκόνης και όχι με σύντηξη ή εν μέρει τήξη, που είναι ο κύριος μηχανισμός της Επιλεκτικής Σύντηξης με Λείζερ (SLS).

Ο βασικός μηχανισμός της SLM ακολουθεί την εξής διαδικασία: μία στρώση σκόνης απλώνεται στη βάση της μηχανής και στη συνέχεια τήκεται από μια ακτίνα λέιζερ, ανάλογα με το σχήμα που ορίζεται σε αρχείο CAD. Στη συνέχεια η βάση της μηχανής κινείται προς τα κάτω και ένα νέο στρώμα σκόνης απλώνεται στη μηχανή ώστε να επαναληφθεί η ίδια διαδικασία, όπως φαίνεται στην Εικόνα 1:



Εικόνα 1 Σχηματικό διάγραμμα του μηχανισμού της SLM.

Η SLM είναι μία σύνθετη κατεργασία καθώς διέπεται από πολλά φυσικά φαινόμενα, όπως είναι η απορρόφηση και η ανάκλαση της ακτίνας του λέιζερ, η ακτινοβολία, η αγωγή και η συναγωγή θερμότητας, η εξάτμιση του υλικού, η πίεση υποχώρησης, το φαινόμενο Marangoni, η λανθάνουσα θερμότητα και η αλλαγή φάσης (Εικόνα 2).



Εικόνα 2 Φυσικά φαινόμενα που λαμβάνουν χώρα στο τήγμα της SLM (αριστερά) και του EBM (δεξιά).

Οι παράμετροι που επιδρούν στην SLM είναι η ισχύς του λέιζερ, η ταχύτητα σάρωσης, το πάχος στρώσης και το διάκενο σάρωσης. Οι παράμετροι αυτοί μπορούν να συνδυαστούν στους παρακάτω δείκτες:

$$VED' = \frac{P}{vst} \left(\frac{J}{mm^3} \right) \quad (1)$$

ή

$$VED = \frac{P}{vD_b t} \left(\frac{J}{mm^3} \right) \quad (2)$$

Όπου:

VED' ή VED = ογκομετρική πυκνότητα ενέργειας $\left(\frac{J}{mm^3} \right)$ ή $\frac{J}{mm^2}$,

P = ισχύς λέιζερ (W),

v = ταχύτητα σάρωσης $\left(\frac{mm}{s} \right)$,

s = διάκενο σάρωσης (mm),

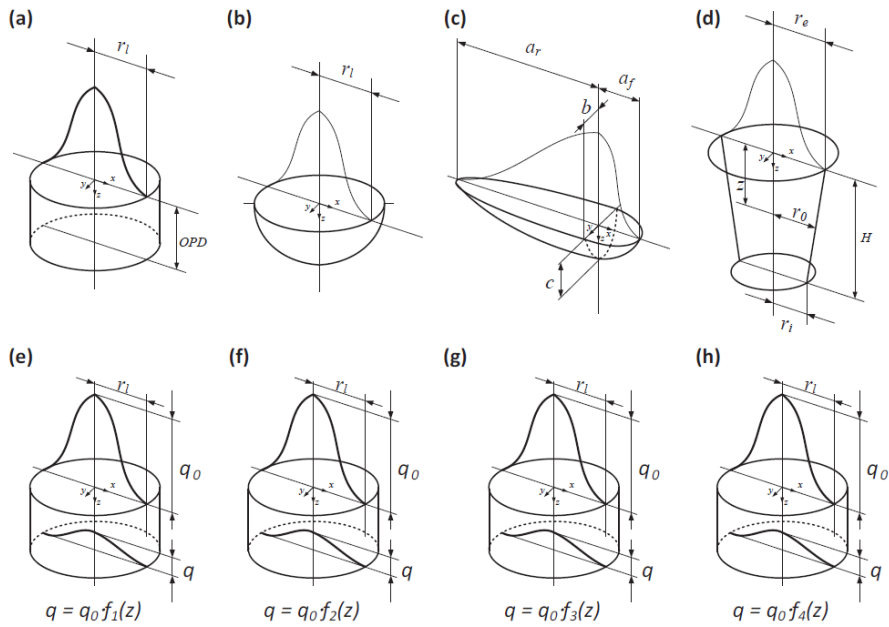
t = πάχος στρώσης (mm).

D_b = διάμετρος ακτίνας λέιζερ (mm).

Δημοσιεύσεις σχετικές με την SLM

Παρακάτω παρουσιάζονται πειραματικές και θεωρητικές εργασίες που προσπαθούν να υπολογίσουν ή να προβλέψουν την γεωμετρία του τήγματος.

Οι Zhang Z. et al. [1] ανέπτυξαν ένα τρισδιάστατο θερμικό μοντέλο πεπερασμένων στοιχείων για την κατεργασία Laser Powder-Bed Fusion (LPBF) για να προβλέψουν με ακρίβεια τη γεωμετρία του τήγματος και τα χαρακτηριστικά της επιφάνειας. Χρησιμοποιήθηκαν οχτώ μοντέλα θερμικών πηγών (Εικόνα 3, Πίνακας 2), τα οποία ανήκουν σε δύο κατηγορίες: 1) γεωμετρικά τροποποιημένη κατηγορία (GMG) και 2) κατηγορία προφίλ απορροφητικότητας (APG). Τα αποτελέσματα των προσομοιώσεων συγκρίθηκαν με πειραματικά δεδομένα. Και οι οχτώ πηγές οδηγούν σε 40% ρηχότερα τήγματα συγκριτικά με τα πειράματα σε ανοξείδωτο χάλυβα 17-4PH.



Εικόνα 3 Σχηματική αναπαράσταση των θερμικών πηγών, (a) κυλινδρικό σχήμα, (b) ημισφαιρικό σχήμα, (c) ημιελλειψοειδές σχήμα, (d) κωνικό σχήμα, (e) μέθοδος μεταφοράς ακτινοβολίας, (f) μέθοδος ανίχνευσης ακτίνων, (g) μέθοδος γραμμικής μείωσης, (h) μέθοδος εκθετικής μείωσης.

Πίνακας 2 Μαθηματική αναπαράσταση των θερμικών πηγών.

GMG1	Cylindrical shape	$I(x, y, z) = \frac{\beta \cdot P}{S \times \alpha_{OPD} \times OPD}$
GMG2	Semi-spherical shape	$I(x, y, z) = \frac{2^{5/2} \beta \cdot P}{\pi^{3/2} r_l^3} \exp\left[-2 \frac{x^2 + y^2 + z^2}{r_l^2}\right]$
GMG3	Semi-ellipsoidal shape	$I_f(x, y, z) = f_f \cdot \frac{2^{5/2} \beta \cdot P}{\pi^{3/2} a_f b c} \exp\left[-2 \left(\frac{x^2}{a_f^2} + \frac{y^2}{b^2} + \frac{z^2}{c^2}\right)\right]$ $I_r(x, y, z) = f_r \cdot \frac{2^{5/2} \beta \cdot P}{\pi^{3/2} a_r b c} \exp\left[-2 \left(\frac{x^2}{a_r^2} + \frac{y^2}{b^2} + \frac{z^2}{c^2}\right)\right]$
GMG4	Conical shape	$I(x, y, z) = \frac{6\beta \cdot P}{\pi H (r_e^2 + r_e r_i + r_i^2)} \exp\left[-2 \frac{x^2 + y^2}{r_0^2}\right], \quad r_0 = r_e + \frac{z}{H}(r_e - r_i)$
APG1	Radiation transfer equation method	$I(x, y, z) = \frac{2P}{\pi r_l^2} \exp\left[-2 \frac{x^2 + y^2}{r_l^2}\right] \cdot \left(-\eta \cdot \frac{dq}{d\xi}\right)$ $q = \frac{\gamma a_0}{(4\gamma - 3)D} \left\{ (1 - \gamma^2) \exp[-\lambda] \cdot \left[(1 - a_0) \exp[-2a_0 \xi] + (1 + a_0) \exp[2a_0 \xi] \right] \right.$ $\left. - (3 + \gamma \exp[-2\lambda]) \times \left\{ [1 + a_0 - \gamma(1 - a_0)] \exp[2a_0(\lambda - \xi)] \right\} \right.$ $\left. + [1 - a_0 - \gamma(1 + a_0)] \exp[2a_0(\xi - \lambda)] \right\}$ $- \frac{3(1 - \gamma)(\exp[-\xi] - \gamma \exp[\xi - 2\lambda])}{4\gamma - 3}$
APG2	Ray-tracing method	$I(x, y, z) = \frac{2P}{\pi r_l^2} \exp\left[-2 \frac{x^2 + y^2}{r_l^2}\right] \frac{d\beta}{dz}$
APG3	Linearly decaying equation	$I(x, y, z) = \frac{2P}{\pi r_l^2} \exp\left[-2 \frac{x^2 + y^2}{r_l^2}\right] f(z), \quad f(z) = \beta \cdot \frac{z}{\delta} \left(1 - \frac{z}{\delta}\right)$
APG4	Exponentially decaying equation	$I(x, y, z) = \frac{2P}{\pi r_l^2} \exp\left[-2 \frac{x^2 + y^2}{r_l^2}\right] f(z), \quad f(z) = \beta \cdot \frac{1}{H} \exp\left[-\frac{z}{H}\right]$

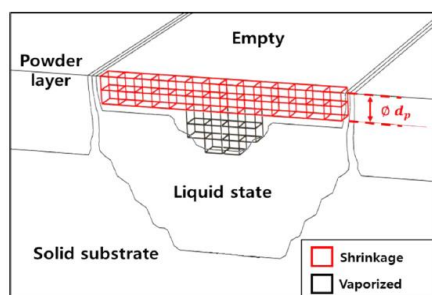
Για να βελτιωθεί η απόδοση του μοντέλου, στο APG4 συμπεριλήφθηκε και η ανισοτροπία του υλικού.

Τα κύρια συμπεράσματα είναι τα ακόλουθα:

1. Η ανισοτροπία μείωσε το σφάλμα πλάτους και βάθους σε 2.9% και 7.3%, αντίστοιχα.
2. Τα αποτελέσματα της προσομοίωσης συμφωνούν με τα πειραματικά ως προς την σταθερότητα της τροχιάς και την γωνία κυματισμού.

Οι Lee K. et al. [2] ανέπτυξαν ένα πρωτότυπο υβριδικό μοντέλο λαμβάνοντας υπόψη τους διαφορετικούς μηχανισμούς απορρόφησης μεταξύ πορώδους και συμπαγούς υλικού. Το μοντέλο μπορεί να προβλέψει τα χαρακτηριστικά του τήγματος, συμπεριλαμβανομένου των διαστάσεων του και των μορφών του στην SLM. Το μοντέλο αποτελείται από την εξίσωση μεταφοράς θερμότητας, λαμβάνοντας υπόψη την αλλαγή των φάσεων και τον βαθμό στερεοποίησης. Χρησιμοποιούνται σαρώσεις απλής τροχιάς 316L τεμαχίων ανοξείδωτου χάλυβα και για την περίπτωση μη χρήσης σκόνης και για την περίπτωση χρήσης σκόνης όλα αυτά τα αποτελέσματα είναι σε συμφωνία με πειραματικά δεδομένα. Επιπλέον, οι μορφές του τήγματος (keyhole και conduction) μπορούν να διακριτοποιηθούν βάσει της μορφολογίας και του βαθμού εξάτμισης, πράγμα που βοηθά στον ορισμό των βέλτιστων συνθηκών κατεργασίας. Επίσης, βρέθηκε ότι το keyhole είναι πιο ευαίσθητο σε αλλαγές των παραμέτρων κατεργασίας συγκριτικά με το conduction.

Παρόλα αυτά, κατά την διεργασία της τήξης στην SLM, μία συγκεκριμένη ποσότητα όγκου συρρικνώνεται λόγω των κενών του στρώματος σκόνης. Η επιφάνεια τότε πηγαίνει χαμηλότερα αφού το κενό γεμίζει με τηγμένο υλικό. Αυτή η συρρίκνωση του όγκου επηρεάζει την μορφολογία του τήγματος επειδή επηρεάζει την αγωγή θερμότητας με την περιβάλλουσα σκόνη. Ακόμα, η ροή θερμότητας για κάθε σημείο του υλικού αλλάζει λόγω των διαφορετικών αποστάσεων από το κέντρο του λέιζερ. Για να ληφθεί υπόψη η συρρίκνωση του όγκου στην προσομοίωση, χρησιμοποιείται μία απλοποιημένη μέθοδος που απενεργοποιεί το συρρικνωμένο στοιχείο. Αφού τηχθεί το στρώμα σκόνης, ο συρρικνωμένος όγκος (Εικόνα 4) εκλαμβάνεται ως κενός χώρος με μηδενική αγωγιμότητα.



Εικόνα 4 Συρρίκνωση όγκου λόγω του αρχικού πορώδους του στρώματος σκόνης και αφαίρεση υλικού λόγω εξάτμισης.

Τα κύρια συμπεράσματα από αυτή τη μελέτη είναι τα ακόλουθα:

1. Τα αποτελέσματα του μοντέλου είναι σε καλή συμφωνία (σφάλμα εντός του 6%) με τα πειραματικά δεδομένα.

2. Η μορφή του keyhole δεν προτιμάται επειδή δεν είναι ενεργειακά αποδοτική και είναι ευαίσθητη σε αλλαγές της ισχύος του λέιζερ.
3. Η απόδοση της υβριδικής πηγής συγκρίνεται με τις παραδοσιακές πηγές. Τα αποτελέσματα δείχνουν ότι ο συνδυασμός χωρικών και επιφανειακών ροών θερμότητας οδηγεί σε πιο ρεαλιστικά μοντέλα.

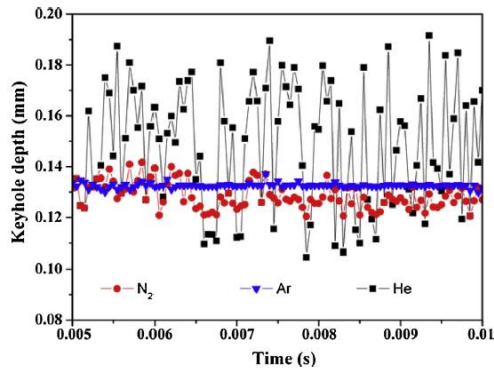
Οι Gu D. et al. [3] παρέχουν μία πολλαπλής κλίμακας μοντελοποίηση και τα αντίστοιχα πειραματικά αποτελέσματα για την SLM κατεργασία μετάλλων, κραμάτων και συνθέτων μεταλλικής μήτρας, συμπεριλαμβανομένου κραμάτων αλουμινίου, νικελίου και συνθέτων αλουμινίου και νικελίου ενισχυμένων με κεραμικά σωματίδια. Η SLM των μετάλλων διέπεται από αρχές πολλαπλής κλίμακας, συμπεριλαμβανομένης της ανάπτυξης της μικροδομής κατά την διάρκεια της διεργασίας (μικροκλίμακα), της απορρόφησης και της τήξης των σωματιδίων της σκόνης (μεσοκλίμακα) και των τάσεων και παραμορφώσεων των κατασκευών με SLM (μακροκλίμακα).

Οι Khairallah S. et al. [4] παρουσιάζουν την επίδραση της πίεσης υποχώρησης και του φαινομένου Marangoni στην LPBF του 316L ανοξειδωτού χάλυβα.

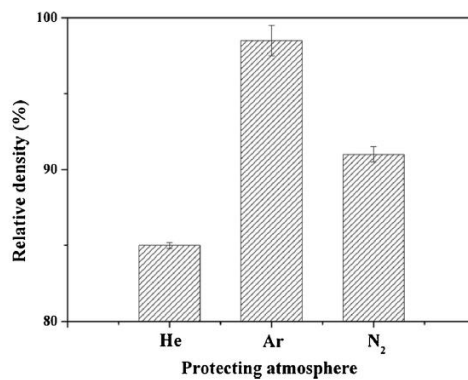
Ενώ η ακτινοβολία είναι πολυώνυμο 4^{ου} βαθμού ως προς τη θερμοκρασία, η εξάτμιση είναι πιο αποτελεσματική στη μείωση της ανώτερης θερμοκρασίας της επιφάνειας λόγω της εκθετικής της εξάρτησης από την θερμοκρασία. Αυτό έχει μεγάλη επίδραση στην πίεση υποχώρησης καθώς και αυτή εξαρτάται εκθετικά από τη θερμοκρασία. Η δύναμη υποχώρησης υπερνικά την τάση επιφάνειας, που αντιτίθεται στην θλιπτική επίδραση της δύναμης υποχώρησης. Όταν το τεμάχιο ψυχθεί η τάση επιφάνειας κυριαρχεί και προκαλεί πόρους όταν τα τοιχώματα συνθλιβονται. Για αυτό, οι μεγάλες πιέσεις πρέπει να αποφεύγονται ώστε να μειωθεί ο σχηματισμός των πόρων. Τέτοιες μεγάλες πιέσεις δημιουργούνται στην απότομη αλλαγή κατεύθυνσης κίνησης του λέιζερ, οπότε σε αυτές τις περιπτώσεις προτείνεται να μειώνεται λίγο η ένταση του λέιζερ.

Οι Dai D. et al. [5] πραγματοποιούν προσομοίωση της δυναμικής του τήγματος μεταβαίνοντας από conduction σε keyhole μορφή των SLM-κατεργασμένων TiC/AlSi10Mg τεμαχίων, χρησιμοποιώντας μέθοδο πεπερασμένου όγκου (FVM). Τα συμπεράσματα που προκύπτουν δίνονται παρακάτω:

1. Το βάθος του τήγματος σταδιακά αυξάνεται και φτάνει ένα σταθερό βάθος και μετά ταλαντώνεται γύρω από αυτό το βάθος καθώς προχωρά η κατεργασία. Το βάθος του τήγματος ελέγχεται από την αγωγή θερμότητας και την πίεση υποχώρησης που προκαλείται από την εξάτμιση του μετάλλου.
2. Υπάρχει σημαντική διαφορά στην ταλαντωτική συμπεριφορά του βάθους του τήγματος για διαφορετικές προστατευτικές ατμόσφαιρες. Φαίνεται ότι η χρήση Ar ως προστατευτική ατμόσφαιρα έχει σταθεροποιητική ικανότητα που μειώνει τις ταλαντώσεις του βάθους του keyhole (Διάγραμμα 1) δίνοντας πυκνά SLM τεμάχια (Διάγραμμα 2).



Διάγραμμα 1 Καμπύλες βάθους τήγματος της keyhole μορφής της SLM χρησιμοποιώντας διαφορετικές ατμόσφαιρες.



Διάγραμμα 2 Σχετική πυκνότητα των SLM-κατεργασμένων τεμαχίων χρησιμοποιώντας διαφορετικές προστατευτικές ατμόσφαιρες.

3. Η προστατευτική ατμόσφαιρα έχει σημαντικό ρόλο στον καθορισμό της ποιότητας της επιφάνειας του SLM-κατεργασμένου τεμαχίου. Με την εφαρμογή της Ar ατμόσφαιρας, προκύπτει ένα σταθερό βάθος τήγματος συνδυασμένο με ομοιόμορφη πίεση επιφάνειας στην ελεύθερη επιφάνεια του τήγματος, οδηγώντας στον σχηματισμό καλής επιφανειακής μορφολογίας.
4. Η ποιότητα επιφανείας και η σχετική πυκνότητα μετρούνται πειραματικά και είναι σε συμφωνία με τα αποτελέσματα της προσομοίωσης.

Οι Le T. et al. [6] χρησιμοποιούν ένα τρισδιάστατο θερμορυστομηχανικό μοντέλο για να εξετάσουν την επίδραση της ανάστροφης ροής Marangoni, που εισάγεται από την συγκέντρωση του θείου στην σκόνη 316L ανοξείδωτου χάλυβα, στις διαστάσεις του τήγματος. Στην προσομοίωση χρησιμοποιείται χωρική πηγή γκαουσιανής κατανομής και η απορροφητικότητα της σκόνης αξιολογείται μέσω προσομοιώσεων ανίχνευσης ακτίνων. Επί πρόσθετα, η επιφανειακή τάση, που ελέγχει την ροή Marangoni, περιλαμβάνεται ως μία απλή γραμμική συνάρτηση της συγκέντρωσης θείου. Τα κύρια ευρήματα αυτής της μελέτης δίνονται παρακάτω:

1. Τα επίπεδα θείου της σκόνης έχουν σημαντικό ρόλο στον καθορισμό της ροής του ρευστού στο τήγμα. Για υψηλότερα επίπεδα θείου (>60ppm), η κατεύθυνση της ροής

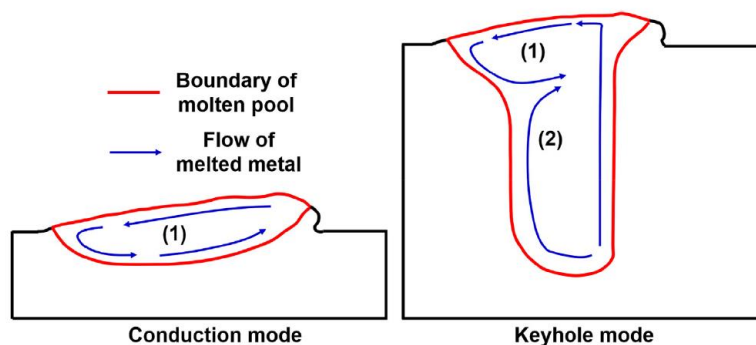
Marangoni αλλάζει από εξωστρεφής σε εσωστρεφής, οδηγώντας σε βαθύτερο και στενότερο τήγμα. Επιπλέον, η ανάστροφη ροή Marangoni απομακρύνει τις αέριες φουσκάλες, μειώνοντας το ελάττωμα των πόρων.

2. Η παρούσα μελέτη επικεντρώνεται στην επίδραση της εσωστρεφούς ροής Marangoni, αγνοώντας την συρρίκνωση του όγκου και την πίεση υποχώρησης. Για αυτό το λόγο η προσομοίωση δίνει μεγαλύτερες τιμές βάθους στην ορφή conduction και μικρότερες στην μορφή keyhole σε σύγκριση με αντίστοιχα πειραματικά δεδομένα.

Οι Miyagi M. et al. [7] διεξήγαγαν παρατηρήσεις σε SLM-κατεργασμένο ωστενιτικό ανοξείδωτο χάλυβα. Το βάθος και το πλάτος του keyhole αυξάνονται, και η διακύμανση του βάθους του keyhole μειώνεται, καθώς η ισχύς του λέιζερ αυξάνεται. Η διακύμανση του βάθους του keyhole αυξάνεται όταν δεν υπάρχει προστατευτικό αέριο. Τέλος, καθώς η εστιακή απόσταση του λέιζερ αυξάνεται, η διακύμανση του βάθους του keyhole αυξάνεται.

Οι Heeling T. et al. [8] παρουσιάζουν ένα τρισδιάστατο αριθμητικό μοντέλο για την SLM-διεργασία, που επιτρέπει μία λεπτομερή οπτική της δυναμικής της κατεργασίας με χαμηλό υπολογιστικό κόστος (χονδροειδές πλέγμα). Το μοντέλο χρησιμοποιεί τη μέθοδο των πεπερασμένων διαφορών και περιλαμβάνει φυσικά φαινόμενα όπως απορρόφηση του λέιζερ, Marangoni, εξάτμιση, πίεση υποχώρησης και θερμοκρασιακά εξαρτώμενες ιδιότητες του υλικού. Το μοντέλο συγκρίνεται με πειραματικά δεδομένα ανοξείδωτου χάλυβα 316L και υπερκράματος νικελίου IN738LC. Τα αποτελέσματα δείχνουν την σημασία της εξάτμισης και της πίεσης υποχώρησης για την ακριβή πρόβλεψη της δυναμικής του τήγματος. Τέλος, παρουσιάζεται ένας τρόπος πρόβλεψης των παραμέτρων της κατεργασίας με χαμηλό υπολογιστικό κόστος.

Οι Wang H. et al. [9] ανέπτυξαν ένα συζευγμένο θερμικό-μηχανικό-ρευστομηχανικό μοντέλο για να μελετήσουν την δυναμική μικροκλίμακας μεταλλικής σκόνης και συγκεκριμένα του Ti6Al4V κατά τη διάρκεια της SLM. Χρησιμοποιώντας διαφορετικές τιμές ισχύος λέιζερ, πάχους στρώσης και ενδιάμεσων διαστημάτων, συγκρίνουν την εξέλιξη της conduction και keyhole μορφής. Υπάρχει μόνο μία κυκλική ροή στη διαμήκη διατομή του τήγματος στην conduction μορφή, ενώ δύο κυκλικές ροές εμφανίζονται στην keyhole μορφή (Εικόνα 5).



Εικόνα 5 Σχηματική αναπαράσταση της κυκλικής ροής σε conduction και keyhole μορφή.

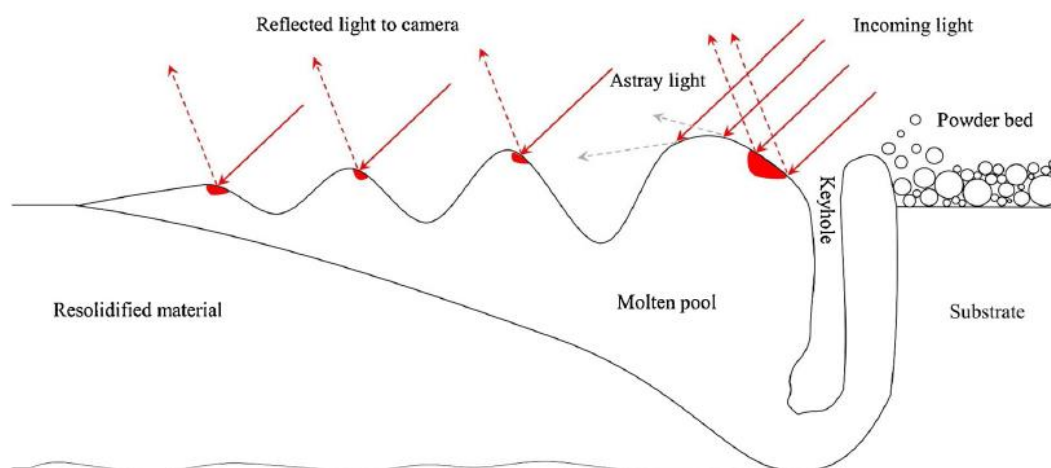
Η βαρύτητα οδηγεί το τηγμένο μέταλλο να γεμίσει τα κενά της σκόνης. Τα αποτελέσματα της προσομοίωσης δείχνουν ότι επιτυγχάνεται μεγαλύτερο πάχος τύπωσης στην keyhole μορφή σε σχέση με την conduction μορφή. Η διανομή της θερμότητας σε τυπώσεις πολλαπλής τροχιάς στην conduction μορφή είναι πιο ομοιόμορφη σε σύγκριση με την keyhole μορφή, οδηγώντας σε πιο ομοιόμορφη μικροδομή. Αυτή η μελέτη παρουσιάζει τρόπους για τον έλεγχο της μικροδομής και των ατελειών, μέσω της ρύθμισης των παραμέτρων της κατεργασίας.

Παρόλα αυτά, η αδυναμία αυτής της μελέτης σχετίζεται με το γεγονός ότι η εξάτμιση του υλικού δεν λαμβάνεται υπόψη.

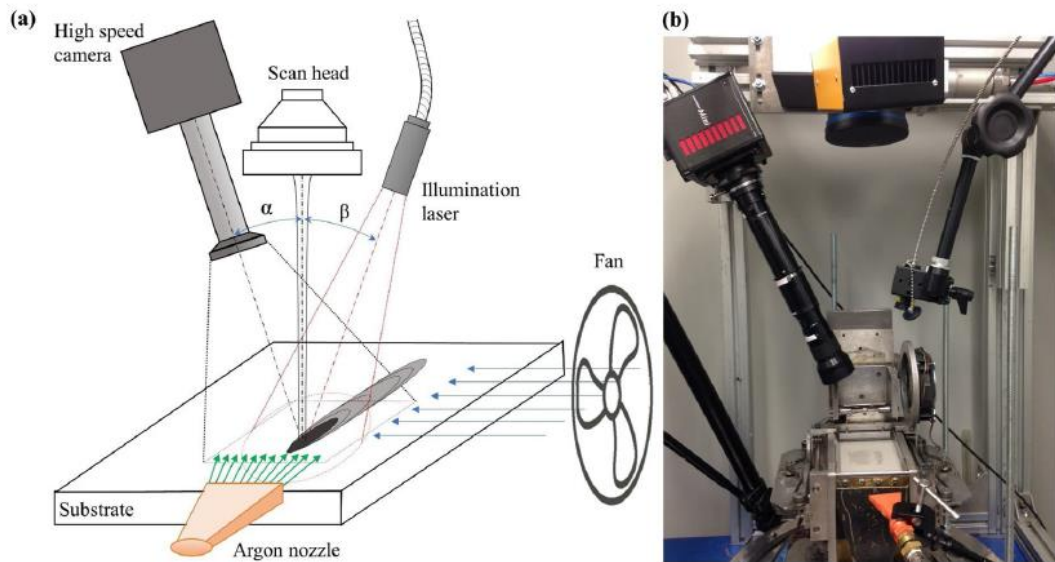
Οι King W. et al. [10] αναζητούν μέσω πειραμάτων απλής τροχιάς τις συνθήκες ύπαρξης της keyhole μορφής σε μεταλλικές ΠΚ ανοξείδωτου χάλυβα 316L. Συγκεκριμένα:

1. Η χρήση της κανονικοποιημένης ενθαλπίας που συνδέει την ισχύ, την ταχύτητα και το μέγεθος της ακτίνας αξιολογείται πειραματικά. Η σχέση αυτή είναι χρήσιμη μέχρι το κατώφλι του keyhole. Πάνω από το κατώφλι, η κανονικοποιημένη ενθαλπία δεν περιλαμβάνει την φυσική που εμφανίζεται στην keyhole μορφή.
2. Υπάρχει ένα κατώφλι μετάβασης από την conduction στη keyhole μορφή που εξαρτάται από την ισχύ, την ταχύτητα και το μέγεθος της ακτίνας λέιζερ που εκφράζεται σε όρους κανονικοποιημένης ενθαλπίας ως $\Delta H/h_s \approx (30 \pm 4)$. Το κατώφλι αναμένεται να εξαρτάται από το πάχος της στρώσης.
3. Το κατώφλι για την keyhole μορφή μπορεί να χρησιμοποιηθεί για την εύρεση της βέλτιστης περιοχής ισχύος, ταχύτητας, μεγέθους ακτίνας και την παραγωγή καλής ποιότητας τρισδιάστατων τεμαχίων.

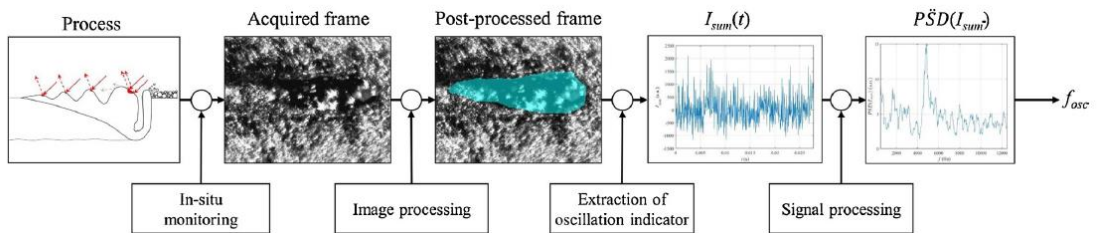
Οι Carpio L. et al. [11] παρουσιάζουν μία μεθοδολογία για τον υπολογισμό του βάθους τήγματος της SLM. Το σύστημα παρακολούθησης στηρίζεται στην μέτρηση των επιφανειακών ταλαντώσεων του τήγματος μέσω των ανακλάσεων μίας δέσμης φωτός (Εικόνα 6) που καταγράφονται σε μία υψηλής ταχύτητας κάμερα (Εικόνα 7). Ένας αλγόριθμος επεξεργασίας εικόνας και ανάλυσης σήματος έχει αναπτυχθεί ώστε να εξάγει έναν δείκτη αντιπροσωπευτικό της συχνότητας της ταλάντωσης της επιφάνειας του τήγματος (Εικόνα 8).



Εικόνα 6 Σχηματική αναπαράσταση του τήγματος κατά τη διάρκεια της LPBF.



Εικόνα 7 Πειραματική διάταξη (α) σχηματική αναπαράσταση, (β) πραγματική διάταξη.



Εικόνα 8 Δομικό διάγραμμα της μεθοδολογίας που αναπτύχθηκε.

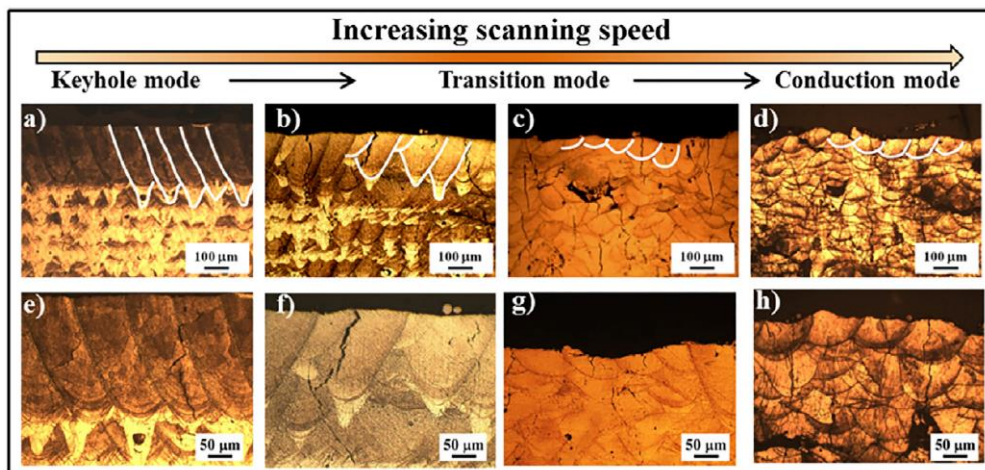
Μετρήθηκαν ταλαντώσεις από 3.5kHz έως 5.5kHz. Για μεγαλύτερη ισχύ, η συχνότητα των ταλαντώσεων μειωνόταν, ενώ αυξανόταν το βάθος του τήγματος. Αντίθετα, αύξηση της συχνότητας των ταλαντώσεων οδηγούσε σε ρηχότερο τήγμα.

Οι Bertoli U. et al. [12] μελετούν την χρήση της Ογκομετρικής Πυκνότητας Ενέργειας (Volumetric Energy Density- VED) ως κύρια παράμετρο της SLM κατεργασίας του ανοξείδωτου χάλυβα 316L. Τα συμπεράσματα είναι τα εξής:

1. Μείωση του VED σε τιμές κάτω των 100 J/mm^3 οδηγεί σε σφαιρικά ελαττώματα (balling). Επιπλέον, πολύ υψηλές τιμές του VED οδηγούν σε ασυνέχειες.
2. Το VED μπορεί πολύ αποτελεσματικά να προβλέψει το πλάτος του τήγματος.
3. Το VED δεν είναι κατάλληλος δείκτης πρόβλεψης του βάθους του τήγματος, ειδικά στην keyhole μορφή.
4. Το VED είναι ένας θερμοδυναμικός δείκτης, που δεν μπορεί όμως να αποτυπώσει τα φυσικά φαινόμενα που σχετίζονται με το SLM.

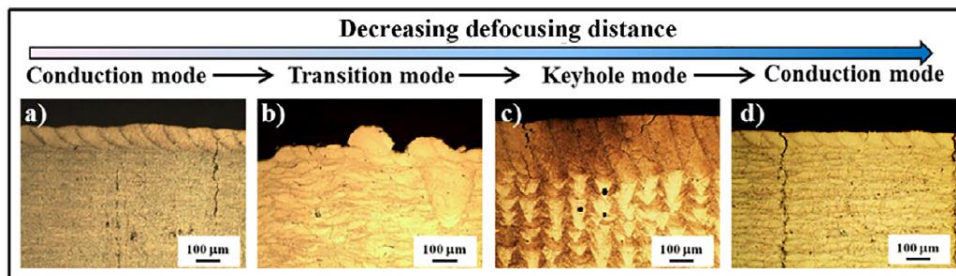
Οι Qi T. et al. [13] μελετούν την μετάβαση μεταξύ conduction και keyhole. Τα συμπεράσματα αυτής της μελέτης δίνονται παρακάτω:

1. Για σταθερή εστιακή απόσταση του λέιζερ, με αύξηση της ταχύτητας σάρωσης η μορφή μετατρέπεται από keyhole σε transition και μετά σε conduction μορφή (Εικόνα 9).



Εικόνα 9 Μορφές τήγματος για αυξανόμενη ταχύτητα σάρωσης.

2. Για σταθερή ταχύτητα σάρωσης, μείωση της εστιακής απόστασης οδηγεί από conduction σε transition σε keyhole και πάλι σε conduction μορφή (Εικόνα 10).



Εικόνα 10 Μορφή τήγματος καθώς η εστιακή απόσταση μειώνεται.

Οι Zhang D. et al. [14] δημιούργησαν ένα τρισδιάστατο μοντέλο πεπερασμένων στοιχείων που περιλαμβάνει τη διείσδυση του λέιζερ και το φαινόμενο Marangoni και το χρησιμοποιούν για τη μελέτη του θερμικού και ρευστομηχανικού πεδίου του τήγματος σε SLM κατεργασία του κράματος Inconel 718. Προέκυψαν τα παρακάτω συμπεράσματα:

1. Χρησιμοποιείται θερμική πηγή που λαμβάνει υπόψη τις θερμοφυσικές ιδιότητες της σκόνης με το πορώδες και τις πολλαπλές σκεδάσεις. Τα αποτελέσματα της προσομοίωσης είναι σε συμφωνία με τα πειραματικά δεδομένα.
2. Οι επιδράσεις της συναγωγής και της αγωγής στο σχήμα του τήγματος μελετήθηκαν στην SLM κατεργασία με χρήση σταθερής πηγής. Τα αποτελέσματα έδειξαν ότι στο τήγμα κυριαρχεί η συναγωγή έναντι της αγωγής και επιταχύνει την ροή, βοηθώντας τη μεταφορά θερμότητας. Η συναγωγή κάνει το τήγμα πλατύτερο και η αγωγή το κάνει βαθύτερο.
3. Οι επιδράσεις της συναγωγής και της αγωγής στο σχήμα του τήγματος μελετήθηκαν στην SLM κατεργασία και με χρήση κινητής πηγής. Τα αποτελέσματα είναι τα ίδια με τη σταθερή πηγή.

4. Η εξάτμιση του υλικού δεν λαμβάνεται υπόψη σε αυτό το μοντέλο.

Οι Parazoglou E. et al. [15] παρουσιάζουν μία μεθοδολογία για την μοντελοποίηση της εξέλιξης και του τελικού σχήματος του τήγματος, όπως επίσης και των θερμικών φαινομένων που πραγματοποιούνται κατά την conduction SLM κατεργασία. Αρχικά, ο συντελεστής απορρόφησης της ακτίνας λέιζερ υπολογίζεται βάσει των εξισώσεων Fresnel, λαμβάνοντας υπόψη τις πολλαπλές σκεδάσεις της ακτίνας λέιζερ καθώς αλληλεπιδρά με τη σκόνη. Για την τηγμένη φάση, ο συντελεστής απορρόφησης καθορίζεται από την θεωρία Drude. Στη συνέχεια, υπολογίζονται οι θερμοφυσικές ιδιότητες του υλικού. Προκειμένου να υπολογιστεί η θερμική αγωγιμότητα της σκόνης, χρησιμοποιείται το μοντέλο των Zehner-Schlünder, ενώ για τις υπόλοιπες ιδιότητες χρησιμοποιήθηκαν αναλυτικές σχέσεις από τη βιβλιογραφία, οι οποίες εξαρτώνται και από τη θερμοκρασία και από τη φάση του υλικού. Ο συντελεστής συναγωγής υπολογίστηκε βάσει του αριθμού Nusselt. Ακόμα, η απώλεια ενέργειας λόγω αφαίρεσης υλικού υπολογίστηκε, ενώ η λανθάνουσα θερμότητα κατά την τήξη και την εξάτμιση λήφθηκαν υπόψη. Επιπλέον, μία κινούμενη ογκομετρική γκαουσιανή πηγή θερμότητας χρησιμοποιήθηκε για να προσομοιώσει την ακτίνα του λέιζερ.

Έγιναν τρεις προσομοιώσεις με διαφορετικά VED και τα αποτελέσματα συγκρίθηκαν με πειραματικά δεδομένα. Τα συμπεράσματα αυτής της μελέτης είναι:

1. Ο συντελεστής απορρόφησης της σκόνης σε στερεή μορφή υπολογίστηκε στο 58.66%. Ο συντελεστής αυτός σταδιακά αυξάνεται καθώς το υλικό τήκεται και φτάνει το 82%.
2. Στα αριθμητικά μοντέλα της SLM, οι θερμοφυσικές ιδιότητες της σκόνης πρέπει να υπολογίζονται βάσει των ιδιοτήτων του πορώδους, καθώς διαφέρουν από αυτές του συμπαγούς υλικού.
3. Τα ονομαστικά βάθη και πλάτη του τήγματος υπολογίστηκαν και βρέθηκαν σε συμφωνία με τα πειραματικά δεδομένα.
4. Οι απώλειες θερμότητας λόγω αφαίρεσης υλικού είναι οι υψηλότερες, ακολουθούμενες από τις απώλειες λόγω ακτινοβολίας που είναι σχεδόν σταθερές, ενώ οι απώλειες λόγω συναγωγής είναι χαμηλές.

Συμπεράσματα:

Η μορφή keyhole έχει μελετηθεί εκτενώς για τις συγκολλήσεις με λέιζερ ([16], [17]). Παρόλα αυτά, η βιβλιογραφία είναι περιορισμένη για το keyhole της SLM κατεργασίας. Οι σχετικές με την SLM δημοσιεύσεις ([1], [3], [6], [8], [11], [12], [14], [15]) εστιάζουν περισσότερο στην conductive μορφή του τήγματος και όχι στην keyhole μορφή.

Επιπλέον, οι περισσότερες δημοσιεύσεις μελετούν το τήγμα μέσω δεικτών και συντελεστών (όπως είναι η κανονικοποιημένη ενθαλπία) ([10]) ή με μοντέλα που δεν λαμβάνουν υπόψη το πολύ σημαντικό φαινόμενο της εξάτμισης υλικού ([4], [5], [9]), πράγμα που οδηγεί σε λιγότερο ακριβή αποτελέσματα.

Τα υλικά που χρησιμοποιούνται στις παραπάνω δημοσιεύσεις είναι ανοξείδωτος χάλυβας, κράματα αλουμινίου και κράματα νικελίου. Πολύ λίγες μελέτες χρησιμοποιούν κράματα αλουμινίου (όπως το Ti6Al4V). Ακόμα, οι περισσότερες δημοσιεύσεις θεωρούν σταθερές

τιμές των ιδιοτήτων των υλικών, ενώ στην πραγματικότητα οι ιδιότητες αυτές εξαρτώνται από τη θερμοκρασία ([8], [15]).

Προκειμένου να μειωθούν το κενό και οι περιορισμοί της υπάρχουσας βιβλιογραφίας, η παρούσα διπλωματική εργασία μελετά την keyhole μορφή σε SLM-κατεργασμένο Ti6Al4V (με ιδιότητες υλικού που εξαρτώνται από τη θερμοκρασία), την μεταφορά θερμότητας και την εξάτμιση του μετάλλου.

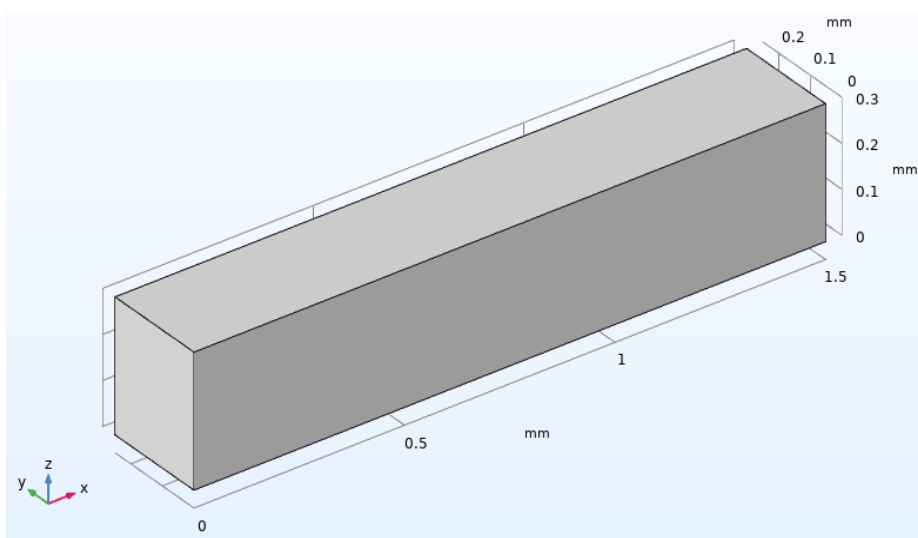
Μοντελοποίηση και Προσομοίωση

Στην παρούσα μελέτη, αναπτύσσεται ένα μοντέλο που προσομοιώνει και προβλέπει τα γεωμετρικά χαρακτηριστικά του τήγματος της SLM. Στόχος είναι να συλλεχθούν ακριβή και ρεαλιστικά αποτελέσματα χρησιμοποιώντας μία γενική μέθοδο, που αποφύγει την ευρεία χρήση ημιεμπειρικών συντελεστών ή σύνθετων και εξειδικευμένων μοντέλων θερμικών πηγών. Συγκεκριμένα, αναπτύχθηκε ένα μοντέλο πεπερασμένων στοιχείων μεταφοράς θερμότητας και παραμορφωμένης γεωμετρίας. Η μεταφορά θερμότητας αποτελεί τον πυρήνα για κάθε προσομοίωση SLM, ενώ η παραμορφωμένη γεωμετρία υιοθετήθηκε για να μοντελοποιήσει και να προσομοιώσει την αφαίρεση υλικού κατά τη διάρκεια της SLM. Η αφαίρεση υλικού και κατά συνέπεια η μεταφορά ενθαλπίας κατά τη διάρκεια της SLM αποτελεί κύριο μηχανισμό που επηρεάζει σημαντικά τα χαρακτηριστικά του τήγματος και παρόλα αυτά συχνά παραβλέπεται ή μοντελοποιείται εν μέρει. Για ορισμένες συνθήκες κατεργασίας, όπως ο σχηματισμός του keyhole, αυτή η αφαίρεση υλικού είναι σημαντική στον σχηματισμό της γεωμετρίας του τήγματος, για αυτό θα πρέπει να λαμβάνεται υπόψη και να μοντελοποιείται. Ακόμα, ένας αριθμός από επιπρόσθετα χαρακτηριστικά έχουν υιοθετηθεί. Οι θερμοφυσικές ιδιότητες του υλικού εξαρτώνται από τη θερμοκρασία και διαφοροποιούνται μεταξύ πορώδους και συμπαγούς υλικού, ενώ η λανθάνουσα θερμότητα κατά τη μεταβολή των φάσεων, η τήξη και η εξάτμιση λήφθηκαν και αυτές υπόψη. Επιπλέον, οι θερμικές απώλειες λόγω της συναγωγής και της ακτινοβολίας έχουν υπολογιστεί, ενώ η απώλεια μάζας και ενθαλπίας λόγω της αφαίρεσης υλικού μοντελοποιήθηκαν μέσω της παραμορφωμένης γεωμετρίας, περιορίζοντας έτσι τους βαθμούς ελευθερίας του μοντέλου. Τέλος, η αξιολόγηση του μοντέλου γίνεται μέσω σύγκρισης των αποτελεσμάτων με πειραματικά δεδομένα από την βιβλιογραφία, μεθοδολογία που χρησιμοποιείται ευρύτατα από πολλές μελέτες.

Το μοντέλο που χρησιμοποιήθηκε για της προσομοιώσεις είναι ένα τρισδιάστατο ορθογώνιο μπλοκ (Εικόνα 11) με τις ακόλουθες διαστάσεις:

- Πλάτος: $W= 1\text{mm}$ or 1.5mm
- Πάχος: $D= 0.25\text{mm}$
- Ύψος: $H=0.3\text{mm}$

Συγκεκριμένα, 0.27mm είναι το ύψος του υποστρώματος και 30mm είναι το ύψος του στρώματος σκόνης.



Εικόνα 11 Το μοντέλο που χρησιμοποιήθηκε στις προσομοιώσεις.

Το αρχικό σημείο Ο (0,0,0) του συστήματος συντεταγμένων τοποθετείται στην μπροστινή-κάτω-αριστερή γωνία του μπλοκ, που δίνεται στην Εικόνα 11.

Στην παρούσα μελέτη, το μοντέλο χρησιμοποιεί τρία «υλικά», που είναι τα ακόλουθα:

- N₂ (το προστατευτικό αέριο),
- Συμπαγές Τί6Α14V,
- Πορώδες μέσο (συνδυασμός Τί6Α14V και N₂).

Επιπλέον, όλες οι ιδιότητες των υλικών εξαρτώνται από τη θερμοκρασία.

Ιδιότητες αζώτου

Στο [18], δίνονται οι τιμές της πυκνότητας, της ειδικής θερμοχωρητικότητας, της συνεκτικότητας, της θερμικής αγωγιμότητας και του συντελεστή θερμικής διαστολής του αζώτου για διάφορες θερμοκρασίες (Πίνακας 3).

Πίνακας 3 Ιδιότητες αζώτου.

T (K)	ρ (kg/m ³)	Cp (KJ/kg K)	μ (μPa s)	k (W/m K)	β (1/K)
Temperature	Density	Specific Heat Capacity	Viscosity	Thermal Conductivity	Thermal Expansion Coefficient
200	1.7108	1.0429	12.947	0.01824	0.005
300	1.1421	1.0408	17.84	0.0262	0.003333333
400	0.8538	1.0459	21.98	0.03335	0.0025
500	0.6824	1.0555	25.7	0.03984	0.002
600	0.5687	1.0756	29.11	0.0458	0.001666667
700	0.4934	1.0969	32.13	0.05123	0.001428571
800	0.4277	1.1225	34.84	0.05609	0.00125
900	0.3796	1.1464	37.49	0.0607	0.001111111
1000	0.3412	1.1677	40	0.06475	0.001
1100	0.3108	1.1857	42.28	0.0685	0.000909091
1200	0.2851	1.2037	44.5	0.07184	0.000833333

Στην παρούσα μελέτη, έχει θεωρηθεί ότι για θερμοκρασίες κάτω των 200K και άνω των 1200K, η τιμή της κάθε ιδιότητας παραμένει σταθερή και ίση με την τιμή στους 200K και 1200K, αντίστοιχα.

Με παρεμβολή στα παραπάνω δεδομένα, υπολογίζονται οι συναρτήσεις θερμοκρασίας των παραπάνω ιδιοτήτων (Διάγραμμα 3, Διάγραμμα 4, Διάγραμμα 5, Διάγραμμα 6):

$$\text{Πυκνότητα } N_2: \rho_{N_2}(T) \left(\frac{kg}{m^3} \right) = \begin{cases} 1.7108, & 0 \leq T(K) \leq 200 \\ 3.048 \cdot 10^{-12} \cdot T^4 - 1.105 \cdot 10^{-8} \cdot T^3 + 1.521 \cdot 10^{-5} \cdot T^2 - 0.009876 \cdot T + 3.007, & 200 \leq T(K) \leq 1200 \\ 0.2851, & 1200 \leq T(K) \leq 10000 \end{cases} \quad (3)$$

With R²=0.9997.

$$\text{Ειδική θερμοχωρητικότητα } N_2: Cp_{N_2}(T) \left(\frac{J}{kgK} \right) = \begin{cases} 1042.9, & 0 \leq T(K) \leq 200 \\ 1.844 \cdot 10^{-10} \cdot T^4 - 8.533 \cdot 10^{-7} \cdot T^3 + 0.001322 \cdot T^2 - 0.6131 \cdot T + 1128, & 200 \leq T(K) \leq 1200 \\ 1203.7, & 1200 \leq T(K) \leq 10000 \end{cases} \quad (4)$$

With R²=0.9997.

Συνεκτικότητα N_2 : $\mu_{N_2}(T)(Pa \cdot s) =$

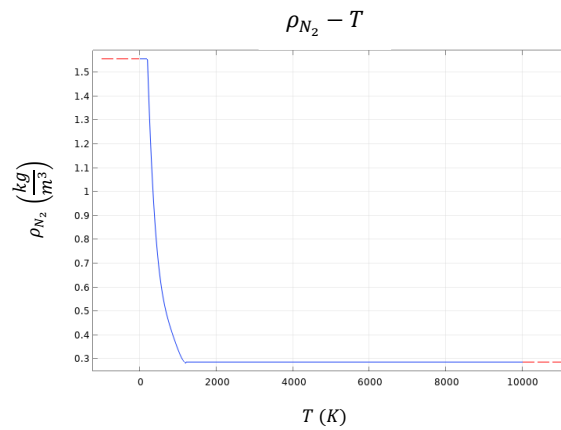
$$\begin{cases} 12.947 \cdot 10^{-6}, & 0 \leq T(K) \leq 200 \\ -4.72 \cdot 10^{-18} \cdot T^4 + 2.246 \cdot 10^{-14} \cdot T^3 - 4.531 \cdot 10^{-11} \cdot T^2 + 6.599 \cdot 10^{-8} \cdot T + 1.541 \cdot 10^{-6}, & 200 \leq T(K) \leq 1200 \\ 44.5 \cdot 10^{-6}, & 1200 \leq T(K) \leq 10000 \end{cases} \quad (5)$$

With $R^2=1$.

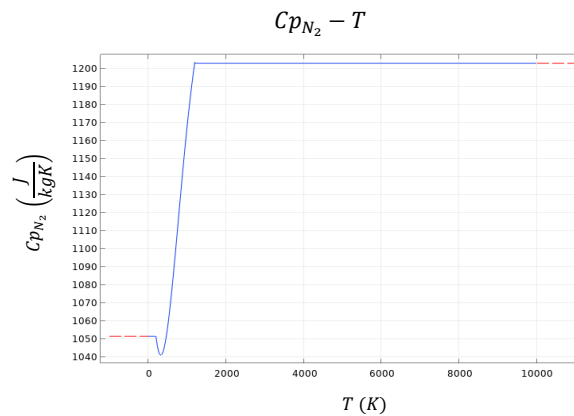
Θερμική αγωγιμότητα N_2 : $k_{N_2}(T) \left(\frac{W}{mK}\right) =$

$$\begin{cases} 0.01824, & 0 \leq T(K) \leq 200 \\ -4.006 \cdot 10^{-15} \cdot T^4 + 1.837 \cdot 10^{-11} \cdot T^3 - 5.027 \cdot 10^{-8} \cdot T^2 + 0.0001006 \cdot T + 8.439 \cdot 10^{-5}, & 200 \leq T(K) \leq 1200 \\ 0.07184, & 1200 \leq T(K) \leq 10000 \end{cases} \quad (6)$$

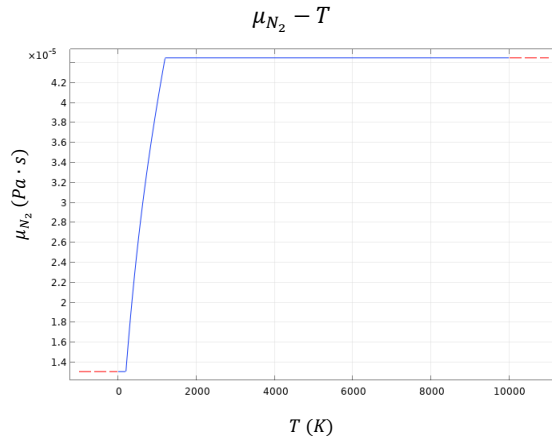
With $R^2=1$.



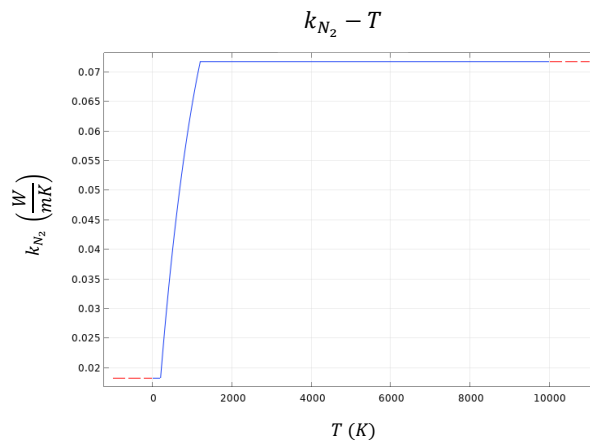
Διάγραμμα 3 Συνάρτηση πυκνότητας αζώτου.



Διάγραμμα 4 Συνάρτηση ειδικής θερμοχωρητικότητας αζώτου.



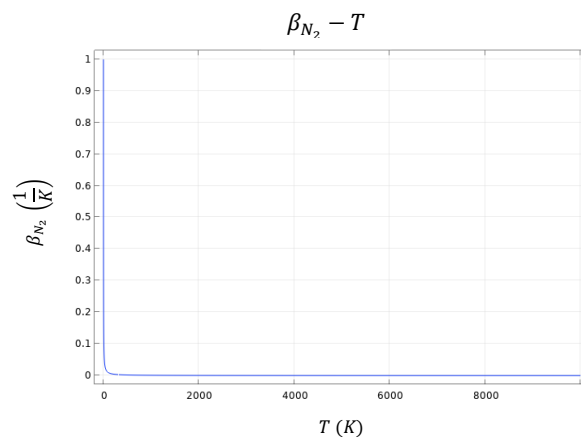
Διάγραμμα 5 Συνάρτηση συνεκτικότητας αζώτου.



Διάγραμμα 6 Συνάρτηση θερμικής αγωγιμότητας αζώτου.

Όλες οι υπόλοιπες ιδιότητες και οι χαρακτηριστικοί αριθμοί του αζώτου, μπορούν να υπολογιστούν ως αναλυτικές συναρτήσεις των παραπάνω κλαδικών συναρτήσεων. Συγκεκριμένα (Διάγραμμα 7),

$$\text{Συντελεστής θερμικής διαστολής } N_2: \beta_{N_2}(T) \left(\frac{1}{K}\right) = \frac{1}{T} \quad (7)$$



Διάγραμμα 7 Συνάρτηση συντελεστή θερμικής διαστολής αζώτου.

Ακόμα, στο [19], δίνονται οι τύποι για τον υπολογισμό των αδιάστατων αριθμών Prandtl (Pr), Grashof (Gr), Rayleigh (Ra) και Nusselt (Nu). Τελικά, υπολογίζεται και ο συντελεστής συναγωγής του αζώτου (h_{N_2}). Συγκεκριμένα (Διάγραμμα 8, Διάγραμμα 9, Διάγραμμα 10, Διάγραμμα 11, Διάγραμμα 12),

$$Pr(T) = \frac{c_{pN_2}(T) \cdot \mu_{N_2}(T)}{k_{N_2}(T)} \quad (8)$$

$$Gr(T) = \frac{g \cdot \rho_{N_2}^2(T) \cdot \beta_{N_2}(T) \cdot (T - T_\infty) \cdot L^3}{\mu_{N_2}^2(T)} \quad (9)$$

Όπου:

- $g \left(\frac{m}{s^2}\right)$ είναι η επιτάχυνση της βαρύτητας.
- $T_\infty (K)$ είναι η θερμοκρασία περιβάλλοντος.
- $L (m)$ είναι ένα χαρακτηριστικό μήκος του τεμαχίου. Πρέπει να διαλέγεται προσεκτικά, έτσι ώστε $10^4 \leq Ra \leq 10^7$.

Στην παρούσα μελέτη, $g = 9.81 \frac{m}{s^2}$, $T_\infty = 293.15K$, $L = 0.1m$, οπότε:

$$Gr(T) = \frac{9.81 \cdot \rho_{N_2}^2(T) \cdot \beta_{N_2}(T) \cdot (T - 293.15) \cdot 0.1^3}{\mu_{N_2}^2(T)} \quad (10)$$

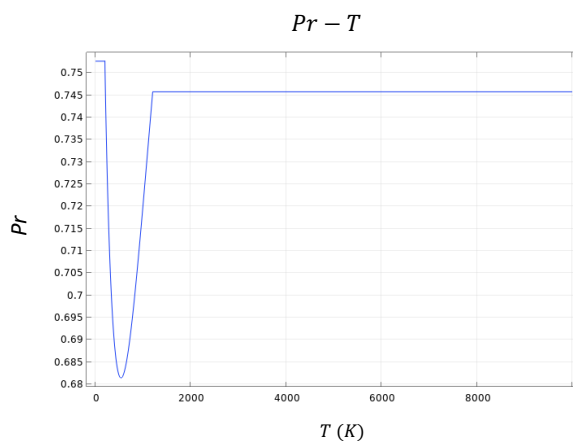
$$Ra(T) = Gr(T) \cdot Pr(T) \quad (11)$$

$$Nu(T) = 0.54 \cdot Ra^{1/4}(T) \quad (12)$$

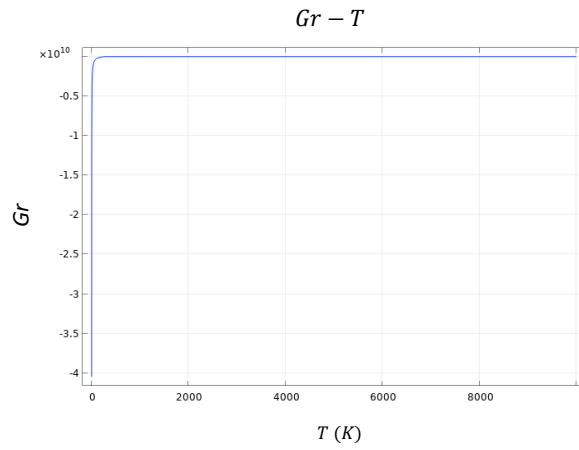
$$h_{N_2}(T) = \frac{Nu(T) \cdot k_{N_2}(T)}{L} \quad (13)$$

Στην παρούσα μελέτη, $L = 0.1m$, οπότε:

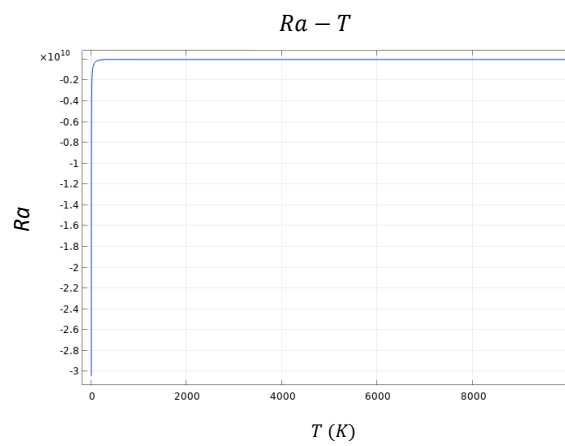
$$h_{N_2}(T) = \frac{Nu(T) \cdot k_{N_2}(T)}{0.1} \quad (14)$$



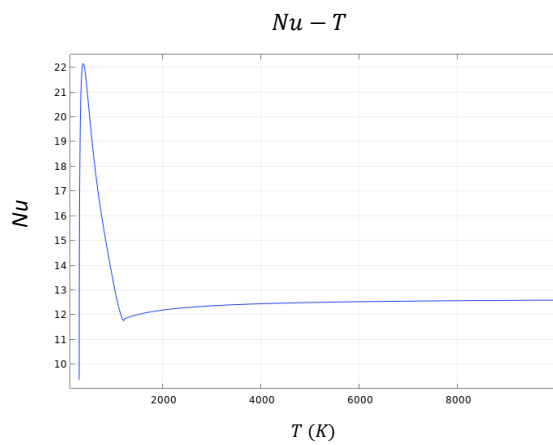
Διάγραμμα 8 Συνάρτηση αριθμού Prandtl αζώτου.



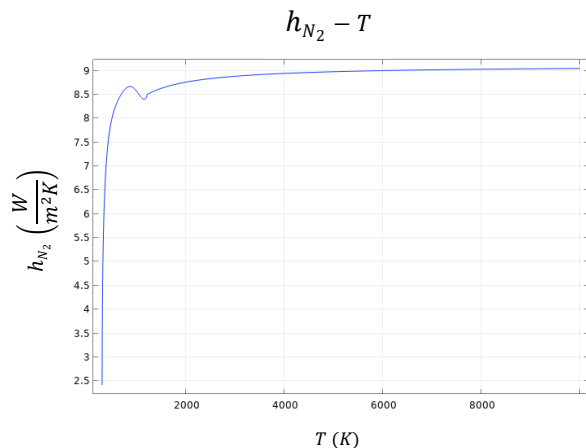
Διάγραμμα 9 Συνάρτηση αριθμού Grashof αζώτου.



Διάγραμμα 10 Συνάρτηση αριθμού Rayleigh αζώτου.



Διάγραμμα 11 Συνάρτηση αριθμού Nusselt αζώτου.



Διάγραμμα 12 Συνάρτηση συντελεστή συναγωγής αζώτου.

Ιδιότητες συμπαγούς Ti6Al4V

Το συμπαγές Ti6Al4V αποτελείται από τέσσερις φάσεις: α, β, υγρή και αέρια. Οι μεταβατικές θερμοκρασίες είναι:

- $T(\alpha \rightarrow \beta) = 1268.15K$
- $T(liquid) = 1923.15K$
- $T(gas) = 3315K$

Οι ιδιότητες του συμπαγούς Ti6Al4V εξαρτώνται από την θερμοκρασία. Για κάθε ιδιότητα και για κάθε φάση, ένα διαφορετικό πολυώνυμο υπολογίζεται.

Στο [20], δίνονται οι τιμές για το συμπαγές Ti6Al4V για διάφορες θερμοκρασίες (Πίνακας 4).

Πίνακας 4 Ιδιότητες συμπαγούς Ti6Al4V.

θ (degrees C)	T(K)	ρ (kg/m ³)	C_p (J/kgK)	k(W/mK)
Temperature	Temperature	Density	Thermal Heat Capacity	Thermal conductivity
25	298.15	4420	546	7
100	373.15	4406	562	7.45
200	473.15	4395	584	8.75
300	573.15	4381	606	10.15
400	673.15	4366	629	11.35
500	773.15	4350	651	12.6
600	873.15	4336	673	14.2
700	973.15	4324	694	15.5
800	1073.15	4309	714	17.8
900	1173.15	4294	734	20.2
995	1268.15	4282	753	22.7
996	1269.15	4282	641	19.3
1100	1373.15	4267	660	21
1200	1473.15	4252	678	22.9
1300	1573.15	4240	696	23.7
1400	1673.15	4225	714	24.6
1500	1773.15	4205	732	25.8
1600	1873.15	4198	750	27
1650	1923.15	4189	759	28.4
1651	1924.15	3920	831	33.4
1700	1973.15	3886	831	34.6

Με παρεμβολή στα παραπάνω δεδομένα, για καθένα από τα διαστήματα [0, 1268.15K], [1268.15K, 1923.15K], [1923.15K, 3315K], [3315K, 10000K], υπολογίζονται οι θερμοκρασιακά εξαρτώμενες κλαδικές συναρτήσεις των ιδιοτήτων του συμπαγούς Ti6Al4V.

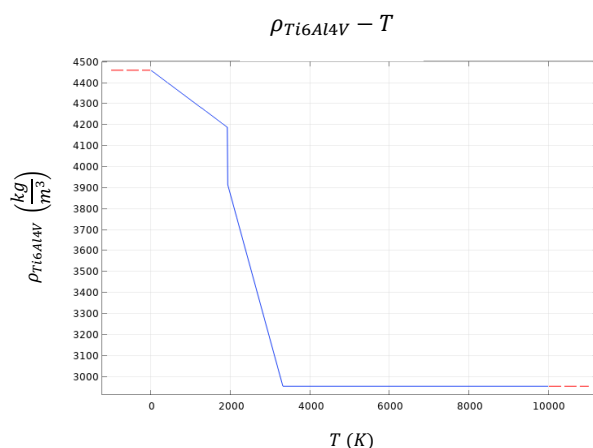
Έχει θεωρηθεί ότι στο διάστημα [1973.15K, 3315K] ισχύει το ίδιο πολυώνυμο με αυτό του διαστήματος [1923.15K, 1973.15K]. Για θερμοκρασίες άνω των 3315K, οι τιμές των ιδιοτήτων είναι σταθερές και ίσες με την αντίστοιχη τιμή στους 3315K.

Συγκεκριμένα, οι ιδιότητες του συμπαγούς Ti6Al4V δίνονται παρακάτω (Διάγραμμα 13, Διάγραμμα 14, Διάγραμμα 15):

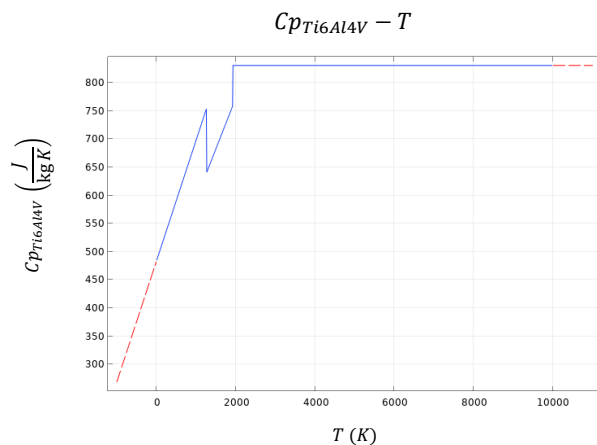
$$\text{Πυκνότητα συμπαγούς Ti6Al4V: } \rho_{\text{Ti6Al4V}}(T) \left(\frac{\text{kg}}{\text{m}^3} \right) = \begin{cases} -0.1419 \cdot T + 4461, & 0 \leq T(K) \leq 1268.15, \text{ with } R^2 = 0.9993 \\ -0.1427 \cdot T + 4463, & 1268.15 \leq T(K) \leq 1923.15, \text{ with } R^2 = 0.9958 \\ -0.6939 \cdot T + 5255, & 1923.15 \leq T(K) \leq 3315, \text{ with } R^2 = 1 \\ 3081.0113, & 3315 \leq T(K) \leq 10000 \end{cases} \quad (15)$$

$$\text{Ειδική θερμοχωρητικότητα συμπαγούς Ti6Al4V: } C_{p\text{Ti6Al4V}}(T) \left(\frac{\text{J}}{\text{kgK}} \right) = \begin{cases} 0.215 \cdot T + 483, & 0 \leq T(K) \leq 1268.15, \text{ with } R^2 = 0.9994 \\ 0.1802 \cdot T + 412.4, & 1268.15 \leq T(K) \leq 1923.15, \text{ with } R^2 = 1 \\ -1.567 \cdot 10^{-15} \cdot T + 831, & 1923.15 \leq T(K) \leq 3315, \text{ with } R^2 = 1 \\ 831, & 3315 \leq T(K) \leq 10000 \end{cases} \quad (16)$$

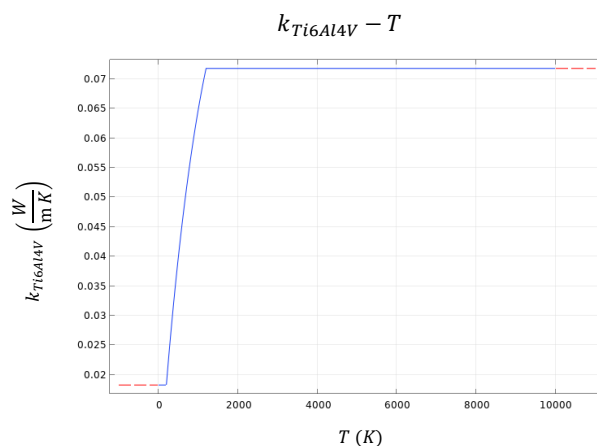
$$\text{Θερμική αγωγιμότητα συμπαγούς Ti6Al4V: } k_{\text{Ti6Al4V}}(T) \left(\frac{\text{W}}{\text{mK}} \right) = \begin{cases} 0.0157 \cdot T + 1.257, & 0 \leq T(K) \leq 1268.15, \text{ with } R^2 = 0.976 \\ 0.01274 \cdot T + 3.492, & 1268.15 \leq T(K) \leq 1923.15, \text{ with } R^2 = 0.9847 \\ 0.02449 \cdot T - 13.72, & 1923.15 \leq T(K) \leq 3315, \text{ with } R^2 = 1 \\ 67.4616, & 3315 \leq T(K) \leq 10000 \end{cases} \quad (17)$$



Διάγραμμα 13 Συνάρτηση πυκνότητας συμπαγούς Ti6Al4V.



Διάγραμμα 14 Συνάρτηση ειδικής θερμοχωρητικότητας συμπαγούς Ti6Al4V.



Διάγραμμα 15 Συνάρτηση θερμικής αγωγιμότητας συμπαγούς Ti6Al4V.

Μία άλλη πολύ σημαντική παράμετρος για την SLM είναι ο συντελεστής εκπομπής. Συντελεστής εκπομπής (ϵ) είναι ο λόγος της ακτινοβολίας που εκπέμπει ένα σώμα ή μία επιφάνεια προς την ακτινοβολία που εκπέμπει ένα μελανό σώμα σε ίδια θερμοκρασία. Για αυτό, είναι αδιάστατος και λαμβάνει τιμές από 0 έως 1, όταν επέρχεται θερμική ισορροπία. Ο συντελεστής εκπομπής $\epsilon(\lambda)$ εξαρτάται και από το μήκος κύματος της ακτινοβολίας. Αν ένας εκπομπός ακτινοβολίας είναι ουδέτερος όσον αφορά το μήκος κύματος, δηλαδή λαμβάνει σταθερή τιμή μικρότερη από 1, τότε ονομάζεται γκρι σώμα [21].

Στο [22] και για το Ti6Al4V, ο συντελεστής εκπομπής είναι συνάρτηση του μήκους κύματος και της θερμοκρασίας (Πίνακας 5).

Συγκεκριμένα,

Πίνακας 5 Συντελεστής εκπομπής ως συνάρτηση του μήκους κύματος και της θερμοκρασίας.

Wavelength (μm)	Linear fit
1.5	$1.1 \cdot 10^{-3}T - 0.634$
1.6	$1.14 \cdot 10^{-3}T - 0.658$
1.7	$1.26 \cdot 10^{-3}T - 0.744$
1.8	$1.35 \cdot 10^{-3}T - 0.832$

1.9	$1.53 \cdot 10^{-3}T - 0.991$
2	$1.69 \cdot 10^{-3}T - 1.780$
2.1	$1.56 \cdot 10^{-3}T - 0.975$
2.2	$1.56 \cdot 10^{-3}T - 0.970$

Για τον υπολογισμό των παραπάνω συναρτήσεων ως συναρτήσεις μόνο της θερμοκρασίας (Διάγραμμα 16), ακολουθείται η παρακάτω διαδικασία:

Όλες οι παραπάνω γραμμικές συναρτήσεις είναι της μορφής:

$$c_1(\lambda) \cdot T + c_2(\lambda) \quad (18)$$

Οπότε, μπορεί να δημιουργηθεί ο Πίνακας 6:

Πίνακας 6 Οι τιμές των c_1 και c_2 για διάφορα μήκη κύματος.

Wavelength λ (μm)	$c_1(\lambda(\mu\text{m}))$	$c_2(\lambda(\mu\text{m}))$
1.5	$1.1 \cdot 10^{-3}$	-0.634
1.6	$1.14 \cdot 10^{-3}$	-0.658
1.7	$1.26 \cdot 10^{-3}$	-0.744
1.8	$1.35 \cdot 10^{-3}$	-0.832
1.9	$1.53 \cdot 10^{-3}$	-0.991
2	$1.69 \cdot 10^{-3}$	-1.780
2.1	$1.56 \cdot 10^{-3}$	-0.975
2.2	$1.56 \cdot 10^{-3}$	-0.970

Η γραμμική παρεμβολή των δεδομένων c_1 δίνει ότι:

$$c_1(\lambda(\mu\text{m})) = 0.8083 \cdot 10^{-3} \cdot \lambda - 0.09667 \cdot 10^{-3}, \text{ with } R^2 = 0.8269 \quad (19)$$

Η γραμμική παρεμβολή των δεδομένων c_2 δίνει ότι:

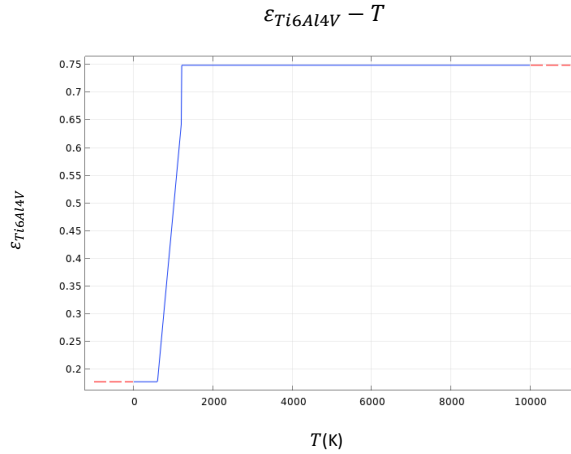
$$c_2(\lambda(\mu\text{m})) = -0.8576 \cdot \lambda + 0.6386, \text{ with } R^2 = 0.8275 \quad (20)$$

Στην παρούσα μελέτη, $\lambda = 1.080 \mu\text{m}$, so $c_1(1.080) = 0.0007763$ and $c_2(1.080) = -0.2876$.

Τελικά, $\varepsilon_{Ti6Al4V}(T) = 0.0007763 \cdot T - 0.2876$. Για θερμοκρασίες κάτω των 800K, ο συντελεστής εκπομπής είναι σταθερός και ίσος με τον συντελεστή εκπομπής στους 800K. Για θερμοκρασίες άνω των 1000K, ο συντελεστής εκπομπής είναι σταθερός και ίσος με τον συντελεστή εκπομπής στους 1000K.

Οπότε,

$$\varepsilon_{Ti6Al4V}(T) = \begin{cases} 0.1782, & 0 \leq T(K) \leq 800 \\ 0.0007763 \cdot T - 0.2876, & 800 \leq T(K) \leq 1000 \\ 0.7493, & 1000 \leq T(K) \leq 10000 \end{cases} \quad (21)$$



Διάγραμμα 16 Συνάρτηση συντελεστή εκπομπής συμπαγούς Ti6Al4V.

Ιδιότητες σκόνης

Στην παρούσα μελέτη, θεωρείται ότι η σκόνη Ti6Al4V έχει περίπου το ίδιο πορώδες με την σκόνη 316L. Από το [23], η πυκνότητα της σκόνης 316L είναι 4.695 g/cm^3 . Ακόμα, από το [20], η πυκνότητα του συμπαγούς 316L είναι 7.950 g/cm^3 .

Οπότε, το πορώδες (φ) του 316L είναι:

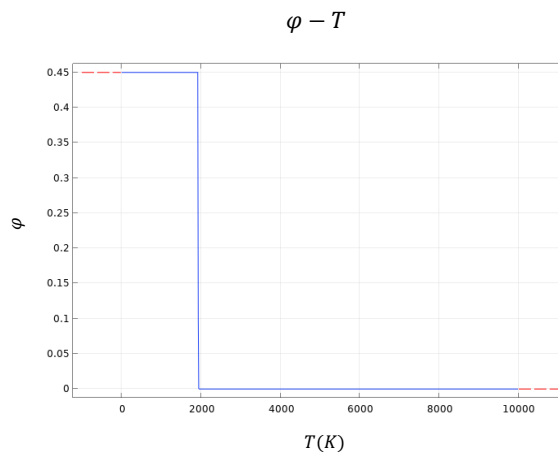
$$\varphi(316L) = 1 - \frac{4.695}{7.950} = 0.41$$

Σε αυτή τη μελέτη, μπορεί να θεωρηθεί ότι το πορώδες της σκόνης Ti6Al4V είναι:

$$\varphi(Ti6Al4V) = 0.45$$

Παρόλα αυτά, το πορώδες ισχύει μόνο για θερμοκρασίες κάτω του σημείου τήξης (1923.15K). Πάνω από το σημείο τήξης, δεν υπάρχει πορώδες. Επιπλέον, για να υπάρχει ομαλή μετάβαση από το πορώδες 0.45 στο 0 (για υπολογιστικούς λόγους), θεωρείται ότι στο διάστημα $[1923.15, 1933.15]$ το πορώδες μειώνεται γραμμικά. Συγκεκριμένα, για σκόνη Ti6Al4V (Διάγραμμα 17),

$$\varphi(T) = \begin{cases} 0.45, & 0 \leq T(K) \leq 1923.15 \\ -0.045 \cdot T + 86.99175, & 1923.15 \leq T(K) \leq 1933.15 \\ 0, & 1933.15 \leq T(K) \leq 10000 \end{cases} \quad (22)$$

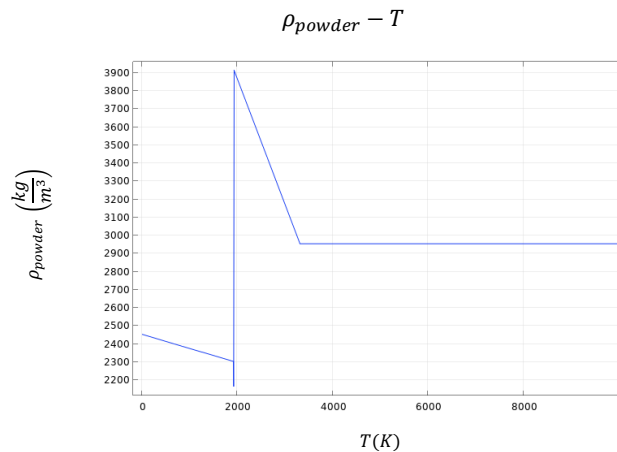


Διάγραμμα 17 Συνάρτηση πορώδους σκόνης.

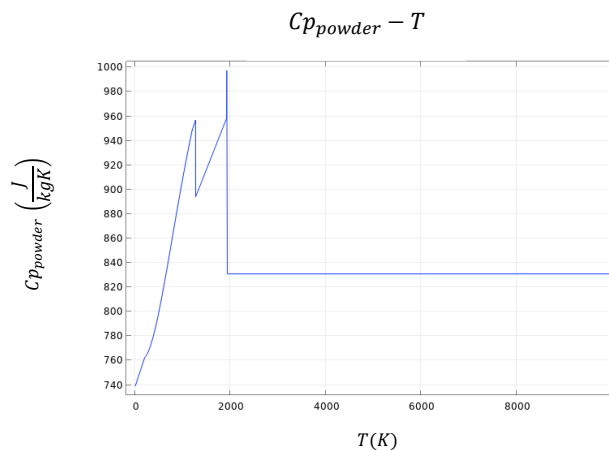
Το πορώδες σημαίνει ότι για θερμοκρασίες κάτω του σημείου τήξης, η σκόνη αποτελείται από 55% ($=1 - \varphi_{Ti6Al4V}$) συμπαγές Ti6Al4V και 45% N₂ (προστατευτικό αέριο). Αυτή η ιδέα χρησιμοποιείται για τον υπολογισμό της πυκνότητας και της ειδικής θερμοχωρητικότητας του πορώδους μέσω του κανόνα των μειγμάτων. Συγκεκριμένα (Διάγραμμα 19, Διάγραμμα 18),

$$\rho_{powder}(T) = \varphi(T) \cdot \rho_{N_2}(T) + (1 - \varphi(T)) \cdot \rho_{Ti6Al4V}(T) \quad (23)$$

$$Cp_{powder}(T) = \varphi(T) \cdot Cp_{N_2}(T) + (1 - \varphi(T)) \cdot Cp_{Ti6Al4V}(T) \quad (24)$$



Διάγραμμα 19 Συνάρτηση πυκνότητας σκόνης.



Διάγραμμα 18 Συνάρτηση ειδικής θερμοχωρητικότητας σκόνης.

Για τον υπολογισμό του συντελεστή εκπομπής και της θερμικής αγωγιμότητας της σκόνης, ακολουθείται η διαδικασία που περιγράφεται στο [24].

Η εκπομπή ακτινοβολίας στο περιβάλλον από μία θερμή πορώδη επιφάνεια, όπως αυτής του στρώματος σκόνης, μπορεί να θεωρηθεί ότι προκλήθηκε από την εκπομπή ακτινοβολίας από τα θερμά σωματίδια και της κοιλότητας του στρώματος σκόνης, όλα στην ίδια θερμοκρασία. Παρόλο που τα τοιχώματα των κοιλοτήτων είναι φτιαγμένα από τα ίδια σωματίδια, η εκπομπή ακτινοβολίας των οπών είναι συνάρτηση της γεωμετρίας τους. Η εκπομπή των οπών είναι πάντα υψηλότερη από την εκπομπή του υλικού της κοιλότητας.

Κατά συνέπεια, είναι αναμενόμενο ότι η εκπομπή ακτινοβολίας της σκόνης είναι υψηλότερη από αυτή του συμπαγούς υλικού και δίνεται από τη σχέση:

$$\varepsilon_{powder}(T) = A_H(T)\varepsilon_H(T) + (1 - A_H(T))\varepsilon_{Ti6Al4V}(T) \quad (25)$$

Όπου:

$\varepsilon_H(T)$ είναι η εκπομπή της οπής. Δίνεται από την σχέση:

$$\varepsilon_H(T) = \frac{\varepsilon_{Ti6Al4V}(T) \left[2 + 3.082 \left(\frac{1-\varphi(T)}{\varphi(T)} \right)^2 \right]}{\varepsilon_{Ti6Al4V}(T) \left[1 + 3.082 \left(\frac{1-\varphi(T)}{\varphi(T)} \right)^2 \right] + 1} \quad (26)$$

A_H είναι το ποσοστό του εμβαδού της επιφάνειας που καταλαμβάνουν οι οπές. Δίνεται από τη σχέση:

$$A_H(T) = \frac{0.908\varphi^2(T)}{1.908\varphi^2(T) - 2\varphi(T) + 1} \quad (27)$$

Επειδή το $\varepsilon_{Ti6Al4V}(T)$ μεταβάλλεται μόνο στο διάστημα $800 \leq T(K) \leq 1000$, τότε και το $\varepsilon_{powder}(T)$ μεταβάλλεται μόνο στο ίδιο διάστημα.

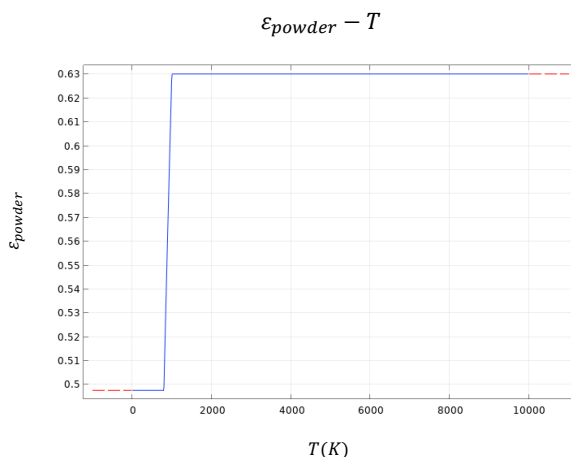
Για αυτό, για τις θερμοκρασίες 800, 900, 1000K, οι τιμές των $A_H(T)$, $\varepsilon_H(T)$ and $\varepsilon_{powder}(T)$ υπολογίζονται και παρουσιάζονται στον Πίνακα 7.

Πίνακας 7 Υπολογισμός των $A_H(T)$, $\varepsilon_H(T)$ και $\varepsilon_{powder}(T)$ για διάφορες θερμοκρασίες.

Temperature (K)	$A_H(T)$	$\varepsilon_H(T)$	$\varepsilon_{powder}(T)$
800	0.3780	0.7676	0.4976
900	0.3780	0.8217	0.5663
1000	0.3780	0.8632	0.6303

Με παρεμβολή των δεδομένων $\varepsilon_{powder}(T)$ και δεδομένου ότι για θερμοκρασίες κάτω των 800K ή πάνω των 1000K, η $\varepsilon_{powder}(T)$ είναι σταθερή και ίση με $\varepsilon_{powder}(800K)$ ή $\varepsilon_{powder}(1000K)$, αντίστοιχα, τότε η συνάρτηση $\varepsilon_{powder}(T)$ (Διάγραμμα 20) δίνεται από τη σχέση:

$$\varepsilon_{powder}(T) = \begin{cases} 0.4977, & 0 \leq T(K) \leq 800 \\ -5.181 \cdot 10^{-13} \cdot T^4 + 2.248 \cdot 10^{-9} \cdot T^3 - 3.782 \cdot 10^{-6} \cdot T^2 + 0.003515 \cdot T - 0.8322, & 800 \leq T(K) \leq 1000, \text{ with } R^2 = 1 \\ 0.6302, & 1000 \leq T(K) \leq 10000 \end{cases} \quad (28)$$



Διάγραμμα 20 Συνάρτηση εκπομπής ακτινοβολίας σκόνης.

Ακόμα, η θερμική αγωγιμότητα της σκόνης υπολογίζεται από την παρακάτω σχέση:

$$\begin{aligned} \frac{k_{powder}(T)}{k_{N_2}(T)} = & (1 - \sqrt{1 - \varphi}) \left(1 + \frac{\varphi k_R(T)}{k_{N_2}(T)} \right) + \\ & + \sqrt{1 - \varphi} \left\{ (1 - \Phi) \left[\frac{2}{1 - \frac{B k_{N_2}(T)}{k_{Ti6Al4V}(T)}} \left(\frac{B}{\left(1 - \frac{B k_{N_2}(T)}{k_{Ti6Al4V}(T)} \right)^2} \left(1 - \frac{k_{N_2}(T)}{k_{Ti6Al4V}(T)} \right) \ln \left(\frac{k_{Ti6Al4V}(T)}{B k_{N_2}(T)} \right) - \frac{B+1}{2} - \right. \right. \right. \\ & \left. \left. \left. \frac{B-1}{1 - \frac{B k_{N_2}(T)}{k_{Ti6Al4V}(T)}} + \frac{k_R(T)}{k_{N_2}(T)} \right) + \Phi \frac{k_{contact}(T)}{k_{N_2}(T)} \right\} \end{aligned} \quad (29)$$

Όπου:

$k_{powder}(T) \left(\frac{W}{mK} \right)$ είναι η θερμική αγωγιμότητα του στρώματος σκόνης.

$k_R(T) \left(\frac{W}{mK} \right)$ είναι η θερμική αγωγιμότητα του στρώματος σκόνης, που οφείλεται στην ακτινοβολία και δίνεται από την εξίσωση Damköhler:

$$k_R(T) = \frac{4\varepsilon_{powder}(T)\sigma_B T^3 x_R}{1 - 0.132\varepsilon_{powder}(T)} \quad (30)$$

Όπου:

$\sigma_B = 5.67 \times 10^{-8} \frac{W}{m^2 K^4}$ είναι η σταθερά Stefan-Boltzmann.

$x_R (m)$ είναι η μέση διάμετρος των σωματιδίων σκόνης. Στην παρούσα μελέτη, $x_R = 30 \times 10^{-6} m$.

Φ είναι το ποσοστό της ανοιγμένης επιφάνειας ενός σωματιδίου που έρχεται σε επαφή με άλλο σωματίδιο. $\Phi = 0$ όταν δεν υπάρχει επαφή σωματιδίων, ενώ $\Phi = 1$ όταν υπάρχει πλήρης επαφή σωματιδίων. Στην παρούσα μελέτη θεωρείται ότι $\Phi = 0.0003$.

B είναι η παράμετρος παραμόρφωσης του σωματιδίου. $B = 1$ όταν το σωματίδιο είναι σφαίρα, ενώ $B < 1$ όταν το σωματίδιο μοιάζει με επιμηκυμένη βελόνα και $\infty > B > 1$ όταν το σωματίδιο είναι βαρελοειδές. Το B μπορεί να υπολογιστεί προσεγγιστικά με βάση το πορώδες φ του στρώματος σκόνης:

$$B \approx 1.25 \left(\frac{1-\varphi}{\varphi} \right)^{\frac{10}{9}} \quad (31)$$

Στην παρούσα μελέτη, $\varphi = 0.45$, οπότε $B = 1.5622$.

$k_{contact}(T) \left(\frac{W}{mK} \right) = 18\Phi k_{Ti6Al4V}(T)$, για $\Phi < 0.0003$. Το $k_{contact}(T)$ είναι σχεδόν ίσο με το $k_{Ti6Al4V}(T)$ μόνο όταν το Φ είναι μεγαλύτερο από 0.01. Στην παρούσα μελέτη, $\Phi = 0.0003$, οπότε θεωρείται ότι:

$$k_{contact}(T) = 0.00054 k_{Ti6Al4V}(T) \quad (32)$$

Χρησιμοποιώντας τις παραπάνω εξισώσεις, η θερμική αγωγιμότητα της σκόνης υπολογίζεται για τις θερμοκρασίες 100,200,...,2000K. Τα αποτελέσματα δίνονται στον Πίνακα 8:

Πίνακας 8 Υπολογισμός του $k_{powder}(T)$ για διάφορες θερμοκρασίες.

Temperature (K)	$k_{powder}(T) \left(\frac{W}{mK} \right)$
100	0.1532
200	0.1713
300	0.2420
400	0.3075
500	0.3686
600	0.4258
700	0.4793
800	0.5295
900	0.5770
1000	0.6218
1100	0.6636
1200	0.7026
1300	0.7041
1400	0.7161
1500	0.7278
1600	0.7394
1700	0.7510
1800	0.7626
1900	0.7743
2000	0.8176

Με παρεμβολή στα παραπάνω δεδομένα:

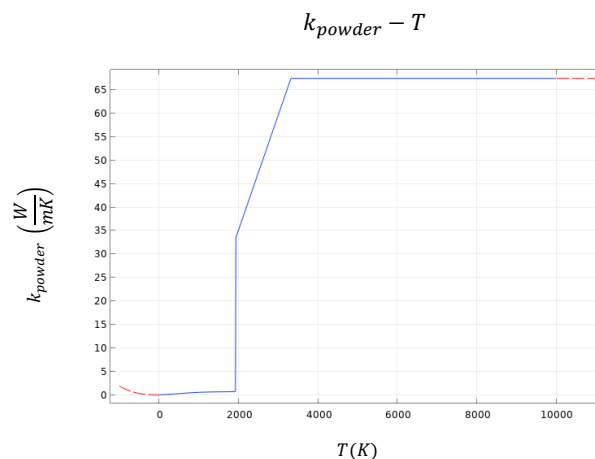
$$k_{powder}(T) = 2.131 \cdot 10^{-13} \cdot T^4 - 8.811 \cdot 10^{-10} \cdot T^3 + 9.916 \cdot 10^{-7} \cdot T^2 + 0.0001841 \cdot T + 0.1183,$$

with $R^2 = 0.9986$

Παρόλα αυτά, όταν η σκόνη τήκεται ή εξατμίζεται δεν έχει πορώδες, οπότε για θερμοκρασίες άνω των 1923.15K, $k_{powder}(T) = k_{Ti6Al4V}(T)$.

Τελικά (Διάγραμμα 21),

$$k_{powder}(T) \left(\frac{W}{mK} \right) = \begin{cases} 2.131 \cdot 10^{-13} \cdot T^4 - 8.811 \cdot 10^{-10} \cdot T^3 + 9.916 \cdot 10^{-7} \cdot T^2 + 0.0001841 \cdot T + 0.1183, & 0 \leq T(K) \leq 1923.15 \\ 0.02449 \cdot T - 13.72, & 1923.15 \leq T(K) \leq 3315 \\ 67.4616, & 3315 \leq T(K) \leq 10000 \end{cases} \quad (33)$$



Διάγραμμα 21 Συνάρτηση θερμικής αγωγιμότητας σκόνης.

Ιδιότητες μοντέλου

Το μοντέλο που χρησιμοποιείται στην παρούσα μελέτη αποτελείται από 0.27mm συμπαγές Ti6Al4V υπόστρωμα και από 30μm σκόνη Ti6Al4V πάνω από το υπόστρωμα. Στο υπόστρωμα, εφαρμόζονται οι ιδιότητες του συμπαγούς Ti6Al4V, ενώ στην σκόνη εφαρμόζονται οι ιδιότητες του πορώδους Ti6Al4V. Οπότε, οι συνδυασμένες ιδιότητες ολόκληρου του μοντέλου είναι συναρτήσεις της θερμοκρασίας, αλλά επίσης και του ύψους του μοντέλου (εκφρασμένο ως προς την z-συντεταγμένη) και δίνονται παρακάτω:

$$\rho_{model}(T) \left(\frac{kg}{m^3} \right) = \begin{cases} \rho_{Ti6Al4V}(T), & 0 \leq z(mm) \leq 0.27 \\ \rho_{powder}(T), & 0.27 \leq z(mm) \leq 0.30 \end{cases} \quad (34)$$

$$Cp_{model}(T) \left(\frac{J}{kgK} \right) = \begin{cases} Cp_{Ti6Al4V}(T), & 0 \leq z(mm) \leq 0.27 \\ Cp_{powder}(T), & 0.27 \leq z(mm) \leq 0.30 \end{cases} \quad (35)$$

$$k_{model}(T) \left(\frac{W}{mK} \right) = \begin{cases} k_{Ti6Al4V}(T), & 0 \leq z(mm) \leq 0.27 \\ k_{powder}(T), & 0.27 \leq z(mm) \leq 0.30 \end{cases} \quad (36)$$

Αλλαγή φάσης

Αυτός ο κόμβος χρησιμοποιείται για να μοντελοποιήσει την αλλαγή φάσης του υλικού, μέσω του τύπου της ειδικής θερμοχωρητικότητας. Σε αυτόν τον τύπο, η λανθάνουσα θερμότητα περιλαμβάνεται ως επιπλέον όρος της ειδικής θερμοχωρητικότητας. Συγκεκριμένα,

$$\left\{ \begin{array}{l} \rho(T) = \rho_{model}(T) \\ Cp(T) = \left(\sum_{j=1}^{Nphases} \theta_j Cp_{model,j}(T) \right) + \left(\sum_{j=1}^{Nphases-1} L_{j \rightarrow j+1} \frac{da_{m,j \rightarrow j+1}}{dT} \right) \\ a_{m,j \rightarrow j+1} = \frac{1}{2} \frac{\theta_{j+1} - \theta_j}{\theta_j + \theta_{j+1}} \\ k(T) = \sum_{j=1}^{Nphases} \theta_j k_{model,j}(T) \\ \sum_{j=1}^{Nphases} \theta_j = 1 \end{array} \right. \quad (37)$$

Όπου:

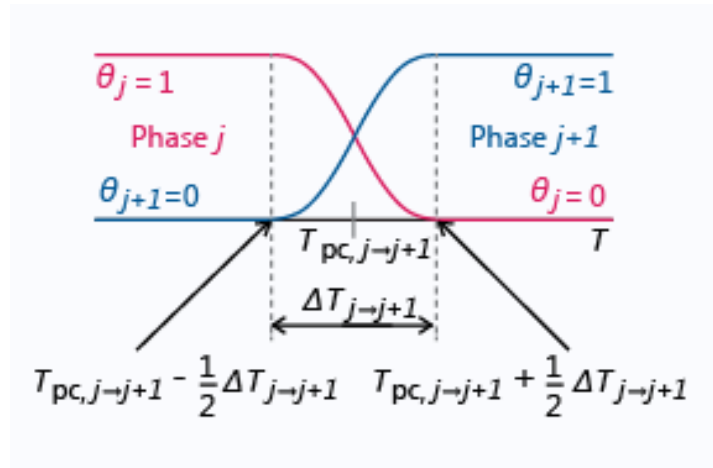
$Nphases$ είναι ο αριθμός των φάσεων του υλικού. Σε αυτή τη μελέτη, για το Ti6Al4V, $Nphases = 4$. Συγκεκριμένα, οι φάσεις είναι: α , β , υγρή και αέρια φάση.

$\rho(T) \left(\frac{kg}{m^3} \right)$ είναι η πυκνότητα του μοντέλου, που περιλαμβάνει την λανθάνουσα θερμότητα και την αλλαγή φάσης του Ti6Al4V.

$Cp(T) \left(\frac{J}{kg \cdot K} \right)$ είναι η ειδική θερμοχωρητικότητα του μοντέλου σε σταθερή πίεση, που περιλαμβάνει την λανθάνουσα θερμότητα και την αλλαγή φάσης του Ti6Al4V.

$k(T) \left(\frac{W}{m \cdot K} \right)$ είναι η θερμική αγωγιμότητα, που περιλαμβάνει την λανθάνουσα θερμότητα και την αλλαγή φάσης του Ti6Al4V.

Οι παράμετροι για τον ορισμό των θερμοκρασιακών διαστημάτων αλλαγής φάσης περιγράφονται με το Διάγραμμα 22:



Διάγραμμα 22 Παράμετροι αλλαγής φάσης.

Κάθε αλλαγή φάσης θεωρείται ότι γίνεται ομαλά εντός ενός θερμοκρασιακού διαστήματος μεταξύ:

$T_{pc,j \rightarrow j+1} - \frac{\Delta T_{j \rightarrow j+1}}{2}$ και $T_{pc,j \rightarrow j+1} + \frac{\Delta T_{j \rightarrow j+1}}{2}$, απελευθερώνεται συνολική θερμότητα ανά μονάδα όγκου ίση με $L_{j \rightarrow j+1}$.

Η θερμοκρασία αλλαγής της φάσης μεταξύ φάσης j και φάσης $j+1$, $T_{pc,j \rightarrow j+1}$, πρέπει να οριστεί στο κέντρο του j διαστήματος. Στην παρούσα μελέτη, $T_{pc,1 \rightarrow 2} = 1268.15K$ ($\alpha \rightarrow \beta$), $T_{pc,2 \rightarrow 3} = 1923.15K$ (θερμοκρασία τήξης), $T_{pc,3 \rightarrow 4} = 3315K$ (θερμοκρασία εξάτμισης).

Το διάστημα μεταβολής μεταξύ φάσης j και φάσης $j+1$, $\Delta T_{j \rightarrow j+1}$, πρέπει να ορίζει το πλάτος του j διαστήματος. Στην παρούσα μελέτη, $\Delta T_{1 \rightarrow 2} = \Delta T_{2 \rightarrow 3} = \Delta T_{3 \rightarrow 4} = 10K$.

Η λανθάνουσα θερμότητα από την φάση j και την φάση $j+1$, $L_{j \rightarrow j+1}$, πρέπει να ορίζει την λανθάνουσα θερμότητα ανά μονάδα μάζας που απελευθερώνεται κατά την διάρκεια της j -αλλαγής φάσης. Στην παρούσα μελέτη, $L_{1 \rightarrow 2} = 48 \frac{kJ}{kg}$, $L_{2 \rightarrow 3} = 282 \frac{kJ}{kg}$, $L_{3 \rightarrow 4} = 10382 \frac{kJ}{kg}$.

Οι ιδιότητες του υλικού της φάσης j ισχύουν όταν $T < T_{pc,j \rightarrow j+1} - \frac{\Delta T_{j \rightarrow j+1}}{2}$, ενώ οι ιδιότητες του υλικού της φάσης $j+1$ ισχύουν για $T > T_{pc,j \rightarrow j+1} + \frac{\Delta T_{j \rightarrow j+1}}{2}$. Εντός του διαστήματος μεταβολής $(T_{pc,j \rightarrow j+1} - \frac{\Delta T_{j \rightarrow j+1}}{2} < T < T_{pc,j \rightarrow j+1} + \frac{\Delta T_{j \rightarrow j+1}}{2})$, υπάρχει μία «ενδιάμεση ζώνη» με ανάμεικτες ιδιότητες υλικού.

Μεταφορά θερμότητας στα στερεά

Η μεταφορά θερμότητας στα στερεά δίνεται από την εξίσωση:

$$\begin{cases} \rho(T)C_p(T)\frac{\partial T}{\partial t} + \nabla \cdot \mathbf{q}(T) = Q(T) \\ \mathbf{q}(T) = -k(T)\nabla T \text{ (Fourier's law)} \end{cases} \quad (38)$$

Όπου:

$q(T)$ ($\frac{W}{m^2}$) είναι η ροή θερμότητας, οπότε $q(T) = q_{LB}(T) + q_{conv}(T) + q_{rad}(T)$ (αυτές οι ροές θερμότητας αναλύονται παρακάτω).

$Q(T)$ ($\frac{W}{m^3}$) είναι η θερμότητα ανά μονάδα όγκου. Στην παρούσα μελέτη, $Q(T) = 0$.

Αρχική συνθήκη

Η αρχική τιμή της θερμοκρασίας T είναι θερμοκρασία δωματίου, 293.15K (20°C).

Οριακή συνθήκη

Η συμμετρία χρησιμοποιείται στην παρούσα μελέτη ως οριακή συνθήκη και σημαίνει ότι δεν υπάρχει ροή θερμότητας διαμέσου αυτού του ορίου.

Η εξίσωση που περιγράφει αυτή την οριακή συνθήκη δίνεται παρακάτω:

$$-\mathbf{n} \cdot \mathbf{q} = 0 \quad (39)$$

Όπου \mathbf{n} είναι το κάθετο διάνυσμα της οριακής επιφάνειας.

Στην παρούσα μελέτη, το επίπεδο γ είναι η οριακή επιφάνεια και χρησιμοποιείται προκειμένου να μειωθεί στο μισό το μοντέλο και να περιοριστεί ο υπολογιστικός χρόνος.

Πηγή Λέιζερ

Οι θερμικές πηγές που προέρχονται από ακτίνες λέιζερ μοντελοποιούνται με την παρακάτω εξίσωση:

$$-\mathbf{n} \cdot \mathbf{q}_{LB} = P_o \cdot f(\mathbf{O}, \mathbf{e}) \frac{|e \cdot \mathbf{n}|}{\|\mathbf{e}\|} \quad (40)$$

Όπου:

q_{LB} ($\frac{W}{m}$) είναι η ροή θερμότητας εξαιτίας του λέιζερ.

P_o (W) είναι η ισχύς που απορροφάται από το μοντέλο.

\mathbf{e} είναι το διάνυσμα προσανατολισμού του λέιζερ.

\mathbf{O} (m) είναι η αρχή του διανύσματος της ακτίνας του λέιζερ.

$f(\mathbf{O}, \mathbf{e})$ είναι η συνάρτηση κατανομής της ακτίνας λέιζερ.

Κάθετο διάνυσμα σε επιφάνεια n

Η ακτίνα λέιζερ προσκρούει στην άνω επιφάνεια του μοντέλου, οπότε σε αυτή την προσομοίωση το \mathbf{n} είναι κάθετο στο z-επίπεδο.

Ισχύς που απορροφάται από το μοντέλο P_o

Η ισχύς που απορροφάται από το μοντέλο δίνεται από τον παρακάτω τύπο:

$$P_o = a \cdot P \quad (41)$$

Όπου:

a είναι ο συντελεστή απορρόφησης του υλικού.

P (W) είναι η ισχύς του λέιζερ.

Στην παρούσα μελέτη, η ισχύς του λέιζερ λαμβάνει τιμές 50W, 100W, 150W και 195W και ο συντελεστής απορρόφησης για το Ti6Al4V θεωρείται σταθερός και ίσος με 0.77, σύμφωνα με το [25].

Διάνυσμα προσανατολισμού του λέιζερ e

Η ακτίνα του λέιζερ είναι κατακόρυφη με φορά προς τα κάτω, οπότε $e = [0 \ 0 \ -1]$.

Αρχή του διανύσματος της ακτίνας του λέιζερ O

Η ακτίνα λέιζερ κινείται στον άξονα x , οπότε η x -συντεταγμένη του O εξαρτάται από τον χρόνο. Ακόμα, η ακτίνα λέιζερ δεν πρέπει να ξεκινά ή να τελειώνει στα άκρα του μοντέλου, επειδή αυτό συχνά οδηγεί σε υπολογιστικά σφάλματα. Στην παρούσα μελέτη, η x -συντεταγμένη του αρχικού σημείου της ακτίνας λέιζερ είναι 0.25[mm]

Οπότε, η χρονικά εξαρτώμενη x -συντεταγμένη του O δίνεται παρακάτω:

$$O_x = 0.25(mm) + v\left(\frac{mm}{s}\right) \cdot t$$

Όπου v ($\frac{m}{s}$) είναι η ταχύτητα του λέιζερ.

Στην παρούσα μελέτη, η ταχύτητα του λέιζερ λαμβάνει τιμές 500 mm/s, 750 mm/s, 1000 mm/s και 1200 mm/s.

Ως προς την κατεύθυνση του άξονα y , η ακτίνα του λέιζερ κινείται πάνω στη γραμμή $y=0$, οπότε $O_y = 0$ mm. Επιπλέον, η ακτίνα προσκρούει στην πάνω επιφάνεια του μοντέλου, οπότε $O_z = 1$ mm.

Συνοψίζοντας:

$$O = \left(0.25(mm) + v\left(\frac{mm}{s}\right) \cdot t, \ 0(mm), \ 1(mm)\right) \quad (42)$$

Συνάρτηση τύπου κατανομής $f(O, e)$

Στην παρούσα μελέτη, η ένταση της ακτίνας του λέιζερ μοντελοποιείται ως γκαουσιανή κατανομή, οπότε:

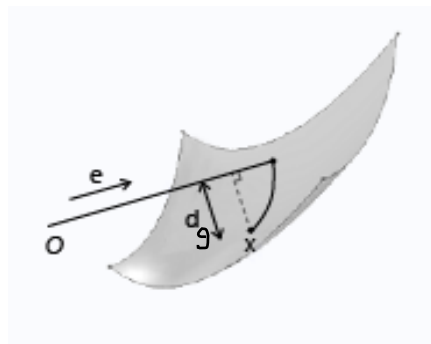
$$\begin{cases} f(\mathbf{O}, \mathbf{e}) = \frac{1}{2\pi\sigma^2} e^{-\frac{d_g^2}{2\sigma^2}} \\ d_g = \frac{\|\mathbf{e} \times (\mathbf{x} - \mathbf{O})\|}{\|\mathbf{e}\|} \end{cases} \quad (43)$$

Όπου:

σ (m) είναι η τυπική απόκλιση της γκαουσιανής κατανομής.

\mathbf{x} (m) είναι η θέση στην οποία υπολογίζεται η ένταση της ακτίνας του λέιζερ μέσω της γκαουσιανής κατανομής.

d_g (m) είναι η απόσταση που απεικονίζεται στην Εικόνα 12:

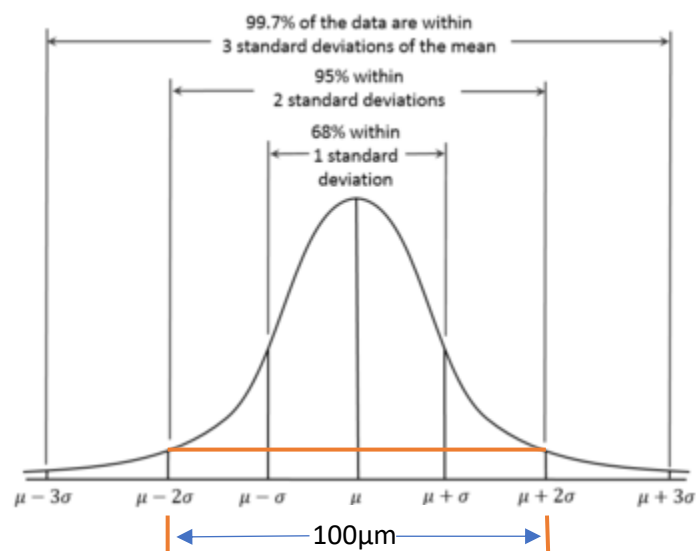


Εικόνα 12 Απεικόνιση της απόστασης d_g .

Τυπική απόκλιση σ

Η διάμετρος της ακτίνας ή αλλιώς το πλάτος της ακτίνας ενός λέιζερ είναι η διάμετρος κατά μήκος μίας γραμμής που είναι κάθετη στον άξονα της ακτίνας και τον τέμνει. Δεδομένου ότι οι ακτίνες συνήθως δεν έχουν αιχμηρές ακμές, η διάμετρος μπορεί να προσδιοριστεί με πολλούς διαφορετικούς τρόπους. Ένας από τους πιο κοινούς ορισμούς είναι ο 4σ . Αυτός ο ορισμός υιοθετείται και στην παρούσα μελέτη. Η διάμετρος της ακτίνας μπορεί να μετρηθεί σε μονάδες μήκους σε ένα επίπεδο κάθετο στον άξονα της ακτίνας.

Στην παρούσα μελέτη, χρησιμοποιείται ακτίνα λέιζερ 4σ διαμέτρου $100\mu m$, όπως παρουσιάζεται παρακάτω (Εικόνα 13):



Εικόνα 13 Γκαουσιανή κατανομή της ακτίνας του λέιζερ.

Οπότε από την Εικόνα 13, $\sigma = \frac{\text{laser beam diameter}}{4} = \frac{100\mu\text{m}}{4} = 25\mu\text{m}$.

Συναγωγή

Η συναγωγή γίνεται μεταξύ του προστατευτικού αερίου (σε αυτή τη μελέτη είναι το άζωτο) και όλων των επιφανειών του μοντέλου. Η ροή θερμότητας λόγω συναγωγής δίνεται παρακάτω:

$$\mathbf{n} \cdot \mathbf{q}_{conv} = h_{N_2} \cdot (T_{\infty} - T) \quad (44)$$

Ακτινοβολία

Στο μοντέλο περιλαμβάνεται η ροή θερμότητας λόγω ακτινοβολίας από το τεμάχιο προς το περιβάλλον. Η ροή θερμότητας λόγω ακτινοβολίας δίνεται από τη σχέση:

$$-\mathbf{n} \cdot \mathbf{q}_{rad} = \varepsilon_{powder}(T) \sigma_B (T_{\infty}^4 - T^4) \quad (45)$$

Όπου το \mathbf{n} είναι κάθετο στην πάνω επιφάνεια του μοντέλου, επειδή η ακτινοβολία εκπέμπεται από την σκόνη.

Παραμορφωμένη γεωμετρία

Η παραμόρφωση του πλέγματος μπορεί να μοντελοποιηθεί με δύο διαφορετικούς τρόπους, την παραμορφωμένη γεωμετρία και το κινούμενο πλέγμα. Η παραμορφωμένη γεωμετρία μοντελοποιεί την προσθήκη ή αποβολή υλικού (δηλαδή την προσθήκη ή αποβολή και μάζας και ενέργειας) από το τεμάχιο, ενώ το κινούμενο πλέγμα μοντελοποιεί τον εφελκυσμό ή την θλίψη του τεμαχίου (μόνο δηλαδή την προσθήκη ή την αφαίρεση ενέργειας) του τεμαχίου.

Στην παρούσα μελέτη έχει χρησιμοποιηθεί η παραμορφωμένη γεωμετρία.

Κάθε στοιχείο του πλέγματος ελέγχεται από μία εξίσωση εξομάλυνσης. Η εξίσωση που χρησιμοποιείται στην παρούσα μελέτη είναι η Υπερελαστική εξομάλυνση, σύμφωνα με το [26].

Η μέθοδος της Υπερελαστικής εξομάλυνσης αναζητά ένα ελάχιστο από την ενέργεια παραμόρφωσης του πλέγματος:

$$W_{mesh} = \int_{\Omega} \frac{\nu}{2} (I_1 - 3) + \frac{\kappa}{2} (J - 1)^2 dV \quad (46)$$

όπου ν and κ είναι τεχνητές παράμετροι διάτμησης και εφελκυσμού, αντίστοιχα και οι αναλλοίωτες J και I_1 δίνονται παρακάτω:

$$\begin{cases} J = \det(\nabla_X x) \\ I_1 = J^{-2/3} \text{tr}((\nabla_X x)^T \nabla_X x) \end{cases} \quad (47)$$

Ταχύτητα πλέγματος

Η ταχύτητα πλέγματος εφαρμόζεται στην πάνω επιφάνεια του μοντέλου και εκφράζει την ταχύτητα με την οποία τα στοιχεία του πλέγματος με θερμοκρασία άνω των 3315K «εξατμίζονται». Στην παρούσα μελέτη θεωρείται ότι για θερμοκρασίες άνω των 6000K η ταχύτητα του πλέγματος είναι σταθερή και ίση με την ταχύτητα στους 6000K. Συγκεκριμένα,

$$v_n = \begin{cases} -V_{evap}(T, \beta_R), & 0 < T(K) \leq 6000 \\ -V_{evap}(6000K, \beta_R), & T(K) > 6000 \end{cases} \quad (48)$$

Όπου:

$v_n \left(\frac{m}{s}\right)$ είναι η ταχύτητα του πλέγματος.

Το “-” μπροστά από την συνάρτηση V_{evap} σημαίνει ότι τα στοιχεία του πλέγματος που «εξατμίστηκαν», «εξαφανίζονται» από το πλέγμα.

$V_{evap}(T, \beta_R) \left(\frac{m}{s}\right)$ είναι η ταχύτητα με την οποία τα στοιχεία του πλέγματος με θερμοκρασία άνω των 3315K «εξατμίζονται» και υπολογίζονται σύμφωνα με το [27], όπως φαίνεται παρακάτω:

Η ολική ροή μάζας από την επιφάνεια του μετάλλου λόγω εξάτμισης, μπορεί να εκφραστεί ως εξής:

$$\begin{cases} V_{evap}(T, \beta_R) = \frac{1}{\rho(T)} (1 - \beta_R) \left(\frac{m}{2\pi k_B T}\right)^{\frac{1}{2}} p_{sat}(T) \\ p_{sat}(T) = p_0 e^{\left(\frac{mL_v}{k_B T_v} \left(1 - \frac{T_v}{T}\right)\right)} \quad (\text{saturated vapor pressure at a temperature } T, \text{ expressed with the Clausius - Clapeyron's relation}) \end{cases} \quad (49)$$

Όπου:

p_0 (Pa) είναι η πίεση περιβάλλοντος. Στην παρούσα μελέτη, $p_0 = 1.01 \cdot 10^5$ Pa.

$k_B = 1.380649 \cdot 10^{-23} \frac{J}{K}$ είναι η σταθερά Boltzmann.

T_v (K) είναι το σημείο βρασμού. Στην παρούσα μελέτη, $T_v = 3315K$.

β_R είναι ο λόγος των ατόμων που ανασυντίθενται στην επιφάνεια προς τα άτομα που εξατμίζονται από την τηγμένη επιφάνεια.

$m \left(\frac{kg}{atom}\right)$ είναι η μάζα ανά άτομο μετάλλου. Υπολογίζεται από την παρακάτω διαδικασία:

- Εύρεση των ατομικών μαζών του Ti, Al και V. Συγκεκριμένα, $A_{Ti} = 47.867 \frac{g}{mol}$, $A_{Al} = 26.981539 \frac{g}{mol}$, $A_V = 50.9415 \frac{g}{mol}$.
- Υπολογίζεται η σταθμισμένη μέση ατομική μάζα του Ti6Al4V. Συγκεκριμένα, $A_{Ti6Al4V} = \frac{6A_{Ti} + 4A_{Al} + A_V}{2} = 40.55178691 \frac{g}{mol}$.
- Η μάζα ανά άτομο Ti6Al4V δίνεται από τον παρακάτω τύπο:

$$m = \frac{A_{Ti6Al4V}}{N_A} \quad (50)$$

Όπου $N_A = 6.0221407 \cdot 10^{23} \frac{\text{atoms}}{\text{mol}}$ είναι ο αριθμός Avogadro.

Τελικά, $m = 6.733782641 \cdot 10^{-23} \frac{\text{g}}{\text{atom}}$.

$L_v \left(\frac{\text{J}}{\text{kg}} \right)$ είναι η λανθάνουσα θερμότητα εξαΐμισης του Ti6Al4V. Στην παρούσα μελέτη, $L_v \left(\sigma\epsilon \frac{\text{kJ}}{\text{mol}} \right) = \max \{ L_v^{Ti}, L_v^{Al}, L_v^V \} = \max \left\{ 421 \frac{\text{kJ}}{\text{mol}}, 293.4 \frac{\text{kJ}}{\text{mol}}, 0.452 \frac{\text{kJ}}{\text{mol}} \right\} = 421 \frac{\text{kJ}}{\text{mol}}$. Ακόμα, η μοριακή μάζα του Ti6Al4V είναι: $M_{Ti6Al4V} = 6 \cdot A_{Ti} + 4 \cdot A_{Al} + A_V = 446.069656 \frac{\text{g}}{\text{mol}}$.

Οπότε, $L_v = \frac{421 \frac{\text{kJ}}{\text{mol}}}{446.069656 \frac{\text{g}}{\text{mol}}} = 10.38178665 \frac{\text{kJ}}{\text{g}} = 10.38178665 \frac{\text{J}}{\text{kg}}$.

Για $T=3330, 3340, \dots, 5000\text{K}$ και $\beta_R=0.1, 0.2, \dots, 1$, υπολογίζονται οι τιμές της $V_{\text{evap}}(T, \beta_R)$ στον Πίνακα 9:

Πίνακας 9 Υπολογισμός του $V_{\text{evap}}(T, \beta_R)$ για διάφορες θερμοκρασίες και β_R .

Temperature (K)	β_R									
	0.1	0.2	0.3	0.4	0.5	0.6	0.7	0.8	0.9	1
3330	0.01526	0.01356	0.01187	0.01017	0.00848	0.00678	0.00509	0.00339	0.0017	0
3340	0.01595	0.01417	0.0124	0.01063	0.00886	0.00709	0.00532	0.00354	0.00177	0
3350	0.01666	0.01481	0.01296	0.01111	0.00926	0.0074	0.00555	0.0037	0.00185	0
3360	0.0174	0.01547	0.01353	0.0116	0.00967	0.00773	0.0058	0.00387	0.00193	0
3370	0.01817	0.01615	0.01413	0.01211	0.01009	0.00807	0.00606	0.00404	0.00202	0
3380	0.01897	0.01686	0.01475	0.01264	0.01054	0.00843	0.00632	0.00421	0.00211	0
3390	0.01979	0.01759	0.0154	0.0132	0.011	0.0088	0.0066	0.0044	0.0022	0
3400	0.02065	0.01836	0.01606	0.01377	0.01147	0.00918	0.00688	0.00459	0.00229	0
3410	0.02154	0.01915	0.01676	0.01436	0.01197	0.00957	0.00718	0.00479	0.00239	0
3420	0.02247	0.01997	0.01747	0.01498	0.01248	0.00998	0.00749	0.00499	0.0025	0
3430	0.02342	0.02082	0.01822	0.01561	0.01301	0.01041	0.00781	0.0052	0.0026	0
3440	0.02441	0.0217	0.01899	0.01628	0.01356	0.01085	0.00814	0.00543	0.00271	0
3450	0.02544	0.02261	0.01979	0.01696	0.01413	0.01131	0.00848	0.00565	0.00283	0
3460	0.02651	0.02356	0.02062	0.01767	0.01473	0.01178	0.00884	0.00589	0.00295	0
3470	0.02761	0.02454	0.02147	0.0184	0.01534	0.01227	0.0092	0.00613	0.00307	0
3480	0.02875	0.02555	0.02236	0.01917	0.01597	0.01278	0.00958	0.00639	0.00319	0
3490	0.02993	0.0266	0.02328	0.01995	0.01663	0.0133	0.00998	0.00665	0.00333	0
3500	0.03115	0.02769	0.02423	0.02077	0.01731	0.01384	0.01038	0.00692	0.00346	0
3510	0.03242	0.02881	0.02521	0.02161	0.01801	0.01441	0.01081	0.0072	0.0036	0
3520	0.03372	0.02998	0.02623	0.02248	0.01874	0.01499	0.01124	0.00749	0.00375	0
3530	0.03508	0.03118	0.02728	0.02338	0.01949	0.01559	0.01169	0.00779	0.0039	0
3540	0.03647	0.03242	0.02837	0.02432	0.02026	0.01621	0.01216	0.00811	0.00405	0
3550	0.03792	0.03371	0.02949	0.02528	0.02107	0.01685	0.01264	0.00843	0.00421	0
3560	0.03942	0.03504	0.03066	0.02628	0.0219	0.01752	0.01314	0.00876	0.00438	0
3570	0.04096	0.03641	0.03186	0.02731	0.02276	0.0182	0.01365	0.0091	0.00455	0
3580	0.04256	0.03783	0.0331	0.02837	0.02364	0.01891	0.01419	0.00946	0.00473	0
3590	0.0442	0.03929	0.03438	0.02947	0.02456	0.01965	0.01473	0.00982	0.00491	0
3600	0.04591	0.04081	0.03571	0.0306	0.0255	0.0204	0.0153	0.0102	0.0051	0
3610	0.04766	0.04237	0.03707	0.03178	0.02648	0.02118	0.01589	0.01059	0.0053	0
3620	0.04948	0.04398	0.03848	0.03299	0.02749	0.02199	0.01649	0.011	0.0055	0
3630	0.05135	0.04565	0.03994	0.03423	0.02853	0.02282	0.01712	0.01141	0.00571	0
3640	0.05328	0.04736	0.04144	0.03552	0.0296	0.02368	0.01776	0.01184	0.00592	0
3650	0.05528	0.04914	0.04299	0.03685	0.03071	0.02457	0.01843	0.01228	0.00614	0
3660	0.05734	0.05097	0.04459	0.03822	0.03185	0.02548	0.01911	0.01274	0.00637	0
3670	0.05946	0.05285	0.04624	0.03964	0.03303	0.02643	0.01982	0.01321	0.00661	0
3680	0.06164	0.0548	0.04795	0.0411	0.03425	0.0274	0.02055	0.0137	0.00685	0
3690	0.0639	0.0568	0.0497	0.0426	0.0355	0.0284	0.0213	0.0142	0.0071	0
3700	0.06622	0.05887	0.05151	0.04415	0.03679	0.02943	0.02207	0.01472	0.00736	0
3710	0.06862	0.061	0.05337	0.04575	0.03812	0.0305	0.02287	0.01525	0.00762	0
3720	0.07109	0.06319	0.05529	0.04739	0.03949	0.0316	0.0237	0.0158	0.0079	0
3730	0.07363	0.06545	0.05727	0.04909	0.04091	0.03273	0.02454	0.01636	0.00818	0
3740	0.07625	0.06778	0.05931	0.05083	0.04236	0.03389	0.02542	0.01694	0.00847	0
3750	0.07895	0.07018	0.06141	0.05263	0.04386	0.03509	0.02632	0.01754	0.00877	0
3760	0.08173	0.07265	0.06357	0.05448	0.0454	0.03632	0.02724	0.01816	0.00908	0
3770	0.08459	0.07519	0.06579	0.05639	0.04699	0.03759	0.0282	0.0188	0.0094	0
3780	0.08753	0.0778	0.06808	0.05835	0.04863	0.0389	0.02918	0.01945	0.00973	0

	3790	0.09056	0.0805	0.07044	0.06037	0.05031	0.04025	0.03019	0.02012	0.01006	0
	3800	0.09368	0.08327	0.07286	0.06245	0.05204	0.04163	0.03123	0.02082	0.01041	0
	3810	0.09688	0.08612	0.07535	0.06459	0.05382	0.04306	0.03229	0.02153	0.01076	0
	3820	0.10018	0.08905	0.07792	0.06679	0.05566	0.04453	0.03339	0.02226	0.01113	0
	3830	0.10357	0.09207	0.08056	0.06905	0.05754	0.04603	0.03452	0.02302	0.01151	0
	3840	0.10706	0.09517	0.08327	0.07138	0.05948	0.04758	0.03569	0.02379	0.01199	0
	3850	0.11065	0.09835	0.08606	0.07377	0.06147	0.04918	0.03688	0.02459	0.01229	0
	3860	0.11434	0.10163	0.08893	0.07622	0.06352	0.05082	0.03811	0.02541	0.01279	0
	3870	0.11813	0.105	0.09188	0.07875	0.06563	0.0525	0.03938	0.02625	0.01313	0
	3880	0.12202	0.10846	0.0949	0.08135	0.06779	0.05423	0.04067	0.02712	0.01356	0
	3890	0.12602	0.11202	0.09802	0.08401	0.07001	0.05601	0.04201	0.028	0.014	0
	3900	0.13013	0.11567	0.10121	0.08675	0.07229	0.05784	0.04338	0.02892	0.01446	0
	3910	0.13435	0.11942	0.10449	0.08957	0.07464	0.05971	0.04478	0.02986	0.01493	0
	3920	0.13869	0.12328	0.10787	0.09246	0.07705	0.06164	0.04623	0.03082	0.01541	0
	3930	0.14314	0.12723	0.11133	0.09542	0.07952	0.06362	0.04771	0.03181	0.01599	0
	3940	0.14771	0.1313	0.11488	0.09847	0.08206	0.06565	0.04924	0.03282	0.01641	0
	3950	0.1524	0.13547	0.11853	0.1016	0.08467	0.06773	0.0508	0.03387	0.01693	0
	3960	0.15721	0.13975	0.12228	0.10481	0.08734	0.06987	0.0524	0.03494	0.01747	0
	3970	0.16216	0.14414	0.12612	0.1081	0.09009	0.07207	0.05405	0.03603	0.01802	0
	3980	0.16723	0.14865	0.13006	0.11148	0.0929	0.07432	0.05574	0.03716	0.01858	0
	3990	0.17243	0.15327	0.13411	0.11495	0.09579	0.07663	0.05748	0.03832	0.01916	0
	4000	0.17776	0.15801	0.13826	0.11851	0.09876	0.07901	0.05925	0.0395	0.01975	0
	4010	0.18324	0.16288	0.14252	0.12216	0.1018	0.08144	0.06108	0.04072	0.02036	0
	4020	0.18885	0.16786	0.14688	0.1259	0.10491	0.08393	0.06295	0.04197	0.02098	0
	4030	0.1946	0.17298	0.15136	0.12973	0.10811	0.08649	0.06487	0.04324	0.02162	0
	4040	0.2005	0.17822	0.15594	0.13367	0.11139	0.08911	0.06683	0.04456	0.02228	0
	4050	0.20655	0.1836	0.16065	0.1377	0.11475	0.0918	0.06885	0.0459	0.02295	0
	4060	0.21274	0.1891	0.16547	0.14183	0.11819	0.09455	0.07091	0.04728	0.02364	0
	4070	0.21909	0.19475	0.17041	0.14606	0.12172	0.09737	0.07303	0.04869	0.02434	0
	4080	0.2256	0.20053	0.17547	0.1504	0.12533	0.10027	0.0752	0.05013	0.02507	0
	4090	0.23226	0.20646	0.18065	0.15484	0.12904	0.10323	0.07742	0.05161	0.02581	0
	4100	0.23909	0.21253	0.18596	0.1594	0.13283	0.10626	0.0797	0.05313	0.02657	0
	4110	0.24609	0.21874	0.1914	0.16406	0.13671	0.10937	0.08203	0.05469	0.02734	0
	4120	0.25325	0.22511	0.19697	0.16883	0.14069	0.11255	0.08442	0.05628	0.02814	0
	4130	0.26058	0.23163	0.20267	0.17372	0.14477	0.11581	0.08686	0.05791	0.02895	0
	4140	0.26809	0.2383	0.20851	0.17873	0.14894	0.11915	0.08936	0.05958	0.02979	0
	4150	0.27578	0.24513	0.21449	0.18385	0.15321	0.12257	0.09193	0.06128	0.03064	0
	4160	0.28364	0.25213	0.22061	0.18909	0.15758	0.12606	0.09455	0.06303	0.03152	0
	4170	0.29169	0.25928	0.22687	0.19446	0.16205	0.12964	0.09723	0.06482	0.03241	0
	4180	0.29993	0.26661	0.23328	0.19995	0.16663	0.1333	0.09998	0.06665	0.03333	0
	4190	0.30836	0.2741	0.23984	0.20557	0.17131	0.13705	0.10279	0.06852	0.03426	0
	4200	0.31698	0.28176	0.24654	0.21132	0.1761	0.14088	0.10566	0.07044	0.03522	0
	4210	0.3258	0.2896	0.2534	0.2172	0.181	0.1448	0.1086	0.0724	0.0362	0
	4220	0.33483	0.29762	0.26042	0.22322	0.18601	0.14881	0.11161	0.07441	0.0372	0
	4230	0.34405	0.30582	0.2676	0.22937	0.19114	0.15291	0.11468	0.07646	0.03823	0
	4240	0.35349	0.31421	0.27493	0.23566	0.19638	0.1571	0.11783	0.07855	0.03928	0
	4250	0.36313	0.32278	0.28244	0.24209	0.20174	0.16139	0.12104	0.0807	0.04035	0
	4260	0.37299	0.33155	0.29011	0.24866	0.20722	0.16577	0.12433	0.08289	0.04144	0
	4270	0.38307	0.34051	0.29794	0.25538	0.21282	0.17025	0.12769	0.08513	0.04256	0
	4280	0.39337	0.34966	0.30596	0.26225	0.21854	0.17483	0.13112	0.08742	0.04371	0
	4290	0.4039	0.35902	0.31414	0.26927	0.22439	0.17951	0.13463	0.08976	0.04488	0
	4300	0.41466	0.36858	0.32251	0.27644	0.23037	0.18429	0.13822	0.09215	0.04607	0
	4310	0.42565	0.37835	0.33106	0.28377	0.23647	0.18918	0.14188	0.09459	0.04729	0
	4320	0.43688	0.38833	0.33979	0.29125	0.24271	0.19417	0.14563	0.09708	0.04854	0
	4330	0.44834	0.39853	0.34871	0.2989	0.24908	0.19926	0.14945	0.09963	0.04982	0
	4340	0.46006	0.40894	0.35782	0.30671	0.25559	0.20447	0.15335	0.10224	0.05112	0
	4350	0.47202	0.41957	0.36713	0.31468	0.26223	0.20979	0.15734	0.10489	0.05245	0
	4360	0.48424	0.43043	0.37663	0.32282	0.26902	0.21522	0.16141	0.10761	0.0538	0
	4370	0.49671	0.44152	0.38633	0.33114	0.27595	0.22076	0.16557	0.11038	0.05519	0
	4380	0.50944	0.45284	0.39623	0.33963	0.28302	0.22642	0.16981	0.11321	0.0566	0
	4390	0.52244	0.46439	0.40634	0.34829	0.29024	0.23219	0.17415	0.1161	0.05805	0
	4400	0.5357	0.47618	0.41666	0.35714	0.29761	0.23809	0.17857	0.11905	0.05952	0
	4410	0.54924	0.48822	0.42719	0.36616	0.30514	0.24411	0.18308	0.12205	0.06103	0
	4420	0.56306	0.5005	0.43794	0.37537	0.31281	0.25025	0.18769	0.12512	0.06256	0
	4430	0.57716	0.51303	0.4489	0.38477	0.32064	0.25651	0.19239	0.12826	0.06413	0
	4440	0.59154	0.52582	0.46009	0.39436	0.32863	0.26291	0.19718	0.13145	0.06573	0
	4450	0.60622	0.53886	0.4715	0.40414	0.33679	0.26943	0.20207	0.13471	0.06736	0
	4460	0.62118	0.55216	0.48314	0.41412	0.3451	0.27608	0.20706	0.13804	0.06902	0
	4470	0.63645	0.56573	0.49502	0.4243	0.35358	0.28287	0.21215	0.14143	0.07072	0
	4480	0.65202	0.57957	0.50712	0.43468	0.36223	0.28979	0.21734	0.14489	0.07245	0
	4490	0.66789	0.59368	0.51947	0.44526	0.37105	0.29684	0.22263	0.14842	0.07421	0
	4500	0.68408	0.60807	0.53206	0.45605	0.38005	0.30404	0.22803	0.15202	0.07601	0
	4510	0.70059	0.62274	0.5449	0.46706	0.38921	0.31137	0.23353	0.15569	0.07784	0
	4520	0.71741	0.6377	0.55799	0.47827	0.39856	0.31885	0.23914	0.15942	0.07971	0
	4530	0.73456	0.65294	0.57132	0.48971	0.40809	0.32647	0.24485	0.16324	0.08162	0
	4540	0.75204	0.66848	0.58492	0.50136	0.4178	0.33424	0.25068	0.16712	0.08356	0
	4550	0.76986	0.68432	0.59878	0.51324	0.4277	0.34216	0.25662	0.17108	0.08554	0
	4560	0.78801	0.70045	0.6129	0.52534	0.43778	0.35023	0.26267	0.17511	0.08756	0
	4570	0.80651	0.71689	0.62728	0.53767	0.44806	0.35845	0.26884	0.17922	0.08961	0
	4580	0.82535	0.73365	0.64194	0.55023	0.45853	0.36682	0.27512	0.18341	0.09171	0
	4590	0.84455	0.75071	0.65687	0.56303	0.4692	0.37536	0.28152	0.18768	0.09384	0
	4600	0.86411	0.7681	0.67209	0.57607	0.48006	0.38405	0.28804	0.19202	0.09601	0
	4610	0.88403	0.7858	0.68758	0.58935	0.49113	0.3929	0.29468	0.19645	0.09823	0
	4620	0.90432	0.80384	0.70336	0.60288	0.5024	0.40192	0.30144	0.20096	0.10048	0
	4630	0.92498	0.8222	0.71943	0.61665	0.51388	0.4111	0.30833	0.20555	0.10278	0
	4640	0.94602	0.84091	0.73579	0.63068	0.52557	0.42045	0.31534	0.21023	0.10511	0
	4650	0.96744	0.85995	0.75245	0.64496	0.53747	0.42997	0.32248	0.21499	0.10749	0
	4660	0.98925	0.87933	0.76942	0.6595	0.54958	0.43967	0.32975	0.21983	0.10992	0
	4670	1.01145	0.89907	0.78669	0.6743	0.56192	0.44953	0.33715	0.22477	0.11238	0
	4680	1.03405	0.91916	0.80426	0.68937	0.57447	0.45958	0.34468	0.22979	0.11489	0
	4690	1.05706	0.93961	0.82216	0.7047	0.58725	0.4698	0.35235	0.2349	0.11745	0
	4700	1.08047	0.96042	0.84036	0.72031	0.60026	0.48021	0.36016	0.2401	0.12005	0
	4710	1.10429	0.98159	0.85889	0.73619	0.6135	0.4908	0.3681	0.2454	0.1227	0
	4720	1.12854	1.00314	0.87775	0.75236	0.62696	0.50157	0.37618	0.25079	0.12539	0
	4730	1.15									

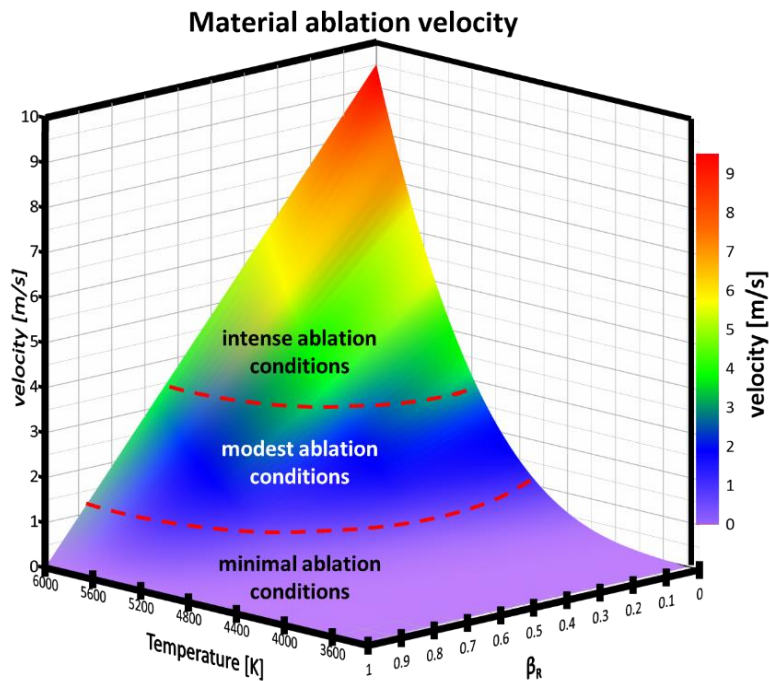
Με παρεμβολή στα παραπάνω δεδομένα και για $T > 3315K$,

$$V_{evap}(T, \beta_R) = \begin{pmatrix} -27.91 + 0.02325T + 27.91\beta_R - 6.501 \cdot 10^{-6}T^2 - 0.02325T\beta_R + 7.696 \\ \cdot 10^{-13}\beta_R^2 + 6.109 \cdot 10^{-10}T^3 + 6.501 \cdot 10^{-6}T^2\beta_R - 2.987 \cdot 10^{-16}T\beta_R^2 \\ -7.238 \cdot 10^{-14}\beta_R^3 - 6.109 \cdot 10^{-10}T^3\beta_R + 3.05 \cdot 10^{-20}T^2\beta_R^2 + 6.115 \\ -7.238 \cdot 10^{-14}\beta_R^3 - 6.109 \cdot 10^{-10}T^3\beta_R + 3.05 \cdot 10^{-20}T^2\beta_R^2 + 6.115 \end{pmatrix}$$

Οπότε τελικά,

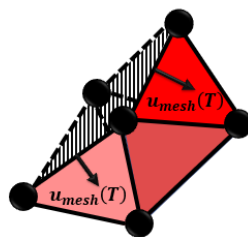
$$V_{evap}(T, \beta_R) = \begin{cases} 0, & T < 3315K \text{ or } \beta_R = 1 \\ -27.91 + 0.02325T + 27.91\beta_R - 6.501 \cdot 10^{-6}T^2 - 0.02325T\beta_R + 7.696 \\ \cdot 10^{-13}\beta_R^2 + 6.109 \cdot 10^{-10}T^3 + 6.501 \cdot 10^{-6}T^2\beta_R - 2.987 \cdot 10^{-16}T\beta_R^2 \\ -7.238 \cdot 10^{-14}\beta_R^3 - 6.109 \cdot 10^{-10}T^3\beta_R + 3.05 \cdot 10^{-20}T^2\beta_R^2 + 6.115 \\ \cdot 10^{-18}T\beta_R^3 + 5.808 \cdot 10^{-15}\beta_R^4, & T \geq 3315K \text{ and } \beta_R \neq 1 \end{cases}$$

Το διάγραμμα που περιγράφει την παραπάνω συνάρτηση δίνεται στο Διάγραμμα 23:



Διάγραμμα 23 V_{evap} ως συνάρτηση της θερμοκρασίας και του β_R .

Η ταχύτητα του κάθε στοιχείου του πλέγματος μπορεί να οπτικοποιηθεί, όπως δίνεται στην Εικόνα 14:



Εικόνα 14 Οπτική αναπαράσταση της ταχύτητας των στοιχείων του πλέγματος.

Υπολογιστική διαδικασία:

Πλέγμα:

Η μέθοδος των Πεπερασμένων Στοιχείων είναι πολύ δημοφιλής και στον υπολογισμό θερμικών μοντέλων. Μέχρι στιγμής υπάρχουν δύο επιλογές πλέγματος: το καρτεσιανό πλέγμα και το τετραεδρικό πλέγμα. Στην παρούσα μελέτη χρησιμοποιείται τετραεδρικό πλέγμα.

Στόχος του τετραεδρικού πλέγματος είναι να απλοποιήσει την αναπαράσταση της λεπτομερειών της γεωμετρίας των τεμαχίων των ΠΚ χωρίς να αυξήσει την συνθετότητα του μοντέλου. Το τετραεδρικό σχήμα των στοιχείων επιτρέπει στον αλγόριθμο του πλέγματος να πετύχει καλύτερα αποτελέσματα με μικρές μόνο παραμορφώσεις των στοιχείων του πλέγματος. Παρά τον μεγαλύτερο αριθμό στοιχείων σε αυτό το μοντέλο, αυτή η μέθοδος δίνει ακριβέστερα αποτελέσματα και σε λιγότερο χρόνο σε σχέση με τα καρτεσιανά πλέγματα [28].

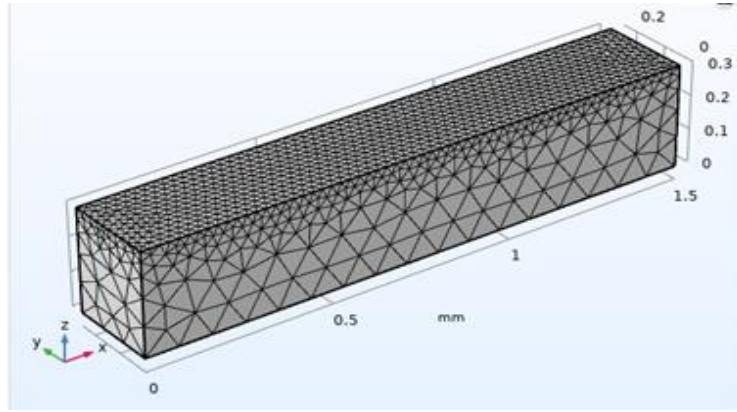
Οι παράμετροι παρακάτω ελέγχουν το μέγεθος των στοιχείων του τετραεδρικού πλέγματος:

- Μέγιστο μέγεθος στοιχείου: Αυτή η παράμετρος περιορίζει το επιτρεπόμενο μέγεθος των στοιχείων.
- Ελάχιστο μέγεθος στοιχείου: Αυτή η παράμετρος προσδιορίζει το ελάχιστο επιτρεπόμενο μέγεθος του στοιχείου. Αυτή η τιμή αποτρέπει την δημιουργία πολλών στοιχείων γύρω από μικρές καμπύλες περιοχές.
- Μέγιστος βαθμός ανάπτυξης στοιχείου: Αυτή η παράμετρος χρησιμοποιείται για τον καθορισμό του μέγιστου βαθμού στον οποίο το μέγεθος του στοιχείου μπορεί να αυξηθεί από μία περιοχή με μικρά στοιχεία προς μία περιοχή με μεγαλύτερα στοιχεία. Η τιμή αυτή πρέπει να είναι ίση ή μεγαλύτερη του 1.
- Παράγοντας καμπύλωσης: Αυτή η παράμετρος καθορίζει το μέγεθος των οριακών στοιχείων σε σύγκριση με την καμπυλότητα των γεωμετρικών ακμών.
- Ανάλυση στενών περιοχών: Αυτή η παράμετρος ελέγχει τον αριθμό των στρώσεων που δημιουργείται σε στενές περιοχές.

Στην παρούσα μελέτη, χρησιμοποιείται τετραεδρικό πλέγμα. Για να μειωθεί ο υπολογιστικός χρόνος, αυτό το πλέγμα αποτελείται από δύο υπο-πλέγματα, ένα λεπτότερο (στην πάνω επιφάνεια του μοντέλου) και ένα πιο χονδροειδές (στο υπόλοιπο μοντέλο). Συγκεκριμένα:

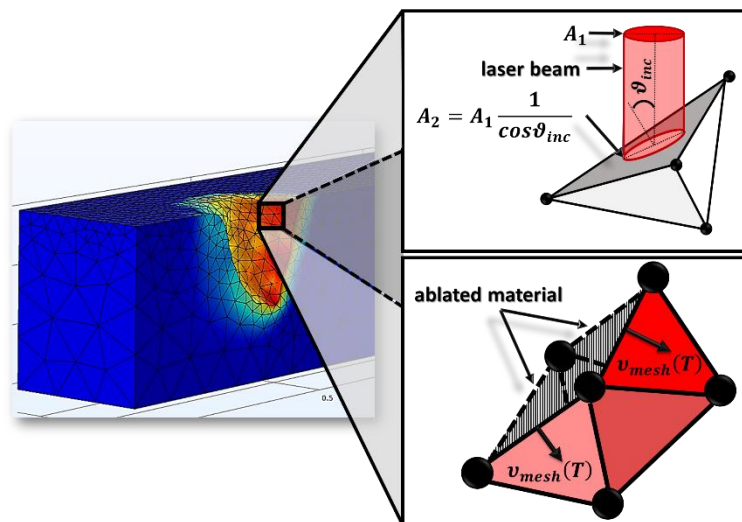
- Λεπτότερο πλέγμα:
 - Μέγιστο μέγεθος στοιχείου: 0.025mm
 - Ελάχιστο μέγεθος στοιχείου: 0.015mm
 - Μέγιστος βαθμός ανάπτυξης στοιχείου: 1.3
 - Παράγοντας καμπύλωσης: 0.9
 - Ανάλυση στενών περιοχών: 0.4
- Χονδροειδέστερο πλέγμα:
 - Μέγιστο μέγεθος στοιχείου: 0.0905mm
 - Ελάχιστο μέγεθος στοιχείου: 0.0192mm
 - Μέγιστος βαθμός ανάπτυξης στοιχείου: 1.4
 - Παράγοντας καμπύλωσης: 1
 - Ανάλυση στενών περιοχών: 0.3

Οπτικά, το πλέγμα δίνεται στην Εικόνα 15:



Εικόνα 15 Το πλέγμα που χρησιμοποιήθηκε στην προσομοίωση.

Η αλληλεπίδραση του πλέγματος με την ακτίνα του λέιζερ οπτικοποιείται στην Εικόνα 16:



Εικόνα 16 Οπτική αναπαράσταση της αλληλεπίδρασης της ακτίνας του λέιζερ με τα στοιχεία του πλέγματος.

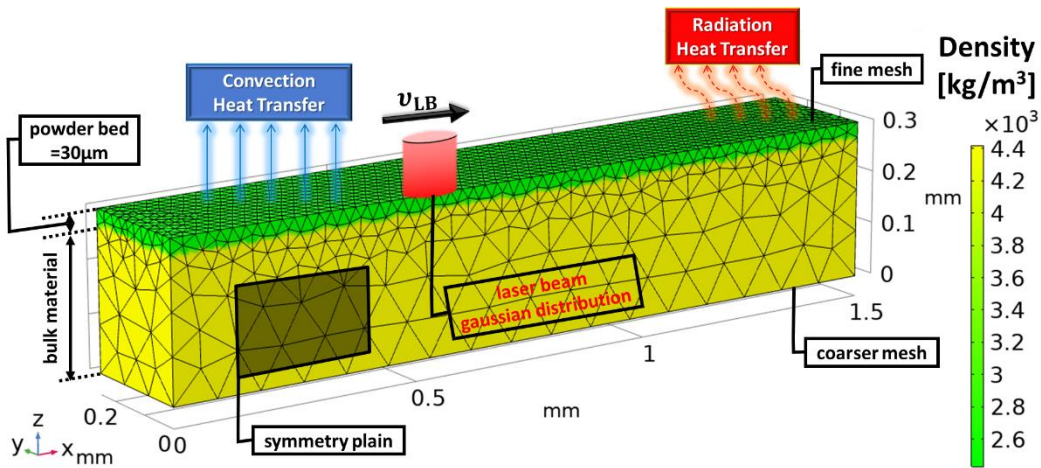
Εκλέπτυνση πλέγματος

Στην προσομοίωση του keyhole, γίνεται μεγάλη παραμόρφωση του πλέγματος, που οδηγεί πολλά στοιχεία να πέφτουν κάτω από το ελάχιστο επιτρεπτό μέγεθος τους, με αποτέλεσμα να προκαλούνται υπολογιστικά σφάλματα. Για την αντιμετώπιση αυτών των σφαλμάτων, πραγματοποιείται εκλέπτυνση του πλέγματος. Η εκλέπτυνση των παραμορφωμένων περιοχών όχι μόνο αναδεικνύει τα γεωμετρικά χαρακτηριστικά της παραμόρφωσης και επίσης να δώσει ρεαλιστικές προσομοιώσεις της παραμόρφωσης [29].

Υπολογιστική επίλυση

Η προσομοίωση πραγματοποιείται για κατάλληλο μήκος μέχρι να επιτευχθεί μόνιμη κατάσταση.

Συνοψίζοντας, το πλήρες μοντέλο που χρησιμοποιήθηκε στην προσομοίωση οπτικοποιείται στην Εικόνα 17:



Εικόνα 17 Οπτική αναπαράσταση του πλήρους μοντέλου που χρησιμοποιήθηκε στην προσομοίωση.

Οπτική αναπαράσταση

Στο τέλος της προσομοίωσης και προκειμένου να παρουσιαστούν ταυτόχρονα οι λύσεις όλων των επιμέρους χρονικών βημάτων, χρησιμοποιείται η ακόλουθη μαθηματική εξίσωση:

$$T_{max} = nojac \begin{cases} T, & T > T_{max} \\ T_{max}, & T \leq T_{max} \end{cases} \quad (51)$$

Όπου T_{max} (K) είναι η μέγιστη θερμοκρασία κάθε στοιχείου.

Αυτή η εξίσωση σημαίνει ότι αν η θερμοκρασία στο προηγούμενο χρονικό βήμα είναι μεγαλύτερη από T_{max} , ορίζεται ότι το T_{max} είναι ίσο με αυτή την. Αλλιώς, το T_{max} μένει ως έχει. Το nojac() αποτρέπει την συνεισφορά αυτής της εξίσωσης στον Ιακωβιανό πίνακα (στον πίνακα του συστήματος).

Μαζί με αυτή τη μαθηματική εξίσωση, εφαρμόζεται και το φίλτρο: $T > 1923.15K$, έτσι ώστε να εμφανίζεται μόνο η λίμνη του τήγματος. Στο τέλος, για κάθε στοιχείο του πλέγματος εμφανίζεται και το συμμετρικό του ως προς το επίπεδο $y=0$, έτσι ώστε να παρουσιάζεται ολόκληρη η λίμνη του τήγματος.

Έλεγχος αποτελεσμάτων

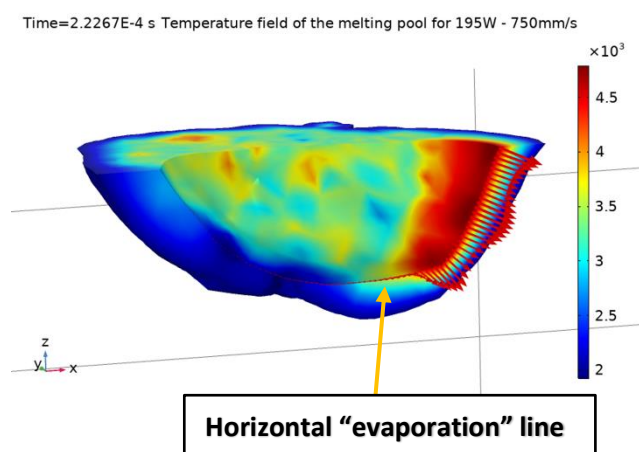
Τα αποτελέσματα των προσομοιώσεων ελέγχονται βάσει των πειραματικών αποτελεσμάτων των Dilip J. et al. [30].

Συζήτηση αποτελεσμάτων

Ορισμός για την μόνιμη κατάσταση του τήγματος

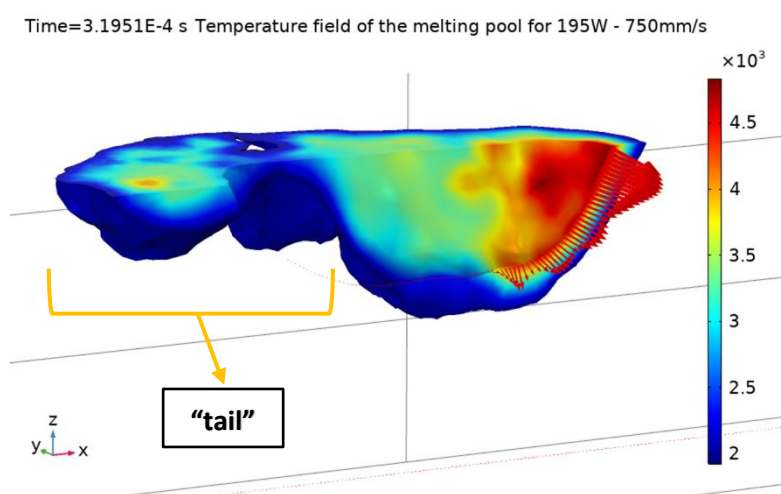
Στην conduction μορφή, όπου μπορεί να εμφανιστούν σφαιρικά ελαττώματα και ασυνέχειες, η μόνιμη κατάσταση εξαρτάται από τον χρόνο ή εναλλακτικά από το πειραματικό μήκος. Συγκεκριμένα, για το 50W-1200mm/s, χρησιμοποιήθηκε μήκος 1.5mm, που επαρκεί για την παρατήρηση όλων των φαινομένων και των χαρακτηριστικών του τήγματος.

Αντίθετα, ως μόνιμη κατάσταση του τήγματος σε keyhole μορφή θεωρείται ο συνδυασμός της μόνιμης κατάστασης εξάτμισης και της μόνιμης κατάστασης μεταφοράς θερμότητας. Συνήθως, η μόνιμη κατάσταση εξάτμισης προηγείται και ορίζεται ως ο σχηματισμός μίας οριζόντιας γραμμής «εξάτμισης» (Εικόνα 18).



Εικόνα 18 Η μόνιμη κατάσταση της εξάτμισης.

Η μόνιμη κατάσταση μεταφοράς θερμότητας ορίζεται από τον σχηματισμό μιας «ουράς» πίσω από την ακτίνα του λέιζερ (Εικόνα 19).



Εικόνα 19 Η μόνιμη κατάσταση μεταφοράς θερμότητας.

Ο προσδιορισμός του β_R

Στην παρούσα μελέτη χρησιμοποιείται η μέθοδος δοκιμής και σφάλματος για τον προσδιορισμό του β_R , οπότε για κάθε συνδυασμό παραμέτρων έτρεξαν περίπου πέντε με έξι

προσομοιώσεις μέχρι να βρεθεί η σωστή τιμή, που οδηγεί σε παρόμοια αποτελέσματα με τα πειραματικά. Επιπλέον, η ακρίβεια της τιμής αυτής περιορίζεται στο πρώτο δεκαδικό ψηφίο, καθώς στόχος της παρούσας εργασίας είναι η πρόταση ενός γρήγορου τρόπου πρόβλεψης του πλάτους και του βάθους του τήγματος, χωρίς εκτεταμένη ανάγκη για καλιμπράρισμα.

Αποτελέσματα προσομοίωσης

Τα αποτελέσματα των προσομοιώσεων ελέγχονται βάσει των πειραματικών αποτελεσμάτων των Dilip J. et al. [30].

Πίνακας 10 Αποτελέσματα προσομοίωσης

Laser power (W)	Scanning speed (mm/s)	VED (J/mm ³)	β_R	Depth error (%)	Width error (%)
50	1000	13.88	1	-10%	8.47%
195	750	86.66	0.55	-15%	-16%
195	500	130	0	-1.7%	-14.6%

Στον Πίνακα 10, το σφάλμα βάθους (depth error) και το σφάλμα πλάτους (width error) έχουν υπολογιστεί βάσει των παρακάτω τύπων:

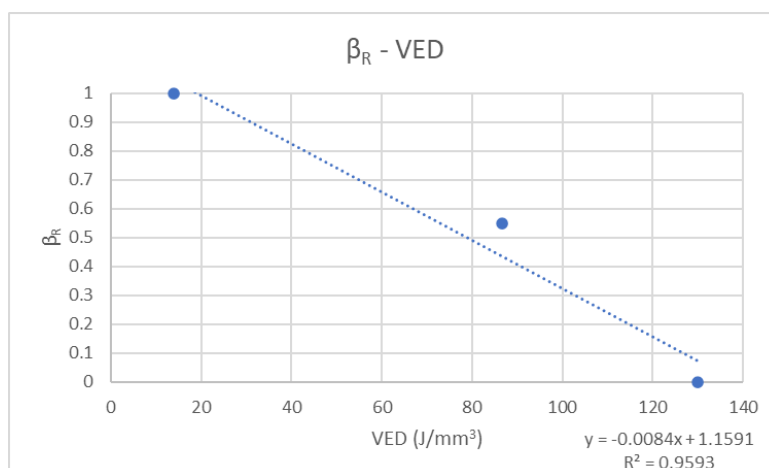
$$\text{Σφάλμα βάθους (\%)} = \frac{\text{Πειραματικό βάθος} - \text{Βάθος προσομοίωσης}}{\text{Πειραματικό βάθος}} \quad (52)$$

$$\text{Σφάλμα πλάτους (\%)} = \frac{\text{Πειραματικό πλάτος} - \text{Πλάτος προσομοίωσης}}{\text{Πειραματικό πλάτος}} \quad (53)$$

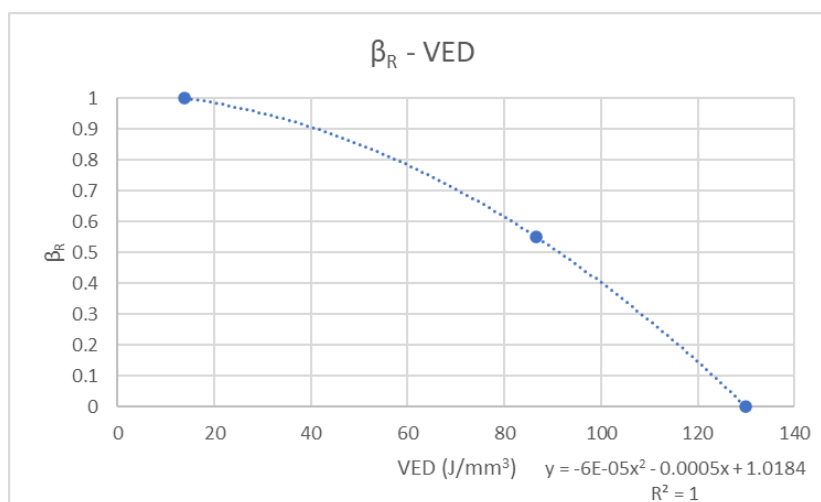
Από τον Πίνακα 10, μπορεί να παρατηρηθεί ότι τα αποτελέσματα της προσομοίωσης είναι σε συμφωνία με τα πειραματικά δεδομένα, καθώς το σφάλμα σε όλες τις περιπτώσεις είναι κάτω από 16%. Αυτά τα σφάλματα εμφανίζονται λόγω της υπόθεσης ότι ο συντελεστής απορρόφησης είναι σταθερός και ίσος με 0.77. Στην πραγματικότητα, ο συντελεστής απορρόφησης εξαρτάται από τη θερμοκρασία και υπολογίζεται από τις εξισώσεις του Fresnel και τη θεωρία του Drude [15]. Παρόλα αυτά, οι εξισώσεις του Fresnel και η θεωρία του Drude εισάγουν μη γραμμικότητα, οδηγώντας σε ένα σύνθετο μοντέλο με υψηλό υπολογιστικό κόστος και χρόνο. Για αυτό τον λόγο, η εξάρτηση από τη θερμοκρασία του συντελεστή απορρόφησης, στην παρούσα μελέτη, αγνοείται. Δευτερευόντως, ένας άλλος λόγος που οδηγεί σε σφάλματα είναι η διαφορά μεταξύ των θεωρητικών ιδιοτήτων του υλικού, που λήφθηκαν από τα [18], [20], και των πραγματικών ιδιοτήτων του υλικού που χρησιμοποιήθηκε στα πειράματα.

Μια ακόμα σημαντική παρατήρηση από τον Πίνακα 10 είναι η σχέση μεταξύ του VED και του β_R (δες Διάγραμμα 24, Διάγραμμα 25). Συγκεκριμένα, καθώς το VED αυξάνεται, το β_R μειώνεται και το αντίστροφο. Αυτό το φαινόμενο μπορεί να εξηγηθεί βάσει της θεωρίας αφαίρεσης υλικού. Όταν το VED αυξάνεται, που σημαίνει ότι η ισχύς του λέιζερ αυξάνεται και/ή η ταχύτητα σάρωσης μειώνεται, μία μεγαλύτερη περιοχή του μοντέλου φτάνει ή ξεπερνά την θερμοκρασία εξάτμισης του Ti6Al4V (3315K), οπότε γίνεται μεγαλύτερη αφαίρεση υλικού. Μεγαλύτερη αφαίρεση υλικού σημαίνει ότι λιγότερα άτομα (που

εξατμίστηκαν) ανασυντίθενται στην επιφάνεια του μοντέλου. Αυτή η μικρή ανασύνθεση των ατόμων μοντελοποιείται στην προσομοίωση ως χαμηλό β_R .



Διάγραμμα 24 Γραμμική σχέση μεταξύ β_R και VED.



Διάγραμμα 25 2^{ου} βαθμού πολυωνυμική σχέση β_R και VED.

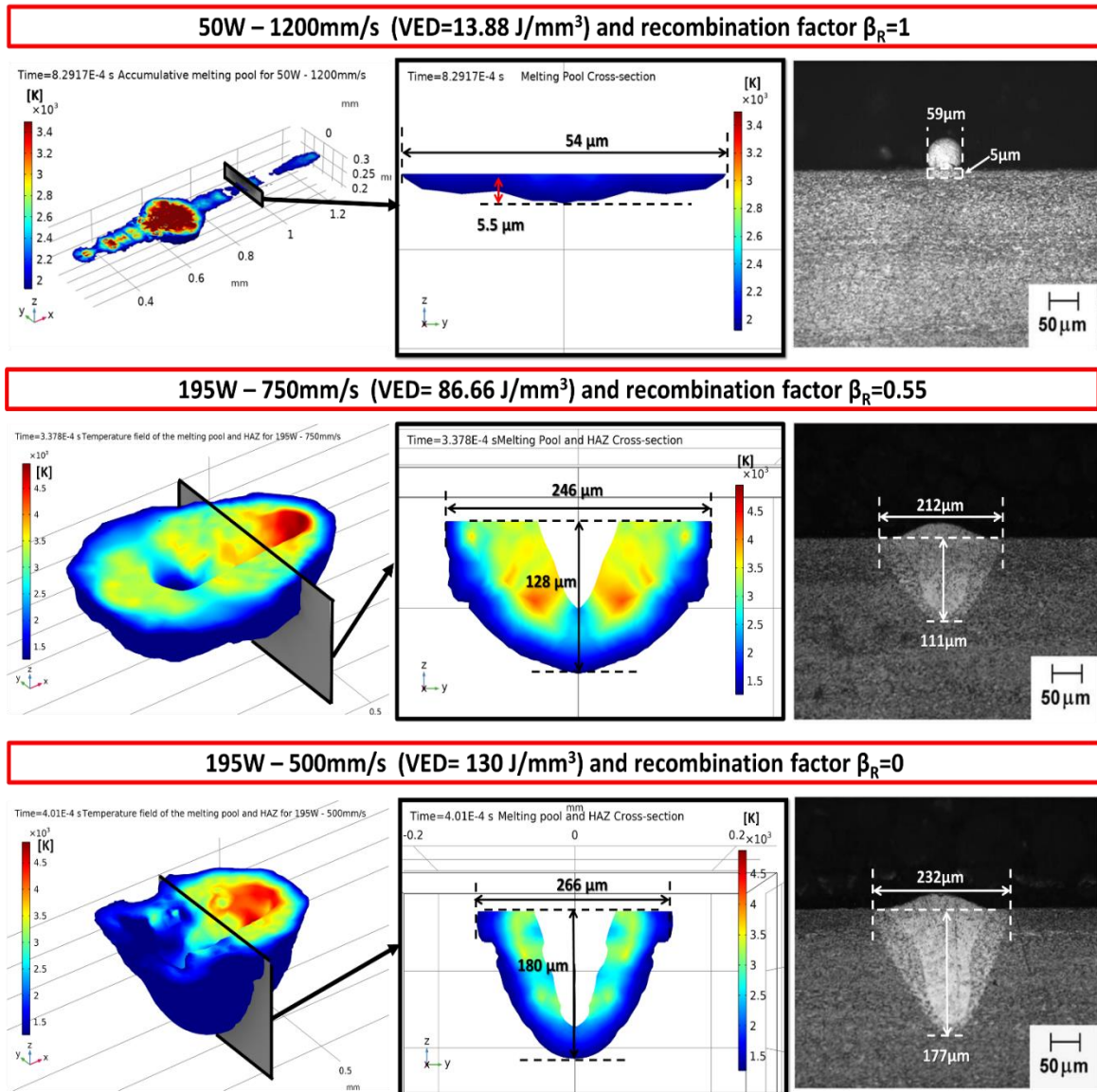
Οι τιμές των VED και β_R αποτελούν ένδειξη ότι μπορεί να υπάρχει μία πολυωνυμική σχέση μεταξύ των VED και β_R . Μια γραμμική (Διάγραμμα 24) και μια 2^{ου} βαθμού πολυωνυμική (Διάγραμμα 25) σχέση προτείνονται παραπάνω. Παρόλα αυτά, οι μόνο τρεις τιμές των VED και β_R δεν επαρκούν για να δώσουν μία ακριβή γραμμή τάσης, οπότε απαιτείται περαιτέρω έρευνα για το ποια συγκεκριμένη σχέση ισχύει.

Σύγκριση προσομοιώσεων με πειραματικά αποτελέσματα

Στην Εικόνα 20, γίνεται άμεση σύγκριση μεταξύ πειραματικών αποτελεσμάτων και προσομοίωσης. Παρατηρείται ότι όλα τα αποτελέσματα των προσομοιώσεων συμφωνούν με τα πειραματικά δεδομένα, καθώς εμφανίζουν σφάλμα κάτω από 16%.

Το 50W-1200mm/s αποτελεί προσομοίωση της conduction μορφής, ενώ το 195W-750mm/s και το 195W-500mm/s είναι μορφής keyhole.

Στην συγκεκριμένη περίπτωση της conduction μορφής του 50W-1200mm/s, η τήξη δεν είναι επαρκής, καθώς εμφανίζονται σφαιρικά ελαττώματα και ασυνέχειες και δεν υπάρχει σύνδεση με το υπόστρωμα.



Εικόνα 20 Σύγκριση προσομοιώσεων με πειράματα

Τα σφαιρικά ελαττώματα μπορεί να συμβαίνουν για δύο λόγους. Ο ένας είναι ο σχηματισμός των σφαιρών λόγω ανεπαρκούς ενέργειας από το λέιζερ με χαμηλό περιεχόμενο σε υγρή κατάσταση. Ο άλλος είναι λόγω σταγονιδίων που οφείλονται στις υψηλές ταχύτητες σάρωσης. Συνεπώς, η ισχύς του λέιζερ και η ταχύτητα σάρωσης έχουν άμεση επίδραση στα σφαιρικά ελαττώματα [25].

Εξάλλου, οι υψηλές ταχύτητες σάρωσης οδηγούν σε μεγάλους λόγους μήκους προς διάμετρος του τήγματος. Τέτοια τήγματα με λόγο μήκους προς διάμετρος μεγαλύτερη από θα προκαλέσει σφαιρικά ελαττώματα [31].

Στην Εικόνα 20, εμφανίζονται σφαιρικά ελαττώματα (και στην προσομοίωση και στα πειραματικά δεδομένα) που προεξέχουν προς τα πάνω και είναι αποτέλεσμα των τάσεων επιφανείας του τηγμένου κράματος.

Ένας τέτοιος συνδυασμός παραμέτρων κατεργασίας οδηγεί σε τεμάχια με μεγάλο ποσοστό πόρων.

Ακόμα, οι ασυνέχειες (Εικόνα 20, προσομοίωση και πειραματικά του 50W-1200mm/s) είναι ένδειξη ότι η ισχύς του λέιζερ είναι ανεπαρκής για να τήξει τη σκόνη, καθώς το λέιζερ σαρώνει με ταχύτερο ρυθμό.

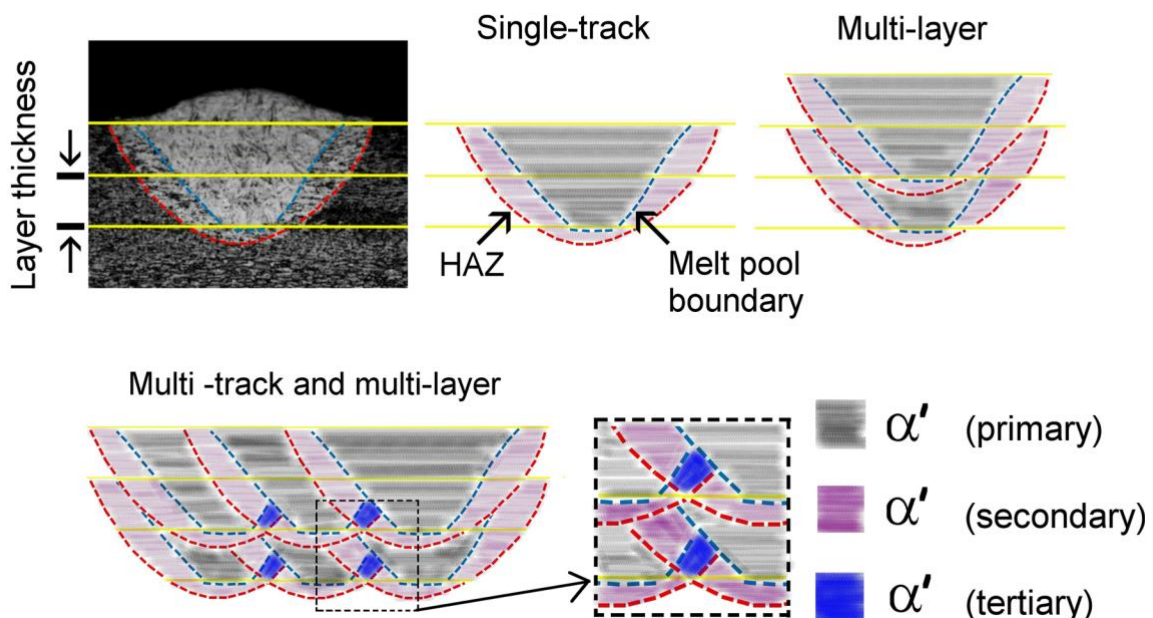
Επιπρόσθετα, όπως παρατηρείται στην Εικόνα 20 για το 50W-1200mm/s, το βάθος του τήγματος είναι μικρότερο από 6μm και στις προσομοιώσεις και στα πειράματα, που είναι μικρότερο από το ύψος της σκόνης (30μm), οπότε η νέα στρώση που δημιουργείται δεν μπορεί να συνδεθεί με το υπόστρωμα.

Συμπερασματικά, η σημασία της μελέτης αυτής της περίπτωσης είναι να αναδείξει ότι το μοντέλο που χρησιμοποιείται στην προσομοίωση είναι χρήσιμο όχι μόνο να προβλέψει το πλάτος και το βάθος του τήγματος, αλλά επίσης και να προβλέψει τα πιθανά ελαττώματα που κάθε συνδυασμός παραμέτρων κατεργασίας μπορεί να εμφανίσει.

Στις περιπτώσεις του keyhole, το σχήμα-V που σχηματίζεται στο 195W-750mm/s και στο 195W-500mm/s είναι πανομοιότυπο με τα αντίστοιχα πειραματικά, οπότε το μοντέλο της παρούσας μελέτης μπορεί να προβλέψει με αρκετή ακρίβεια την γεωμετρία του keyhole.

Ακόμα, μπορεί να παρατηρηθεί ότι για σταθερή ισχύ λέιζερ, το βάθος του τήγματος αυξάνεται όταν η ταχύτητα σάρωσης μειώνεται. Αυτό συμβαίνει επειδή για χαμηλές ταχύτητες σάρωσης, κάθε περιοχή του μοντέλου επηρεάζεται για περισσότερο χρόνο από την ισχύ του λέιζερ, οπότε η θερμοκρασία της κάθε περιοχής αυξάνεται, επηρεάζοντας και τα βαθύτερα στρώματα. Αυτή η αύξηση του βάθους για χαμηλές ταχύτητες σάρωσης μπορεί επίσης να προβλεφθεί από την προσομοίωση της παρούσας μελέτης.

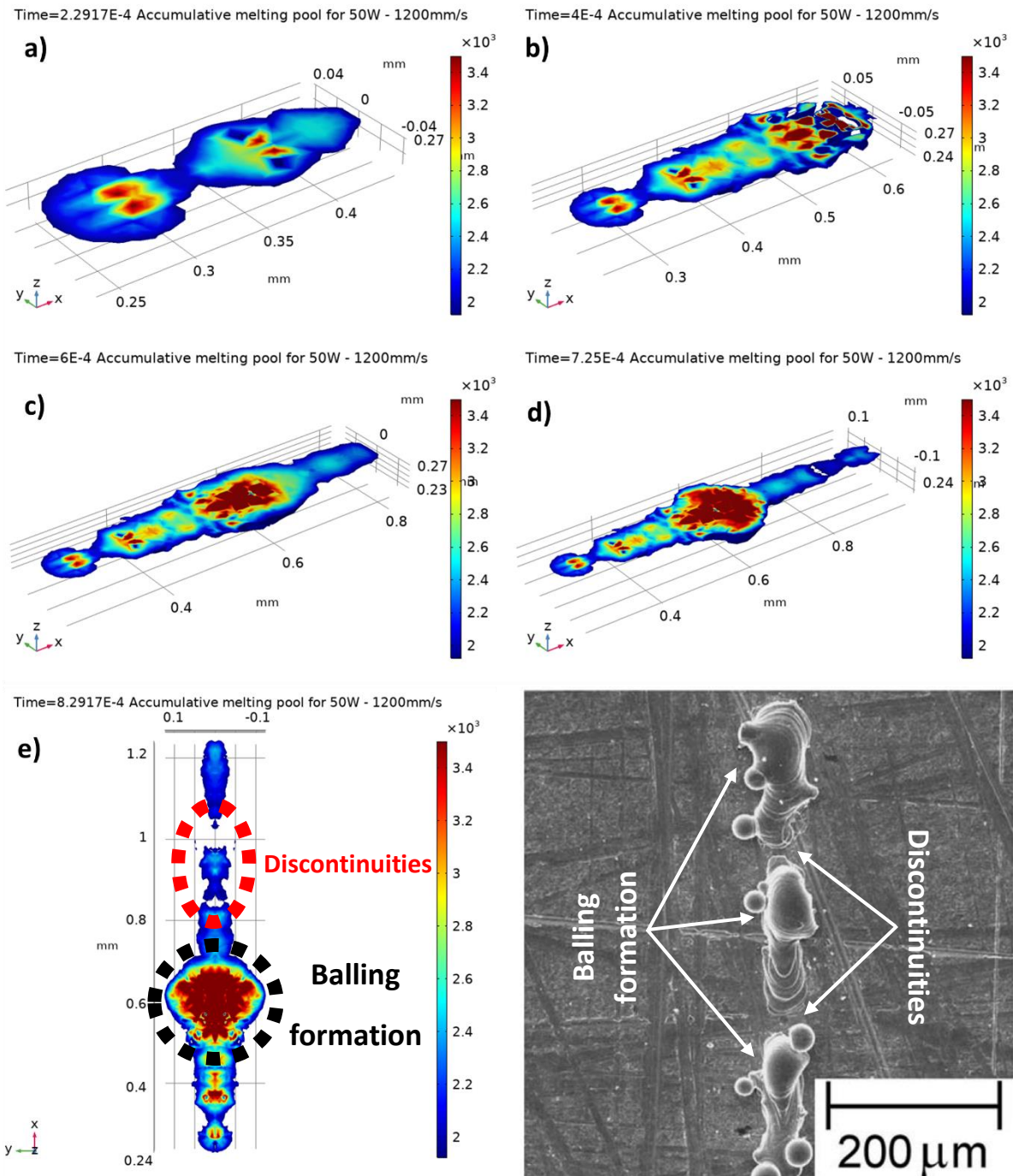
Τέλος, στην παρούσα μελέτη, όπου προσομοιώνονται μόνο δοκίμια μονού περάσματος (single tracks), εμφανίζονται τόσο στις προσομοιώσεις όσο και στα πειραματικά δεδομένα, οι δομές των μαρτενσιτών α' (πρωτεύων), α' (δευτερεύων) (Εικόνα 21). Αυτό σημαίνει ότι το μοντέλο της παρούσας μελέτης μπορεί να προβλέψει και την μικροδομή του SLM-κατεργασμένου Ti6Al4V.



Εικόνα 21 Η εξέλιξη της μικροδομής σε διάφορα είδη δοκιμών Ti6Al4V.

Ανάλυση του 50W-1200mm/s

Δεδομένου ότι ο συνδυασμός των παραμέτρων που χρησιμοποιείται σε αυτή την περίπτωση είναι ακατάλληλος, το τήγμα παρουσιάζει ελαττώματα ήδη από την έναρξη της κατεργασίας (Εικόνα 22a). Το πλάτος και το βάθος του τήγματος και η κατανομή της θερμοκρασίας στο τηγμένο υλικό είναι ασαφή. Για αυτό τον λόγο, στο Εικόνα 22b, γίνεται θρυμματισμός του τήγματος που οδηγεί στην συσσώρευση περισσότερης θερμότητας στο κέντρο του τηγμένου υλικού.

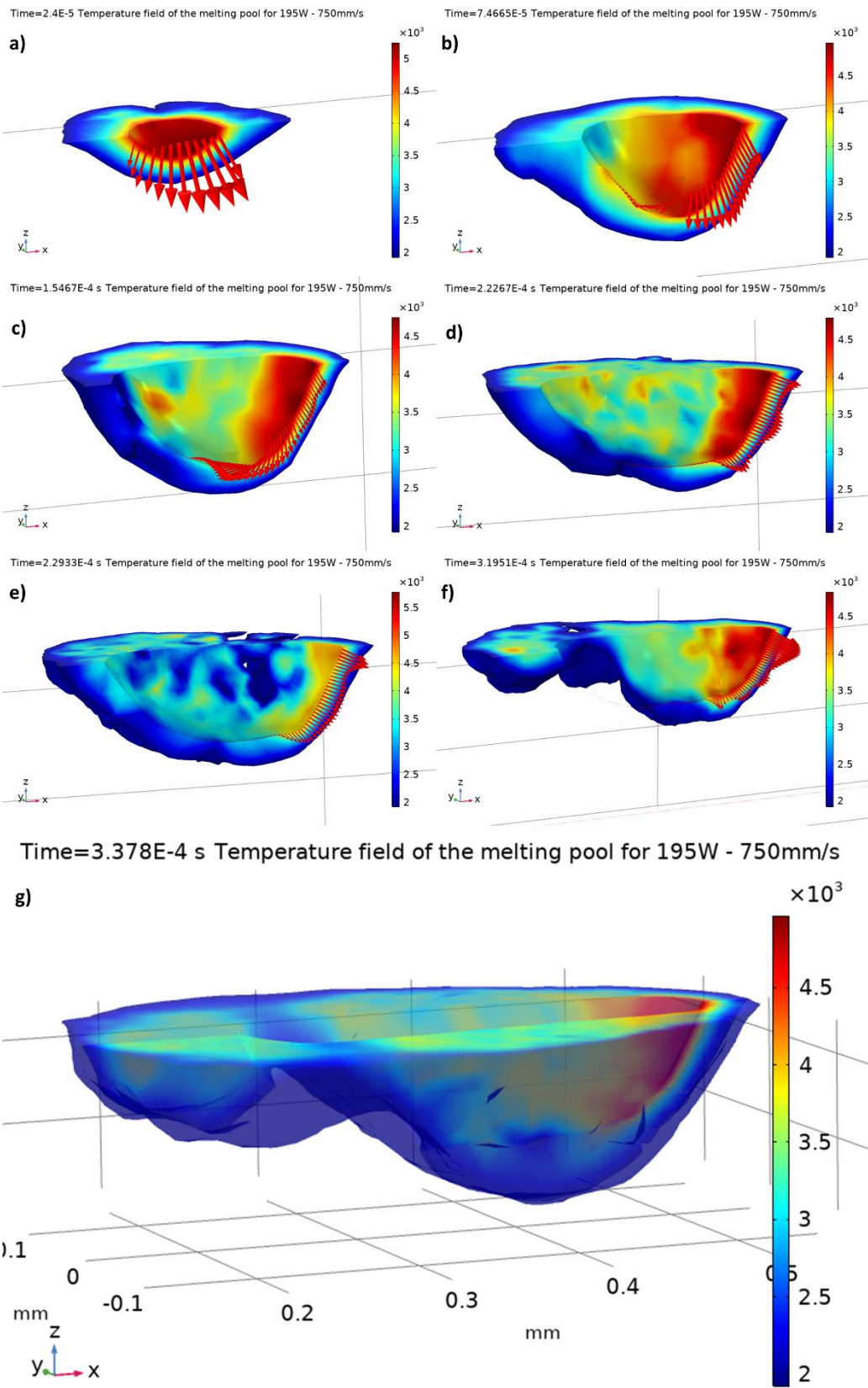


Εικόνα 22 Εξέλιξη του τήγματος στο 50W-1200mm/s.

Αυτή η συσσωρευμένη θερμότητα οδηγεί σε πολύ υψηλές θερμοκρασίες σε αυτή την περιοχή, με αποτέλεσμα την υπερμεγέθυνση του βάθους και του πλάτους αυτής της περιοχής (Εικόνα 22c) και τελικά, στον σχηματισμό σφαιρικού ελαττώματος (Εικόνα 22d). Παρόλα αυτά, ταυτόχρονα με τον σχηματισμό του σφαιρικού ελαττώματος, το λέιζερ τήκει μία «νέα περιοχή» μπροστά από το σφαιρικό ελάττωμα, με σταθερό βάθος και πλάτος, που αποδεικνύει την μόνιμη κατάσταση (Εικόνα 22c). Όμως, λόγω του υψηλού λόγου ταχύτητας σάρωσης-ισχύος λέιζερ, αυτή η μόνιμη κατάσταση είναι δύσκολο να διατηρηθεί και αμέσως αρχίζουν να εμφανίζονται ασυνέχειες (Εικόνα 22d). Τέλος, στην Εικόνα 22e, γίνεται σύγκριση μεταξύ της προσομοίωσης και των πειραμάτων, που αποδεικνύει την ικανότητα του μοντέλου να προβλέψει πιθανά ελαττώματα.

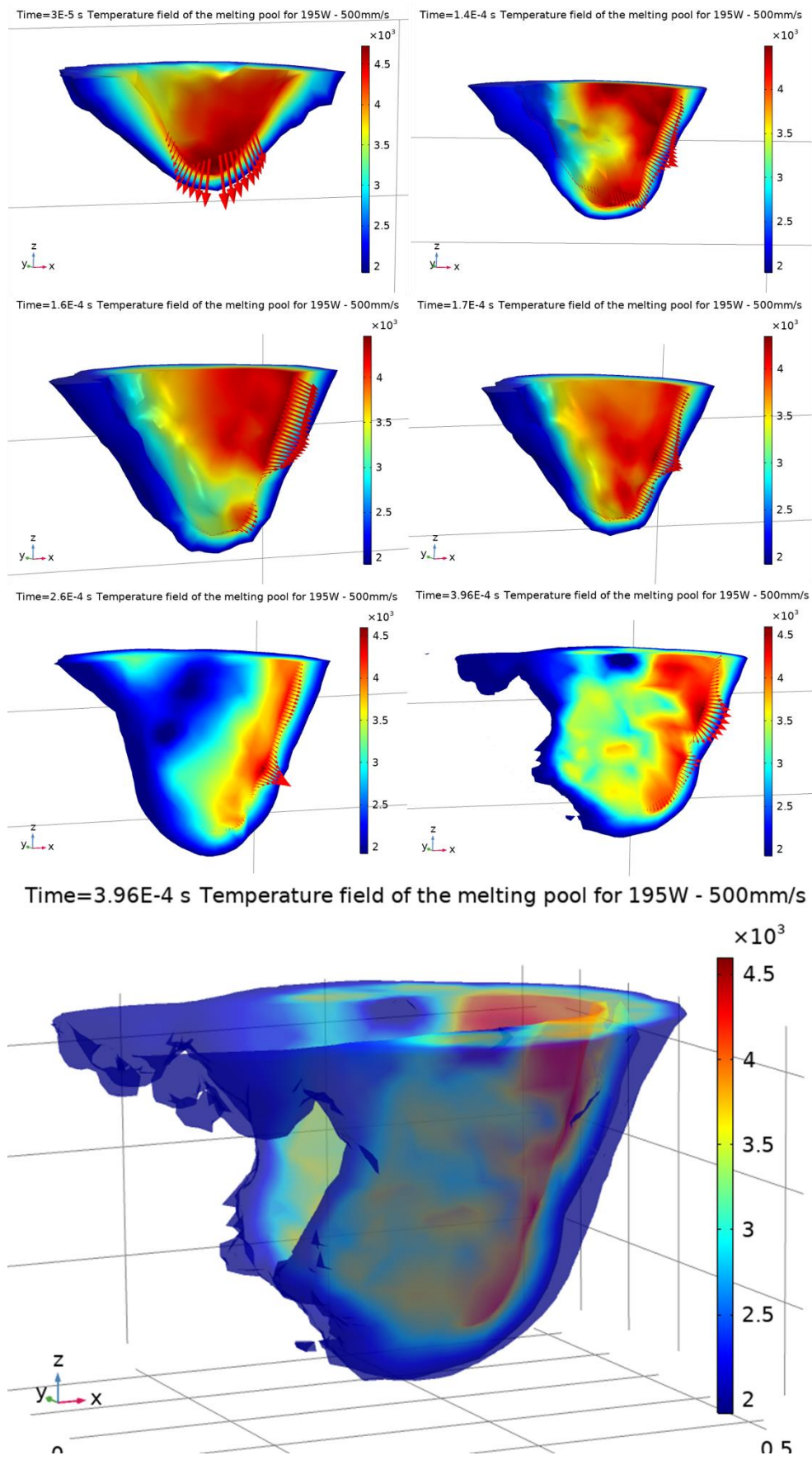
Ανάλυση του 195W-750mm/s

Στην αρχή της κατεργασίας, το λέιζερ «σκάβει» το υλικό ώστε να δημιουργήσει το keyhole, οπότε η ταχύτητα αφαίρεσης της μάζας είναι κατακόρυφη με φορά προς τα κάτω (Εικόνα 23a). Καθώς το keyhole αυξάνεται, η ταχύτητα έχει περισσότερο διαγώνια κατεύθυνση, ώστε όχι μόνο να σκάβει το υλικό, αλλά και να κινεί το keyhole προς τα εμπρός (Εικόνα 23b, c). Όταν επιτευχθεί η μόνιμη κατάσταση εξάτμισης, η ταχύτητα έχει κυρίως οριζόντια κατεύθυνση, που σημαίνει ότι το σκάψιμο σταματά (και το βάθος του τήγματος δεν αλλάζει) και το keyhole κινείται μόνο προς τα μπροστά (Εικόνα 23d, e). Επιπλέον, σε αυτή την κατάσταση, η ταχύτητα είναι ομοιόμορφα κατανεμημένη στο μπροστινό τμήμα του πλαϊνού τοιχώματος του keyhole, επειδή σε αυτή τη χρονική στιγμή το λέιζερ περνά ακριβώς πάνω από αυτή την περιοχή. Τέλος, όταν επιτυγχάνεται και η μόνιμη κατάσταση μεταφοράς θερμότητας, η ταχύτητα συνεχίζει να είναι κυρίως οριζόντια (Εικόνα 23f). Παρόλα αυτά, εδώ η ταχύτητα δεν είναι ομοιόμορφα κατανεμημένη, αλλά η αφαίρεση υλικού είναι μεγαλύτερη στο πάνω μέρος του πλαϊνού τοιχώματος από ότι στο κάτω μέρος. Αυτό συμβαίνει επειδή αυτή τη χρονική στιγμή, το λέιζερ έχει προσπεράσει αυτή την περιοχή και η ισχύς του λέιζερ δεν μπορεί να φτάσει σε ολόκληρο το πλαϊνό τοίχωμα. Είναι επίσης χρήσιμο να παρατηρηθεί ότι μια μικρή κατακόρυφη και με φορά προς τα κάτω ταχύτητα αναπτύσσεται στις απότομες ακμές που έχουν παραμείνει στον πυθμένα του keyhole. Αυτό σημαίνει ότι το SLM σύστημα προσπαθεί από μόνο του να σκάψει και να διορθώσει απότομα ελαττώματα, οδηγώντας σε μία ομαλή επιφάνεια του keyhole. Στην Εικόνα 23g δίνεται το πλήρες μοντέλο, όπου είναι ορατές οι περιοχές των μαρτενσιτών α' (πρωτεύων) και α' (δευτερεύων).

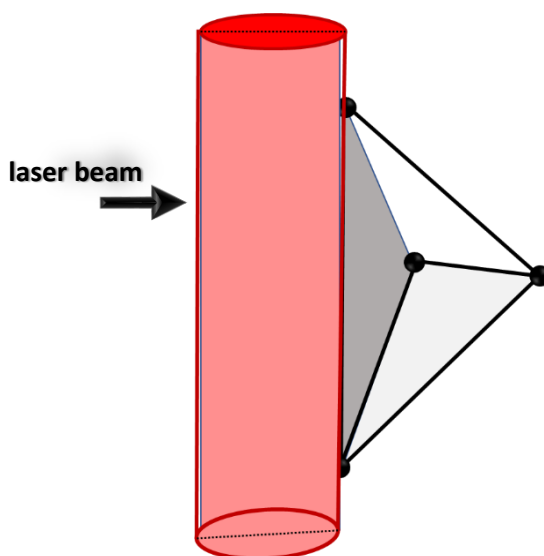


Εικόνα 23 Η εξέλιξη του keyhole στο 195W-750mm/s.

Ανάλυση του 195W-500mm/s



Στην αρχή της κατεργασίας, το λέιζερ «σκάβει» το υλικό ώστε να δημιουργήσει το keyhole, οπότε η ταχύτητα αφαίρεσης της μάζας είναι κατακόρυφη με φορά προς τα κάτω (Εικόνα 24a). Καθώς το keyhole αυξάνεται, η ταχύτητα έχει περισσότερο διαγώνια κατεύθυνση, ώστε όχι μόνο να σκάβει το υλικό, αλλά και να κινεί το keyhole προς τα εμπρός (Εικόνα 24b). Όταν επιτευχθεί η μόνιμη κατάσταση εξάτμισης, η ταχύτητα έχει κυρίως οριζόντια κατεύθυνση, που σημαίνει ότι το σκάψιμο σταματά (και το βάθος του τήγματος δεν αλλάζει) και το keyhole κινείται μόνο προς τα μπροστά (Εικόνα 24c, d, e). Επιπλέον, σε αυτή την κατάσταση, η ταχύτητα είναι ομοιόμορφα κατανεμημένη στο μπροστινό τμήμα του πλαϊνού τοιχώματος του keyhole, επειδή σε αυτή τη χρονική στιγμή το λέιζερ περνά ακριβώς πάνω από αυτή την περιοχή. Παρόλα αυτά, αυτή η ομοιόμορφη κατανομή διακόπτεται σε μια μικρή απότομη περιοχή και μετά εμφανίζεται ξανά μετά από αυτή την περιοχή (Εικόνα 24c). Σε αυτή την περιοχή μπορεί να παρατηρηθεί ότι σχηματίζεται μία γωνία σχεδόν 90° , όπου η επιφάνεια του πλαϊνού τοιχώματος σε αυτή την περιοχή είναι κατακόρυφη (παράλληλη με τον άξονα z). Αυτό έχει ως αποτέλεσμα οι ελεύθερες επιφάνειες των στοιχείων του πλέγματος αυτής της περιοχής να είναι επίσης κατακόρυφες, που σημαίνει ότι αυτά τα στοιχεία του πλέγματος μπορούν μόνο να εφάπτονται με την περιφέρεια του «κυλίνδρου του λέιζερ» και ποτέ δεν μπορούν να τμηθούν από την ακτίνα του λέιζερ. Επιπλέον, η περιφέρεια του κυλίνδρου του λέιζερ δεν έχει καθόλου ισχύ (λόγω της γκαουσιανής κατανομής της έντασης του λέιζερ), οπότε δεν υπάρχει μεταφορά θερμότητας σε αυτή την περιοχή (Εικόνα 25). Προκειμένου να μετακινηθεί αυτή η περιοχή προς τα εμπρός, αυτή η απότομη γωνία πρέπει πρώτα να σκαφτεί. Όταν η περιοχή αυτή σκαφτεί (Εικόνα 24d, e) η οριζόντια ταχύτητα που αναπτύσσεται εκεί είναι μεγαλύτερη από την ταχύτητα του υπόλοιπου πλαϊνού τοιχώματος, έτσι ώστε να το προφτάσει καθώς κινείται προς τα εμπρός. Τέλος, όταν επιτυγχάνεται και η μόνιμη κατάσταση μεταφοράς θερμότητας, η ταχύτητα συνεχίζει να είναι κυρίως οριζόντια (Εικόνα 24f). Παρόλα αυτά, εδώ η ταχύτητα δεν είναι ομοιόμορφα κατανεμημένη, αλλά η αφαίρεση υλικού είναι μεγαλύτερη στο πάνω μέρος του πλαϊνού τοιχώματος από ότι στο κάτω μέρος. Αυτό συμβαίνει επειδή αυτή τη χρονική στιγμή, το λέιζερ έχει προσπεράσει αυτή την περιοχή και η ισχύς του λέιζερ δεν μπορεί να φτάσει σε ολόκληρο το πλαϊνό τοίχωμα. Είναι επίσης χρήσιμο να παρατηρηθεί ότι ακόμα και στην πλήρη μόνιμη κατάσταση, απότομες ακμές μπορεί να δημιουργηθούν στο μέσο του πλαϊνού τοιχώματος, που διακόπτουν την οριζόντια ταχύτητα σε αυτή την περιοχή μέχρι να σκαφτεί. Στην Εικόνα 24g δίνεται το πλήρες μοντέλο, όπου είναι ορατές οι περιοχές των μαρτενσιτών α' (πρωτεύων) και α'' (δευτερεύων).



Εικόνα 25 Δεν υπάρχει αλληλεπίδραση μεταξύ της ακτίνας λέιζερ και της κατακόρυφης επιφάνειας ενός στοιχείου του πλέγματος.

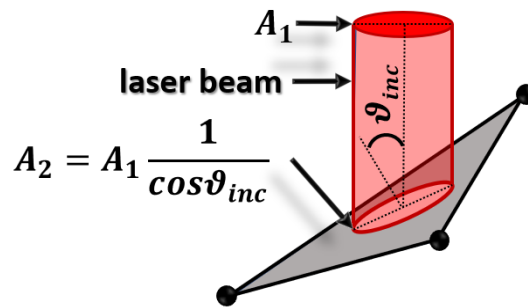
Ποσοστό μείωσης της μέγιστης έντασης του λέιζερ

Η ένταση του λέιζερ $\left(\frac{W}{mm^2}\right)$ ορίζεται ως η ισχύς του λέιζερ ανά μονάδα επιφάνειας.

Όταν μία ακτίνα λέιζερ με αρχική επιφάνεια ακτίνας A_1 προσπίπτει σε μία επιφάνεια, τότε το εμβαδόν της ακτίνας που έρχεται σε «επαφή» με την επιφάνεια δίνεται από την παρακάτω σχέση:

$$A_2 = A_1 \frac{1}{\cos\vartheta_{inc}} \quad (54)$$

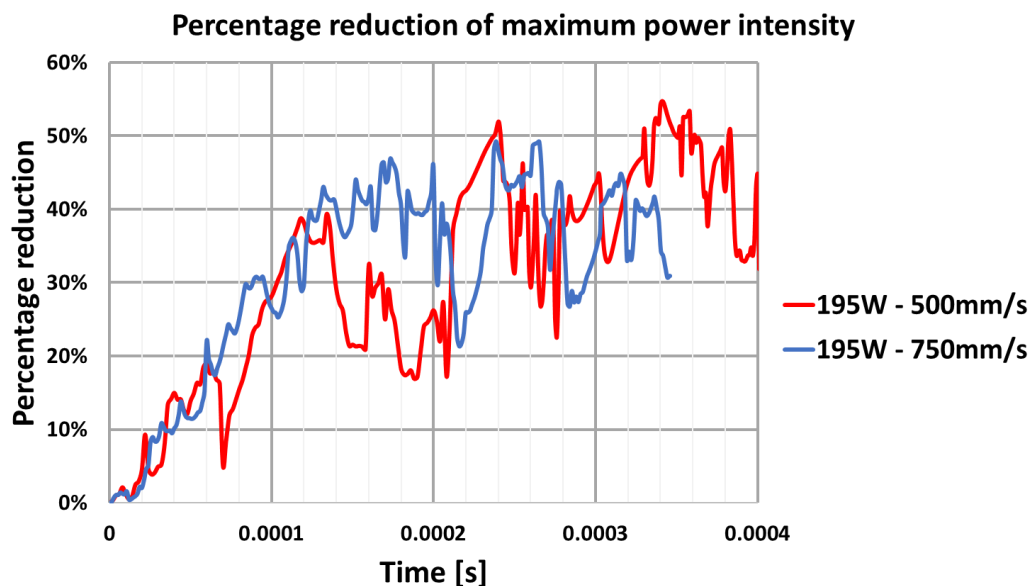
Όπου τα A_1 , A_2 και ϑ_{inc} περιγράφονται από την Εικόνα 26:



Εικόνα 26 Η ακτίνα λέιζερ σε «επαφή» με μία επιφάνεια.

Όπως παρατηρείται από την (54), για $\vartheta_{inc} = 0$, όπου η επιφάνεια είναι οριζόντια (το οποίο αντιπροσωπεύει την αρχική επιφάνεια που έρχεται σε επαφή με την ακτίνα του λέιζερ), $A_2 = A_1$. Αντίθετα, όταν $0^\circ < \vartheta_{inc} < 90^\circ$ (το οποίο αντιπροσωπεύει την επικλινή επιφάνεια του keyhole), $A_2 > A_1$. Φυσικά, καθώς το keyhole γίνεται βαθύτερο, η κλίση αυξάνεται, οπότε η A_2 αυξάνεται και η ένταση του λέιζερ μειώνεται.

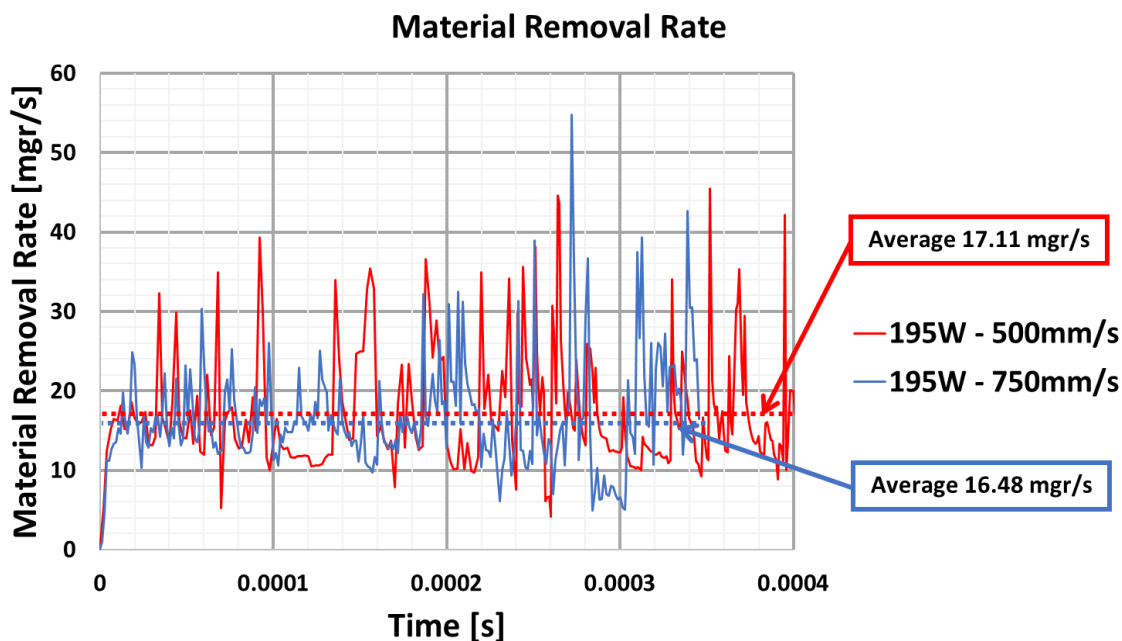
Αυτό το φαινόμενο ποσοτικοποιείται στο Διάγραμμα 26:



Διάγραμμα 26 Ποσοστό μείωσης της μέγιστης έντασης του λέιζερ.

Στην αρχή, όπου το keyhole συνεχώς γίνεται και βαθύτερο, το ποσοστό μείωσης της μέγιστης έντασης του λέιζερ αυξάνεται. Όταν το keyhole φτάνει στη μόνιμη κατάσταση και το βάθος του δεν αλλάζει, το ποσοστό μείωσης της μέγιστης έντασης του λέιζερ ταλαντώνεται γύρω από μία σταθερή τιμή.

Ρυθμός αποβολής υλικού



Διάγραμμα 27 Ρυθμός αποβολής υλικού.

Όπως παρατηρείται στο Διάγραμμα 27, ο ρυθμός αποβολής υλικού δεν είναι σταθερός, αλλά εξαρτάται από την σχετική θέση μεταξύ της ακτίνας του λέιζερ και του τήγματος. Συγκεκριμένα, οι κορυφές του διαγράμματος αναπαριστούν τις στιγμές που η ακτίνα του λέιζερ είναι πάνω από το τηγμένο υλικό (υλικό με θερμοκρασίες άνω των 1923.15K) αυξάνοντας ακόμα περισσότερο την θερμοκρασία σε αυτή την περιοχή, που αυξάνει την εξάτμιση του υλικού. Αντίθετα, τα ελάχιστα του διαγράμματος αντιπροσωπεύουν τις στιγμές που η ακτίνα του λέιζερ κινείται μπροστά προς μία «νέα» στερεή περιοχή (με θερμοκρασίες κάτω των 1923.15K). Σε αυτή την περίπτωση το υλικό χρειάζεται πρώτα να τηχθεί, οπότε ο ρυθμός εξάτμισης εδώ είναι χαμηλότερος.

Ακόμα, για σταθερή ισχύ λέιζερ και ταχύτητα σάρωσης, οι τιμές του ρυθμού αποβολής υλικού φαίνεται να είναι ανεξάρτητες από το βάθος και το πλάτος του keyhole. Αντίθετα, για ίδιες ισχύς λέιζερ και διαφορετικές ταχύτητες σάρωσης ο μέσος ρυθμός αποβολής υλικού αλλάζει. Συγκεκριμένα, για χαμηλές ταχύτητες σάρωσης, περισσότερη θερμότητα απορροφάται από την κάθε περιοχή του μοντέλου, οπότε η θερμοκρασία αυξάνεται περισσότερο και μεγαλύτερη μάζα αφαιρείται. Αυτό οδηγεί σε μεγαλύτερο μέσο ρυθμό αποβολής υλικού στο 195W-500mm/s από ότι στο 195W-750mm/s.

Συμπεράσματα

Στην παρούσα διπλωματική εργασία, αναπτύσσεται ένα θερμικό μοντέλο για την πρόβλεψη του πλάτους και του βάθους SLM-κατεργασμένων τεμαχίων Ti6Al4V μονού περάσματος με ιδιότητες που εξαρτώνται από τη θερμοκρασία και χρησιμοποιώντας μόνο έναν άγνωστο συντελεστή που απαιτεί καλιμπράρισμα. Η εξάτμιση του υλικού και η αφαίρεση μάζας, μέσω της παραμόρφωσης του πλέγματος, έχουν επίσης συμπεριληφθεί προκειμένου να προσομοιωθεί το φαινόμενο του keyhole. Οι προσομοιώσεις που πραγματοποιήθηκαν είναι οι εξής: α) 50W-1200mm/s (conduction μορφή), β) 195W-750mm/s (keyhole μορφή), γ) 195W-500mm/s (keyhole μορφή).

Τα αποτελέσματα έδειξαν ότι:

- Η πρόβλεψη του πλάτους και του βάθους σε όλες τις περιπτώσεις είναι σε συμφωνία με τα πειραματικά δεδομένα από τη βιβλιογραφία, καθώς όλα τα σφάλματα είναι κάτω από 16%.
- Ο υψηλός λόγος ταχύτητας σάρωσης προς ισχύ λέιζερ που χρησιμοποιήθηκε στην conduction μορφή οδηγεί σε ακατάλληλα τελικά προϊόντα με σφαιρικά ελαττώματα και ασυνέχειες. Παρόλα αυτά, το μοντέλο της παρούσας εργασίας μπορεί να προβλέψει αυτά τα ελαττώματα.
- Στην keyhole μορφή, συμπεριλαμβάνεται η εξάτμιση του υλικού και η αφαίρεση μάζας. Επιπλέον, το μοντέλο που προτείνεται στην παρούσα εργασία όχι μόνον προβλέπει το πλάτος και το βάθος του keyhole, αλλά επίσης προσομοιώνει και τις περιοχές των μαρτενσιτών α' (πρωτεύων) και α' (δευτερεύων).

Πρόταση για μελλοντική έρευνα

Προκειμένου να μειωθεί ο υπολογιστικός χρόνος και το κόστος, το παρών μοντέλο δεν περιλαμβάνει ρευστομηχανικά φαινόμενα, όπως είναι η ροή του τήγματος και το φαινόμενο Marangoni, με αποτέλεσμα να μην μπορεί να προβλέψει την σύνθλιψη των πλαϊνών τοιχωμάτων του keyhole. Οπότε, ως μελλοντική έρευνα, το παρών μοντέλο θα μπορούσε να συμπληρωθεί με τα ρευστομηχανικά φαινόμενα, προκειμένου να προσομοιώσει πλήρως την SLM κατεργασία.

Βιβλιογραφία

- [1] Z. Zhang *et al.*, “3-Dimensional heat transfer modeling for laser powder-bed fusion additive manufacturing with volumetric heat sources based on varied thermal conductivity and absorptivity,” *Opt. Laser Technol.*, vol. 109, no. August 2018, pp. 297–312, 2019, doi: 10.1016/j.optlastec.2018.08.012.
- [2] K. H. Lee and G. J. Yun, “A novel heat source model for analysis of melt Pool evolution in selective laser melting process,” *Addit. Manuf.*, vol. 36, no. August, p. 101497, 2020, doi: 10.1016/j.addma.2020.101497.
- [3] D. Gu, C. Ma, M. Xia, D. Dai, and Q. Shi, “A Multiscale Understanding of the Thermodynamic and Kinetic Mechanisms of Laser Additive Manufacturing,” *Engineering*, vol. 3, no. 5, pp. 675–684, 2017, doi: 10.1016/J.ENG.2017.05.011.
- [4] S. A. Khairallah, A. T. Anderson, A. Rubenchik, and W. E. King, “Laser powder-bed fusion additive manufacturing: Physics of complex melt flow and formation mechanisms of pores, spatter, and denudation zones,” *Acta Mater.*, vol. 108, pp. 36–45, 2016, doi: 10.1016/j.actamat.2016.02.014.
- [5] D. Dai and D. Gu, “Effect of metal vaporization behavior on keyhole-mode surface morphology of selective laser melted composites using different protective atmospheres,” *Appl. Surf. Sci.*, vol. 355, pp. 310–319, 2015, doi: 10.1016/j.apsusc.2015.07.044.
- [6] T. N. Le and Y. L. Lo, “Effects of sulfur concentration and Marangoni convection on melt-pool formation in transition mode of selective laser melting process,” *Mater. Des.*, vol. 179, p. 107866, 2019, doi: 10.1016/j.matdes.2019.107866.
- [7] M. Miyagi and J. Wang, “Keyhole dynamics and morphology visualized by in-situ X-ray imaging in laser melting of austenitic stainless steel,” *J. Mater. Process. Technol.*, vol. 282, no. October 2019, p. 116673, 2020, doi: 10.1016/j.jmatprotec.2020.116673.
- [8] T. Heeling, M. Cloots, and K. Wegener, “Melt pool simulation for the evaluation of process parameters in selective laser melting,” *Addit. Manuf.*, vol. 14, pp. 116–125, 2017, doi: 10.1016/j.addma.2017.02.003.
- [9] H. Wang and Y. Zou, “Microscale interaction between laser and metal powder in powder-bed additive manufacturing: Conduction mode versus keyhole mode,” *Int. J. Heat Mass Transf.*, vol. 142, p. 118473, 2019, doi: 10.1016/j.ijheatmasstransfer.2019.118473.
- [10] W. E. King *et al.*, “Observation of keyhole-mode laser melting in laser powder-bed fusion additive manufacturing,” *J. Mater. Process. Technol.*, vol. 214, no. 12, pp. 2915–2925, 2014, doi: 10.1016/j.jmatprotec.2014.06.005.
- [11] L. Caprio, A. G. Demir, and B. Previtali, “Observing molten pool surface oscillations during keyhole processing in laser powder bed fusion as a novel method to estimate the penetration depth,” *Addit. Manuf.*, vol. 36, no. June, 2020, doi: 10.1016/j.addma.2020.101470.
- [12] U. Scipioni Bertoli, A. J. Wolfer, M. J. Matthews, J. P. R. Delplanque, and J. M. Schoenung, “On the limitations of Volumetric Energy Density as a design parameter for Selective Laser Melting,” *Mater. Des.*, vol. 113, pp. 331–340, 2017, doi: 10.1016/j.matdes.2016.10.037.

- [13] T. Qi, H. Zhu, H. Zhang, J. Yin, L. Ke, and X. Zeng, "Selective laser melting of Al7050 powder: Melting mode transition and comparison of the characteristics between the keyhole and conduction mode," *Mater. Des.*, vol. 135, pp. 257–266, 2017, doi: 10.1016/j.matdes.2017.09.014.
- [14] D. Zhang, P. Zhang, Z. Liu, Z. Feng, C. Wang, and Y. Guo, "Thermofluid field of molten pool and its effects during selective laser melting (SLM) of Inconel 718 alloy," *Addit. Manuf.*, vol. 21, no. 100, pp. 567–578, 2018, doi: 10.1016/j.addma.2018.03.031.
- [15] E. L. Papazoglou, N. L. Karkalos, and A. P. Markopoulos, "A comprehensive study on thermal modeling of SLM process under conduction mode using FEM."
- [16] S. Pang, L. Chen, J. Zhou, Y. Yin, and T. Chen, "A three-dimensional sharp interface model for self-consistent keyhole and weld pool dynamics in deep penetration laser welding," *J. Phys. D. Appl. Phys.*, vol. 44, no. 2, 2011, doi: 10.1088/0022-3727/44/2/025301.
- [17] J. Volpp and F. Vollertsen, "Analytical modeling of the keyhole including multiple reflections for analysis of the influence of different laser intensity distributions on keyhole geometry," *Phys. Procedia*, vol. 41, pp. 460–468, 2013, doi: 10.1016/j.phpro.2013.03.102.
- [18] V. Holman, *Heat Transfer (10th edition)*, vol. 15, no. 3. 1999.
- [19] J. R. Zhuang, Y. T. Lee, W. H. Hsieh, and A. S. Yang, "Determination of melt pool dimensions using DOE-FEM and RSM with process window during SLM of Ti6Al4V powder," *Opt. Laser Technol.*, vol. 103, pp. 59–76, 2018, doi: 10.1016/j.optlastec.2018.01.013.
- [20] K. C. Mills, *Recommended Values of Thermophysical Properties for Selected Commercial Alloys*. 2002.
- [21] M. Bass, E. Stryland, D. Williams, and W. Wolfe, *Handbook of Optics- Devices, Measurements and Properties*, Second. McGraw-Hill, 1377.
- [22] L. Li, K. Yu, K. Zhang, and Y. Liu, "Study of Ti-6Al-4V alloy spectral emissivity characteristics during thermal oxidation process," *Int. J. Heat Mass Transf.*, vol. 101, pp. 699–706, 2016, doi: 10.1016/j.ijheatmasstransfer.2016.05.069.
- [23] J. Yan, Y. Zhou, R. Gu, X. Zhang, W. M. Quach, and M. Yan, "A comprehensive study of steel powders (316L, H13, P20 and 18Ni300) for their selective laser melting additive manufacturing," *Metals (Basel)*, vol. 9, no. 1, 2019, doi: 10.3390/met9010086.
- [24] S. S. Sih and J. W. Barlow, "The prediction of the emissivity and thermal conductivity of powder beds," *Part. Sci. Technol.*, vol. 22, no. 4, pp. 427–440, 2004, doi: 10.1080/02726350490501682.
- [25] E. Mirkoohi, D. E. Seivers, H. Garmestani, and S. Y. Liang, "Heat source modeling in selective laser melting," *Materials (Basel)*, vol. 12, no. 13, pp. 1–18, 2019, doi: 10.3390/ma12132052.
- [26] M. Courtois *et al.*, "The numerical challenges in multiphysical modeling of laser welding with arbitrary Lagrangian-Eulerian method," *COMSOL Conf.*, no. 1, p. 8, 2018.
- [27] K. Hirano, R. Fabbro, and M. Muller, "Study on temperature dependence of recoil pressure near the boiling temperature - Towards better modeling and simulation," *ICALEO 2012 - 31st Int. Congr. Appl. Lasers Electro-Optics*, no. December 2017, pp.

- 678–684, 2012, doi: 10.2351/1.5062526.
- [28] P. Cirp, S. Weber, J. Montero, M. Bleckmann, K. Paetzold, and A. Siadat, “Study of Layered Tetrahedral and Cartesian meshing in Additive Manufacturing Simulation A new methodology to analyze the functional and physical architecture of Cartesian meshing in Additive Manufacturing Simulation Web,” *Procedia CIRP*, vol. 91, pp. 522–527, 2020, doi: 10.1016/j.procir.2020.02.209.
- [29] L. Qi, C. Guo-Dong, and W. Shu-Zhen, “Softness-based adaptive mesh refinement algorithm for soft tissue deformation,” *BioSystems*, vol. 191–192, no. February, 2020, doi: 10.1016/j.biosystems.2020.104103.
- [30] J. J. S. Dilip *et al.*, “Influence of processing parameters on the evolution of melt pool, porosity, and microstructures in Ti-6Al-4V alloy parts fabricated by selective laser melting,” *Prog. Addit. Manuf.*, vol. 2, no. 3, pp. 157–167, 2017, doi: 10.1007/s40964-017-0030-2.
- [31] Y. Fu, C.;Guo, “3-Dimnsional Finite Element Modeling of Selective Laser Melting Ti6Al4V Alloy,” p. 283, 1386.